



University
of Glasgow

Redzuan, Norizah (2010) *Cold plasma air decontamination*. PhD thesis.

<http://theses.gla.ac.uk/2286/>

Copyright and moral rights for this thesis are retained by the author

A copy can be downloaded for personal non-commercial research or study, without prior permission or charge

This thesis cannot be reproduced or quoted extensively from without first obtaining permission in writing from the Author

The content must not be changed in any way or sold commercially in any format or medium without the formal permission of the Author

When referring to this work, full bibliographic details including the author, title, awarding institution and date of the thesis must be given

COLD PLASMA AIR DECONTAMINATION

Norizah Redzuan

**Submitted for the Degree of Ph. D. in the
Department of Mechanical Engineering,
University of Glasgow**

May 2010

Acknowledgements

“In the name of Allah, the Most Gracious and the Most Merciful”

Most gratitude to Allah for giving me time and strength to write this humble theses. Many thanks to The Malaysian Government and Universiti Teknologi Malaysia for sponsoring my PhD programme. This work was funded in part by Nvirocleantech PLC. Overall, the money provided by them was used to research and develop laser and plasma based systems for cleaning air. Takashi Mine and Anand Krishnan developed many of the experimental and microbiological protocols and supported the experimental work on seeded air and Takashi contributed with the laser marked electrode. Dan McNulty and Ian Watson developed the Dome booster concept in conjunction with the electrode development, reported herein.

My sincere thanks and appreciation to my supervisor Dr Ian A Watson who always provided his time, guidance, encouragement, sourcing funds and advice throughout this work. My special thanks to Mr Ian A. Peden for always being there, ready to help in the project development and achieving the goals. I always sought his advice, especially in programming. My appreciation also goes to the technical staff: Mr Kaz Pechiowiak, Mr Brian Robb, Mr Denis Kearns, Mr Gordon Hicks, Mr Bernard Hoey and Mr. George Silvie; without their help, my project would never have been completed. I appreciate and love all my dear friends: Takashi, Eimear, Anand, Dan, Luciano, Adrian and Weeam. We worked together in a large group and supported each other's research.

For you

Dearest husband, Omar
Understanding children, Anas, Sakinah & Raihan.
Loving mother, Jumi
Beloved late father, Haji Redzuan
My late nephew, Sabri
Father-in-law Haji Ahmad
Mother-in-law Maimunah

“Love with Tenderness is Endless”

ABSTRACT

Cold Plasma Air Decontamination

Cold Plasma Discharges offer wide decontamination scenarios relevant to environmental, food and drink or clean room applications. The option to operate the discharge system in atmospheric or sub-atmospheric condition provides an opportunity to investigate a low-cost and simple system design. UV to NIR (200nm to 700nm) can be emitted by pulsed cold plasma discharge systems that operate at atmospheric pressure. Different wavelengths emitted from the discharge depend on the pressure and the type of gas mix used in the systems. The scope of the work involved in this research was to design and develop a prototype cold plasma system for air at atmospheric pressure. The prototype was used for air decontamination by passing seeded and unseeded air between the electrodes gap.

Modelling of the discharge and pulse forming network circuit systems was carried out in MultiSim to investigate the circuit characteristic. The components values ie: capacitors, stray inductors and resistors in the model system are interchangeable which enabled simulation of individual component effects on the output pulse shape and magnitude. The optimum component properties from the modelling were used as a guide to designing the system.

The main discharge system contained a pair of Chang Uniform Field Electrodes which were manufactured in-house, and provided a discharge area of 1.0cm x 60.0 cm. The discharge volume is varied depending on the gap between of the anode and cathode. Preionisation was achieved via trigger wire, built within the discharge system. This promotes the ionisation of the gas in between the electrodes in enhancing uniform discharge characteristics. Different types of electrodes were made from aluminium with the discharge size 300mm x 200mm, laser marked and unmarked surface were also used in the system in order to obtain wider discharge surface and reduce manufacturing costs.

The DC discharge system used 75 nF charging capacitors and was charged to maximum of about 7.8 kV DC. The system was mounted on low inductance copper plate. High Voltage DC between 6 to 8 kV DC, 80mA constant current power supply was connected to the discharge circuit, thus a high current pulse in very narrow time (1ns) was produced. The shape of the pulse was observed by using an oscilloscope. The preionisation (from commercial spark plugs) were used with independent control switching which was manually triggered just before the operational breakdown voltage was achieved. Nearly stable discharges were recorded at gas mixed of CO₂:N₂:He for the gas ratio 1:1:8 with various gas pressures ranging from 10 to 900 mbar.

An AC transformer was used in the prototypes of the Dome and the Tubular discharge systems to develop a switchless air discharge system to produce plasma. Capacitors of 1.4 nF, 2.7, 5.4 and 8.1 nF were used. This approach was to determine the optimum V-I characteristics which were provided from this simple operation procedure. Investigation was focused on obtaining deposition with a stable plasma discharge output. Micro-organisms decontamination using the plasma were done and the kill percentage were considered.

Potential applications of the developed prototype systems are on air quality treatment for small room or in-flight air quality. The discharge system also can be used to treat water, food and drink and other environmental research concerning cold plasma applications.

Table of Contents	Page
Chapter 1 Introduction and Objective of Work	
1.1 Cold pulsed plasma discharge system	1
1.1.1 Plasma discharge	2
1.2 Pulse Circuit	2
1.2.1 Storing energy	3
1.2.1.1 Resistive charging	3
1.2.1.2 DC charging	4
1.2.1.3 Resonant charging with switch mode power supply (SMPS)	5
1.2.1.4 AC charging	7
1.2.2 Discharging the stored energy	8
1.2.2.1 Switched discharges	9
1.2.2.2 Switchless main discharge switch in TEA CO ₂ laser operation	10
1.2.2.3 Transverse discharge	10
1.2.2.4 Segmented discharge	11
1.2.2.5 UFE discharge	11
1.3 Preionisation	12
1.3.1 UV preionisation	12
1.3.1.1 Double discharge plasma	13
1.3.1.2 Delay between the auxiliary pre-discharge and the main discharge	13
1.3.2 Corona preionisation	14
1.3.2.1 Preionisation dielectric materials	15

1.4	Uniform field electrodes	16
1.4.1	UFE analytical functions	17
1.4.1.1	Rogowski profile	18
1.4.1.2	Chang profile	18
1.5	Paschen Law	19
1.6	Cold plasma application on air treatment	21
1.7	Objective of research	22

Chapter 2 Modelling Discharge Systems and Uniform Field Electrode

2.1	Modelling of the system	32
2.2	Discharge model	32
2.3	Equivalent circuit of spark gap and main electrode	33
2.3.1	Calculation of equivalent electrical value	34
2.3.1.1	Equivalent of resistance (R) value from numerical modelling	34
2.3.1.2	Equivalent R-L-C values from pulse discharge	35
2.4	Modeling of main discharge circuit on Multisim8	36
2.4.1	DC discharge parameters	36
2.4.2	DC discharge simulation results	36
2.4.3	AC discharge simulation	37
2.4.4	AC discharge with dielectric simulation	37
2.5	The Blumlein discharge	38
2.6	Modelling of electric field and flux density between electrode	38
2.6.1	Conformal mapping	39
2.7	Conclusions	41

Chapter 3 Development of Discharge System

3.1	Introduction	57
3.2	Switchless, self-sustained discharge systems	57
3.2.1	High voltage DC charging power supply	58
3.2.2	Storage capacitor (C_s)	59
3.2.3	Electrodes	59
3.2.3.1	Anode and Cathode holder	60
3.3	Electrode types	60
3.3.1	Planar brass electrode	60
3.3.2	Chang's uniform field electrode	61
3.4	Independent spark plug preionisation	61
3.5	Discharge chamber	62
3.6	Gas systems	63
3.6.1	Vacuum systems	64
3.7	Flow shaping and clearance ratio	64
3.8	Data acquisition	65
3.9	DC Experiment	65
3.9.1	Experimental set-up	66
3.9.1.1	Discharge chamber cleaning	67
3.9.1.2	Electrode gap setting	67
3.10	Results on general test of discharge system	68
3.10.1	Breakdown voltages for air at atmospheric pressure and partial vacuum	68
3.10.2	Breakdown of He, N ₂ and CO ₂	69
3.10.3	Voltage and current characteristic for gas ratio 1:1:4 (CO ₂ : N ₂ : He)	70

3.10.4	Influence of flow shaping and static pressure gas circulation	72
3.10.4.1	Axial flow fan clearing ratio	72
3.10.4.2	Radial flow fan clearing ratio	73
3.11	AC discharge	74
3.11.1	AC transformer	75
3.11.2	Capacitors	75
3.11.3	Preionisation	76
3.11.4	Spectrum measurement	76
3.12	AC on He and N ₂ discharge	77
3.12.1	Results of the discharge for gas ratio 1:1:4 (CO ₂ : N ₂ : He)	77
3.13	AC air discharges	78
3.13.1	Air discharge with trigger wire preioniser	78
3.13.2	Air discharge with dielectric material over the cathode	79
3.13.2.1	Mylar	79
3.13.2.2	Duralar	80
3.13.2.3	Dielectric discharge comparison	81
3.14	Air discharge for Blumlien system	82
3.15	Discussions and conclusions	82
Chapter 4 Electrode Design		
4.1	Introduction	131
4.2	Electrode attributes	131
4.2.1	Electrode materials	132
4.2.1.1	Brass	132
4.2.1.2	Aluminium	132

4.3	Types of electrode	133
4.3.1	Planar electrode	133
4.3.1.1	Planar electrodes profile	133
4.3.1.2	Manufacturing of planar electrodes	134
4.3.2	Uniform field electrode	135
4.3.2.1	Chang's uniform field electrode	135
4.3.2.2	Manufacturing of Chang uniform field electrode	136
4.3.2.3	Compact Chang's electrode	137
4.3.3	Aluminium electrode	138
4.3.3.1	Aluminium electrode profile	138
4.3.3.2	Manufacturing of aluminium electrode	138
4.3.4	Laser marked aluminium electrode	139
4.3.4.1	Marked aluminium electrode profile	139
4.3.4.2	Manufacturing of aluminium marked electrode	140
4.4	Electrode surface roughness measurement	141
4.5	Electrode holder	142
4.6	Scanning electron microscope (SEM) for electrodes surface analysis	143
4.6.1	Energy dispersive X-ray (EDAX) analysis on electrodes	144
4.7	Conclusions	144

Chapter 5 Air Treatment Using Plasma Discharge

5.1	Introduction	168
5.2	Dome discharge system	169
5.3	Tubular discharge system	169
5.4	The experimental protocol for <i>Bacillus Globigii</i> (BG)	170
5.4.1	The micro-organism preparation	170

5.4.2	The BG decontamination experiment procedures	170
5.4.3	The BG decontamination experimental set-up	171
5.5	Effect of plasma on micro-organism decontamination	171
5.5.1	Stand alone UFE Chang discharge with trigger wire preionisation	171
5.5.2	Dome plasma discharge effect on BG with dielectric material	172
	5.5.2.1 Results of the Dome discharge decontamination	173
5.5.3	Tubular discharge with aluminium electrodes air plasma discharge with dielectric material	174
	5.5.3.1 Aluminium unmarked electrode plasma	175
	5.5.3.2 Aluminium marked and unmarked electrode plasma	176
5.6	Ozone measurement	177
5.6.1	Measurement set-up	177
5.6.2	Ozone measurement for the Chang profiled Dome discharge	178
5.6.3	Ozone creation for marked and unmarked electrodes	178
5.6.4	Ozone production rates compared to commercial ozone generator	179
5.6.5	Power consumption rates	180
5.7	Conclusions	180
Chapter 6	Conclusions and Future Work	204
	References	211
	Appendices	
	Appendix 2A	216
	Appendix 2B	217
	Appendix 3A	232
	Appendix 3B	233

Appendix 3C	234
APPENDIX 4A	237
Appendix 4A-1	240
Appendix 4B	241
Appendix 4C	242
Appendix 5A	243

List of Figures

Chapter 1	Page
Figure 1-1	A typical electrical high voltage pulse circuit for TE laser discharge [Spyrou <i>et al</i> , 1995]. 25
Figure 1-2	R-C network by Serafetinides [Serafetinades <i>et al</i> , 1989]. 25
Figure 1-3	(a) Typical D-C network , (b) The charging current (i), the voltage across the capacitor (V_c) and voltage across the inductor (V_L). 25
Figure 1-4	(a) D-C resonant network with diode, (b)The charging current (i) and voltage across the capacitor (V_c) is twice of source voltage (V_s). 26
Figure 1-5	Block diagram of SMPS operation on AC –DC output voltage regulator. 27
Figure 1-6	High voltage switch mode schematic diagram [Saleh <i>et al</i> , 1991]. 27
Figure 1-7	(a) Circuit diagram of the developed portable prototype of the ozone generator, (b) Portable ozone generator [Alonso <i>et al</i> , 2004]. 28
Figure 1-8	Single phase AC resonant circuit [Bhadani, <i>et al</i> ,1984]. 29
Figure 1-9	Schematic diagram of the AC pulser circuit with full wave bridge rectifier [Bhadani, <i>et al</i> , 1984]. 29
Figure 1-10	Comparison of the performance of a helical TEA laser with inductance and resistance [Pearson <i>et al</i> , 1972]. 30
Figure 1-11	Double discharge circuit by Laflamme [Laflamme, 1970]. 30
Figure 1-12	Uniform field electrode , (a) Plane x & y, (b) Electrostatic flux (U) and potential plane (V). 31
Figure 1-13	Paschen Curve for air at various pressures, where minimum was ~0.012 torr and maximum of about 160 torr [Naidu and Kamaraju, 1995]. 31

Chapter 2	Page
Figure 2-1	The model circuit of the discharge system. 42
Figure 2-2	Spark gap equivalent circuit 43
Figure 2-3	Electrode equivalent circuit. 43
Figure 2-4	The modelling discharge circuit (a) Main discharge circuit (b) An equivalent circuit with stray inductance (L_d) 11.5 nH, Capacitance $C_d = 1.01$ nF and $R_d = 100$ m Ω . This DC discharge was modeled in vacuum condition. 44
Figure 2-5	Comparison of capacitor charging pulses for model in Figure 2-4 (a) Pulse from the 75 nF capacitor bank of the DC main discharge (b) 750 nF capacitor pulse. 45
Figure 2-6	An AC simulation discharge (a) The electrical circuit (b) An equivalent modelling circuit diagram for the AC in air at atmospheric pressure with Chang electrodes and 2.7 nF capacitors and 6 kV RMS supply. 46
Figure 2-7	The simulation result showing the discharge current and voltage measured from the AC air discharge in Figure 2-6 (a) The current peak is about 5.25 kA (b) The maximum peak voltage is about 12 kV. 47
Figure 2-8	The simulation results with the AC discharge with a pair of 2.7 nF capacitors with duralar (a) The modeling circuit (b) The discharge current across the electrodes gap (c) The discharge voltage. 48
Figure 2-9	The AC discharge transient analysis with 2 layers of duralar and 3 pairs of 2.7 nF capacitors (a) The discharge model with two layers of duralar and 6 kV RMS supply (b) The discharge current from the model. At node 1 (c) The discharge voltage at node 1. 49
Figure 2-10	The Blumlien discharge system (a) The Blumlien discharge modelling system (b) The discharge current with maximum pulse of about 3.75 kA. 50
Figure 2-11	The mesh of flux (horizontal lines) and potential (vertical lines) function of: (a) The Rogowski profile and (b) The Chang profile. 51
Figure 2-12	Linearity in the central electric field strength using: a) The Rogowski function and b) The Chang function. 52

Figure 2-13	The plot of inverse function of: a) the Rogowski and (b) the Chang functions.	53
Figure 2-14	The inverse electrical potential function changes across the central plane: (a) the Rogowski , and (b) the Chang.	54
Figure 2-15	The inverse of the flux function on: a) the Rogowski and b) the Chang.	55
Figure 2-16	The effect of the empirical constant k value effect on the electrode edges a) k= 0.6, b) k=0.2 and c) k=0.02.	56

Chapter 3

Figure 3-1	(a) The main discharge electrical circuit with the electrode storage capacitor $C_1= 75 \text{ nF}$, $R_1 =100 \text{ k}\Omega$ discharge current limiter, $R_2 = 100 \text{ M}\Omega$. (b) The electrical equivalent with the stray inductance of the electrode and the circuit $L_d =11.5 \text{ nH}$ and voltage divider $R_d= 100\text{m}\Omega$.	84
Figure 3-2	(a). Constant current 6 kV DC power supply unit, (b) the interface controller with adjustable voltage, (c) reset toggle to confirm the complete discharging of the power supply and (d) the storage capacitor in insulation box.	85
Figure 3-3	(a) Storage capacitance (75 nF) rated at 25 kV with 100 M Ω resistor as voltage divider and 100 k Ω resistor to limit the discharge time. (b) Storage capacitors insulation enclosure shows the connection to the DC 6 kV PSU, the voltage monitor is to connect to control box digital display or multi meter.	86
Figure 3-4	Cathode holder was adjustable by inserting washers in between the bracket and the base plate.	87
Figure 3-5	Plane brass electrodes used in the discharge.	87
Figure 3-6	Changes uniform field electrode: (a) Top view of flat surfaces (b) Side view and (c) Edge view.	88
Figure 3-7	Spark plug preioniser setting distance to alongside electrodes.	89
Figure 3-8	The schematic model of the spark plug preioniser circuit.	89

Figure 3-9	Development of the spark plugs preionisation system. (a) The mounting. (b) The set-up in the discharge chamber and (c) The set of the of the preionisation system.	90
Figure 3-10	The gas flow system.	91
Figure 3-11	(a) The vacuum system illustration and, (b). the set up on the system development.	92
Figure 3-12	Experimental set up.	93
Figure 3-13	The electrode holder set-up illustration.	93
Figure 3-14	Voltage breakdown of air at atmospheric pressure and partial vacuum (500 mbar). The plane brass electrode gap was varied from 3 to 7 mm. No error bar because one set data was used.	94
Figure 3-15	The intermittent arcs that occurred with an electrode gap of 7 mm.	94
Figure 3-16	Paschen breakdown for helium, nitrogen and carbon dioxide relative to gas pressure. The electrode gap is constant at 5 mm. No error bar because one set data was used.	95
Figure 3-17	E/N values for N ₂ , CO ₂ and He versus pressures.	95
Figure 3-18	Example of oscilloscope display to measure discharge currents and voltages. The top display is the voltage and bottom is current (~3.0 kA/cm).	96
Figure 3-19	Discharge voltage at total gas pressure of 120 mbar, 130 mbar and 140 mbar in function of time. The ratio of the gas was 1:1:8.	96
Figure 3-20	Glow discharge for 1:1:8 viewed from the discharge chamber window.	97
Figure 3-21	Peak discharge voltages for various total gas pressure wit a gas ratio of 1:1:8 with about 5%.	98
Figure 3-22	The E/N values for 1:1:8 versus pressure with about 5%.	98
Figure 3-23	Discharge current in function of tine at different total gas pressure. The ratio of the gas is 1:1:8.	99

Figure 3-24	Discharge pulse currents on close up time scale. The currents pulse length are broader. at 140 mbar, 270mbar, 404 mbar and 501 mbar, indicating more energy were produced.	100
Figure 3-25	Peak discharge current for different pressures with a gas ratio of 1:1:8.	100
Figure 3-26	(a) The peak voltages and peak currents at different gas pressure with ratio of 1:1:8 with 5% error and (b) The peak power of the discharge.	101
Figure 3-27	The V-I waveform for the discharge with gas ratio 1:1:8 at pressure of 140 mbar, captured separately with the same time base.	102
Figure 3-28	The position of the fan to investigate the clearing ratio where v is the flow velocity, (a) transverse flow and (b) longitudinal flow.	103
Figure 3-29	Flow shaping used with the axial flow computer fan.	104
Figure 3-30	Radial flow fan used for the clearing ratio tests, fan was placed longitudinally to the electrode.	104
Figure 3-31	Influence of longitudinal flow on discharge currents measured at different gas pressure. The clearing ratio $CR = 0.5$.	105
Figure 3-32	Influence of longitudinal flow on discharge voltages measured at different gas pressure. The clearing ratio $CR = 0.5$.	105
Figure 3-33	Influence of longitudinal flow on discharge currents pulse length measured at different gas pressure. The clearing ratio $CR = 0.5$.	106
Figure 3-34	Influence of longitudinal flow on discharge voltages pulse length measured at different gas pressure. The clearing ratio $CR = 0.5$.	106
Figure 3-35	Influence of longitudinal flow on discharge voltages pulse frequency measured at different gas pressure. The clearing ratio $CR = 0.5$.	107
Figure 3-36	TEC AC transformer with trigger wire preioniser set-up.	108

Figure 3-37	TEC AC transformer with three pairs of 2.7nF capacitors.	108
Figure 3-38	Resin Block transformer with center tap made the voltage ± 5 kV. Diode may be used to rectify the voltage to +5 kV.	109
Figure 3-39	The AC transformers: (a) TEC transformer and (b) The Resin block transformer.	110
Figure 3-40	Preionsation held with the PTFE disk.	111
Figure 3-41	The setup for the helium glow discharge with preioniser.	112
Figure 3-42	Photon Control spectrograph fibre optic with the helium glow discharge.	112
Figure 3-43	Helium discharge spectrum captured with Photon Control Spectrograph. The amplitude for the helium at 20 mbar discharge was not strong.	113
Figure 3-44	Glow discharge of N ₂ at 20 mbar, (a) The set-up and glow view from the discharge chamber window. (b) The close up view of the glow. Stronger glow near the surface of the electrodes.	114
Figure 3-45	Nitrogen discharge spectrum at 50 mbar. The colour of the glow was brighter compare to 20 mbar.	115
Figure 3-46	Nitrogen discharge spectrum for 50 mbar with maximum amplitude at 1480 unit with narrow spikes within the range of deep UV to NIR (390 t- 860nm).	115
Figure 3-47	The glow chronology for 1:1:4 discahrge at 20 mabr. The glow became stronger as the input voltage increases. (a) The glow started at 4.87 kV input voltage, (b) 5.2 kV, (c) 5.8 kV and (d) 6.8 kV.	116
Figure 3-48	Discharge current from an AC discharge system with gas ratio 1:1:4 at total pressure of 50 mbar.	117
Figure 3-49	The air discharge set up with trigger wire preioniser. (a) The trigger wire was coupled to the anode. The distance of the centre of trigger wire to the side of the electrode was 7mm. (b) The cathode (bottom) was vertically adjustable to by the micrometer in Z direction . The probe was used to measure the drop voltage across the electrodes.	118
Figure 3-50	The misalignment of the preioniser glass tube where at a point,	119

	it touched the electrode and caused very strong localise arcs to develop it, melted and broke the glass tube which was deposited on the electrode surface.	
Figure 3-51	The electrode was cleaned and polished, however the stain was embedded.	120
Figure 3-52	Air discharge set-up which was done outside the discharge chamber. The gap of the electrodes was 3 mm. The circuitry is as shown in Figure 4-36.	120
Figure 3-53	The air discharge glow started at input voltage was 4.8 kV. When the voltage increases, the glow was maintained and then arcing at 7.2 kV.	121
Figure 5-54	AC discharge current in air at atmospheric pressure.	121
Figure 3-55	Two layers of mylar film were used to cover the electrode in order to improve the discharge quality. The mylar film total thickness was 100 μm .	122
Figure 3-56	Mylar was used to cover the cathode as replacement to the trigger wire preioniser. This was done in order to improve the quality of the discharge and minimize arcing in air discharge.	122
Figure 3-57	The condition of the electrodes after the discharge The bright mark on cathode was the result from the torn mylar.	123
Figure 3-58	The total thickness of the two layers of duralar was 150 μm . (a) The first layer of duralar developed white marks caused by the electrical discharge. The second layer had less white marks. No holes were punctured in the film by the discharges.	123
Figure 3-59	The air discharge pattern at 3 to 6mm electrode gap when two layers of duralar were used over the cathode. (a) Uniform discharge at 3mm gap, (b) strong filamentary discharge at 4mm gap, (c) Filamentary discharge at 5 mm gap. Discharges were stronger nearer the cathode.	124
Figure 3-60	Discharge current with two layers of duralar in air at atmospheric pressure.	125

Figure 3-61	The voltage drop ($V_d = V_{in} - V_{out}$) versus electrode gap for various dielectric materials were used over the electrode. Duralar could withstand the greatest voltage for 2 to 5mm gap. However when the electrode gap increases, the V_d increases and at 5 mm gap, the V_d values were close for all dielectric materials.	125
Figure 3-62	The output voltage discharge versus the electrode gap on Chang profile electrode with the dielectric material placed over the cathode. The output voltage for duralar and glass were linear .	126
Figure 3-63	The discharge current (I_d) for duralar was constant for electrode gap of 2-4 mm, compare to glass and mylar. Discharge current with mylar had a sudden increased when the gap increased.	126
Figure 3-64	The Blumlein circuit used in the air discharge. The Resin Block transformer was used to charge the 2 layers of duralar which acted as a 44 nF capacitance. The a spark gap was used to initiate the charging power into the main discharge system.	127
Figure 3-65	The illustration of the Blumlein system. The electrodes were made from stainless steel with diameter of 25 mm. The gap between electrodes was 3mm and the ball switch gap 1mm. Two layers of duralar were placed over the aluminium plates to serve as capacitance. Mild steel plate thickness was 1.mm.	128
Figure 3-66	The electrodes and the spark gap before the discharge.	129
Figure 3-67	The Blumlein discharge.	129
Figure 3-68	The Blumlein discharge spectral intensity.	130

Chapter 4

Figure 4-1	Electrodes attributes [Trtica <i>et. al</i> , 2003].	147
Figure 4-2	CAD drawing of planar brass electrode profile.	148
Figure 4-3	(a) Plane brass electrode machined marks surface with HSS end mill cutter average 32 $\mu\text{m Ra}$, (b) Polished surface with average 0.5 $\mu\text{m Ra}$.	149

Figure 4-4	Planar brass electrode (a) Top view with 10 mm width and 60 mm length (b) Side view with 6 mm thicknes. (c) Two screw holes to mount the electrodes to holders.	150
Figure 4-5	Chang function curves generated in Maple software.	151
Figure 4-6	Chang's electrode CAD three dimensional parts drawing.	152
Figure 4-7	Fixture for the machining of Chang UFE in CNC machine.	152
Figure 4-8	Machining tool path and orientation.	153
Figure 4-9	Machining of Chang's profile electrode with new set up fixture that reduces the machining time to 30 minutes.	153
Figure 4-10	Machined surface texture on Chang's profile electrode machine using tungsten carbide tool.	154
Figure 4-11	(a) Machine marks by carbide tool with average surface roughness of 26 $\mu\text{m Ra}$. (b) Polished surface of Chang's electrode. Different colour shows the different flatness. Average surface flatness in 0.5 $\mu\text{m Ra}$.	155
Figure 4-12	Compact Chang's profile electrode	156
Figure 4-13	Aluminium electrode profile	156
Figure 4-14	Flow of air sample through the aluminium electrode discharge.	157
Figure 4-15	Polished aluminium electrode.	158
Figure 4-16	Laser marking layout using regional method.	159
Figure 4-17	Laser marking process.	159
Figure 4-18	Finished laser marked aluminium electrode.	160
Figure 4-19	Aluminium bracket and PTFE plate holder of the first electrode holders designed in the research.	160
Figure 4-20	Adjustable x-y-z table electrode holder.	161
Figure 4-21	Vacuum feed-through mechanism.	162
Figure 4-22	Electrode holders for the Dome discharge with preionisers.	163

Figure 4-23	Clip-on aluminium electrode holder for maximum discharge exposure time.	
Figure 4-24	SEM electrodes surface analysis: (a) Aluminium electrode with 3 zones A, B and C, (b) Zone A the unmarked electrode surface, (c) Zone B with 50mm/s laser marked scan speed and (d) Zone C with 10 mm/s laser scan speed.	164
Figure 4-25	Comparison of brass and aluminium laser marked surface at scan speed of 50 mm/s.	165
Figure 4-26	EDAX for laser marked aluminium electrodes at different scan speed.	166
Figure 4-27	EDAX analysis on unmarked and marked brass electrodes.	167

Chapter 5

Figure 5-1	Stand alone electrodes and trigger wire preionisation with nutrient agar plate lawned with <i>E. coli</i> .	182
Figure 5-2	The Dome discharge system (a) The CAD drawing (b) Photograph of the Dome discharge made from rapid prototyping process with ABS material (c) The discharge circuit used with the Dome discharge system.	183
Figure 5-3	The Tubular discharge (a) The CAD drawing of the Tubular discharge with the electrode holders (b) The clipped on electrodes holders were attached (c) The prototype of the Tubular discharge.	184
Figure 5-4	The Tubular discharge capacitive arrangement (a) 1.4 nF (b) 2.7 nF (c) 5.4 nF and (d) 8.1 nF.	186
Figure 5-5	The micro-organism preparation and aerosol generator [Takashi Mine Personal Contact].	187
Figure 5-6	The Dome system experimental set-up where the plasma discharge was placed in a vertical position.	188
Figure 5-7	<i>E. coli</i> treatment with plasma discharge on UFE Chang profiled electrodes stand alone discharge.	189

Figure 5-8	The air discharge glow with two layers of durala placed over the cathode to test the Dome system with trigger wire preionisation . The electrode gap was 2.5 mm and the input voltage was 9 kV.	190
Figure 5-9	The spectrum of the air discharge with 2.5mm electrodes gap and the input voltage was 9 kV.	190
Figure 5-10	BG decontamination with the Dome system discharge, 2.5mm electrode gap with 2 layers of duralar, 1.4 nF capacitance, 2 minutes treatment and 9 kV input voltage.	191
Figure 5-11	The results from the repeated experiment results of BG decontamination on the Dome system discharge with 2.5mm gap, 2 layers of duralar, 1.42 nF and 9 kV input voltage.	192
Figure 5-12	BG decontamination % kill when passed through the Chang profiled discharge over 2 minutes in the Dome discharge system. The average of the killing was about 63% shown by the solid horizontal line.	193
Figure 5-13	BG kill % in a function of time (2,3,4 and 5 mins) in the Dome discharge system with 9 kV input voltage. (a) BG before and after treatment (b) BG Kill % in function of time.	194
Figure 5-14	Aluminium electrodes set-up with the air flow rate was 50 l/min.	195
Figure 5-15	Tubular plasma discharge system: (a) Aluminium electrode holder, (b) The electrode holder mounted to the Tubular discharge system, (c) The Tubular discharge in the clear plastic tube for air flow connection.	195
Figure 5-16	BG decontamination with both unmarked aluminium electrodes at 7.5 and 9 kV input voltage.	196
Figure 5-17	Comparing killing efficiency of marked and unmarked aluminium electrodes decontamination performance for input voltages of 5, 6, 7.5 and 8.5 kV.	197
Figure 5-18	The comparison of the BG decontamination averages with the pair of aluminium electrodes where, the marked and the unmarked pair (A) with standard deviation of 3% and the pair of both unmarked electrodes (B) with standard deviation of 1.25 %.	198
	The decontamination percentage kill against BG with the	198

Figure 5-19	pair of marked and unmarked electrodes with various input voltage.	
Figure 5-20	Decontamination percentage with various capacitances for the pair of marked and unmarked electrodes and the pair of both unmarked aluminium electrodes.	199
Figure 5-21	Decontamination of BG for unmarked aluminium electrodes at 7.5 and 8.5 kV input voltage and various capacitances.	199
Figure 5-22	Ozone measurement schematic experimental setup.	200
Figure 5-23	The ozone produced as a function of time for Chang profiled electrodes with units of ppb, $\mu\text{g}/\text{m}^3$ and μg .	200
Figure 5-24	Graph shows ozone formation as a function of time for the Chang profiled discharge was 4.25 ugs^{-1} (3.06 mgh^{-1}).	201
Figure 5-25	Ozone production rate on marked and unmarked aluminium electrodes with a 3mm gap for 1.4 to 8.1 nF. No error bars are shown because this was only done once.	201
Figure 5-26	Ozone production rate on marked and unmarked of aluminium electrodes with 3mm gap at 44.2 mgh^{-1} and 35.3 mgh^{-1} respectively.	202
Figure 5-27	The BG decontamination relative to the ozone production rate on marked and unmarked of aluminium electrodes at 3 mm gap for different capacitance. No error bar because only one data reading was used.	202
Figure 5-28	The plug-in commercial ozone generator.	203

List of Tables

Tables		Page
Chapter 1		
Table 1-1	Electrical properties of dielectric materials.	16
Chapter 2		
Table 1-2	The minimum breakdown voltage for various gases [Naidu, M. S. and Kamaraju, 1995]	20
Chapter 4		
Table 4-1	Electrode definition and dimension used referred from Trtica <i>et. al</i> , 2003.	146
Chapter 5		
Table 5-1	Total BG cfu before and after 7.5 and 9 kV on both unmarked electrodes.	175
Table 5-2	Percentage of <i>BG</i> kill with both the unmarked and marked-unmarked aluminium electrode pairs as a function of the capacitance.	177
Table 5-3	Relationship of the ozone generation for marked and unmarked aluminium electrodes with the variation of capacitance and the % kill.	179
Table 5-4	Ozone power consumption for the aluminium marked-unmarked and unmarked pair of electrodes.	180

Nomenclatures

AC	Alternative Current
ASSE	All-solid-state-exciter
ASTM	American Society for Testing and Materials
DC	Direct Current
HEPA	High Efficiency Particulate Air
HVAC	Heat Ventilation & Air Conditioning
HVDC	High Voltage Direct Current
L	Inductor
L_s	Spark gap inductor
MOSFET	Metal Oxide Semiconductor Field Effect Transistor
MPC	Magnetic pull compression
PRF	Pulse repetitive rate
Q	Coulomb
RC	Resistive Charging
R_s	Spark gap resistance
SCWP	Surface Wire Corona Preionisation
SMPS	Switch Mode Power Supply
TE	Transverse Excited
TEA	Transverse Excited at Atmospheric
U	Flux function
UFE	Uniform field electrode
UVGI	Ultraviolet Germicidal Irradiation
V	Potential function
V_s	Supply voltage
I	Current
ϵ_o	Absolute permittivity
ϵ_r	Relative permittivity
E_{in}	Input energy
E_o	Output energy
A	Area

d	Dielectric thickness
C	Capacitor
d	Electrode gap
k	Empirical constant
CR	Clearing ratio
SG	Spark gap
C_s	Storage capacitor
EMI	Electro Magnetic Interference
E_s	Energy stored
L_d	Main discharge inductance
R_d	Main discharge resistance
P	Power
l	Electrode length
w	Electrode width
V_c	Voltage across the capacitor
V_L	Voltage across the inductor
f	Frequency
v_d	Electron drift velocity
v	Flow velocity
L_e	Electrode inductance
U	Flux function
V	Electric potential
W	Imaginary plane
τ	Time constant
∇	Delta
ω	Resonant frequency
t	Time
σ	Discharge conductivity
n_e	Electron density
α	Townsend ionisation coefficient
E/N	Energy to no of electron ratio

Chapter 1

Introduction

1.1 Cold pulsed plasma discharge system

Pulse plasma systems share several common characteristics with TE laser systems. The most important is that they use electrical pulses over relatively short discharge times to excite volumes of gas in sealed chambers at atmospheric pressure or lower. This short pulse duration and high peak power discharge operation has two advantages. Firstly, it makes atmospheric pressure operation easily obtainable by applying voltages from about 20 to 50kV. Secondly, large amounts of energy can be deposited into the discharge to optimise the operating efficiency. However, short electrical pulse excitation is required, preferably of the order of nanoseconds to increase the discharge stability. This kind of discharge system with prolonged operation was reported by many including: Stark *et al* [1975], Walter [1984], Encinas *et al* [1991] and Torkamany *et al* [2006]. There is interest in investigating and developing plasma discharge systems by modifying concepts from commercially available pulsed, TEA CO₂ lasers [Dadelszen *et al*, 1991] or using similar electrical pulse discharge techniques [Korytchenko *et al*, 2004]. The gas mixture concentration, flow rate, pulse repetition frequency (prf) as well as the preionisation technique have been investigated to obtain the optimum pulse energy, system efficiency and discharge stability. Plasma discharge applications are varied and include treatment of material surfaces, food, water and air, additionally they provide portability and cost effectiveness. With the awareness of increasing air pollutants in a range of environments, there are more challenges to develop effective systems. Besides, the cold plasma discharge technique has significant advantage in air treatment due to its high efficiency in removing pollutants. For example Yan *et al*, [1988] and Noguchi *et al* [1997] used cold plasma discharge with low power consumption to remove sulphur and nitrogen in air.

According to Hu *et al* [2002] gas discharge can be divided into five categories: corona, medium gas barrier, glow, radio frequency and microwave discharges.

Sometimes, any two or more of these can be combined to produce higher density plasmas. A brief review is given of discharge techniques, paying particular attention to those facets that were identified as being able to contribute towards the development of air treatment systems. The scope of the current work is then described.

1.1.1 Plasma discharge

The most common plasma is generated in a discharge region or in a plasma chamber. In developing the discharge system, the main discharge contains at least one pair of parallel electrodes (anode and cathode). The discharge volume is determined by the distance (d) between the anode and cathode the so called gap, multiplied by the width (x) and length (y) of the electrode. The anode is connected to the charging capacitor bank or to a pulsed circuit. The pulse circuit is connected to a high voltage power supply. The cathode is normally connected to the common ground. This is the basic configuration of a discharge system using a DC high voltage power supply to drive the pulse circuit. Spyrou *et al* [1995] indicated details of a pulsed TEA discharge system and studied the high voltage behaviour and secondary ionisation effects in the discharge. Pure He or N₂ can be used to generate stable and uniform plasma. However, if the gap contains impurities, or other chemical substances or other gases are present, the stability of the plasma decreases significantly. Some examples of gases that reduce the plasma stability are O₂, NO, CO₂.

1.2 Pulse circuit

The pulse circuit performs the crucial task of transforming the gas medium to a transverse electrical discharge, which in a laser system leads to the population inversion. This circuit is used to generate high voltage to charge storage capacitors; this stored energy is then made to discharge rapidly into the main discharge and some becomes the internal energy of the lasing gas. The ability of the pulse circuit to

transfer energy effectively to the gas medium determines the wall plug efficiency of the system.

For some discharge systems, it is necessary to use short, high pulse energy to maintain the glow and avoid arc formation. This can be achieved by optimizing the circuit parameters. Spyrou *et al* [1995] suggested the main general characteristics of the discharge circuit are the very low inductance with very fast current and voltage rise-times (< 5 ns) and subsequently very high peak discharge currents (>10 kA). A typical electrical circuit to drive a laser or plasma discharge is shown in Error! Reference source not found.. The high voltage in the first loop is used to charge the capacitor storage bank (C_s), from which the energy is transferred to the second loop when the spark gap switch fires, with a time constant τ . The time constant τ is taken from the ratio of the spark gap inductance to spark gap resistance, $\tau = L_g/R_s$. The spark-gap switch triggers the fast discharge to breakdown automatically when the voltage across the gap becomes greater than the breakdown voltage.

1.2.1 Storing up energy

The main storage capacitor or capacitor bank can be charged to the required voltage which is often in the range of kV depending on the type of load. Normally two different charging methods are used: the DC resonant charging or AC charging.

1.2.1.1 Resistive charging

Resistive charging through a high voltage resistor is a common technique in pulsed discharge operation especially in single pulsed mode systems. Reports from previous researchers using the single mode resistive charging method are such as Howells *et al* [1982], Marchetti *et al* [1982] and Bhadani *et al* [1991]. The TE CO₂ laser discharge using RC charging techniques was demonstrated earlier by Lafflamme [1970], later by Hasson *et al* [1979] and Bhadani *et al* [1979]. Hasson *et al* [1979] also used the same technique to charge the N₂ laser, as well as

Serafetinides *et al* [1989] in compact pulsed TEA discharge design. This charging was also used by Tanaka *et al* [1987] for pumping KrF Excimer and TEA CO₂ lasers.

Resistive charging is adequate for single pulsed mode or low pulse repetitive rate (PRF) discharge systems, however for higher frequency repetitive modes it is not efficient due to the stored energy dissipation caused by the charging resistance. Beside the low repetitive rate, almost 50% of the stored energy may be wasted and this is the major disadvantage of the resistive charging. In order to overcome this poor efficiency, recovery methods have been established by using high voltage switches to control the charging and discharging cycle. Error! Reference source not found. refers to the basic resistive charging circuit.

1.2.1.2 DC charging

DC charging is an option used to obtain better wall plug efficiency as reported by Bhadani *et al* [1989] and to overcome the problem in RC charging efficiency. This method of charging has become widely used for repetitive TE laser pulses, as reported by Rickwood *et al* [1982], Sylvan *et al* [1990], Qu *et al* [1999] in CO₂ pulsed systems. In excimer lasers this method was also used by Yatsui *et al* [1992] and Bernard *et al* [1996]. Higher repetition rates of up to 300 Hz can be achieved by using this method of charging.

Using Kirchoff's Laws the equations for a typical circuit as shown in **Figure 1-3** with the power source (V_s) to charge the capacitor (C) through an inductance (L), can be derived and solved. By assuming there is no resistance in the charging loop, Kirchoff's equation can be written as:

$$V_s - L \frac{di}{dt} - \frac{q}{C} = 0 \quad (1.1)$$

By substituting $i = \frac{dq}{dt}$, and dividing through by L, (1.1) becomes

$$\frac{d^2q}{dt^2} + \frac{q}{LC} - \frac{V_s}{L} = 0 \quad (1.2)$$

By solving the above equation it is easily shown that

$$q = V_s C (1 - \cos(\omega t)) \quad (1.3)$$

Where ω is the resonant frequency of the circuit which is given by

$$\omega = \frac{1}{\sqrt{LC}} \quad (1.4)$$

The expression for the current (i) flowing through the circuit and voltages across the capacitor (V_C) and inductance (V_L) can be found from

$$i = \frac{dq}{dt} = V_s C \omega \sin(\omega t) \quad (1.5)$$

$$V_C = V_s (1 - \cos(\omega t)) \quad (1.6)$$

$$V_L = V_s \cos(\omega t) \quad (1.7)$$

The sum of the voltages across the capacitor and inductor is equal to the voltage source V_s . During the half cycle when the voltage is charging and drives the current in the forward direction, the capacitor has the voltage source value ($2V_s$). During the reverse direction on the second half cycle the capacitor loses all of the charges. This condition can be controlled by introducing a diode to stop the reverse current flow, and retain the charge on the capacitor. Error! Reference source not found. (a) shows the D-C charging circuit with the diode, the switch and the load. The rectified current is shown in Error! Reference source not found.(b). When the switch closes, the voltage across the capacitor will discharge into the load and voltage across the capacitor is zero

1.2.1.3 Resonant charging with switch mode power supply (SMPS)

A switch mode power supply (SMPS) is an electronic power supply unit that is integrated with a switching regulator. It rapidly switches a power transistor between saturation (full on) and cut off (completely off) with a variable frequency regulator to match the desired output voltage. Usually SMPS can cope with a wide variation of

input voltage before the output voltage changes. SMPS power sources can be DC or single phase AC. **Figure 1-5** shows the SMPS operation block diagram used to regulate the voltage output of the DC to HVDC.

The circuitry of SMPS is split into three groups of components:

- i. Power semiconductor device
- ii. Reactive components
- iii. Control circuits

Reactive components are used for energy storage and direct converting of AC voltages and currents with galvanic isolation. Capacitors and inductances are used to store energy. The inductance is specially designed to configure the system for specification requirements. For plasma generation, high frequency of 25 to 35 kHz of AC voltages are often required. Saleh *et al* [1991] designed a DC to HVDC shifted RF SMPS to charge and excite low power CO₂ lasers. They exploited and modified a pulse voltage multiplier combined with a step-up ferrite core transformer to limit leakage. This step-up transformer produced secondary voltages of average peak values of ± 1.625 kV, average currents 6.5 mA, with switching frequencies of 100 kHz. This output performance helped to maintain the stability of the laser output. The size and weight of the gas laser power supply was also reduced. **Figure 1-6** shows the SMPS schematic diagram they designed.

As the size and weight of the power supply is greatly reduced with high RF and with higher current condition, it can operate with higher efficiency. Alonso *et al* [2004] modelled and built a prototype of low power (1 W) high frequency power supply (SMPS) to be used in ozone generation for room size of 20 m³. The RMS voltage output from this system was nearly 1 kV and it used MOSFETs as the switches. The simplified electrical circuit diagram and the prototype of the ozone generator are shown in Error! Reference source not found. **(a) and (b)**.

Conventional power supplies such as the shunt or linear regulator are relatively low efficiency, operate only for low current and are difficult to regulate for variation of the loads or AC supplies. They are bulky and heavy due to the transformer winding. Additionally, the electromagnetic interference (EMI) or radio frequency interference

(RFI) is produced because the current is switched on and off rapidly. Thus shielding to provide galvanic isolation is used to reduce the disruptive interference.

1.2.1.4 AC charging

Resistive charging limits repetition rate (~300 Hz) and has poor efficiency, whereas RF plasma generation needs 25 to 35 kHz via expensive RF power supplies. DC charging however, when combined with other elements such as magnetic switches, conventional switches, rotary spark gaps or dielectric switches, very high repetition rates of the order of kHz can be achieved. This is because the flow of current through the short circuit switch is controlled. Such control of the current is a fundamental requirement of the AC charging principle. The idea was conceived by Jennings [1961] with a simple AC circuit to charge a very high energy capacitor bank.

The total current flow I from the AC source of RMS voltage V_S with frequency ω is given by

$$I = \frac{V_S}{\left[j\omega L + \left\{ \frac{R_L}{(1 + j\omega C R_L)} \right\} \right]} \quad (1.8)$$

Where R_L is the resistance of the load, while C and L is the capacitance and inductance, respectively, connected in series with the AC voltage source. Thus the current flow through the load is given by

$$I_{RL} = \left[\frac{V_S}{\left[j\omega L + \left\{ \frac{R_L}{(1 + j\omega C R_L)} \right\} \right]} \right] \times \left[\frac{\frac{1}{(j\omega C)}}{\left\{ \frac{1}{(j\omega C)} + R_L \right\}} \right] \times \quad (1.9)$$

If the values of C and L are resonate with the supply frequency ω , i.e $\omega = \frac{1}{LC}$, then the above equation reduces to

$$I_{RL} = j\omega V_S C = \frac{V_S}{j\omega L} \quad (1.10)$$

A simple AC source also has been used to operate a TE laser as reported by Bhadani *et al* [1983]. The capacitor bank is charged in the positive cycle and discharged in the negative cycle. This method has limited use for low power applications due to the low transformer utilisation factor. An improved technique by utilising the full wave charging as reported by Bhadani *et al* [1985] with 3 phase constant current pulse network as seen in Error! Reference source not found.. The capacitor voltage reaches the peak of the transformer voltage in a quarter cycle of the voltage supply. The low voltage SCR is placed in the charging path to prevent any current flow until the breakdown voltage is reached. This method isolates the power supply during and some period immediately after the discharge. This period is normally made to be greater than the deionisation time of the thyatron by choosing suitable SCR breakdown characteristics. The maximum repetition rate that is achievable is double the frequency of the supply.

It can be seen from equation (1.10) that the current through the load is independent of the load resistance at resonant condition. This principle can be used to charge the capacitor bank in the discharge pulse system. Bhadani *et al* [1984] demonstrated this for a high repetition rate TE laser.

1.2.2 Discharging the stored energy

In a fixed volume gas discharge system, discharging the stored energy initiates the glow mode, it may eventually turns into arc after a time called the glow-to-arc transition time if conditions prevail. This transition time reduces with increasing gas pressure. At atmospheric pressure the energy typically discharges within the

transition time of hundreds of nanoseconds. Any local instabilities will result in filamentary arcs which drains the stored energy and reduces the efficiency of the excitation. To avoid this from happening and arc formation, the switching time must be much shorter than the glow-to-arc transition time. This is followed by the impedance of the pulse circuit which must be low enough to ensure the discharge expires before arcing sets in. In the TE discharge however, preventing a high current arc is difficult. The system parameters leading to the glow discharges while maintaining suitable conditions for efficient excitation are dependant on several system components, detailed in the following sections.

1.2.2.1 Switched discharges

The switch used in such systems must have a very fast switching time which is characterised by the maximum allowed value of $\frac{dI}{dt}$. In the operation of a TE discharge, the main energy storage capacitor discharges its energy effectively into the load by a fast, high current capability switch with a hold-off voltage of tens of kV.

The simplest switch in such a requirement is a spark gap. Spark gaps are less suitable for high repetitive operation because they operate in the arc mode and may suffer from recovery and life-time problems. However, they can be enhanced by incorporating additional features such as a rotating dielectric spark gap. Thayer *et al* [1988] suggested by removing the ionised hot gases in the gap by circulating fresh gas the hold-off capability will be restored.

Thyratrons can operate in glow mode and have controlled recovery features that are compatible with high repetition rate discharges and can replace the spark gaps. However, thyratrons are rather expensive and have limited life-times.

There is a growing interest in replacing these switches by all-solid-state-exciter (ASSE) in conjunction with magnetic pulse compression (MPC). These systems

have a high degree of reliability but low wall plug efficiency and may be bulky [Tanaka *et al*, 1990]. Efforts have been extended to eliminate the main discharge switch altogether in the operation of CO₂ lasers [Jayarama *et al*, 1985; Sylvan *et al*, 1992; Singal *et al*, 2003]. Because of the high cost element of the switch, methods to do away with this completely are attractive to the current research. A brief explanation of systems without a main switch is explained in the following section.

1.2.2.2 Switchless main discharge switch in TEA CO₂ laser operation

In switchless TEA CO₂ laser operation, the main capacitor is directly connected across the laser electrodes and is charged to a voltage below the self-breakdown level of the gas mixture in the electrode discharge volume. Automatic switching of this capacitor occurs when the gas mixture in the electrode discharge volume is preionised by X-ray [Jayarama *et al*, 1985], UV [Selvan *et al*, 1992], or photons or electrons from an external source [Kumar *et al*, 1997]. All these methods demonstrated the main discharge functions without a switch; however, the preionisation of the discharge region is initiated by a switch but generally with reduced pulse power requirements.

1.2.2.3 Transverse discharge

Transverse discharge configurations are normally designed with a small inductance and capacitor bank that is charged to the required voltage, then the energy is discharged to the active discharge medium with the satisfying $\frac{dI}{dt}$. Even if the $\frac{dI}{dt}$ is reached, the collapse of the discharge into arcs is still possible. This is because the random distribution of the stray charges in the active volume causes inhomogeneities in the conductivity along the longitudinal direction. More current tends to flow across the high conductivity zone leading to further increase in its conductivity. This positive process results in draining the stored energy into strong streamers. There are two basic methods to overcome streamer formation. First is by segmenting the

discharge along the length into small parts to limit the current flow through each of them by connecting a resistor or inductance in series, as used demonstrated by Beaulieu [1970]. The second is a popular method to produce stable volumetric discharges between a pair of specially contoured electrodes, the so called Uniform Field Electrodes (UFE) [Tanaka *et al*, 1990], [Dyer *et al*, 1983], [Bhadani *et al*, 1994], [Lafflamme, 1970]. These two methods are briefly discussed in the next sections.

1.2.2.4 Segmented discharge

Segmented discharge systems were first attempted by Beaulieu [1970] with preionisation on the main discharge and also investigated by Watson *et al* [1995]. The resistors limit the current flow to the segmented circuits which were arranged parallel to each other. This configuration generates a number of smaller, more stable discharges with the current resistance limited. However, the efficiency of the laser or discharge system reduces due to the energy dissipation in the ballast resistors.

To overcome the low efficiency, Laurie *et al* [1970] demonstrated a low inductance, segmented preionisation discharge loop. Pearson *et al* [1972] also found that the low inductances allow higher energy stored in the capacitor bank and pumped into the main discharge. They compared the efficiency of the operating output system using inductive and resistive segmented systems. **Figure 1-10** shows the results of Pearson's *et al* [1972] work by comparing the discharge energy of inductive and resistive systems at various pressures. The inductive system showed about double the output laser energy of that resistive system.

1.2.2.5 UFE discharge

Uniform field electrodes have emerged as an attractive method to obtain uniform glow discharges over a large volumes. Rogowski profiled electrodes where the central planer region is abruptly joined to curved edges has been widely used on

large aperture TE CO₂ lasers [Harris, *et al*, 1991], [Pearson *et al*, 1972] and excimer lasers [Mangano *et al*, 1975]. Chang profiled electrodes [Chang, 1973] have been used in all kinds of TE laser discharges. The reduction between the ratio of the discharge width to the overall electrode width in Chang's profiled electrodes makes the laser discharge more compact. The compact electrode profile allows a smaller distance between the UV preionisers to the centre of the discharge region, which make the preionisation more effective. Also by using compact electrodes, this loop inductance is reduced. In UV lasers, low inductance is important in order to obtain very short discharge durations in order to be faster than the spontaneous decay rate of the upper laser level.

1.3 Preionisation

TEA discharge systems produce a pulsed output and are capable of large output energies per unit discharge volume (10-50 J/liter). To maintain the glow discharge mode and avoid arc formation in TEA discharges, preionisation is also required. Preionisation enhances the main discharge pulse stability by producing uniform gas excitation.

Pulsed TEA discharge systems have been designed with various preionisation techniques and are widely adopted by researchers to investigate the characteristics of TEA CO₂ lasers, excimer lasers and plasma discharges. UV preionisation techniques in TEA systems is the interest in this work. Discussion on UV preionisation is in the next section.

1.3.1 UV preionisation

This technique of preionisation is suitable to TE discharges and can be classified into two main categories: double discharge laser plasma and corona preionised laser plasma.

1.3.1.1 Double discharge plasma

The double discharge system operation was pioneered by Laflamme [1970] and followed by Pearson [1972], Tou *et al* [1998], Trtica [2002], and many other researchers. Double discharge preionisation has an advantage when this technique is used at, below or above atmospheric pressure.

The general principle of the double discharge is the main discharge occurs sometime later, after some delay from an auxiliary preionisation discharge. **Figure 1-11** shows a schematic diagram of the double discharge circuit used by Laflamme. The auxiliary discharge (pre-discharge) was generated using a spark gap or trigger spikes, and built along the main discharge region. The trigger spikes or spark gap were placed very close to the cathode side. The array of spark gaps or trigger spikes produces bright arcs and induces UV formation. The UV ionises the gas producing free electrons that promote the uniform glow during electron avalanche. Hamilton *et al* [1975] designed a repetitively pulsed double TEA CO₂ discharge with an average output power of 400W and pulse repetition frequency 200 Hz and which lasted for 20 s before arcs started to appear. Shimosaki *et al* [2004] used the double discharge system to develop ozone generation and configured the optimum number of the trigger electrodes to optimise the ozone production.

1.3.1.2 Delay between the auxiliary pre-discharge and the main discharge

To optimise the system performance a delay is introduced between the auxiliary discharge and the main discharge pulse. The delay often time between the preionisation discharge and the main discharge has to be kept within limits, otherwise the discharge arcs. The lower limit of the delay comes from the fact that the preioniser current takes a relatively long time to reach its peak value and to sustain the current for supporting the glow discharge in the main region. The upper limit of the permissible delay time is set by the process of electron attachment. It has been found that during the delay period, the electrons created in the main discharge

volume by preionisation rapidly attach themselves to oxygen molecules [Norris *et al*, 1979]. The negative ions that are formed leads to arc formation.

Several methods have been reported of synchronising the two discharges by means of two sets of high voltage, variable delay triggers [Stark *et al*, 1978], [Suzuki *et al*, 1982]. Other researchers developed techniques to obtain synchronization between the main discharge with respect to the preionisation [Howells *et al*, 1980], [Trtica *et al*, 1984]. A single discharge circuit with one power source and one switch provides an automatic delay between the preionisation and main discharge. However, there is believed to be 50-100 ns delay existing in this scheme. Measurement of the very short delay is important in order to quantify the photoelectron concentration and the discharge breakdown.

Kumar *et al*, [2001] has demonstrated a method of measuring the delay between the two discharges. Light emitted from the preionisation and the glow from the main discharges was collected independently by using separate fibre optics. The light emission from these discharges were measured using an opto-electronic circuit. The measured delay varied as function of the discharge loop inductance and was typically from 50 to 160 ns.

1.3.2 Corona preionisation

Many reserches have investigated corona preionisation for sealed TEA CO₂ lasers by using different dielectric materials and varying the gap between the dielectric material and electrodes. Walter [1984] used a Surface Wire Corona Preionisation (SWCP) technique with different dielectric materials. The results showed that macor has the highest efficiency in term of E_{in}/E_o (where E_{in} is input energy and E_o is output energy), followed by pyrex glass. The dielectric constant for macor is 5.92 and for pyrex glass it is 5.0. This showed that the dielectric constant was important in determining the amount of energy that could be subsequently deposited into the discharge. The total discharge volume was 95.2 cm³ and aluminium Rogowski electrodes were used with a discharge gap of 14 mm.

Qu *et al* [1999] also used the SWCP technique with a 25 cm³ discharge volume. The preionisation system consisted of SiO₂ tube (dielectric constant 3.9) inserted with metal metallic rods which were connected to the anode. The tube length was the same as the length of the main discharge electrodes. A fine wire was strained and attached onto the dielectric tube surface. A corona discharge occurred between the fine wire and the SiO₂ tube surface. This was used to preionise the gas within the discharge region. They achieved efficient laser operation with overall efficiency of 9.8%.

1.3.2.1 Preionisation dielectric materials

The choice of dielectric material is paramount for efficient preionisation because of the influence of the dielectric on the performance of the discharge stability and laser output. The energy in the corona discharge is determined by the value of the distributed capacitance given by the geometrical dimensions of the preionisation system and by the dielectric constant. The higher the dielectric constant then the higher the energy deposition into the discharge. The types of dielectric materials will also influence the UV spectrum of the surface photoemission, as shown by Beverly *et al*, [1977], and influence the maximum energy deposition into the discharge before the onset of arcing.

The capacitance C (μF) value for the dielectric material can be calculated from

$$C = \frac{A\epsilon_r\epsilon_o}{d} \quad (2.11)$$

Where A is the area of the dielectric, ϵ_r is relative permittivity of the dielectric or dielectric constant and ϵ_o is the absolute permittivity of vacuum ($\sim 8.85 \times 10^{-12}$ F/m). **Table 2.1** shows properties of some of the dielectric materials that may be selected for preionisation. The dielectric film thickness was typically from 50 μm to few hundreds μm .

Table 1-1 Electrical properties of dielectric materials.

Material	Dielectric Strength (kVmm ⁻¹)	Dielectric Constant
Borosilicate Pyrex glass	0.5	5.6
Macor	120	5.92
Acrylic	30	3.6
Teflon	260	2.1
Mylar	280	3.1
Silicon dioxide	100	3.7
Aramid paper (Nomex)	17	2
PTFE	269	2.1
Kapton	118	2.9
Air	3	1.05

1.4 Uniform field electrodes

The well known UFE began with the Rogowski profile [Rogowski, 1923] which used three joined segments of an infinitely wide analytical profile. Rogowski produced the curves by considering the $1/2V_0$ (for 90° profile) and $2/3V_0$ (for 120° profile) equipotentials of a finite plane at potential V_0 , which is parallel to an infinite earthed plane. The 90° and 120° Rogowski profile electrodes were formed by rotating the $1/2V_0$ equipotential about a suitable axis. Jones [1956] has discovered that the 120° profile had a higher electric field on the curved edge part than in the central region.

The Bruce profile [Bruce, 1947] is taken from empirical curve calculations to minimise the sharp edges. Harrison [Harrison, 1967] introduced a profile which compromised the Rogowski and Bruce profiles with an accurate value of the field profile.

Chang's profile [Chang, 1973] is more compact and a completely smooth electrode, thus producing more control over the uniform field. This was achieved by using

hyperbolic functions. Chang describes the method of developing a complete three-dimensional UFE from two dimensional (x & y) functions. Narrower and more compacted profiles of UFE were developed by Ernst [Ernst, 1984]. The following section assesses the analytical function for Rogowski and Chang profiled electrodes. This is taken further in Chapter 3 where these functions are modelled in Maple to produce the desired electrodes for the discharge systems, these were subsequently tested and evaluated for plasma generation and air decontamination.

1.4.1 UFE analytical functions

In a homogeneous charge free region as referred to in **Figure 1-12**, the electric field force or the potential between the two electrodes is a solution from Laplace equation,

$$\nabla^2 V = 0 \quad (1.12)$$

Or in Cartesian coordinates,

$$\frac{\partial^2 V}{\partial x^2} + \frac{\partial^2 V}{\partial y^2} = 0 \quad (1.13)$$

Electrostatic theory can be used to solve this equation by using the theory of complex variables. Consider a function z , defined as $z = x + iy$ (real coordinate) as shown in **Figure 1-12 (a)** and another function $W(z) = U + iV$ (imaginary). Here, U is the flux function and V is the potential function, as referred to **Figure 1-12 (b)**. If the function of $W(z)$ has the derivative function of $W'(z)$, it satisfies the Cauchy-Reimann equation on a pair of real value function which is,

$$\frac{\partial U}{\partial x} = \frac{\partial V}{\partial y} \quad \text{and} \quad \frac{\partial U}{\partial y} = -\frac{\partial V}{\partial x}$$

Thus

$$\frac{\partial U}{\partial x} - \frac{\partial V}{\partial y} = 0 \quad \text{and} \quad \frac{\partial U}{\partial y} + \frac{\partial V}{\partial x} = 0$$

Simple differentiation of the above function yields,

$$\frac{\partial^2 U}{\partial x^2} + \frac{\partial^2 U}{\partial y^2} = 0 \text{ and}$$

$$\frac{\partial^2 V}{\partial x^2} + \frac{\partial^2 V}{\partial y^2} = 0 \quad (1.14)$$

Both U and V satisfy the Laplace equation.

1.4.1.1 Rogowski profile

For the Rogowski profile, the analytical function that is used is given by

$$z = \frac{A}{\pi}(W + e^w) \quad (1.15)$$

Where A is the electrode gap and W is the

The Rogowski profile calculate the edges of the two semi-infinite electrodes. The

distance between one electrode to the mid-plane is $\frac{A}{2}$. The x and y profile are given

by

$$x = \frac{A}{\pi}(U + e^u \cos V)$$

$$y = \frac{A}{\pi}(V + e^u \sin V) \quad (1.16)$$

The method used to design the coordinate value is to take a value of V . V is chosen

as, $V = \frac{\pi}{2} + \theta$ where θ is an angle in radians, then substitute $V = \frac{\pi}{2} + \theta$ into the equation for y and this will determine the value for U , which is then used to find x .

1.4.1.2 Chang profile

The analytical function for the Chang profile is

$$z = W + k \sinh W \quad (1.17)$$

Here k is an empirical constant and can be chosen arbitrarily. Each value of k will give different x and y profiles. In the W plane the equipotential value is given by a constant value of V and a variable value of U . In the z plane, the equipotential surfaces is given by,

$$\begin{aligned} x &= U + k \cos V \sinh U \\ y &= V + k \sin V \cosh U \end{aligned} \quad (1.18)$$

The value of the electric field on the electrode surface is given by

$$\begin{aligned} E^2 &= \left[\frac{dz}{dW} \right]^2 \\ &= (1 + K \cos V \cosh U)^2 + (k \sin V \sinh U)^2 \end{aligned} \quad (1.19)$$

Chang [1973] showed that in order to get a flat distribution field near the centre of the electrode, the value of V should be chosen as

$$V = \frac{\pi}{2} + \arcsin k \quad (1.20)$$

Value of k can be chosen (e.g. $k=0.2$, $k = 0.01$, $k = 0.06$ etc.), so that V can be determined. V is substituted into equation (1.18), and the x and y coordinates can be generated. The lower the value of k , then the broader the electrode width.

The Chang profiled electrode were selected to be used in this research due to their compactness and uniform generation of charge distribution.

1.5 Paschen Law

Paschen Law states that the breakdown voltage (V_b) between two parallel electrodes in a gas is a function of the pressure (p) and the electrode gap (d). It is written as,

$$V_b = f(pd) \quad (1.21)$$

in torr cm. Generally there is a minimum value of V_b and it is constant for a given gas and electrode material. Extensive experiments were done for different gases and electrode materials [Schümann *et al*, 2003; Han *et al*, 2001] and the Paschen Curve as shown in **Figure 1-13** was earlier obtained by Naidu *et al*, [1995]. The breakdown voltage is non-linear to the (pd) function because of the gas. The equation used for the Paschen Curve is

$$V_b = \frac{a(pd)}{\ln(pd) + b} \quad (1.22)$$

The non-linear function is $\frac{a}{\ln(pd) + b}$. The constants a and b depends on the composition of the gas. For air at standard atmospheric pressure (760 torr ~ 0.9999 atm), the constant value, $a = 43.6 \times 10^8$ V/atm.m and $b = 12.8$ with the electrode gap $d = 7.5$ mm. **Table 1-2** shows the minimum breakdown voltage for various gases.

Table 1-2 The minimum breakdown voltage for various gases [Naidu, M.S. and Kamaraju, 1995]

Gas	V_b (min) V	Pd (min) torr
Air	327	0.567
Ar	137	0.900
H ₂	273	1.150
He	156	4.000
CO ₂	420	0.510
N ₂	251	0.670
N ₂ O	418	0.500
O ₂	450	0.700
SO ₂	457	0.330
H ₂ S	414	0.600

1.6 Cold plasma application on air treatment

Cold plasmas have been proven to inactivate many different types of micro-organisms, such as viruses and bacteria on different surfaces of materials. There have been significant scientific studies of air sterilization using cold thermal plasma [Chen *et al*, 2008; Lee *et al*, 2006; Dřimal *et al*, 1988]. Researchers that have investigated plasma decontaminate of air, relied on high efficiency particulate air (HEPA) filters to remove a large portion of micro-organisms. These HEPA filters are effective at trapping particles down to 0.3 μm in size; however, studies have shown that they are not as effective at capturing airborne viruses, which are among the smallest (20-300 nm) known micro-organisms. HEPA filters also cause significant pressure losses in HVAC systems, giving rise to higher energy requirement and maintenance costs. There are several alternative methods for air cleaning, which include electrostatic precipitators. Ultraviolet Germicidal Irradiation (UVGI) devices, and some portable negative air ionizers are capable of reducing particulates and even certain levels of microbial contamination in indoor environments.

In this study, the construction of different discharge systems, many based on laser discharge methods, are developed and their sterilization effects investigated. In order to prove that cold plasma is the main factor responsible for decontamination, one must first build a system that is capable of creating, handling, and analyzing dense concentrations of viable bio-aerosols. Designing and building an air decontamination system is challenging because there are many factors that contribute to losses of aerosolized micro-organisms in moving air streams. These factors include diffusion of aerosol to the walls of the air flow system, desiccation stress on the micro-organism due to evaporation of bio-aerosol droplets in flight, and inertial and gravitational forces which can remove larger droplets from the air stream. The factors causing these losses must be carefully considered in order to avoid misinterpretation of sterilization data and may also be one reason why bio-aerosol sterilization studies are limited in comparison to studies involving water or surfaces, because of their complexity.

1.7 Objectives of research

The principle behind this research investigated how knowledge from laser discharge systems could be adapted into developing plasma based, atmospheric discharges that could operate in air, with the view to achieve efficient air decontamination. This work was commercially funded, and as such, real working systems were prototyped with a view to potential commercialisation at a later stage. The end user applications that were considered included, for example, decontamination of air on aeroplanes, cleaning air in office buildings, hospitals or even the home environment. This list is not exhaustive and the market for such devices is not discussed.

This chapter has provided an overview of cold plasma discharge and laser discharge systems. This has included different methods of charging such as AC, DC, resonant and resistive. The requirements for high voltage switching with thyratrons were discussed with a view to try and develop switchless systems to provide cost effective plasma generation without the need for expensive HV switches. Various electrode geometries were discussed including low inductance circuits, segmented electrodes and uniform field electrodes. The theory behind uniform field electrodes was introduced and this is developed further in Chapters 2. Preionisation plays an important role in laser discharge physics, particularly in discharge stability and maximising the laser output. Various methods that have been commonly used were briefly described with a view to see how these systems could be used for atmospheric air discharges. This list is not exhaustive and does not include information on X-ray or γ -ray, for example, but more on systems that were considered that could be realistically implemented or commercialised in atmospheric plasma systems, such as UV, dielectric sheets or corona preionisation.

Chapter 2 describe some electrical circuit models that were developed of the discharge circuit, including electrodes and discharge circuit, and models that were written to facilitate fabrication of Uniform Field Electrodes.

The discharge circuits were modelled with AC or DC excitation with different forms of preionisation. The preliminary results from running the discharge, reported in

Chapter 3, were used to estimate the stray inductance of the circuit and allow some steps to be made towards circuit optimisation.

Chapter 3 then, as intimated, addresses preliminary discharge behaviour using DC excitation and trigger wire preionisation. Two electrode configurations were used: simple planar or Chang profiled electrodes. Various gas mixtures were used to assess the performance of the discharge for possible laser use and allow comparison with known laser discharge performance. Spark plugs were used to preionise the gas volume and also to act as a switch for DC excitation. An AC discharge was also developed using dielectric sheet (mylar, duralar and glass) as the main source of preionisation. The AC discharge was successfully developed without the need for HV switches, providing a significant cost saving on plasma generation. Various methods of moving the gas from the electrodes were considered and included longitudinal or transverse removal. This was considered the precursor to developing the atmospheric air discharge, with air moving between the electrodes. The effects of the air flow on the voltage and current characteristics were investigated.

Chapter 4 addresses in detail the steps required to manufacture the electrodes used throughout the work. It describes the electrode manufacture for the systems used in Chapter 3, and additionally new electrodes that were fabricated for testing against contaminated air in Chapter 5. Various electrode materials were considered, including aluminium, brass and stainless steel. Aluminium was the material of choice because of ease of manufacture and less likelihood of contaminating the air through electrode sputtering, as is the case with Brass for example. Additionally, a laser marking process of the electrodes was developed to investigate how laser marked electrodes behaved in the discharge. Various roughness measurements were taken to try and quantify the relationship between the surface finish and discharge quality. SEM and EDAX were taken of the electrodes for further analysis.

Chapter 5 shows the results from some of the systems that were fabricated and tested against seeded air flow. Two systems were prototyped based on the atmospheric air discharge development; these were known as the Dome and Tubular system. The performance of these systems was compared with the Chang profiled electrode system and the other electrodes that were fabricated and discussed in Chapter 4. The

systems were designed to be scaleable to provide different levels of contamination or throughput depending on the end users requirements. The seed organisms for the air experiments were *Bacillus globigii* which is an Anthrax simulant. The spectral output from the discharge was measured to investigate whether it provided additional killing through UV killing. Experimental protocols were developed to allow testing and validating the systems. These were through necessity quite complex requiring microbiological aerosol handling and HV and plasma generation skills. As part of the comparison of these different systems, the ozone created from the plasmas were investigated and compared to a commercially available “plug in the wall” ozone generator.

Chapter 6 provides conclusions of the research and identifies future work.

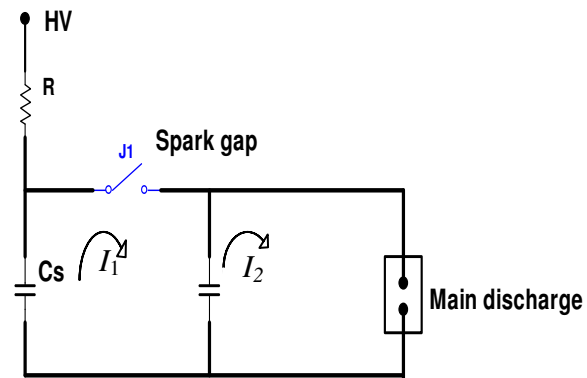


Figure 1-1 A typical electrical high voltage pulse circuit for TE laser discharge [Spyrou *et al*, 1995].

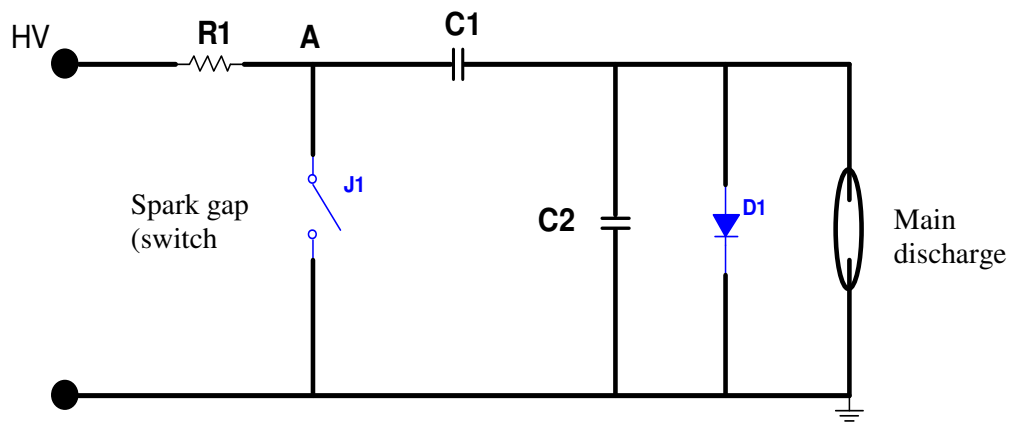


Figure 1-2 RC network by Serafetinides [Serafetinides *et al*, 1989]

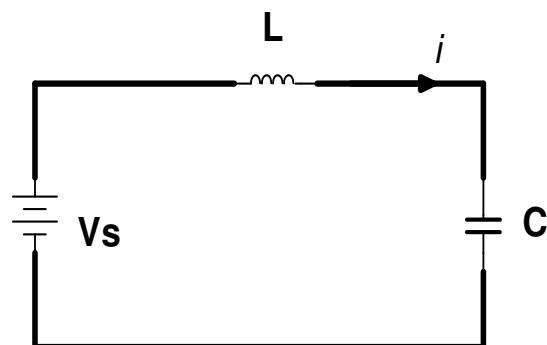
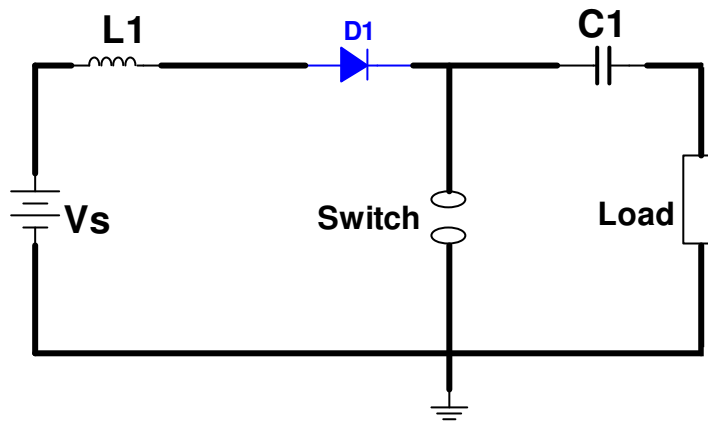
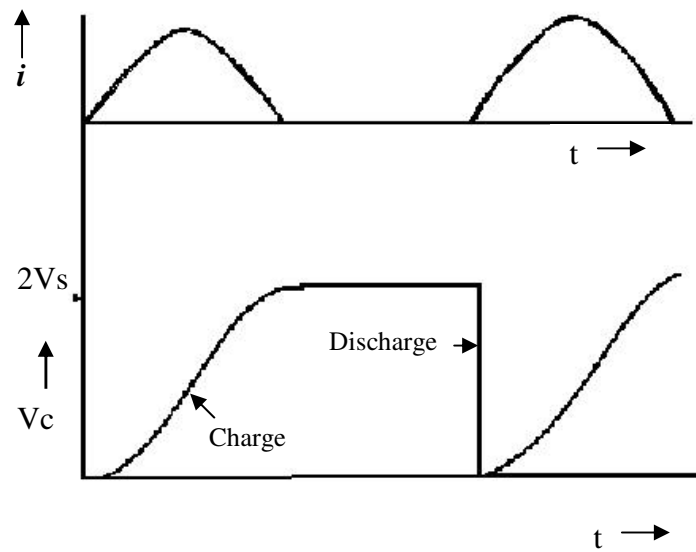


Figure 1-3 A typical DC network , where the charging current (i), the voltage across the capacitor (V_c) and voltage across the inductor (V_L).



(a)



(b)

Figure 1-4 (a) D-C resonant network with diode, (b) The charging current (i) and voltage across the capacitor (V_c) is twice of source voltage (V_s).

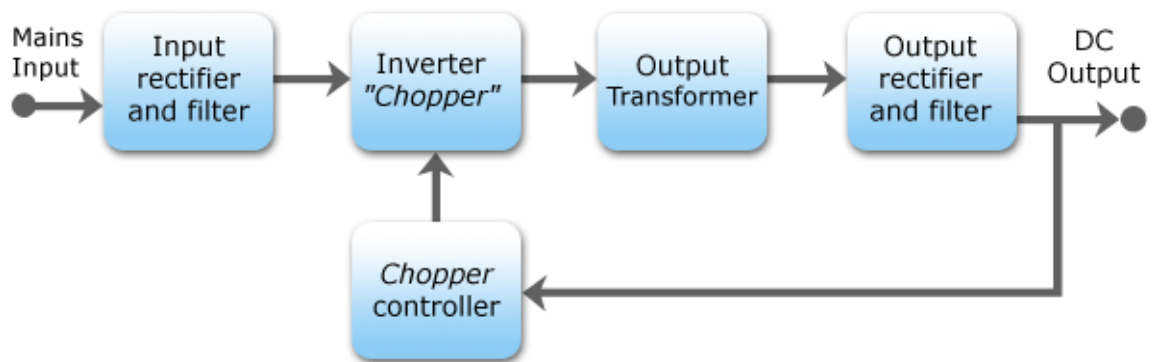


Figure 1-5 Block diagram of SMPS operation on AC –DC output voltage regulator.

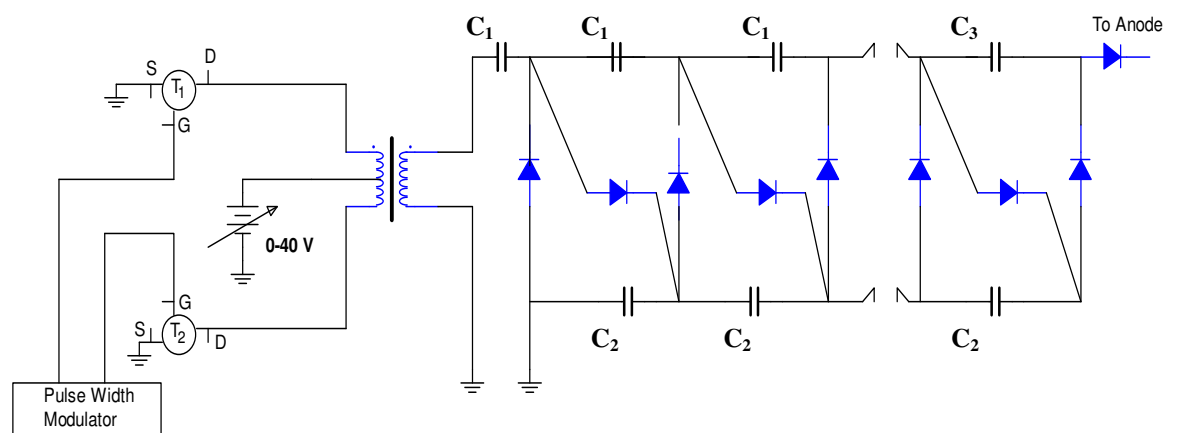
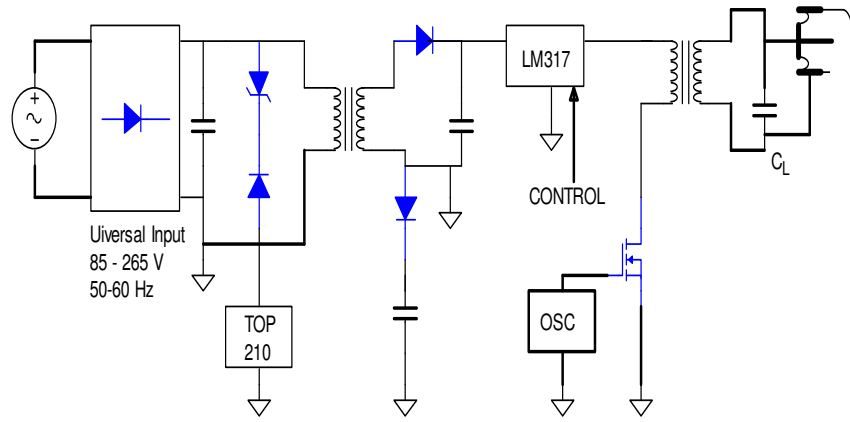
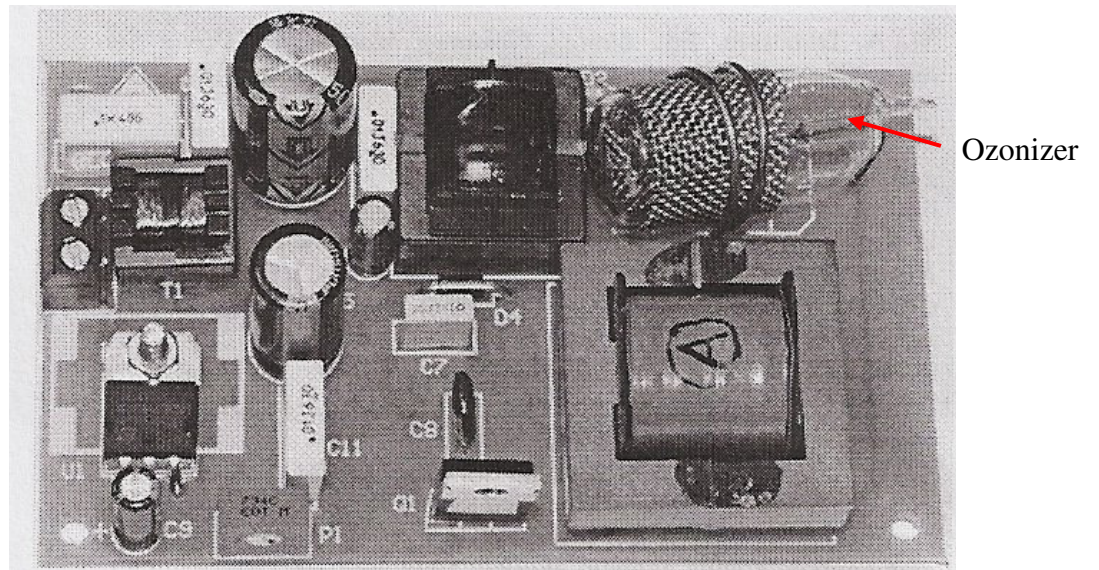


Figure 1-6 High voltage switch mode schematic diagram [Saleh *et al*, 1991]



(a)



(b)

Figure 1-7 (a) Circuit diagram of a portable prototype of the ozone generator, (b) Portable ozone generator [Alonso *et al*, 2004].

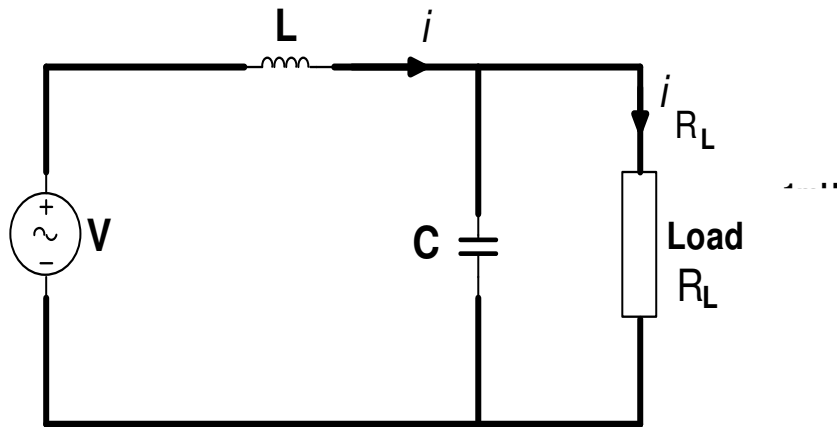


Figure 1-8 Single phase AC resonant circuit [Bhadani *et al*, 1984].

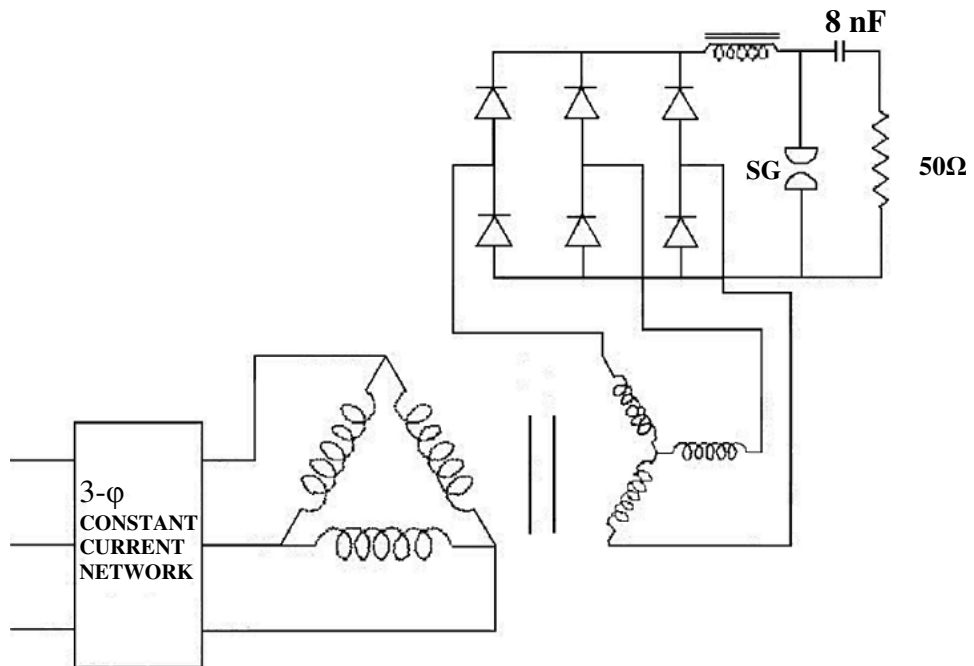


Figure 1-9 Schematic diagram of the AC pulser circuit with full wave bridge rectifier [Bhadani *et al*, 1984].

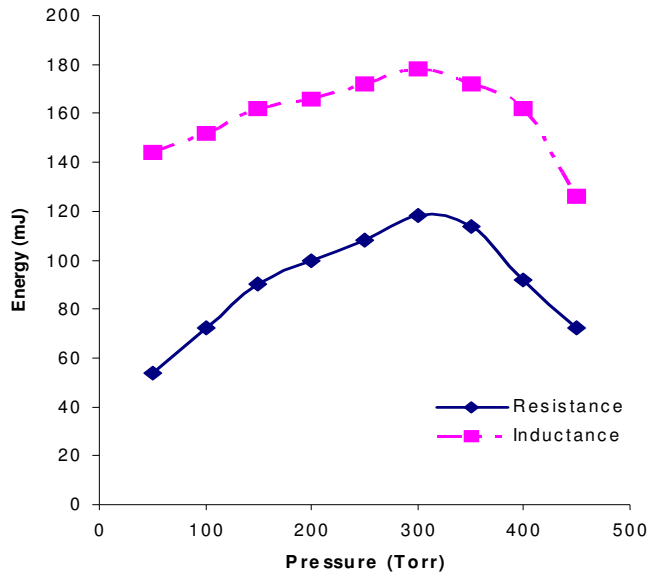


Figure 1-10 Comparison of the performance of a helical TEA laser with inductance and resistance [Pearson *et al*, 1972].

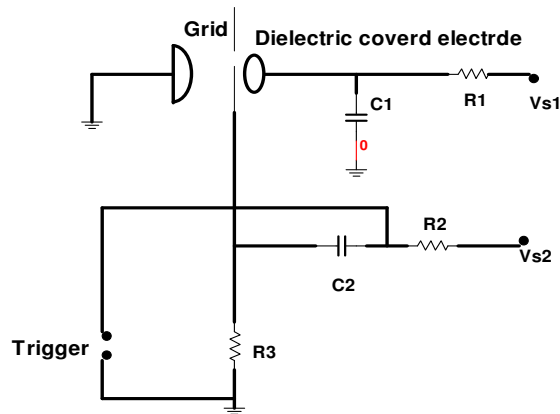
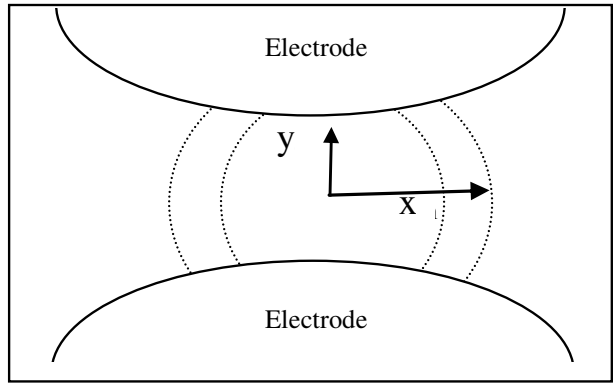
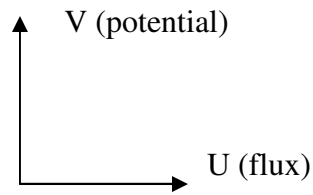


Figure 1 -11 Double discharge circuit by Laflamme [Laflamme, 1970].



(a)



(b)

Figure 1-12 Uniform field electrode (a) Plane x & y, (b) Electrostatic flux (U) and potential plane (V).

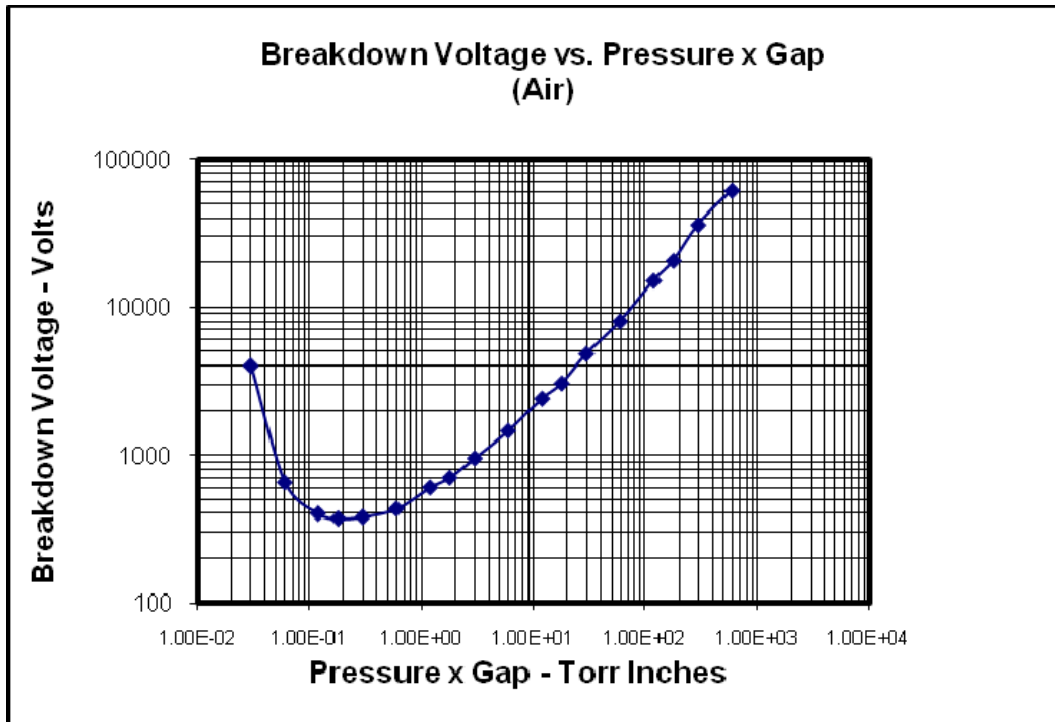


Figure 1-13 Paschen Curve for air at various pressures, where minimum was ~0.012 torr and maximum of about 160 torr [Naidu, M.S. and Kamaraju, 1995].

Chapter 2

Modelling Discharge Systems and Uniform Field Electrode

2.1 Modelling of the system

Various discharge circuits were modelled using MultiSim. Feedback from the modelling and simulation were used in optimising the system and to obtain the preliminary experimental results of the discharge performance. The modelling of the electrodes' discharge potential and flux between the electrodes was done to help with the electrode design and electrode selection (between the Rogowski or the Chang UFE). The selected electrodes were manufactured in-house and used with the prototype which is discussed in Chapters 4 and 5.

2.2 Discharge model

The model of the R-L-C discharge system is shown in **Figure 2-1** which shows the steps taken in simplifying the discharge system into an equivalent electrical circuit. **Figure 2-1(a)** shows the charging capacitors, C_1 is the initial charging capacitor and C_2 is a second capacitor that was used to increase the impedance of the path to ground when AC charging was used. The capacitors were arranged in series with the electrodes. The electrodes were modelled as an L-R-L circuit (**Figure 2-1 (b)**) as suggested by Tou *et al* [1998]. The model was simplified to L_e and R_e in (**Figure 2-1 (c)**). This transient circuit system produces a very high frequency discharge current in order to maintain stable discharge and power. The frequency is directly dependent on the capacitance and inductance of the circuit. In this circuit the capacitance value can be easily determined in practice but not the inductance, because its value is influenced by the nonlinear condition within the circuit such as the material of the wire and material of the electrode. The frequency response of the circuit is given by

$$f = \frac{1}{2\pi\sqrt{LC}} \quad (2.1)$$

Where L and C are the total inductance and capacitance of the circuit respectively. For very large frequency (f), the inductance-capacitance product must be very small. In order to meet this condition, the capacitors were arranged in series to obtain a relatively small total capacitance for the system. However, with a low capacitance the discharge energy is small but high peak powers are achievable. In a typical transient circuit, the time for one complete cycle of the discharge frequency is Δt where:

$$\Delta t = 1/f \quad (2.2)$$

The discharge power (P):

$$P = \frac{E}{\Delta t} \quad (2.3)$$

Here the energy (E) is the discharge energy which under perfectly matched conditions is equivalent to the energy stored on the capacitors when they are charged to a constant voltage (V), which is given by

$$E = \frac{1}{2}CV^2 \quad (2.4)$$

In order to achieve a relatively large discharge energy, a total of five storage capacitors were used with an equivalent capacitance of 75 nF and a constant current supply was used capable of supplying 6 kV.

2.3 Equivalent circuit of spark gap and main electrode

For modelling and simulation software such as MultiSim8, none of the components listed can directly represent the spark gap or main discharge electrodes. Some researchers have suggested that the spark gap can be represented by a resistance R and inductance L in series [Spyrou *et al* ,1991; Tou *et al*, 1998], this depends on the size of the spark-gap and discharge volume. The spark gap and its an equivalent electrical circuit are shown in **Figure 2-2**, a series resistor (R_s) and inductance (L_s). To model the main discharge electrode, the equivalent electrical circuit as suggested by Tou *et al* [1998] was used, this was simply L_d - R_d - L_d in series, as shown in **Figure**

2-3. The anode and cathode gap was equivalent to a resistance R_d . The equivalent resistive value (R_d) of the planar electrodes was calculated. The calculation of the equivalent value of the main electrodes is explained in the following section.

2.3.1 Calculation of equivalent electrical value

Various methods can be employed to determine the values of resistance, inductance and capacitance to use in the model such as a numerical iterative approach or by using initial values as determined experimentally from the pulse discharge system. These methods are briefly described below.

2.3.1.1 Equivalent of resistance (R) value from numerical modelling

In the numerical method derived by Tou *et al* [1998], the resistance R_d of the main discharge electrode was determined. First the electric field (E) or discharge voltage in the main electrode discharge can be calculated using the expression

$$E = \frac{IR_d + L_d \frac{dI}{dt}}{d} \quad (2.5)$$

Where d is the electrode gap with its equivalent resistance R_d , which was given by

$$R_d = \frac{d}{lw\sigma} \quad (2.6)$$

Where l and w are the electrode length and width respectively, while σ is the discharge conductivity which is related to the electron density n_e . The discharge conductivity σ is given by the expression

$$\sigma = \frac{en_e v_d}{E} \quad (2.7)$$

The v_d is the electron drift velocity. The electron density is given by the equation

$$\frac{dn_e}{dt} = \alpha v_d n_e \quad (2.8)$$

Where α is the first Townsend ionisation coefficient, if $\alpha = 1.4 \times 10^{-8} (E/p)^{3.7} \text{ torr.cm}^{-1}$ and $v_d = 2.9 \times 10^5 (E/p) \text{ cms}^{-1}$, then n_e is found. Substituting the value of n_e into (2.7) for σ and E into equation (2.5), from (2.6) the R_d value can be determined. This numerical method was not used in this research, however this might be of interest in future work.

2.3.1.2 Equivalent R-L-C values from pulse discharge system

In this method, the inductance was calculated based upon the measured discharge frequency from initial experiments on the discharge system in vacuum conditions with the storage capacitor connected. The discharge system is shown in **Figure 2.4(a)**. The discharge frequency was observed on a LeCroy 9310, 350 MHz, oscilloscope. The pulse length (Δt) was 1.6 μs , thus, the frequency f , was 626 kHz.

Using the formula, $f = \frac{1}{2\pi\sqrt{LC}}$, the calculated inductance L_e was 11.5 nH.

The effective capacitance of the electrodes (C_e) was calculated by considering the planar electrode discharge volume of $60 \times 10 \times 5 \text{ mm}^3$, the relative permittivity of air ϵ_r (1.00059) at atmospheric pressure, and the permittivity of vacuum ϵ_o

($\sim 8.8542 \times 10^{-12} \text{ Fm}^{-1}$). Taking equation (1.11) for $C_d = \frac{A\epsilon_r\epsilon_o}{d}$, the capacitance of

the planar electrode in vacuum was approximately 1.01 nF. The resistance of the electrode gap R_d value was assumed at 0.1Ω . **Figure 2-4(b)** shows the discharge system equivalent component values which included inductance, resistance and capacitance and the storage capacitor values. These were used in the Multisim8 simulation.

2.4 Modelling the main discharge circuit on Multisim8

Multisim8 circuit modelling software was used to model the main discharge circuit. The modelling was done to provide further insight into the circuit characteristics before building the prototype system. The oscilloscope and current probe models in Multisim8 were connected to the model circuit during the simulation. The discharge voltages and currents were available for analysis.

2.4.1 DC discharge parameters

The design consideration for the discharge system was dependent on how much output power was needed for the prototype system. First to consider is the total value of the storage capacitors, which in this case the value $C_s = 75 \text{ nF}$ was selected and the charging source was a 6kV DC voltage (80 mA constant current). Using equation in (2.4), the energy stored in the capacitors was 1.35J.

2.4.2 DC discharge simulation results

The voltage trace shown in **Figure 2-5 (a)** is for a 75 nF storage capacitor. The charging and discharging time was about 50 ms. The switching frequency was ~2.1 Hz with a time before discharging the storage capacitor of about ~480 ms.

To compare the discharge characteristics the storage capacitor C_s value was varied, the storage capacitor value was changed to 750 nF and the other components values remained the same. **Figure 2-5 (b)** shows the charging time of 400 ms and the voltage plateau length was about 10 ms. The discharge time was more than 300 ms. The storage capacitor size was 10 times higher, however the charging and discharging time was 8 and 6 times higher, respectively. This indicates that the larger capacitor takes a longer time to charge and discharge.

2.4.3 AC discharge simulation

The AC discharge simulation circuit is shown in **Figure 2-6 (a)** and its electrical equivalent is in **Figure 2-6 (b)**. In this case a pair of 2.7 nF capacitor were used and arranged in series with the electrodes. The supply voltage was 6 kV RMS with an AC source with 50 Hz. The electrode gap was 3 mm. Transient analysis was used with MultiSims' default parameters, with the starting and end measurement times of 0 and 500 ns, respectively. The time step used was 62.5 ns. The output current (I) and voltage (V) across node 1 was measured; this was equivalent to the discharge voltage and current. The transient simulation results show that the discharge current was an exponentially decaying oscillation (**Figure 2-7**). The maximum peak current was 5.25 kA, and the oscillation decayed completely after about 750 ns.

The supply voltage used was 6 kV RMS, and this voltage will be used for the next simulations with various total capacitance value. This AC circuit simulation results show high discharge currents (> 5 kV) and the higher voltage supply up to 30 kV might be an interest in future investigation.

2.4.4 AC discharge with dielectric simulation

Dielectric material can be placed between the electrodes to improve the preionisation and discharge stability. The discharge circuit was modelled with the effect of dielectric material placed between the electrodes modelled to investigate the circuit characteristic. The dielectric model used duralar film with an estimated capacitance and resistance of 57 pF and 1.5 T Ω respectively. The circuit model is shown in **Figure 2-8(a)**. All other component models remained the same as in section 2.4.3. The measurement of current and voltage was taken at node 1, representing the discharge voltage and current. The maximum peak discharge current was 4.25 A (**Figure 2-8(b)**) which was about 70 % higher than the discharge without the dielectric (**Figure 2-7**). This indicates that the dielectric material improved the ionization between the electrodes. The discharge voltage of 20 V is shown in **Figure 2.8(c)**. The same circuit model was used to investigate how much current would be discharged when 3 pairs of 2.7 nF capacitors were used, see **Figure 2-9(a)**. The

discharge current was 23 A (**Figure 2-9(b)**), where this was about 5 times higher than with a pair of capacitors. The discharge voltage with the 3 pairs of capacitors was reduced to 10 V.

2.5 The Blumlein discharge

The Blumlein discharge was simulated using MultiSim8 and later fabricated (see section 3.14). The rationale was to develop a N₂ based laser (typical wavelength 337 nm) for decontamination that operated in air. Various reports [Law *et al*, 1997; Nagata *et al*, 1973] have shown that rapid discharges achieved using large plate capacitors and spark gap switches can be used to pump N₂ lasers. In the present case the Blumlein discharge system was modeled to investigate the effect of using different values of capacitance by using larger metal plates and dielectric films. The left and right metal plates, either side of the electrodes were covered with duralar film giving an effective capacitance of 44 nF, 1.5Ω resistance, and 750 pH inductance with a spark gap as the main switch. **Figure 2-10 (a)** shows the Blumlein discharge systems and the components used. **Figure 2-10 (b)** shows the discharge current when a 5 kV RMS voltage was supplied to the system. The maximum peak discharge current was 4 kA, with an exponential decaying oscillation which had decayed after 400 ns.

2.6 Modelling of electric field and flux density between electrode

As well as the circuit simulation, it is important that the electrode behaviour is as well understood as this influences the discharge properties. In the present case Uniform Field Electrodes were designed. In Chapter 1, the derivative of the Laplace's equation ($\nabla^2 f = 0$) was used as a harmonic potential function over a particular space-charge volume between the anode and cathode. This harmonic function can be transformed into another space via mapping with the conformal function. This conformal mapping was done with a function that preserved angles in the complex plane. The conformal function was

$$w = f(z) \quad (2.6)$$

$$w = e^{-jv} \quad (2.7)$$

Where w is the imaginary function which gives the V and U values, and z is the real function for the x - y coordinates. The lines of the electric field or the electric potential, V with energy E (Vm^{-1}) and the flux lines (U), were perpendicular to each other. Between the two identical parallel electrodes, the equipotential lines are seen on which the electrical potential are the same value everywhere. If higher electric field existed, it may cause the electric breakdown or arcing. To view the lines of these electric fields and the flux between the Rogowski and Chang electrodes, the Rogowski and Chang functions were modelled with Maple11 software.

2.6.1 Conformal mapping

Maple11 software was used to model the conformal mapping of the electric field and flux function between the anode and cathode. The Rogowski function (equation 1.15) and the Chang function (equation 1.17) were modelled in order to compare the stability of the electrical discharge relative to the geometry of the electrode. The geometry of the electrode helps shape the potential electric field flow and its boundaries. For the modelling, the electrode gap was 1 cm and the imaginary plane W was taken from -2 to 2 spatial units.

The potential and flux functions for the Rogowski function is shown in **Figure 2-11(a)** and the Chang in **Figure 2-11(b)** profiles. The electric potential (V) is indicated by the vertical red lines and the flux (U) as the horizontal green lines which are perpendicular to each other. Referring to the 0-0 points, the distribution of the equipotential of the electric potential and flux for the Chang is symmetrical compared to the Rogowski. The Chang shows that the imaginary of the flux U and the potential V were mapped symmetrically to the real x - y coordinate region. For the Rogowski however, the 0-0 points were non-symmetrical.

Figure 2-12(a) and (b) show the linearity of the central electric potential strength for Rogowski and Chang electrodes, respectively. It was clearly shown that the electro-potential (V) for the Rogowski was 8.0×10^{-5} V/m which was twice that of the Chang for the same distance $U = 2$ (a.u). The higher electric potential strength when $U = 2$ (a.u), shows that the Rogowski has the greater chance of breakdown than the Chang.

Figure 2-13(a) and (b) show the inverse function for Rogowski and Chang, respectively. The inverse function is used to obtain the opposite map of the functions of x-y (or the real coordinates). The Rogowski shows a high electric potential and non-symmetrical (**Figure 2-13(a)**). By the 0-0 points, the inverse Chang function almost maintains the symmetrical distribution of the electrical potential.

Figure 2-14(a) and (b) show the inverse potential electric functions for the Rogowski and Chang geometries, respectively. The electric potential for the Rogowski function shows that the potential decreased linearly as a function of the distance from the central plane to $U = 1$ (a. u). On the other hand, with the Chang profile it decreased exponentially, which indicates that the high potential was preserved until very near to the curved edge of the geometry.

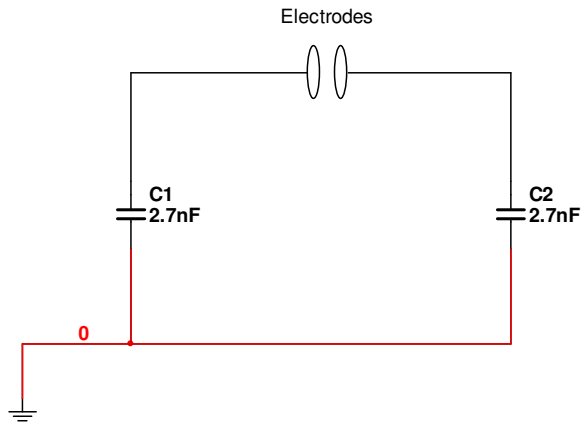
Figure 2-15(a) and (b) show the inverse flux (U) function for the Rogowski and the Chang. The inverse flux functions were linear where the maximum flux value for the Rogowski was -0.58 at central plane where $U = 0$ and minimum when $U = 1$ (a.u). The Chang had an opposite value, the minimum flux was 0 at central, where $U = 0$ and maximum was 0.5 where $U = 1$ (a.u).

The modelling showed that the Rogowski had a disadvantage in terms of the electric potential uniformity from the central region to the outer regions the so called U distance. These models helped to decide the selection of electrode profiles to use in the research. The Chang' which is more compact and uniform in terms of the electric potential distribution was chosen. **Figure 2-15(a), (b) and (c)** show the Chang function with various constant values of k. The constant k was varied from 0.6 to 0.02. The profile with $k = 0.02$ and 0.2 were selected to be used in the Chang UFE in-house manufacture, which is discussed further in Chapter 4.

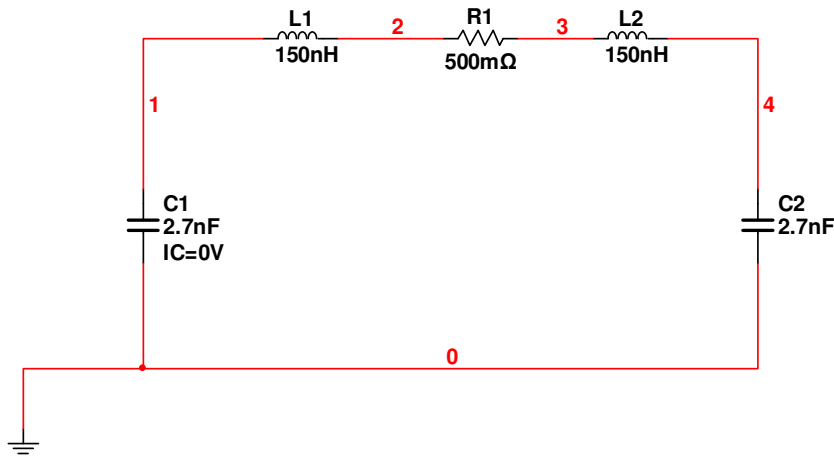
2.7 Conclusions

This chapter explained circuit models that were developed in MultiSim8 to model the discharge voltage and current. Different discharge models with various circuit component values were investigated. The discharge currents and voltages showed the likely discharge energy and the discharge duration.

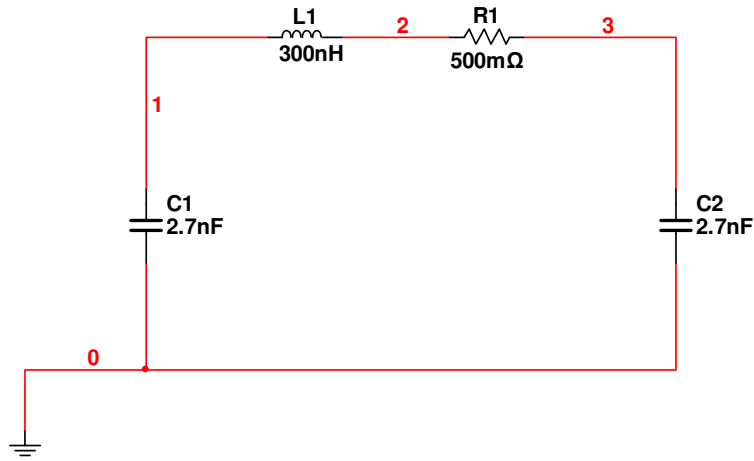
The modelling of the Rogowski and Chang functions in Maple 11 demonstrated the analytical approach towards understanding the electrical potential and flux functions. The modelling results contributed to the selection of electrode parameters for the UFE . The development and UFE manufacture is discussed in Chapter 4.



(a) The model circuit.



(b) The electrical equivalent circuit



(c) The simplified equivalent circuit.

Figure 2-1 The model circuit of the discharge system.

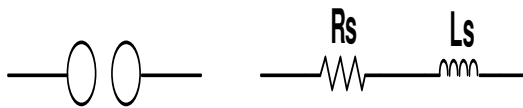


Figure 2-2 Spark gap equivalent circuit

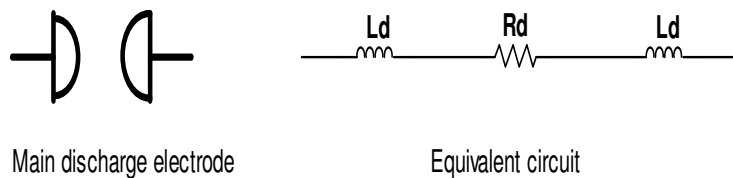
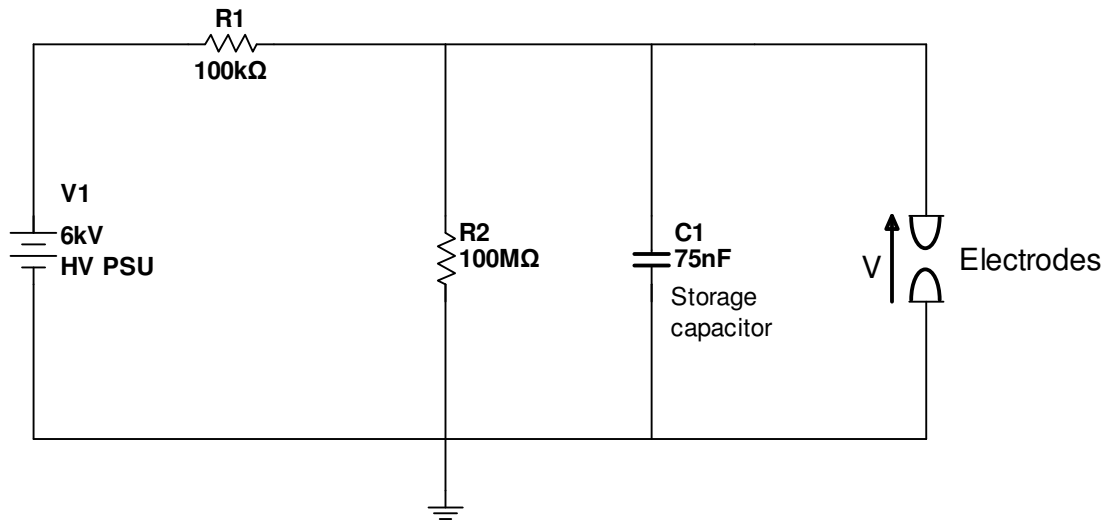
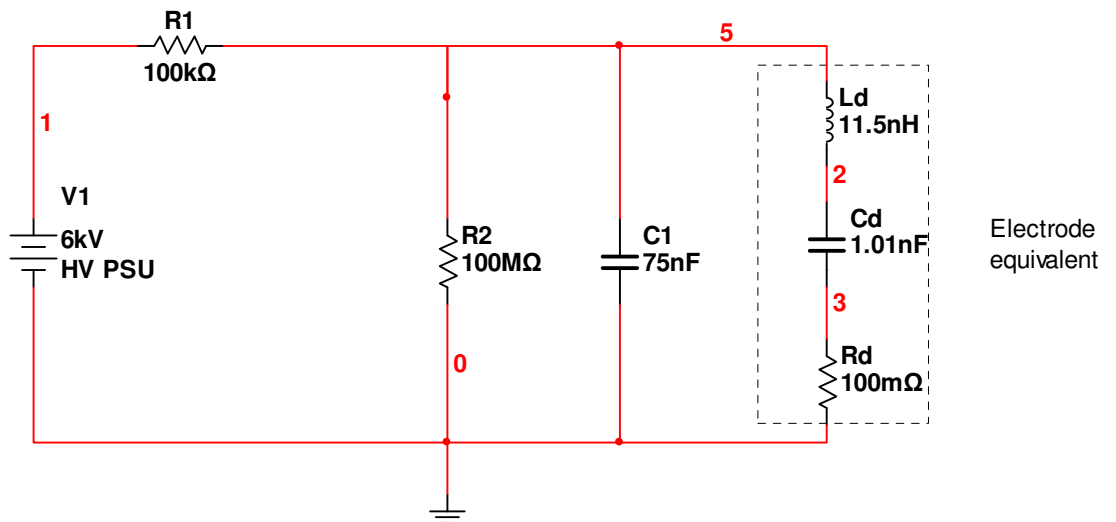


Figure 2-3 Electrode equivalent circuit.

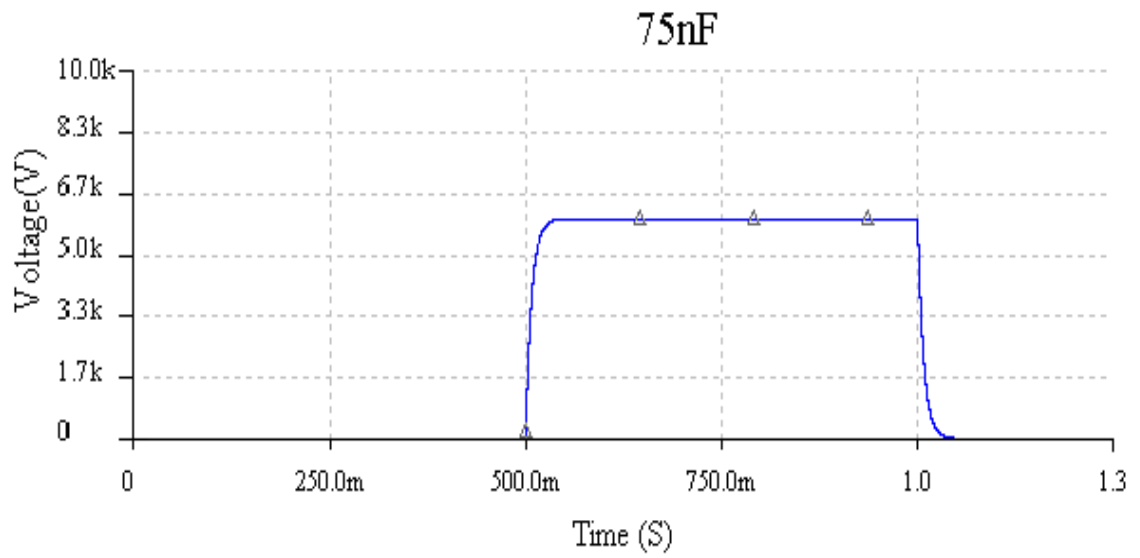


(a) Main discharge system with the electrodes.

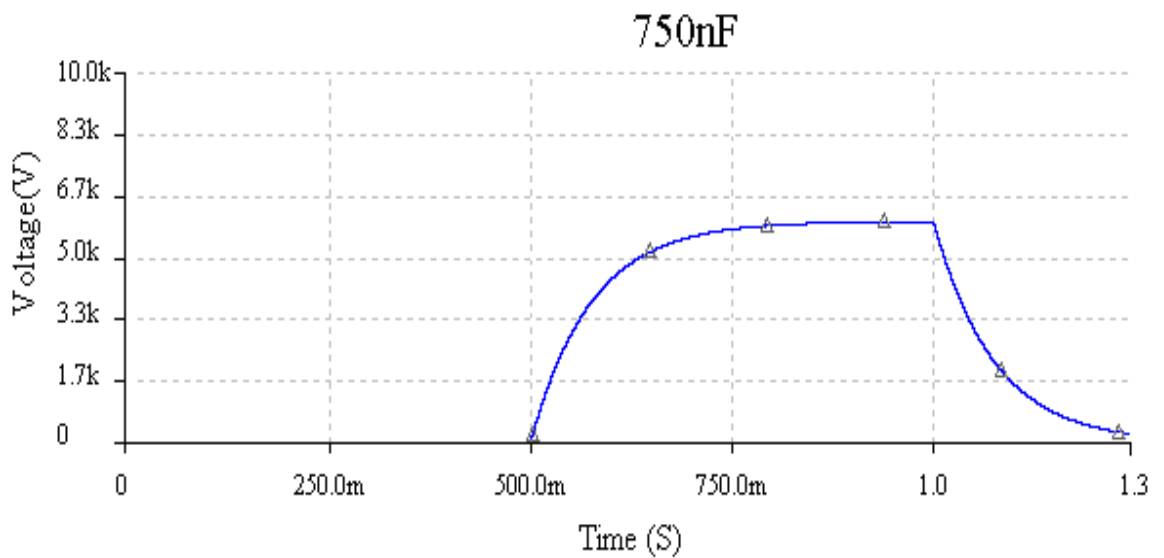


(b) An electrical equivalent circuit to (a)

Figure 2-4 The modelling discharge circuit (a) The main discharge circuit (b) An equivalent circuit with stray inductance (L_d) was 11.5 nH, capacitance $C_d = 1.01$ nF and $R_d = 100\text{m}\Omega$. This DC discharge was modelled in vacuum condition.

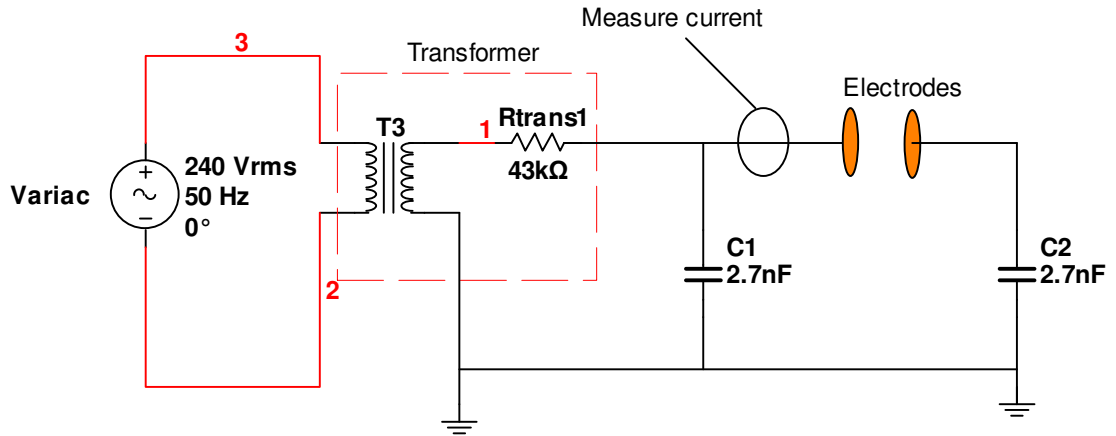


(a) 75 nF capacitor charging and discharging

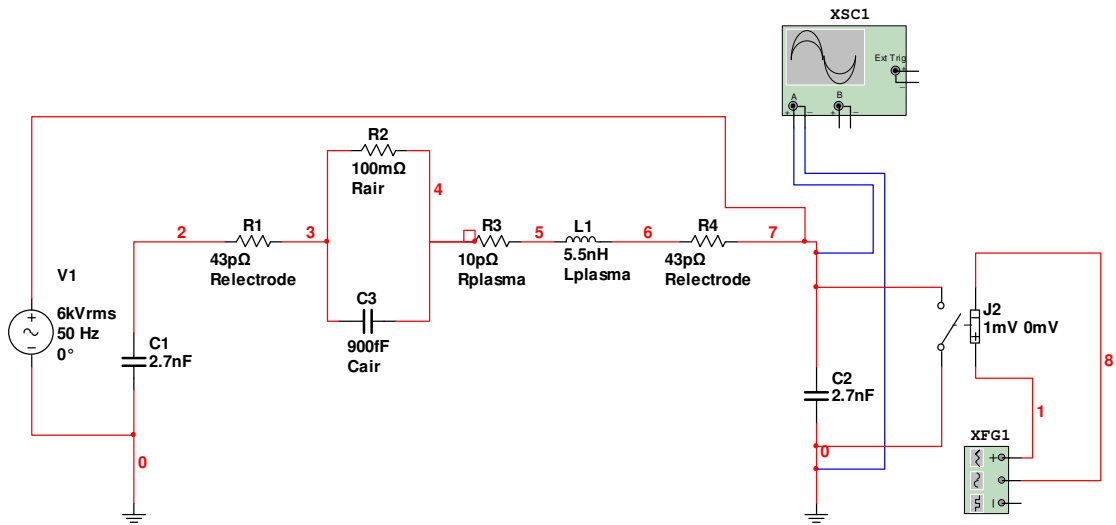


(a) 750 nF capacitor charging and discharging

Figure 2-5 Comparison of capacitor charging pulses for model in Figure 2-4 (a) Pulse from the 75 nF capacitor bank of the DC main discharge (b) 750 nF capacitor pulse.

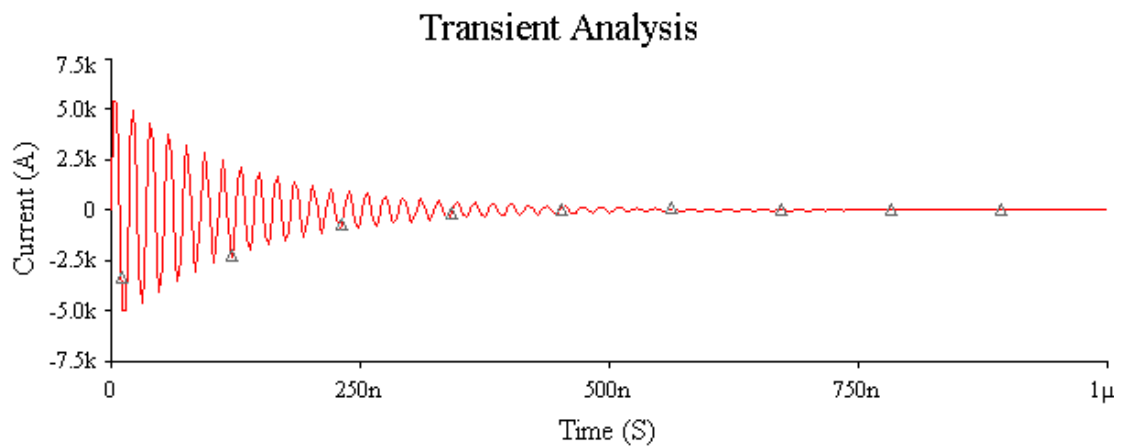


a) The AC air discharge circuit with the Chang electrodes.

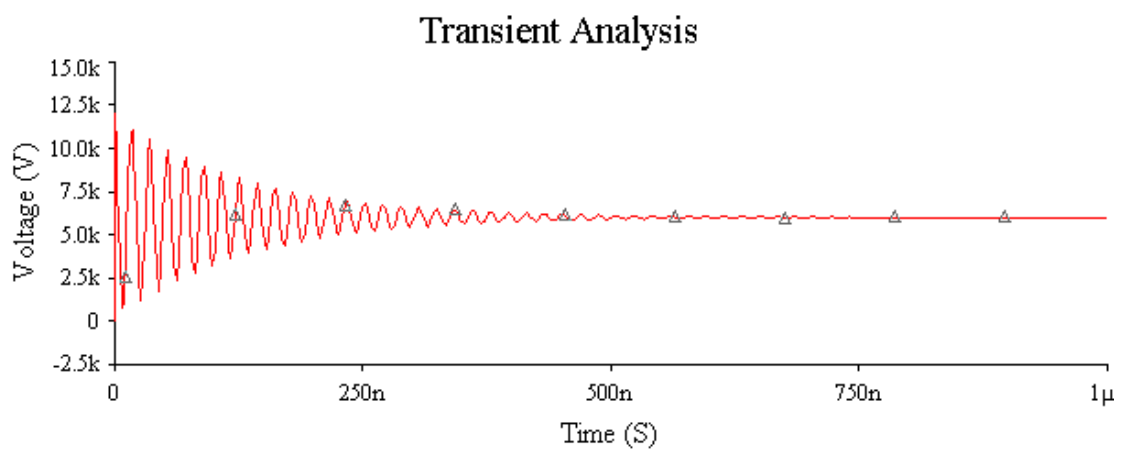


b) The electrical equivalent air discharge circuit

Figure 2-6 An AC simulation discharge (a) The electrical circuit (b) An equivalent modelling circuit diagram for the AC in air at atmospheric pressure with Chang electrodes and 2.7 nF capacitors and 6 kV RMS supply.

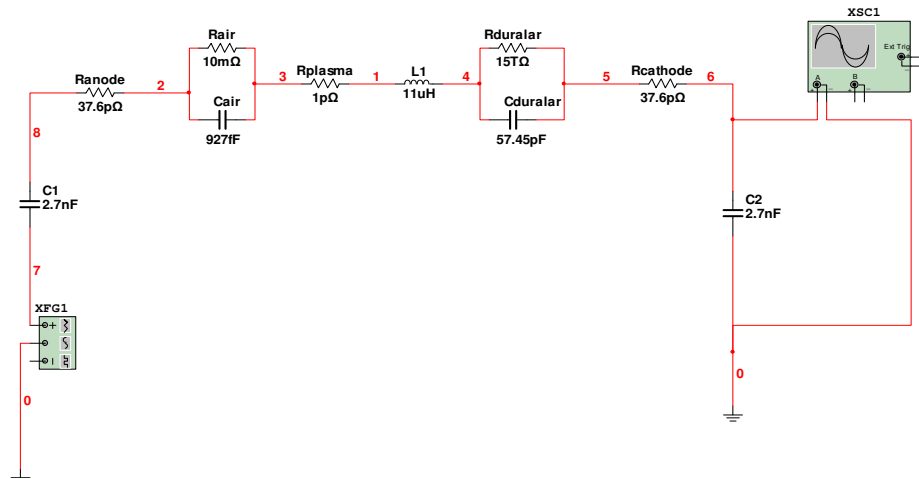


(a) The discharge current.

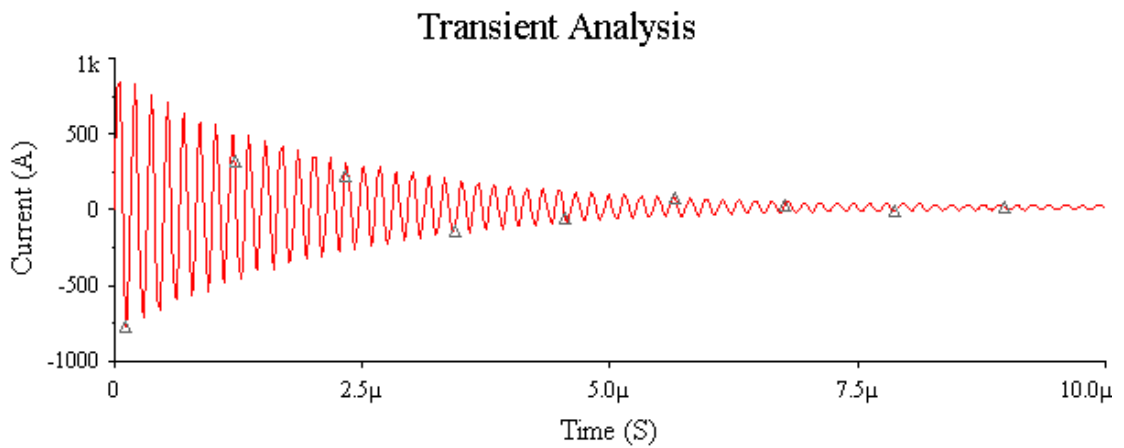


(a) The discharge voltage.

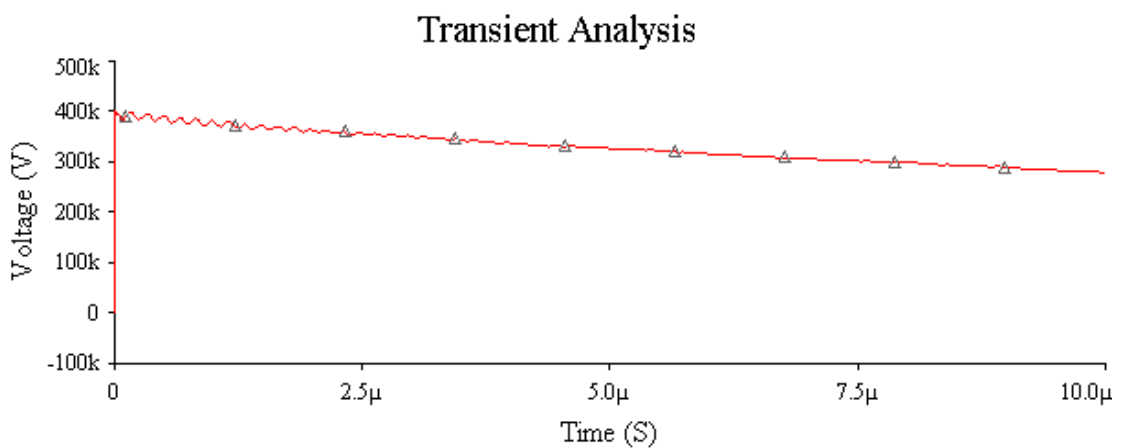
Figure 2-7 The simulation result showing the discharge current and voltage measured from the AC air discharge in Figure 2-6 (a) The current peak is about 5.25 kA (b) The maximum peak voltage is about 12 kV.



(a) The AC discharge circuit with two layers of duralar between the electrodes. The voltage source is 6 kV.

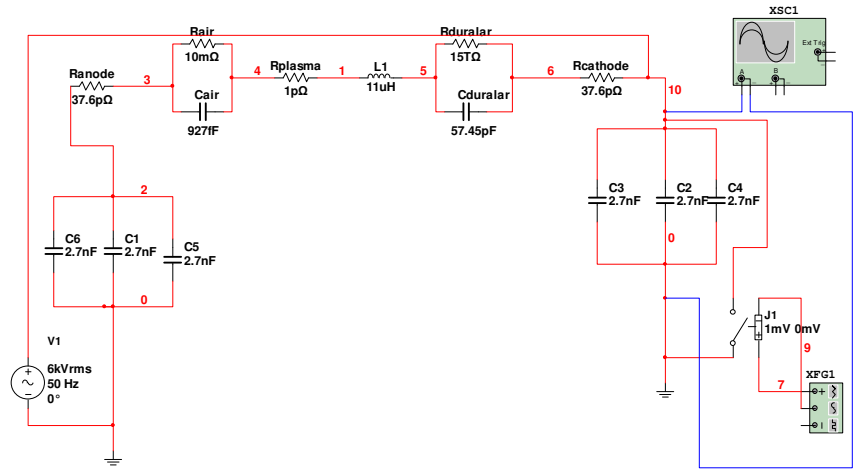


(b) The transient current from the AC circuit at node 1 with duralar.



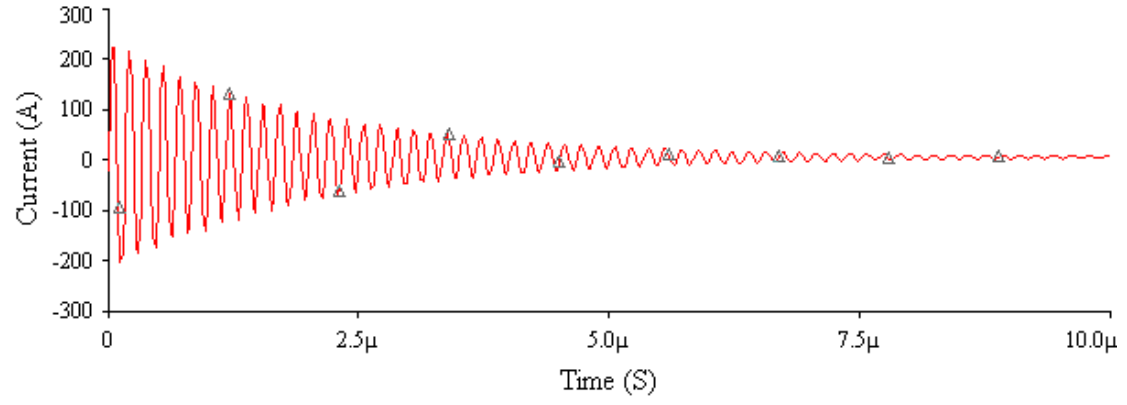
(c) The discharge voltage at node 1.

Figure 2-8 The simulation results with the AC discharge with a pair of 2.7 nF capacitors with duralar (a) The modeling circuit (b) The discharge current across the electrodes gap (c) The discharge voltage.



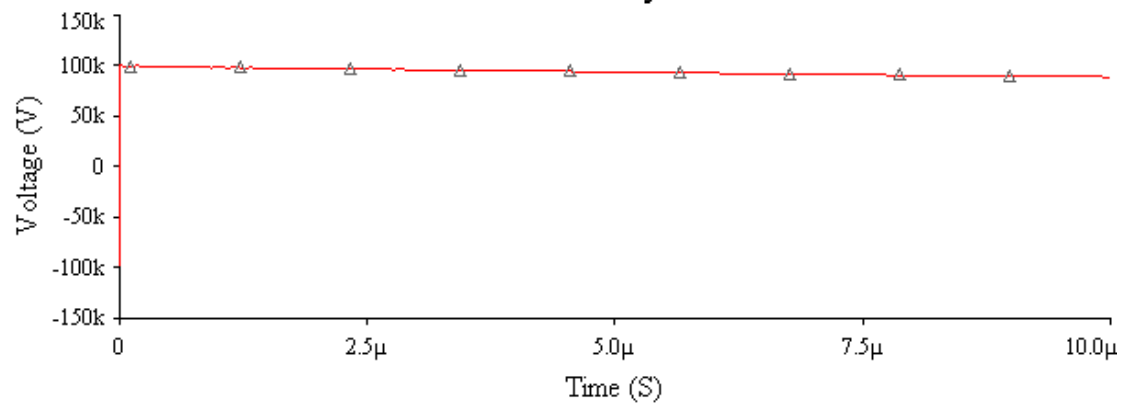
(a) The AC discharge circuit with two layers of duralar between the electrodes and 3 pairs of 2.7 nF capacitors and 6 kV RMS supply.

Transient Analysis



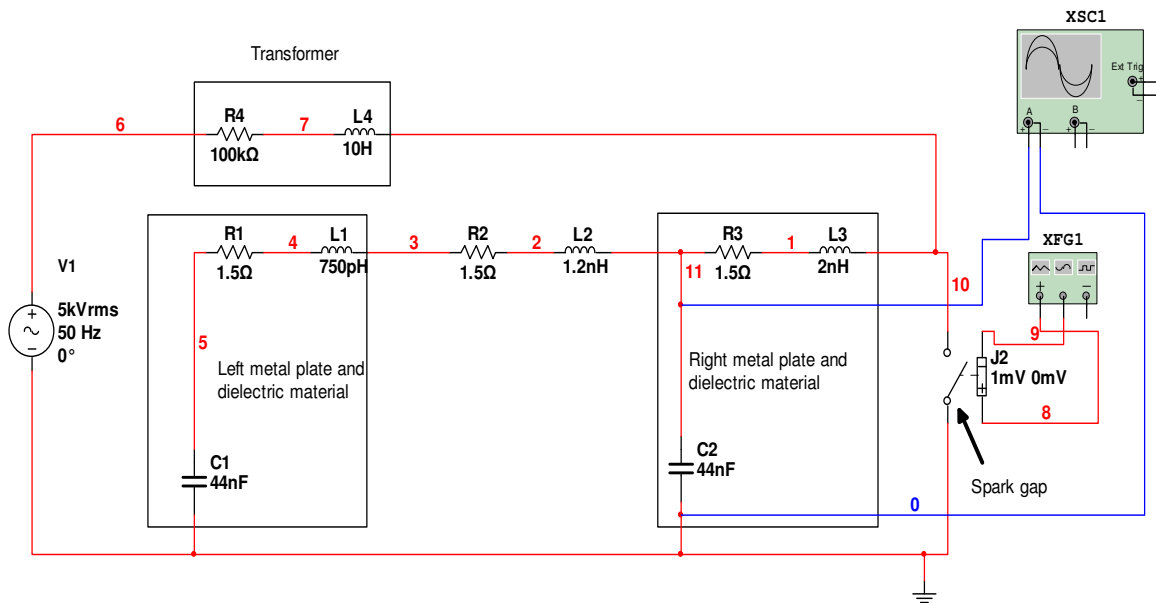
(b) The transient current from the AC circuit at node 1.

Transient Analysis

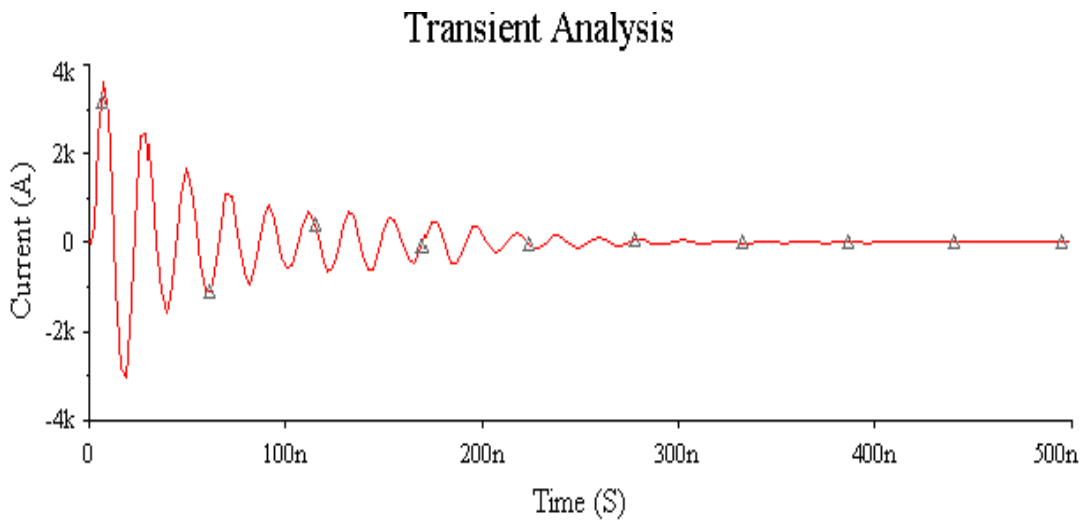


(c) The discharge voltage at node 1.

Figure 2-9 The AC discharge transient analysis with 2 layers of duralar and 3 pairs of 2.7 nF capacitors (a) The discharge model with two layers of duralar and 6 kV RMS supply (b) The discharge current from the model. At node 1 (c) The discharge voltage at node 1.



(a) The Blumlein discharge system.



(b) The discharge current from the Blumlein discharge system.

Figure 2-10 The Blumlein discharge system (a) The Blumlein discharge modelling system (b) The discharge current with maximum pulse of about 3.75 kA.

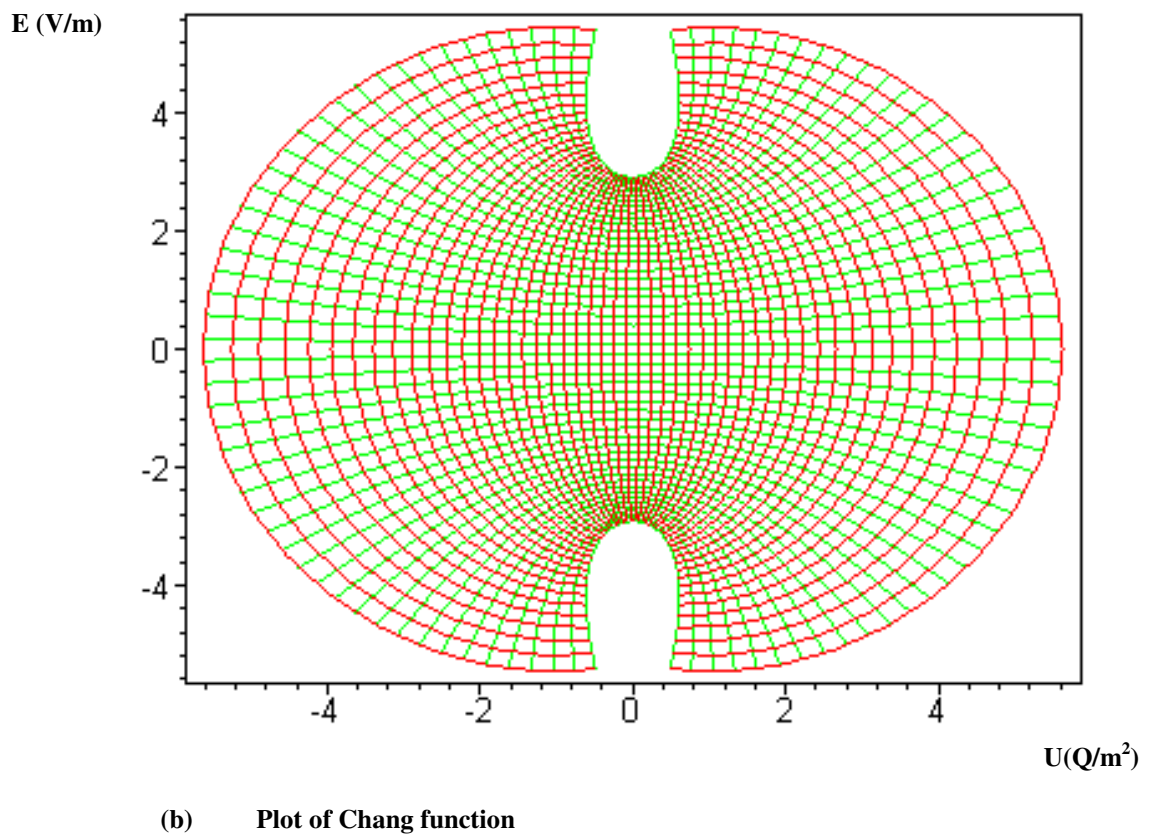
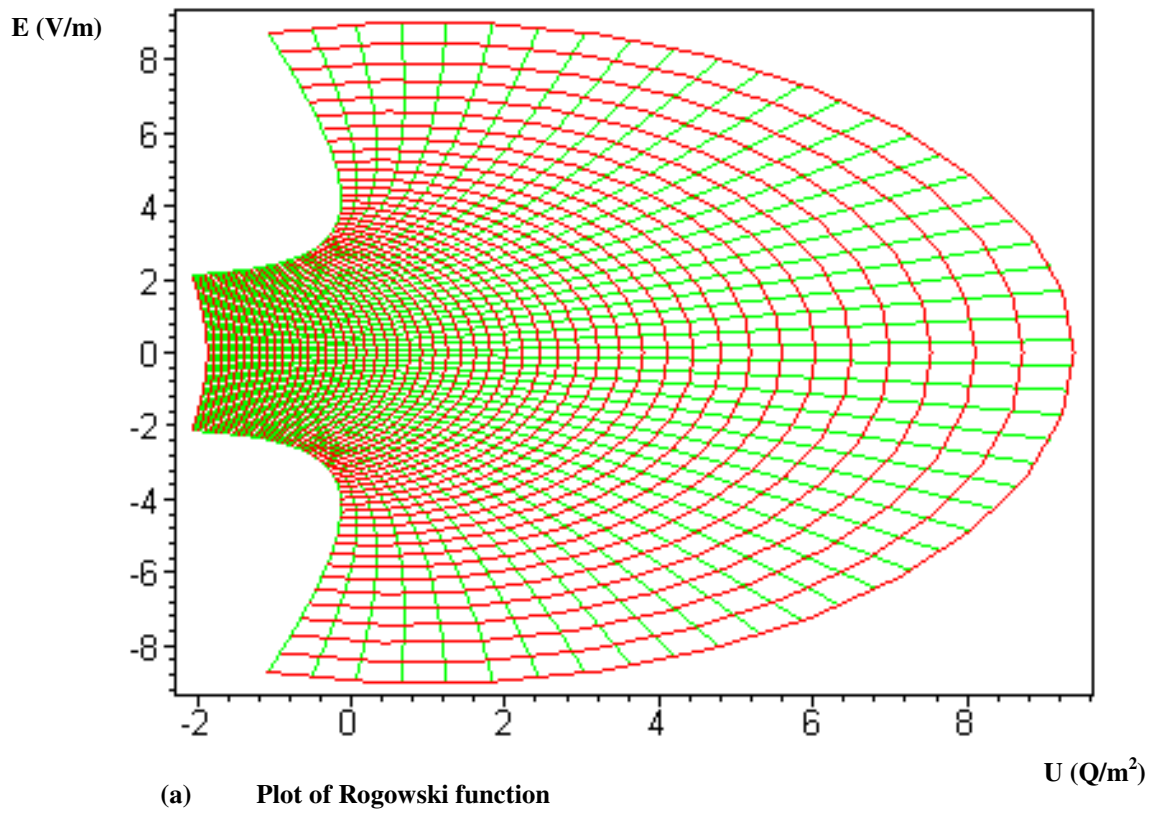
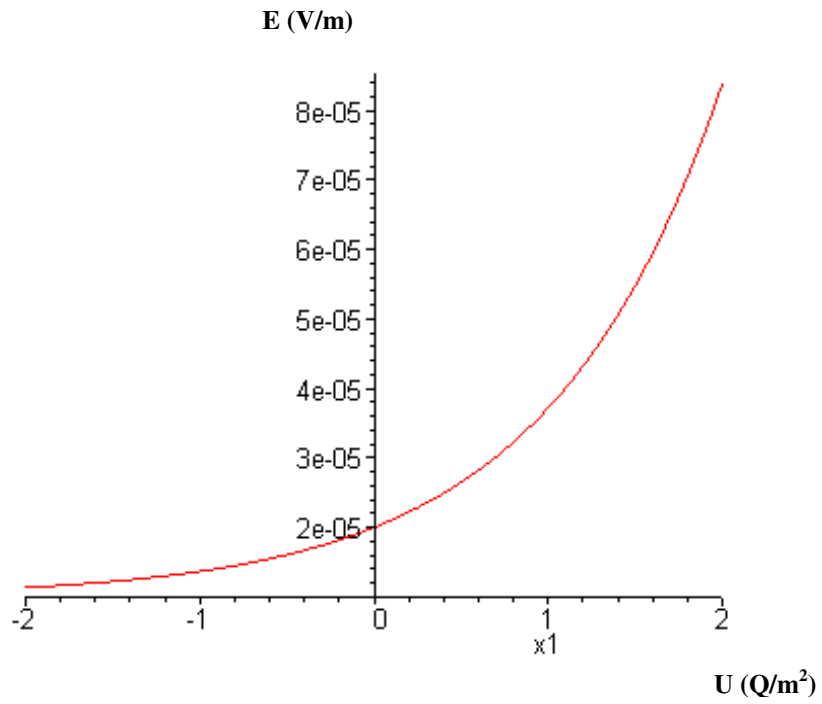
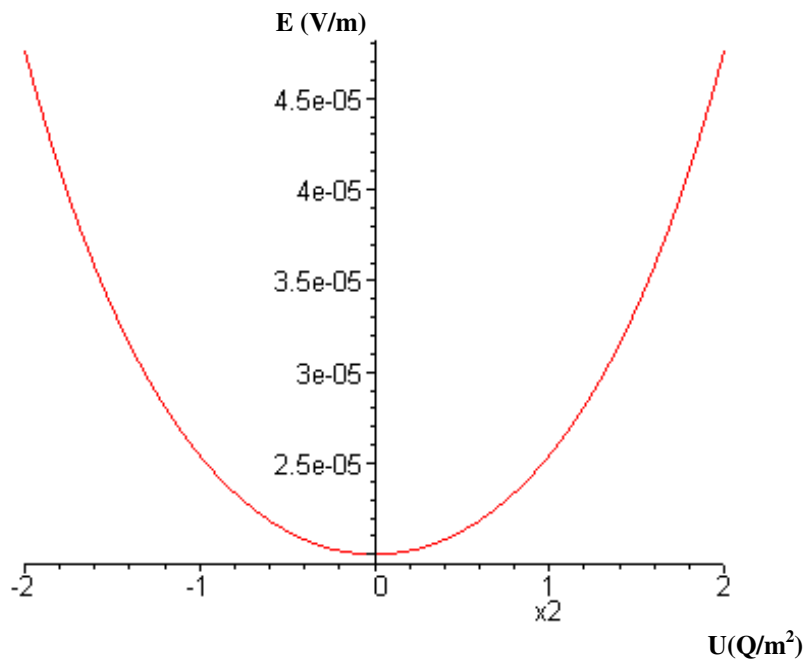


Figure 2-11 The mesh of flux (green horizontal lines) and potential (red vertical lines) function of (a) The Rogowski profile and (b) The Chang profile.

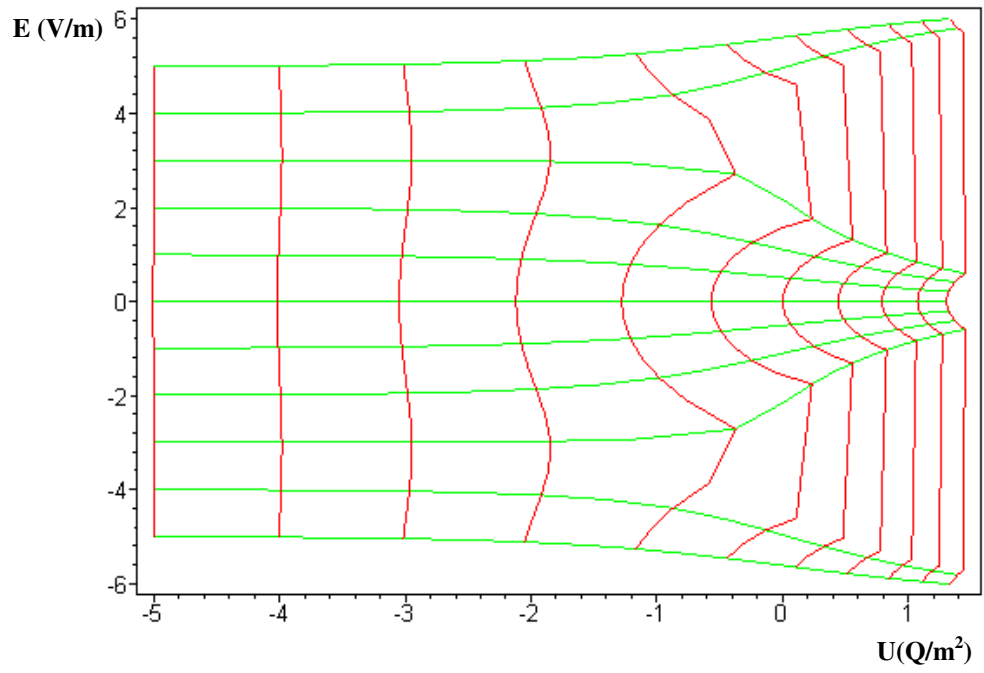


(a) The Rogowski function.

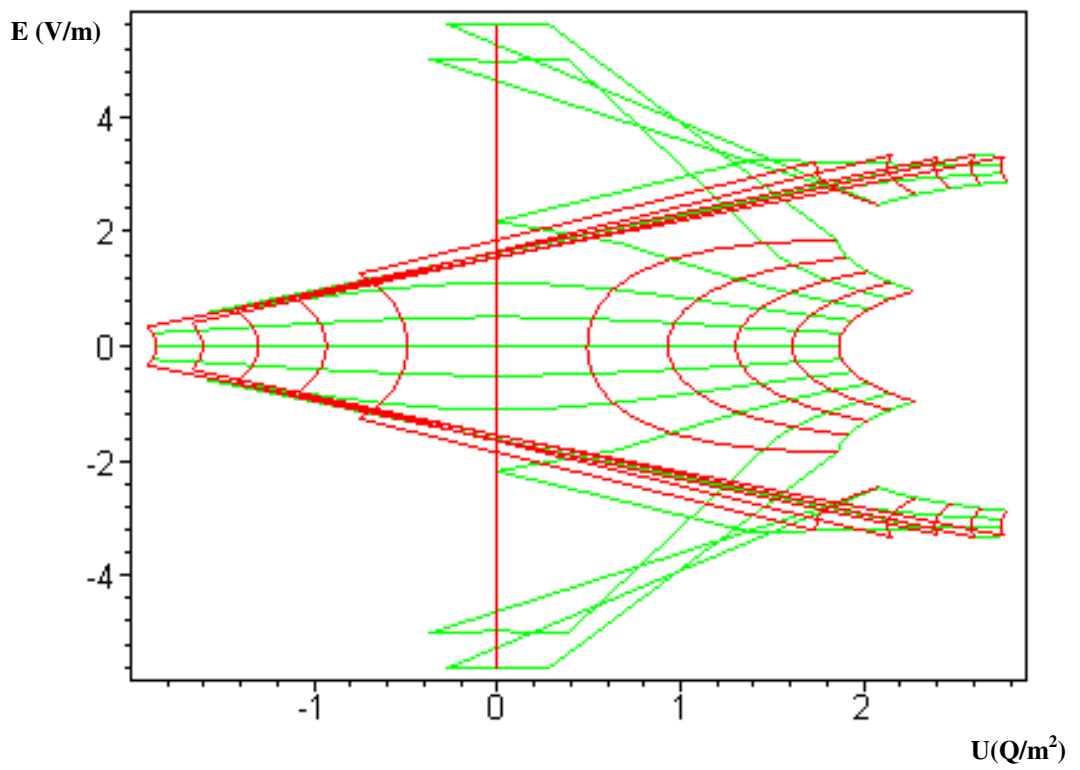


(b) The Chang function.

Figure 2-12 Linearity in the central electric field strength using: a) The Rogowski function and b) The Chang function.

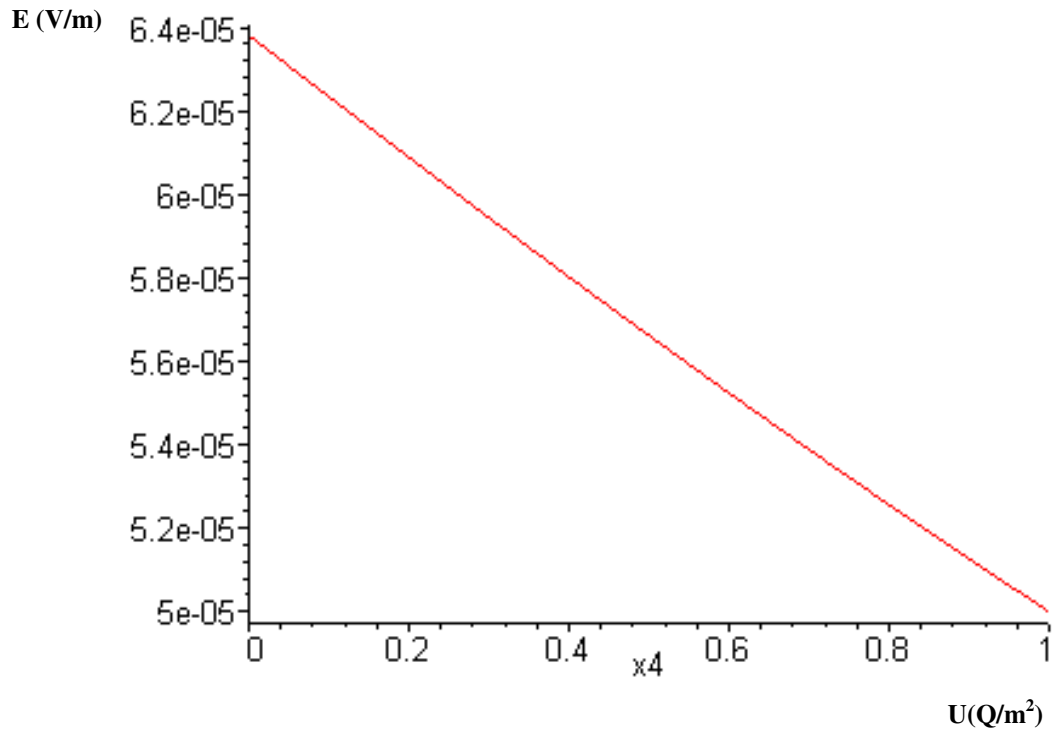


(a) Rogowski inverse function

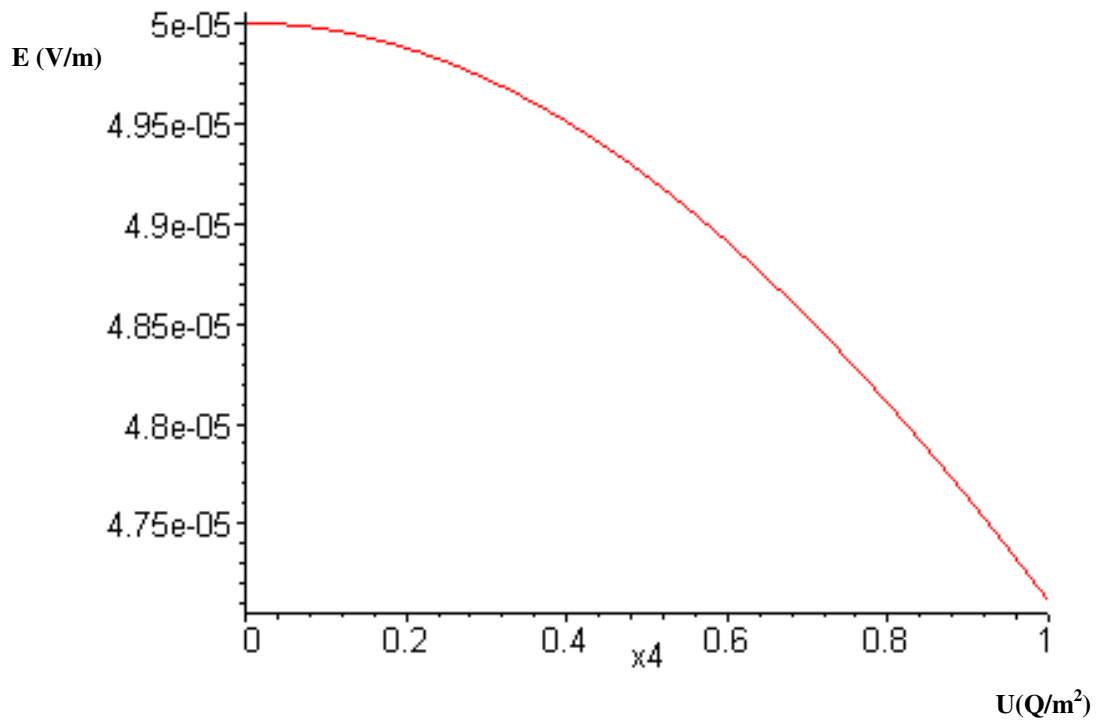


(b) Chang inverse function

Figure 2-13 The plot of inverse function of a) the Rogowski and (b) the Chang functions.

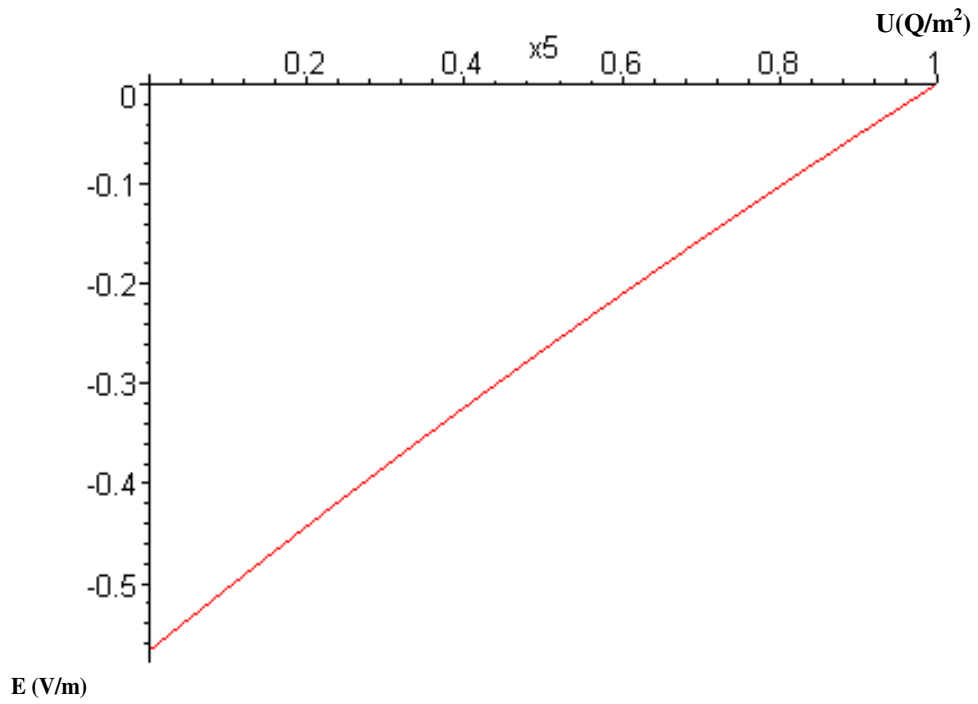


(a) The inverse Rogowski electric potential function.

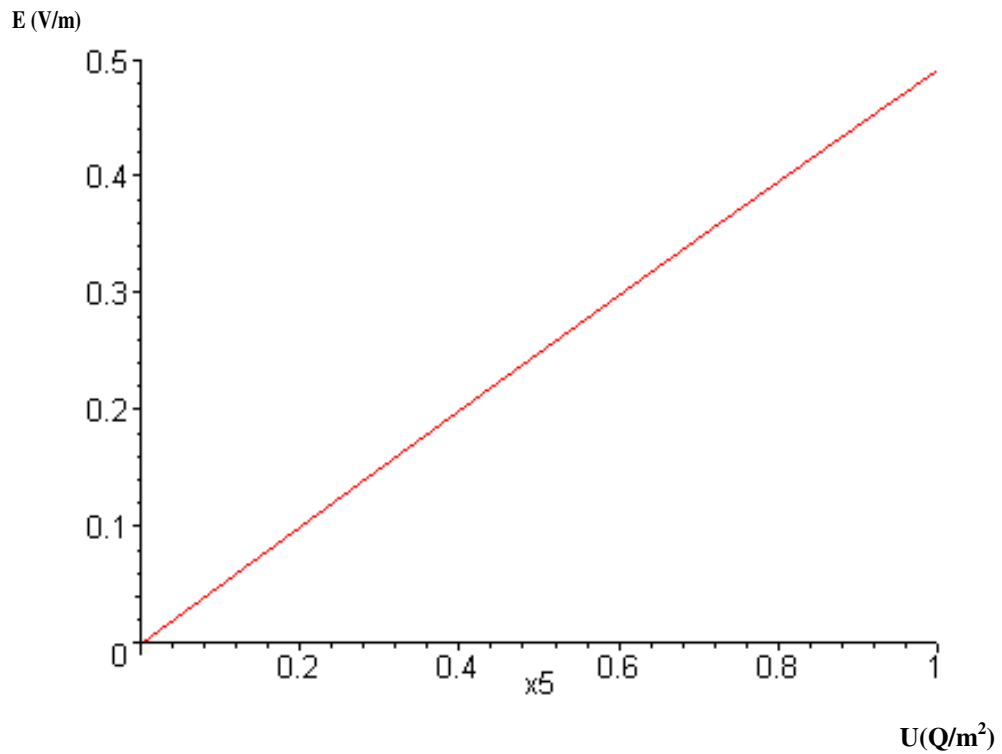


(b) The inverse Chang electric potential function.

Figure 2-14 The inverse electric potential function changes across the central plane (a) the Rogowski and (b) the Chang



(a). The inverse flux strength changes across central plane



(b) Changs inverse flux function

Figure 2-15 The inverse of the flux function on a) the Rogowski and b) the Chang

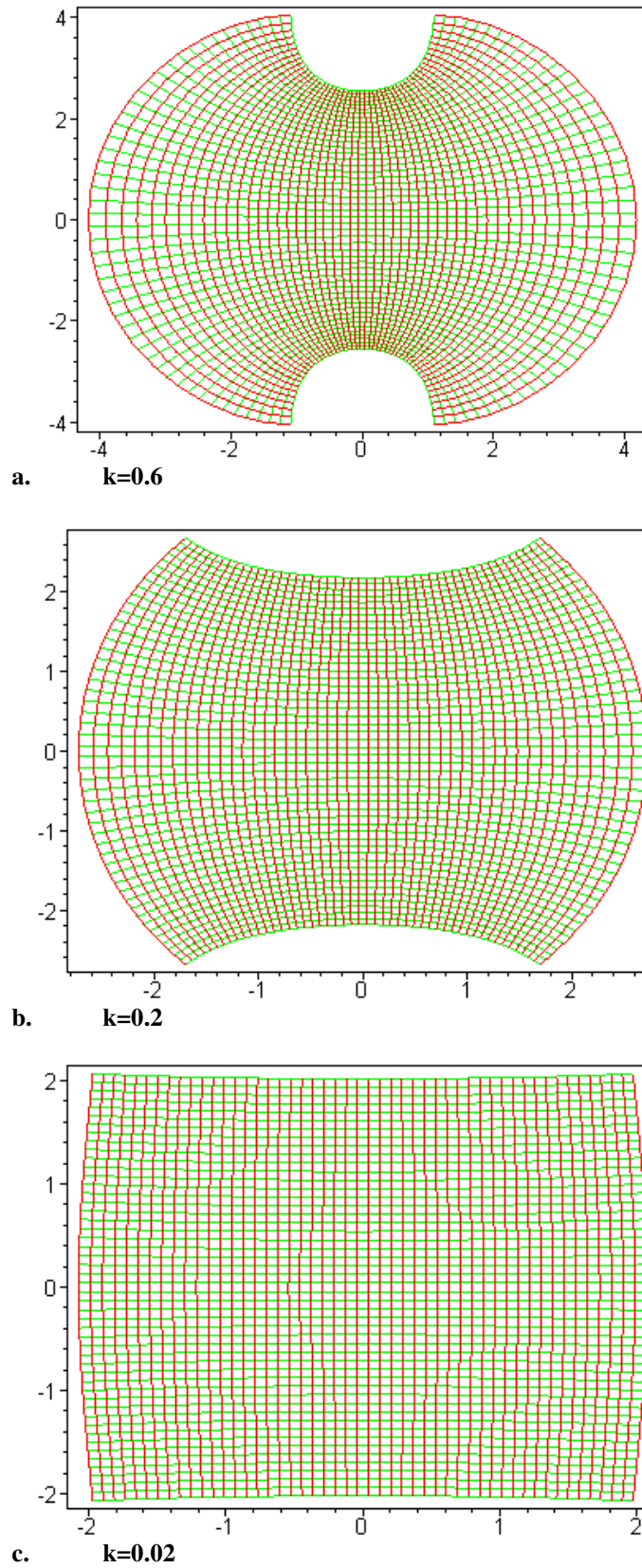


Figure 2-16 The effect of the empirical constant k value on the electrode edges (a) $k=0.6$, (b) $k=0.2$ and (c) $k=0.02$.

Chapter 3

Development of the Discharge System

3.1 Introduction

This chapter reports the development of the charging system and characterization of the discharge. The development began with the modelling of the pulse discharge circuit which was discussed in Chapter 2. The system was developed starting with the concept of a DC single pulse initiation via an independent preioniser and followed by an AC self-sustained discharge, with preionisation via trigger wires capacitively coupled to the anode. Both systems were developed with the ability to flow gas through the electrodes. Two types of electrodes were used in the system: planar brass electrodes with a non-specific standard profile and the Chang uniform field electrode. The DC discharge performance with the planar electrodes together with the independent preionisation system was assessed. This was followed by testing the system and investigating the Paschen breakdown voltage with air, nitrogen, carbon dioxide and helium gases. The discharge voltage and current with a gas mixture of 1:1:8 (CO₂: N₂: He) was also measured. Flow shaping was added to the DC discharge system to study the clearing ratio and its affect on the discharge characteristics.

Additionally, an AC discharge system with trigger wire preionisation and Chang profiled electrodes was developed. The discharge characteristics with a gas mixture of 1:1:4 at 20 mbar and air at atmospheric pressure were studied. Various dielectric materials were placed over the cathode to improve the electron charge distribution and preionisation uniformity. The dielectric materials used were: mylar, duralar and glass. The Blumlien air discharge at atmospheric pressure was also developed and investigated. This is discussed in section 3.14.

3.2 Switchless, self-sustained discharge systems

Both gas discharge systems briefly described above were designed to be switchless, whereby the electrodes acted as the switch and the main discharge electrodes. The

discharge initiation system should be capable of producing fast voltage-rise times to obtain a stable discharge. Ideally, the desired condition for fast pulsed discharge circuits should satisfy the critically damped condition, the design equation of this condition is

$$\frac{1}{LC} - \frac{R^2}{4L^2} = 0 \quad (3.1)$$

The time constant of the circuit, $\tau = RC$ is approximately equal to the pulsed duration of the current pulse (t) which is about 1/3 of the rise time. Furthermore, to produce efficient preionisation $di/dt > 10^{10} \text{ As}^{-1}$ is essential [Mcken *et. al*, 1976].

The main discharge circuit is shown in **Figure 3-1** (this was shown in Chapter 2, Figure 2-5 but reproduced here for convenience). The stray inductance (L_s) from the mounting unit and other components was estimated from measurement to be around, $L_s = 11.5 \text{ nH}$. The pulse circuitry contains the following components:

1. High voltage DC charging power supply
2. Storage capacitors
3. Resistor to limit the maximum current
4. Electrodes

The circuit with these listed components above was developed and discussed in the following sections.

3.2.1 High voltage DC charging power supply

Pulse Power & Measurement (PPM) electronic High Voltage power supply unit (HV PSU, Model 500A (USA)) was employed for the DC voltage source. The DC power supply rating was $V = 6 \text{ kV}$, with a charging energy of 500 J/s with constant current of 80 mA (**Figure 3-2**). Although the PSU (**Figure 3.2a**) was rated for V of 6 kV , the measured maximum voltage range was in the range of $0\text{-}8.7 \text{ kV}$. An interface to control the output voltage from the PSU was built in-house (see **Appendix 3A** for

the interface circuit). The control output features include a voltage regulator (**Figure 3.2b**), a voltage monitoring display, reset button (**Figure 3.2c**) to dismiss any residual charge in the PSU and an emergency stop switch. The output voltage from the PSU was connected to the storage capacitors that were housed in an insulation box.

3.2.2 Storage capacitor (C_s)

The TPM (tubular-paper-mylar) range storage capacitors (C_s) (HighVolts, Ireland), are manufactured using a mix of dielectric materials that consists of polypropylene or polyester film and capacitor tissue, which is then impregnated with mineral oil. The capacitors were rated at 20kV (DC or AC). Each capacitor was 15nF and by using 5 capacitors, the total value of the storage capacitance was 75nF.

The storage capacitors were mounted inside an insulation box, as shown in **Figure 3-3 (a)**. A 100 k Ω limiting resistor and voltage divider 100M Ω resistor were also placed inside the insulation box. HV BNC connectors were used to connect the input voltage from the HV PSU and the output voltage to the anode (**Figure 3-3(b)**).

3.2.3 Electrodes

The anode was connected directly to the high voltage source from the box storage capacitor C_s and the cathode was earthed. The main discharge was produced between the electrodes in the form of plasma. The electrodes were mounted on holders (see section 3.2.3.1) and placed inside a stainless steel discharge chamber with dimensions of 390 x 355 x 290 mm ($40.1505 \times 10^6 \text{ mm}^3$). The ratio of the discharge chamber volume to the active discharge volume was approximately 67000:1. This large volume ratio may enable a longer discharge operational time due to the high volume of gas. Further details of the electrode types that were used in the system can be found in section 3.3.

3.2.3.1 Anode and cathode holder

The anode holder was made from PTFE plate and was supported with two PTFE brackets that were mounted to the base metal plate. Two metal M6 screws were used to mount the anode on the PTFE plate. These screws were also used as connectors to the high voltage source. The anode was in a fixed position.

Figure 3-4 shows the electrode holder used to mount the cathode. The cathode was mounted via two metal screws on an aluminium bracket that was specially designed to provide support as well as an earth connection. The size of the cathode holder was 50 mm (width) x 150 mm (length) x 45 mm (height). The height of the bracket determined the anode and cathode gap. At 45 mm of bracket height, the maximum electrode gap was 7 mm. The height of the bracket was aligned by inserting washers underneath the bracket before bolting it down to the base metal plate. Each washer thickness was around 0.5 mm, thus making alignment of the electrode gap possible. The bracket was secured to the base metal plate with 2 M6 bolts.

3.3 Electrode types

Two types of electrodes were used in the DC discharge; they were planar brass electrodes and uniform field electrodes based on Chang's design [Chang, 1973], see Chapter 1, section 1 4.1.2 and Chapter 4. The planar brass electrodes were made first to use as a test bed for discharge design modelling.

3.3.1 Planar brass electrode

Figure 3-5 shows a photograph of machined and polished electrodes that were used in the early prototype of the DC discharge system. The planar brass electrode size was 60 (length) x 10 (width) mm with an edge fillet radius of 1 mm. The electrode was machined on a CNC machining centre and finished with a hand and wet polishing process. Emery paper No 800 was used for the polishing to obtain a

smooth surface electrode which was necessary to avoid arc formation during the discharge. Details of the planar brass electrode design and manufacturing are reported in Chapter 4 section 4.3.1, which discusses the Electrode Design and Manufacturing for all types of electrodes that were used in this research.

3.3.2 Chang's uniform field electrode

The electrode design based on Chang's uniform field electrode were built to a size of 60 mm (length) x 10 mm (width) and fabricated from solid brass stock. The CNC machining centre was used to machine the electrodes with inputs from MASTERCAM software for the machining path profile. The machined electrode was finished with a hand wet polishing process using emery cloth No 800. Details of the Chang electrode design and manufacturing can be found in section 4.3.2 in Chapter 4, which discusses each step of the development process. **Figure 3-6** shows a photograph of the Chang profiled electrodes ready to be mounted on the electrode holder.

3.4 Independent spark plug preionisation

The preioniser circuit was designed to provide energy to a row of car spark-plugs mounted alongside the discharge volume. The car spark plugs served as a spark gap, to produce UV emission to ionise the gas and induce electron production from the gas surrounding the main discharge region. This ionisation helps to provide a uniform breakdown across the main discharge volume. The spark plugs were placed between the cathode and anode, within 24 mm distance to the side of the electrode as illustrated in **Figure 3-7**.

Figure 3-8 shows a schematic diagram of the preioniser circuit. The main components of the preioniser are: the car spark plug (spark gap), primary and secondary coil (ignition coil, Unipart GLC 186, made in EC) step up transformer, 12 V power supply and a switch on the primary side of the step up transformer.

A commercially available driver circuit (Smart Kit, 1058KT by Smart Electronics Ltd, made in EEC, distributed by Quasar Electronics) to fire the spark-plugs was used (see **Appendix 3B**). This system was modified to fire all four spark plugs simultaneously. The operation of the preioniser starts by connecting the primary coil to a 12V DC power supply. The output voltage from the primary coil was 380V, and then by pressing the switch on the primary side, a transient is induced in the output of the secondary coil. The output voltage from the secondary coil was capable of reaching 35kV, The current of ~ 0.04 A was also measured by using a Rogowski coil looped around the spark plug cable and connected to a LeCroy 9310 oscilloscope. **Figure 3-9(a)** shows the mounting of the spark plugs using PTFE board and copper plate as the earth strip **(b)** the illustration of the spark plug position and mounting in the discharge chamber, **(c)** the assembly of the spark plug driver circuit.

3.5 Discharge Chamber

The discharge chamber contained the electrodes, gases, the secondary coil and the spark plug preionisation system. It was a rectangular stainless steel box (dimensions, 390 x 356 x 290 mm) with a few port holes on all four sides for access connections to the electrical power supply, gas, gauges and pump. The top cover was made from 1.0 inch thick acrylic plate with a sealed 'O' ring groove. It was bolted down with 18, M10 nuts and bolts. The thick 'O' ring was 7 mm diameter and sealed with vacuum grease. To secure the discharge chamber's top cover, a torque wrench was used together with an adjustable spanner to tighten the nuts and bolts. The tension of the bolts must be uniform in order to avoid cracking the acrylic cover and to ensure the 'O' ring seal was evenly compressed.

To prepare the discharge chamber for operation, the gas inlet valve and then the air was pumped out of the chamber to the order of mbar. The pump valve was closed and the vacuum pump switched off. Closing the pump valve before switching off the vacuum pump is important to prevent the back-flow of oil from the pump into the

discharge chamber due to the negative pressure in the chamber. This was followed by flooding the gas or mix of gases into the chamber to the required partial pressures. Two types of vacuum gauges were used in monitoring the pressure in the chamber: an Edwards EMV 251 to monitor the inlet gases pressure and APG Pirani Penning to monitor the vacuum pumping.

3.6 Gas systems

The gases used in the system were carbon dioxide, nitrogen, helium and air. The flow of all gases (except air) into the chamber was controlled using a needle valve. Polyethylene 8 mm ID tubes were used to transport the gas from the primary to secondary valve systems and into the discharge chamber. The gas pressure in the chamber was controlled manually via a needle valve and monitored with an Edwards, EMV251 pressure gauge. Only one gas was admitted at a time. The pressure of the supplied gas before the primary valves was 6.0 bar, thus extra caution was needed when controlling the gas flow into the chamber to avoid over running the required test pressure. The flow of helium gas was the most difficult to control manually to meet the exact required pressure, because of its low molecular weight (4.002602 (2) g/mol). There was less problem in controlling the nitrogen (molecular weight of 14.0067 g/mol) and carbon dioxide (44.0095 g/mol) flow to meet the pressure requirements.

The bleed valve was used to increase the air pressure in the chamber from lower to atmospheric pressure when required. All tube and valve connections were sealed with rubber 'O' rings and vacuum grease to minimise leaks. **Figure 3-10** illustrates the gas system connection to the discharge chamber.

3.6.1 Vacuum systems

An Edwards EM12 vacuum pump was used to pump the air out from the discharge chamber with a pumping rate of $\sim 12.0 \text{ m}^3/\text{hour}$. The vacuum gauge used to monitor the pumping was APG10, Active Pirani Gauges (sensitivity 0.001mbar) with a Pirani Penning 1500 digital display. **Figure 3-11(a)** shows the vacuum systems and **Figure 3-11(b)** show a photograph of the gas and vacuum systems.

The vacuum testing was conducted by pumping out the air from the discharge chamber until the pressure (P_1) reached ~ 0 mbar, the vacuum valve was closed, the date and time were recorded, and the system was left for few hours or overnight for leak testing. The leak rate was detected by recording the increase of the pressure to (P_2) on the Pirani Penning display, and the length of time (t) was known and the leak rate calculated from $[(P_2 - P_1)/t]$. The average pumping out time was about 6 minutes with a typical leak rate of 0.1 mbar/hour being easily achievable.

3.7 Flow shaping and clearing ratio

Efficient gas flow between the electrodes is often necessary to clear the discharge of by-products such as heat and dissociation species around the active discharge volume region. These by-products perturb the stability of the discharge and may promote arcing. The arcing problem will become critical when operating at high repetition rates. The clearing ratio (CR) is defined by

$$CR = \frac{v}{wf} \quad (3.2)$$

where v is the flow velocity, w the electrode width and f is the repetition rate (frequency) of the discharge. For a clearing ratio of 1 the gas is cleared between pulses. For high discharge energies it is possible for by-products to be accelerated in the reverse direction to the flow. Under these circumstances a clearing ratio of >1 would be needed. For lower discharge energies a $CR < 1$ may be adequate for discharge performance.

Two flow shaping and clearing ratio tests were done to investigate the influence of flow shaping and the circulation of the otherwise static gas on the discharge characteristics, this is reported in section 3.9.4.

3.8 Data acquisition

Basic C++ programming was used to allow the preliminary data gathering on a PC. Data from the discharge was captured with GPIB 488 and a LeCroy 9310 oscilloscope (300 MHz). The discharge voltage and current waveforms were captured. Two Channels (A and B) were used separately to capture the discharge signals. The data were saved in text file and analysed in Excel. The signal plots were generated almost immediately on the PC monitor by using the GIMP processor (plotter software).

At one stage, the LeCroy 9310 oscilloscope was replaced with LabView8.2 through GPIB 488 interface. The LabView8.2 block programming was done in the Block Diagram Panel and the LeCroy oscilloscope was represented by the Front Panel which behaves identically as the LeCroy oscilloscope. However, because the discharge system was unstable and this may have caused damaged to the PC, the data gathering using LabView was done only with a few experiments and was abandoned.

A high voltage Tektronix probe with voltage ratio 1:1000 V was used along with the oscilloscope. The current was measured by using a current probe, Mini Rogowski Coil CWT1500 with sensitivity scale of 0.02mV/A.

3.9 DC experiment

The DC discharge experiments were designed in 3 levels. The first level was to test that the general experimental set up was reliable for data gathering and glow observation. This general test provided preliminary results of the system by looking

at the Paschen breakdown voltage for air, helium, nitrogen and carbon dioxide inside the discharge chamber. The value of the Paschen breakdown voltage was used to determine the operating voltage for the system with different gas mixes at different pressures and allowed the operational envelop of the discharge to be extended.

The second experiment investigated the discharge output characteristics such as the discharge quality (continuous or intermittents), and the life-time of the glow with static pressure conditions for individual gases. This was followed by a study of the performance of the spark plug preionisation. Further analysis was done on the discharge voltage and current characteristics with different gas pressures and gas mixes.

The third experiment investigated the influence of flow shaping and circulation on the discharge characteristics. The flow shaping and fan was installed either longitudinally or transverse to the electrodes. The electrodes used in this experiment were the planar brass electrodes and Chang's uniform field electrodes.

All of the discharge experiments were conducted with the main electrode discharge system placed inside the discharge chamber.

3.9.1 Experimental set-up

Figure 3-12 shows the overall setup of the experiment. The discharge voltage was measured with a Tektronix voltage probe P6015A with a voltage ratio of 1:1000V. The preionisation discharge current was captured by Mini Rogowski Coil, CWT1500 with sensitivity 0.02mV/A. The voltage and current probe were connected to the LeCroy 9310, 300 MHz oscilloscope and via a GPIB interface to a PC. The data gathering was performed with proprietary C⁺⁺ program. The C⁺⁺ program only recorded the voltage or current at one time.

3.9.1.1 Discharge chamber cleaning

The discharge chamber was regularly cleaned with iso-propanol alcohol to remove dirt, oil or grease before installing the electrodes. The cleaning ensured contamination was a minimum inside the chamber because impurities may reduce the efficiency and the uniformity of the discharge. Purging the discharge chamber with nitrogen before each new experiment significantly reduced the contamination and discharge residue from previous tests.

3.9.1.2 Electrode gap setting

The electrode gap was set via washers and measured with a parallel block covered with plastic cling film (to avoid scratches on the electrodes surface) placed in between the anode and cathode. Tolerances of about 0.3 mm were applied to enable the parallel block to be removed from the gap quite smoothly. **Figure 3-13** shows the electrode holder designed with adjustable cathode height. The electrodes misalignment depends on the tolerance of the washers which were known to be $\pm 0.05\text{mm}$. Each washer thickness was $0.5 \pm 0.05\text{mm}$. The set-up process was finished by cleaning the electrode and the surrounding area with iso-propanol alcohol to eliminate contamination.

To change the electrode gap setting, the top cover of the chamber was removed. This was followed by removing the anode plate holder with the brackets to allow access to the cathode. The cathode holder height was adjusted by varying the quantity of the washers used as mentioned in section 3.2.4.1. The process was completed by securing the anode holder, bracket, cleaning the system and bolting down the discharge chamber cover.

3.10 Results on the general test of the discharge system

The test began with the investigation of the breakdown operating voltage of the system. The operating voltage was determined by obtaining the Paschen breakdown for air and specific individual gases. The type of gases used for the individual gas breakdown voltages were air at atmospheric pressure, partial vacuum air, He, N₂ and CO₂, all at room temperature. The planar brass electrode gaps used for air were 3, 5, 6 and 7 mm, while for He, N₂ and CO₂ it was held constant at 5 mm. The spark plug preionisation was used for all gases with manual switching. The preionisation was switched on after the high voltage DC input to the anode almost reached the breakdown voltage. The results are discussed in the following sections.

3.10.1 Breakdown voltages for air at atmospheric pressure and partial vacuum

The breakdown discharge for air at atmospheric pressure was conducted at room temperature. The discharge chamber was pumped to nearly vacuum and the bleed valve was used to let in the air to desired pressure. The discharge was operated with different electrode gaps of 3 to 7 mm. The breakdown of air in partial vacuum (527mbar) was also conducted in order to compare the discharge characteristics with atmospheric pressure. The results are shown in **Figure 3-14**. It is seen that as expected, for a given gap size the breakdown voltage is greater for atmospheric pressure in air. For an electrode gap $d = 3$ mm, the breakdown electric field (V_b/d) was measured at 10 kVcm^{-1} for the partial vacuum, increasing to 19.3 kVcm^{-1} for atmospheric pressure (mbar). As the electrode gap increases, the breakdown voltages increases quite steadily for the sub-atmospheric discharge upto about 6 mm, then at $d = 7$ mm V_b is closed to that at 6 mm. For the atmospheric discharge, V_b seems to plateau at about $7.070 \pm 0.060 \text{ kV}$. At $d = 7$ mm, the electric field at breakdown is 10.14 and 8.9 kVcm^{-1} for the atmospheric and partial pressure discharges respectively.

It should be realised that the stability of the discharge is generally dependent on the pressure and of course one of the objectives was to achieve a stable discharge at

atmospheric pressure. A stable discharge was achieved for both atmospheric and partially atmospheric pressures for an electrode gap of 5 mm. However for a gap of 7 mm the discharge for both became intermittent and after approximately 1 minute an arc developed that ran along the electrode, see **Figure 3-15**. This may be due to the small irregularities on the electrode, leading to a localised increased electric field and eventually arc breakdown, or non-uniform preionisation from the spark plugs or possibly dust and dirt contaminating the discharge system.

The electric field for achieving the breakdown of air is known to be 30 kVcm^{-1} at atmospheric pressure [IEEE standard]. In the present case when the electrode gap was 5 mm the breakdown voltage was only 7.1 kV (equivalent to an electric field of 14.2 kVcm^{-1}), which is only about 50% of the theoretical value. The lower breakdown voltage may be caused by the high humidity in the air or the high levels of preionisation.

3.10.2. Breakdown of He, N₂ and CO₂

Even though the performance of the discharge operating in air, particularly at atmospheric pressure, was of particular interest for air decontamination, it was useful to investigate the operating regime for other gas compositions. The breakdown voltage was measured for He, N₂ and CO₂ gases with a constant electrode gap of 5 mm. This gap was chosen because of the optimum breakdown voltage obtained from the air and partial air discharges occurred at 5 mm. The pressure was varied between 10 to 250 mbar for He and N₂ and 10 to 80 mbar for CO₂. **Figure 3-16** show the curves of the voltage breakdown values for each gas. The breakdown voltage for CO₂ showed the classic Paschen voltage breakdown pattern. When the gas pressure was 50 mbar, the discharge voltage was 4000 V which dropped to 3560 V at 60 mbar. The nitrogen discharges displayed linear characteristics, where the voltage breakdown value was proportional to the pressure. At a pressure of 10 mbar and 250 mbar, the nitrogen discharge voltage was 1100 V and 8600 V respectively. The helium discharge voltage was 650 V at 50 mbar and 1100 V at 250 mbar. At a lower pressure (10 to 40 mbar), helium always had the lowest breakdown voltage. Among

the three gases, CO₂ displayed the classic Paschen curve characteristics most significantly.

Figure 3-17 shows a graph of the E/N (V.m²) versus pressure, in mbar, for the different gas discharge. The graphs show that the reduced electric field was highest at the lowest pressure (10 mbar) for all these three gases and dropped exponentially until the pressure almost reached 80 mbar. As the pressure for N₂ and He increases above 80 mbar, the E/N value decreases approximately linearly. No results for CO₂ for pressures above 80 mbar were available with this system configuration because a stable discharge could not be achieved.

3.10.3 Voltage and current characteristics for a gas ratio of 1:1:8 (CO₂: N₂: He)

This experiment was done to investigate the performance of the discharge system for potential laser operation by measuring the discharge voltage (V) and current (I) with a typical CO₂ laser gas composition. The V-I characteristics were measured with a constant electrode distance of 5 mm and various gas pressures. An example of the voltage and current measurement on the LeCroy 9310 oscilloscope is shown in **Figure 3-18**. Channel 1 (top) was the voltage display and channel 2 was the current. It is seen that the current pulse duration was almost 100 ns (here the time scale was set at 100 ns per division). The discharge voltage and current rise-time were very fast compared to the decay-time which however, depends on peak values. This indicates the discharge energy was low.

Results of the discharge voltages as a function of time for a gas ratio of 1:1:8 for pressure of 120, 130 and 140 mbar are shown in **Figure 3-19**. The peak discharge voltage for 140 mbar was 2000 V, which was the highest and had a duration of 200 ns. The discharge voltage for 130 mbar was about 800 V, and this pressure had the longest discharge time of 275 ns. The lowest discharge voltage and shortest discharge duration time was for 120 mbar at 500 V and 10 μ s. From these results, it is seen that the higher the pressure the higher the discharge voltage and the shorter the voltage pulse width. It is seen that there is a residual voltage prior to breakdown,

this is due to the self-charging of the discharge system even though a complete earth discharge system was used. Note that the peak discharge voltage was read from the residual voltage value. A glow photograph of the discharge is shown in **Figure 3-20**, which was viewed from the discharge chamber window.

More results of the discharge peak voltage for the same gas compositions, with pressure variation from 140 to 950 mbar are shown in **Figure 3-21**. The peak discharge voltage for 140 mbar showed an increase of almost 100% compared to the previous tests. The increase of the discharge voltage is probably due to the reduced impurities in the discharge chamber, because the chamber was cleaned using isopropanol and also by purging nitrogen into the chamber before refilling the gas mix. The results show that as the pressure increases from 240 to 501 mbar, the discharge voltage decreases linearly from 8 to 6 kV, however it started to increase steadily from 6.7 to 8.1 kV, when the pressure increased from 680 to 950 mbar. This suggests that for 1:1:8 gas mix at sub-atmospheric pressure, the discharge voltages were higher at lower pressure (ie: 8kV at 140mbar) and at 950 mbar (8.1 kV). This indicates the Paschen's curve for 1:1:8 mix of gases was probably observed.

A graph of E/N versus pressure, in mbar, for a gas mixture of 1:1:8 is shown in **Figure 3-22**. The E/N values are between 0.8 to 4.8×10^{-17} Vcm². The value of E/N is highest at the lowest gas pressure (140 mbar) and decreases steadily while the gas pressure increases upto approximately 500 mbar, and E/N became almost constant from this pressure to 950 mbar. This result is in agreement with Watson [PhD thesis, 1993] in measuring different E/N values for different gas mixtures with gas pressures used from 30 to 130 Torr (~40 to 173 mbar).

The discharge current as a function of time, for various gas pressures with the same gas compositions is shown in **Figure 3-23**. Most of the peak currents occurred at a time between 0.65 to 0.70 μ s relative to the trigger point at 0 and the discharge oscillation for all cases decayed completely at about $t = 1 \mu$ s. Interestingly for pressures of 270 and 680 mbar, a small discharge current again appeared at around $t = 1.8 \mu$ s, this region is indicated with the arrows A and B in the figure. Further investigation on this small discharge might be of interest in future work.

A close up view of the discharge current is shown in **Figure 3-24**. The graphs show that the highest discharge current (2.5 kA) occurred for gas pressure of 501 mbar with 120 ns pulse duration. This current pulse produced $di/dt = 2.08 \times 10^{10} \text{ As}^{-1}$ for the minimum electrode gap. This is followed by 750 and 950 mbar, however the pulse duration was nearly less than half of the discharge current for 501 mbar. **Figure 3-25** shows the peak discharge currents with a standard error of 5%.

The peak discharge voltage and current, V-I for the gas ratio of 1:1:8 with standard error of 5% is shown in **Figure 3-26**. **Figure 3.26(b)** shows an estimate of the peak discharge power calculated from the multiplication of the peak discharge voltage and current. An example of the voltage and current discharge versus time for 140 mbar is shown in **Figure 3-27**.

3.10.4 Influence of flow shaping and static pressure gas circulation

Two types of fan systems were used in the system discharge chamber. Firstly an ordinary computer cooling fan, DC, 2.6 W (plastic blade axial flow). The diameter of the blades was about 75 mm. Secondly, a DC, 6.0 W radial flow fan with aluminium blades. The length of the blades was 150mm. The effect of the flow from both fans on the discharge stability was investigated. To test the effect of the longitudinal flow, the fan was placed at one end of the electrode for the flow test. To test the effect of the transverse flow, the fan was placed alongside the electrodes. The relative positions of the fans to the electrodes are illustrated in **Figure 3-28 (a) and (b)**.

3.10.4.1 Axial flow fan clearing ratio

The speed of the flow (v) for the computer cooling fan was not measured. Flow shaping (**Figure 3-29**) was used for the longitudinal flow to optimise coupling the flow with the discharge geometry. If the incoming flow into the flow shaping was v_1 , and using conservation of mass flow, the estimated flow for v_2 was $v_2 = 0.377 \text{ m/s}$ (see **Appendix 3C** for the calculation).

The transverse flow effect on discharge experiment was not carried out due to the restriction of the discharge chamber size to install the fan. However the clearing ratio can be estimated by taking the frequency of the discharge of 40 Hz and the width of the discharge is $w=10 \times 10^{-3}$ m, the transverse flow clearing ratio was estimated to be $CR = 0.9425$, which is much more acceptable.

3.10.4.2 Radial flow fan clearing ratio

No flow shaping was used with the axial flow fan (**Figure 3-30**) because the size of the fan was much bigger than the discharge width or length. The transverse flow arrangement was set up and the speed of the air flow velocity was measured to be 1.2 ms^{-1} , the frequency and width of the discharge was 40 Hz and $w = 60 \times 10^{-3}$ m respectively. Thus the estimated clearing ratio CR was 0.5. The results of the influence of the radial flow fan over the discharge characteristics for a gas mixture 1:1:8 at various pressures are discussed.

Figure 3-31 shows the results of the effect of the clearing ratio on discharge peak current for a gas mixture of 1:1:8 at pressures of: 50, 100 and 500 mbar. Here, the discharge currents for 50 and 500 mbar are compared. With the fan on, the discharge current I_d for 50 and 500 mbar were: 180 A and 1060 A respectively. These are significant differences, compared to the discharge currents without the fan, which were 260 A and 680 A for the same respective pressures. With the help of the fan to clear the discharge by-products, the discharge current seemed to increase as the gas pressure increased. However, it seemed to be lower for 50 mbar. At 100 mbar there was little difference between the discharge currents with or without flow shaping.

Figure 3-32 shows the result of using the fan and its influence over the discharge voltage for a gas mixture of 1:1:8 at pressures 50, 100 and 500 mbar. The clearing ratio did not influence the discharge voltage. The average discharge voltage values with and without the fans are almost equal at all pressures. This would be expected as the gas pressure is essentially unchanged.

Figure 3-33 shows the current pulse duration (μs) for 50, 100 and 500 mbar at 1:1:8. As the pressure increases, the pulse duration for the current discharge with the fan on became shorter: for 100 mbar the current pulse duration was 340 μs compared to 500 mbar where it reduced to 160 μs . On the other hand, the current pulse duration without the fan for 100 mbar was 380 μs and this reduced to 180 μs for 500 mbar. Thus by considering the percentage differences with and without the fan, it is seen that the width of the discharge currents increased by an average of about 15%.

Figure 3-34 shows the discharge voltage pulse duration (ms) for the 50, 100 and 500 mbar with a gas mixture of 1:1:8. The pulse duration for the voltage discharge with the fan on linearly increases as the pressure increases (14, 18 and 23 ms). Therefore as shown in **Figure 3-35**, as the pulse duration increases, the frequency decreases (65, 61 and 44Hz).

3.11 AC discharge

Results from the DC discharge experiments, discussed above, demonstrated that a cold plasma discharge can be generated by using the system set-up. However, for industrial or commercial applications of air decontamination, there is always a need to reduce the component costs and to simplify the design and operation of the discharge system. Some of the DC discharge systems previously discussed, required a vacuum chamber with efficient gas flow to sustain a long duration stable discharge. Technically, there are often difficulties when working with vacuum systems and additional costs. For example, the cost for the PPM, 6 kV DC power supply was over £3000. It was a design constraint to find a commercially available, small, efficient, cheap and high voltage power supply. Nevertheless, it was one of the research objectives to develop a low cost, cold plasma discharge system with simple operation. These problems lead the research to an option of using an AC source to operate the system.

The main advantage of AC discharge systems is that they can be operated at sub-atmospheric and atmospheric pressure in air, without the need for rectification and

expensive switching solutions. As they can operate in air, there is no need for the discharge chamber to meet vacuum standards and it is simpler to allow gas to flow in between the electrodes. **Figure 3-36** shows the discharge circuit that contained an AC transformer (TEC, UK), a pair of high voltage capacitors (measured at 2.39 and 2.61 nF), trigger wire preioniser and electrodes which also acted as a switch. **Figure 3-37**, shows 3 capacitors (nominally 2.7 nF) on either side of the electrodes. These were used to investigate higher energy deposition into the discharge. **Figure 3-38(a)** shows a 10 kV (RMS) AC transformer (FART, Italy), with an earthed centre which was used with a pair of 2.7 nF capacitors and **Figure 3-38(b)** which shows the same circuit with diode rectification of the output voltage. The next section describes the details of the AC transformers, brief information on the type of capacitors that were used and the preionisation used with these AC transformers.

3.11.1 AC transformer

The two types of AC transformer employed in the research were: firstly an AC transformer, manufactured by The Transformer & Electrical Co. (TEC) Ltd, Basildon UK, with specifications 240V, 4.6A on the primary and 20 kV_{rms}, 0.2 KVA on the secondary (50 Hz). Secondly, was a neon lamp resin block FART Transformer with 240V on the primary, and +5 kV to -5kV on the secondary (an earthed centre tap), 100 mA at 50 Hz (manufactured in Italy). Both transformers when used were connected to a variac 0-230V, 8A, 50 Hz, to control the input voltage to the primary. **Figure 3-39 (a) and (b)** show the photographs of the TEC AC and the resin block transformer respectively.

3.11.2 Capacitors

For the AC discharge, high voltage ceramic capacitors, Genvolt (UK) DXU 30-272, 2.7nF, with screw size M5 x 4 mm were used. Another high voltage capacitor, measured value of 2.39 and 2.61nF $\pm 10\%$ tolerance, rating 30 kV DC with screw size

M8 x 5 mm were also used. These capacitors were mounted directly onto the electrode mounts or to the perforated metal base plate.

3.11.3 Preionisation

The set-up of the AC discharge system with the preionisation with 3 mm electrodes gap is shown in **Figure 3-40**. The trigger wire preionisers were coupled to the anode and ran each side of the electrodes. They were made from 2.5 mm diameter copper rod inserted through a glass quartz tube with 3 mm ID. The effective length of the preioniser was 180 mm. The preioniser tubes were held by the PTFE support disks.

3.11.4 Spectrum measurement

The spectral output was measured to determine whether the radiation output from the discharge could be used to kill microorganisms, where ideally a wavelength emission between 248 to 255 nm would be most effective. Two models of spectrometer were used to measure the spectral output from the discharge. First, it was a Photon Control SPM-002-ET, with spectral range from 200 to 1090 nm, Hamamatsu S9840 back-thinned CCD detector (Photon Control Inc, British Columbia Canada). The integration time range was programmable between 2.2 ms to 10 s, the fibre input was SMA905 type. It used a USB-2 high speed interface with Spectsoft pro for Windows software. The second spectrometer was Stellar Net model EPP2000 HR, with a spectral range from 160 to 1600 nm (USA). It used a USB-1 interface with Spectra-Wiz® Windows software. Both spectrometers measured the spectrum in real time. The measured discharge spectrums are discussed in sections 3.12 and 3.14.

3.12 AC on the He and N₂ discharge

The experimental set-up for the AC discharge where 2.69 and 2.61 nF (nominal 2.7 nF) capacitors were used is shown in **Figure 4-41**. The Photon Control fibre optic was used to record the discharge spectrum. The fibre optic was fixed to one position through all experiments. Helium was used to test the system performance because it was the easiest gas to work with in order to obtain a stable glow discharge. For 100 mbar of He, the glow discharge occurred when the input voltage reached 7.21 kV (**Figure 3-42**). The bright, deep pink glow was uniform and was stable for at least an hour, before the glow dissipated. The spectrum of the helium glow was taken within the near infrared region (580 to 780 nm) with a peak amplitude of 750 a.u. (**Figure 3-43**).

When the system was stable with He gas, the system was tested on N₂ which was then used in order to investigate the different spectral output. The N₂ pressure was 20 mbar and it started to glow when the input voltage reached 2.2 kV. The glow was viewed through the discharge chamber window (**Figure 3-44 (a)**) and with a close up view, a stronger glow near the electrode surface was observed (**Figure 3-44 (b)**). The N₂ pressure was increased to 50 mbar and the glow discharge occurred when the input voltage was 5.2 kV. The glow at 50 mbar pressure was brighter and more uniform than at 20 mbar (**Figure 3-45**). The spectrum of the discharge at this pressure is shown in **Figure 3-46**, which showed a broader range, from deep UV at a wavelength of about ~390 nm with an amplitude of 820 a.u., to about ~860 nm with an amplitude of 1150 a.u. The peak amplitude of 1480 a.u. was greatest at 520 nm. The peaks however, were narrower than those observed with the He discharge.

3.12.1 Results of the discharge for gas ratio 1:1:4 (CO₂:N₂:He)

The glow discharge performance was evaluated for the 1:1:4 gas mixture with a total pressure of 100 mbar. There was no spectral measurement made because the fibre optic sensor was damaged. A series of studies of the glow brightness (from video) were made when the input voltage was increased. **Figure 3-47(a)** shows that the

uniform glow started when the input voltage reached 4.87 kV. A more uniform and brighter glow was observed when the input voltage was increased to 5.20 kV (**Figure 3-47(b)**). With the input increased to 5.8 kV an even brighter and more uniform glow was achieved (**Figure 3-47(c)**). The glow was very bright when the input voltage was 6.8 kV, which can be seen from **Figure 3-47(d)**. However, the glow discharges for all of these voltage inputs were brightest on the right hand side of the photographs potentially indicating the development of a non-uniform discharge.

Figure 3-48 shows the discharge current for gas ratio 1:1:4 at 100 mbar. The maximum peak current was about 400 A and the oscillation decayed completely after 400 ns. The simulation results model (see Chapter 2 Figure 2-8) of the same capacitance From this discharge current further modelling of the circuit can be done to improve the discharge output

3.13 AC air discharges

All of the gas glow discharges at sub-atmospheric pressure (see sections 3.12 and 3.12.1) were of sufficient strength potentially to be used in the decontamination systems however, the wavelength emission profiles were not ideal for killing microorganisms. Consequently the investigation led towards the development of atmospheric air discharges where air could be passed through the discharge directly.

3.13.1 Air discharge with trigger wire preioniser

The Chang profiled electrode with trigger wire preionisation running parallel with the electrodes was set-up in air at atmospheric pressure as shown in **Figure 3-49**. The trigger wires were coupled to the anode with a distance between them of 14 mm. The TEC transformer was used. The cathode was vertically adjustable by the micrometer in the upward-downward (Z) direction. The electrode gap was 3 mm. There was intermittent arcing when the input voltage was 5.4 kV and then the arcs were persistent at one spot. The persistent arcs were caused by a broken glass tube due to misalignment and the glass touching one point on the cathode. **Figure 3-50**

(a) and (b) show the broken tube and the spot after arcing. The electrode was cleaned and polished however, the spot was still visible (**Figure 3-51**) indicating that the arcs were sufficiently strong and to damage the surface.

To overcome the alignment of the trigger wire preioniser problem, the air discharge was set-up outside of the discharge chamber (**Figure 3-52**). The glow discharge was uniform which started to glow when the input voltage reached 4.8 kV (**Figure 3-53**). The glow became brighter as the input voltage increased and the system arced at 7.2 kV. No spectral measurement was made. **Figure 3-54** shows the discharge current from the AC discharge in air at atmospheric pressure. The discharge exponentially decayed with a maximum peak value of about 1100 A.

This result was considered to be a starting point to work with air discharges at atmospheric pressure. The ability of the system to achieve a stable glow discharge for a relatively long period of time suggested that the discharge stability could be improved further by improving the preionisation stability around the cathode. Subsequently, dielectric material was placed over the cathode to produce uniform preionisation, increase stability and minimise the probability of breakdown.

3.13.2 Air discharge with dielectric material over the cathode

Various dielectric materials were used to produce uniform preionisation and to prevent electrode damage. It was shown that the dielectric material improved the preionisation performance [Walter, 1984] and promoted stable discharges. In this research, a number of dielectric materials were investigated (**Appendix 3D**), but only mylar and duralar films are reported in detail. Mylar and duralar are cheap, commercially available and easy to handle.

3.13.2.1 Mylar

Mylar film with an electric field breakdown of $\sim 140 \text{ kVmm}^{-1}$ (ASTM 3.5 kVmils^{-1}) was the first dielectric material used over the cathode to stabilise the discharge. Two

layers of mylar film with total thickness of 100 μm were first used (**Figure 3-55**). The electrode gap was maintained at 3 mm and the trigger wire preioniser was removed. When the input voltage reached 5.8 kV, a stable glow discharge was obtained for the first three minutes and began to breakdown into random arcs before complete breakdown occurred.

The mylar films were examined, and showed the top layer had a few holes pierced completely through the films caused by the arcs (**Figure 3-56(a)**). The bottom layer film was torn at the centre of the electrode. This was due to the arcs and heat produced on the cathode (**Figure 3-56(b)**). Marks on the cathode were observed and likely caused by the arcs, the torn mylar film is shown in **Figure 3-57**. The mylar film failed to withstand the high voltage discharge between the electrodes, thus duralar was an option investigated to replace the mylar.

3.13.2.2 Duralar

The thickness of the duralar film was 75 μm with an electrical strength of $\sim 280 \text{ kVmm}^{-1}$ (ASTM 7 kVmils^{-1}). Two layers of duralar were placed over the cathode with an electrode gap from 3-5mm. A uniform glow discharge was initiated with 3 mm electrode gap and the discharge was left to run continuously for 5 minutes without arcing. **Figure 3-58(a) and (b)** show the condition of the top and bottom layer of duralar respectively. The white marks on the duralar were from the discharge but there were no holes or tears in the film.

Tests using duralar as the dielectric preioniser were done in air at atmospheric pressure with 3, 4 and 5 mm electrode gaps. The discharge for 3 mm (**Figure 3-59 (a)**) was uniform and it was observed that a brighter glow was seen on the cathode. The discharge became filamentary for the 4 mm gap as seen in **Figure 3-59(b)**, and stronger filaments were seen from the for 5 mm gap (**Figure 3-59(c)**). All discharges seemed stronger nearer the cathode than the anode, probably because the preionisation was closer to the cathode.

Figure 3-60 shows the discharge current when two layers of duralar were used over the cathode with the maximum peak was about 2000 A. The electrode gap was 4.5 mm. This was an interesting result because the long period of oscillation indicating that the system might suffer unstable damping factor from the circuit configuration.

3.13.2.3 Dielectric discharge comparison

The discharge characteristics with dielectric materials: mylar, duralar and glass (glass data not reported) were used over the cathode with various electrode gaps (between 2-5 mm). The voltage drop (V_d) for three dielectric materials are shown in **Figure 3-61** as a function of gap, where duralar had the highest discharge voltage for all gaps (6 to 10 kV). Mylar however, had the largest range of voltage drop across the discharge (2 to 9.6 kV). The voltage drop across the discharge with the 5 mm gap for all three dielectrics was close in value, with an average of 9.62 ± 0.34 kV.

The output voltage ($V_{out} = V_{in} - V_d$) for duralar was linear (200 – 390 V) compared to the mylar and the glass (**Figure 3-62**). When the gap was 5 mm, duralar and mylar films had the same measured output voltage of 390 V. The discharge current was unstable and only few readings were taken. **Figure 3-63** shows the discharge current, interestingly duralar film produced a constant current at 360 A for gaps of 2 – 4 mm, while mylar experienced a sharp increase of discharge current (from 500 – 1300A) due to the failure of the mylar layers.

From the results, duralar seemed to provide most consistent results in all measurements, such as glow pattern and discharge characteristics. These criteria made it the dielectric of choice material for further experiments to investigate decontamination, which is discussed in Chapter 5.

3.14 Air discharge for Blumlein system

The Blumline discharge system was another technique developed for generating air discharges at atmospheric pressure. The electrical circuit is shown in **Figure 3-64**. A symmetrical system (left and right plates) with two layers of duralar films was used. The electrodes were made from stainless steel rod with dimensions of 25 mm diameter and 300 mm in length. The electrodes were mounted at the edge of the metal plates and set parallel to each other with a 3 mm gap. **Figure 3-65** show a schematic of the system with the side and top views. A spark-gap was used as the HV switch.

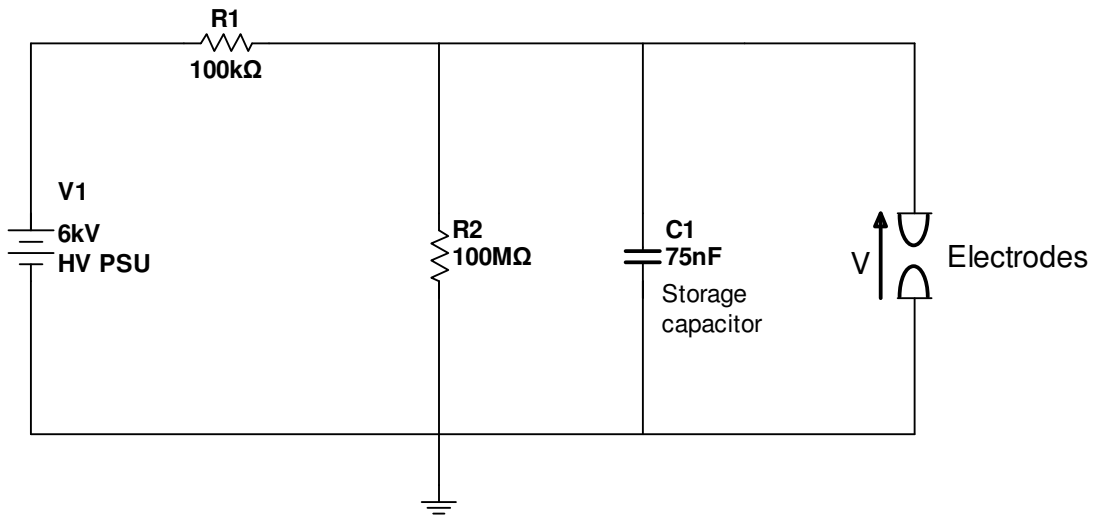
This system was connected to a resin Block transformer (FART, Italy) of 5 kV RMS. This transformer was used to charge the 44 nF capacitance, formed from the metal plates and the duralar film. **Figure 3-66** shows the position of the electrode and the spark-gap HV switch. The Blumlein discharge is shown in **Figure 3-67** and the spectral measurement is in **Figure 3-68**. The spectral of the Blumlein was broad between 286 to 900 nm with a strong output gain in the UV range. The highest spectral gain was 340 a.u at 267 and 510 nm. The discharge output appeared much stronger than for the compact Chang discharge; this probably due to the rapid spark gap switching. This may be an interesting area for future investigation into atmospheric pressure air discharges.

3.15 Discussion and conclusions

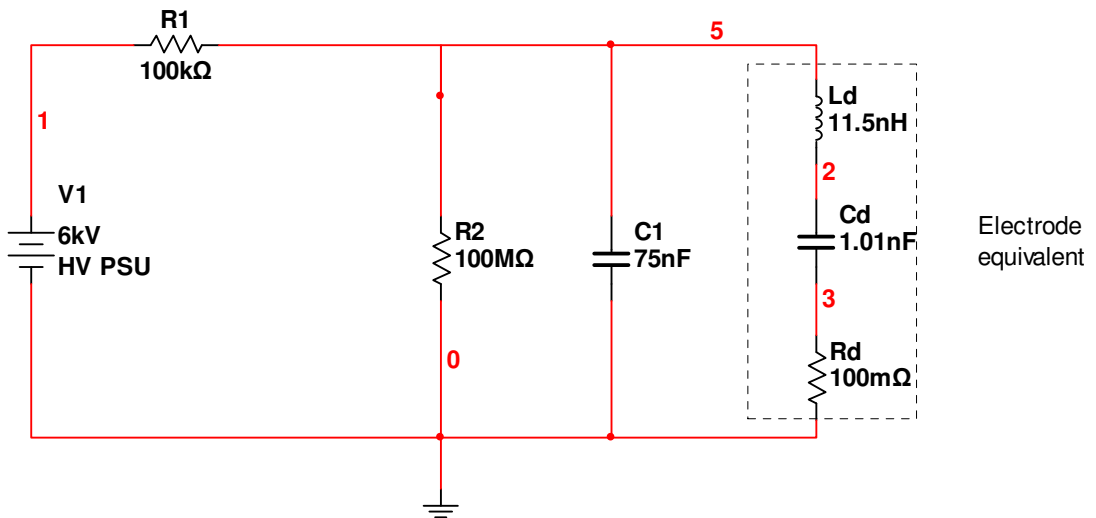
The DC test results proved that the discharge system was able to produce plasma discharges within sub-atmospheric pressure for a gas ratio of 1:1:8. These discharge characteristics were investigated. Due to the difficulty of developing air decontamination systems with the vacuum, the design was extended to an AC discharge in air at atmospheric pressure. The price of the DC power supply unit was expensive thus the AC discharge offered an advantage with the research to commercialize the systems. The results from the experiments can be used as the inputs to the model such as the circuit modelling in Multisim8 (or vice-versa) and

also to the electrode design. The discharge properties can be classified as cold plasma discharge. The use of dielectric materials have significantly improved the UV preionisation between the electrodes. Duralar was a choice of dielectric for preionisation and maybe BK7 glass sheets could be used as another dielectric material in future.

These AC cold plasma discharges in air were used for the decontamination research in air treatment using plasma discharge because of their simplicity and cost effectiveness. The Blumlein discharge may be advantageous since the system development was simple.



(a) Discharge circuit.



(b) The electrical equivalent main discharge circuit.

Figure 3-1 (a) The main discharge electrical circuit with the electrode and the storage capacitor $C_1 = 75 \text{ nF}$, $R_1 = 100 \text{ k}\Omega$ discharge current limiter and $R_2 = 100 \text{ M}\Omega$. (b) The electrical equivalent with the stray inductance of the electrode and circuit was $L_d = 11.5 \text{ nH}$, capacitance 1.01 nF and $R_d = 100 \text{ m}\Omega$.

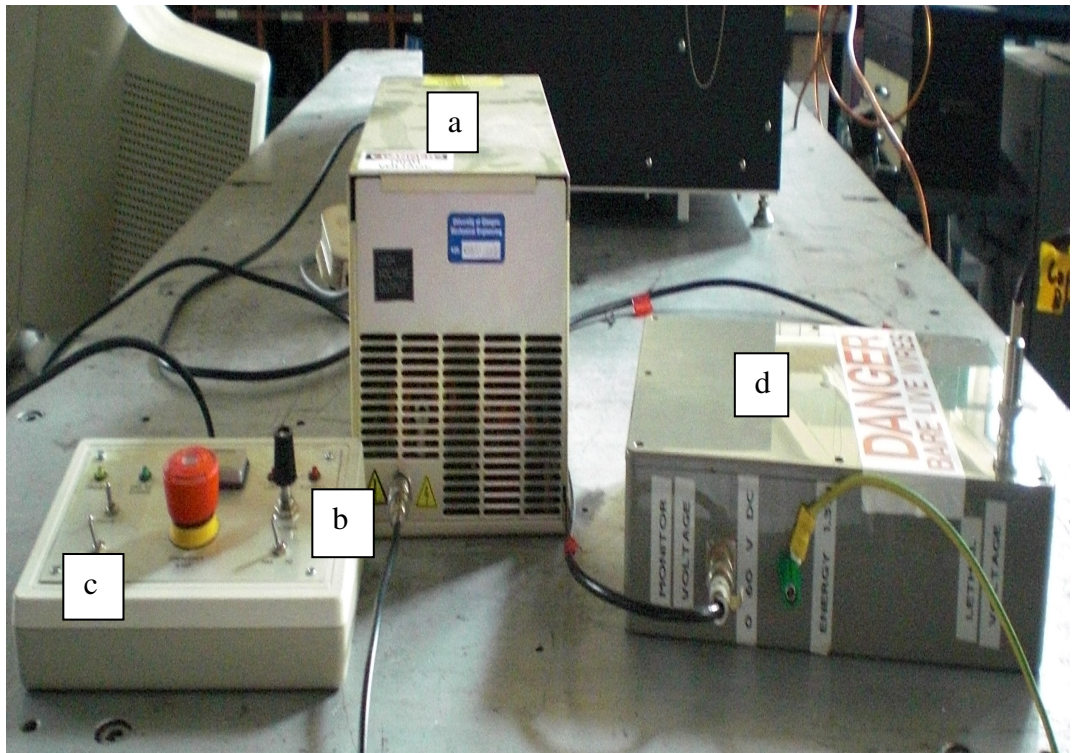


Figure 3-2 (a). Constant current 6 kV DC power supply unit, (b) the interface controller with adjustable voltage, (c) reset toggle to confirm the complete discharging of the power supply and (d) the storage capacitor in insulation box .



(a)



(b)

Figure 3-3 (a) Storage capacitance (75 nF) rated at 25 kV with 100 MΩ resistor as voltage divider and 100 kΩ resistor to limit the charging current. (b) Storage capacitors insulation enclosure shows the connection to the DC 6 kV PSU, the voltage monitor is used to connect the control box to a digital display or multimeter.

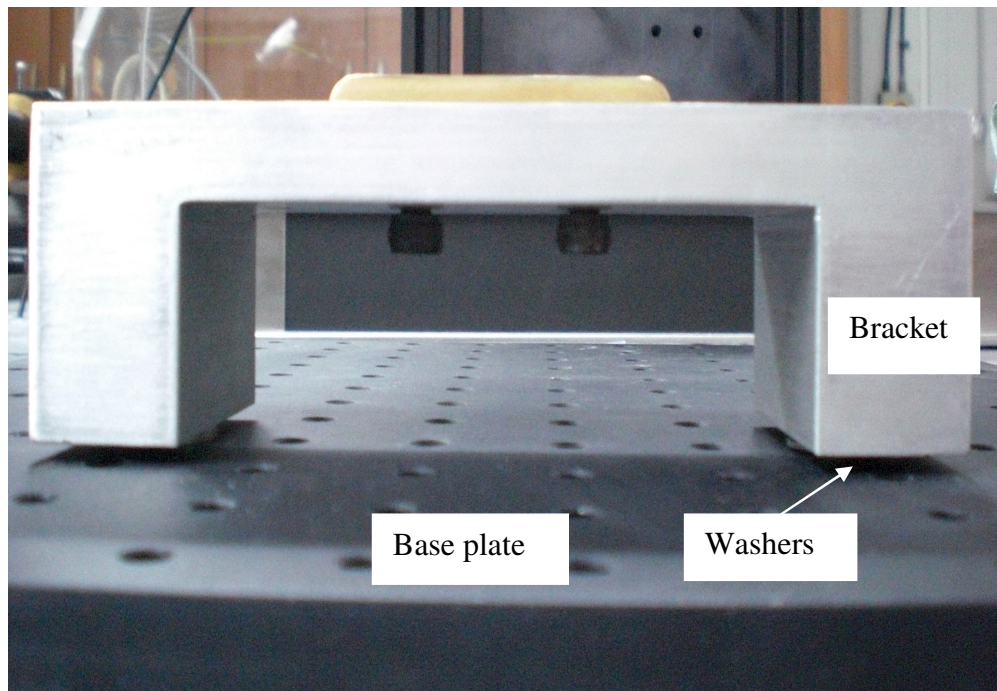


Figure 3-4 Cathode holder was adjustable by inserting washers in between the bracket and the base plate.



Figure 3-5 Planar brass electrodes used in the discharge.



(a)



(b)



(c)

Figure 3-6 Changs uniform field electrode: (a) Top view of flat surfaces (b) Side view and (c) Edge view.

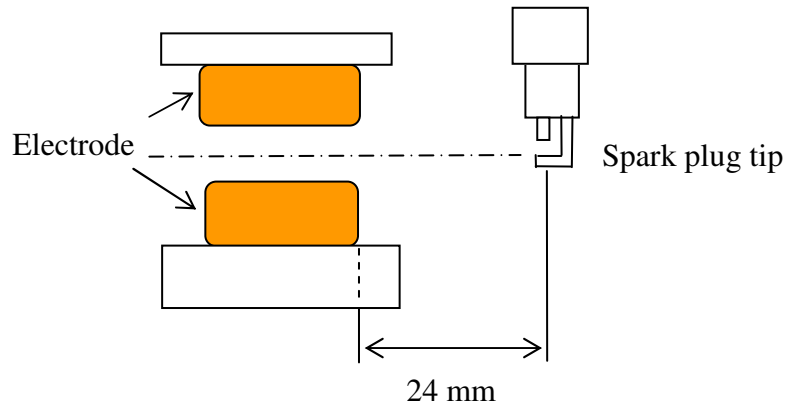


Figure 3-7 Spark plug preioniser setting distance alongside electrodes.

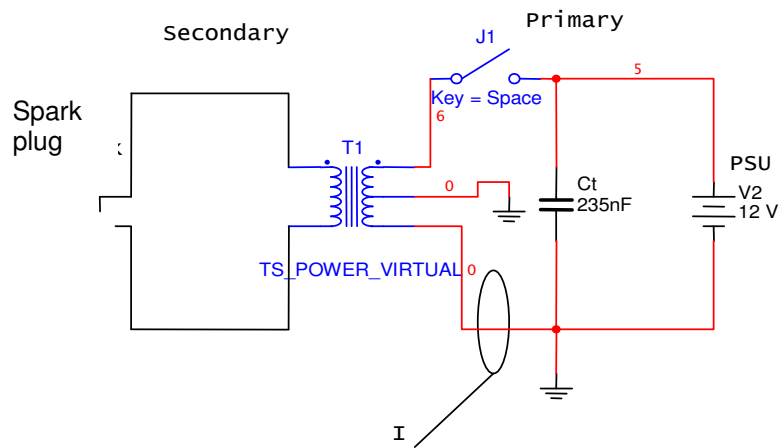
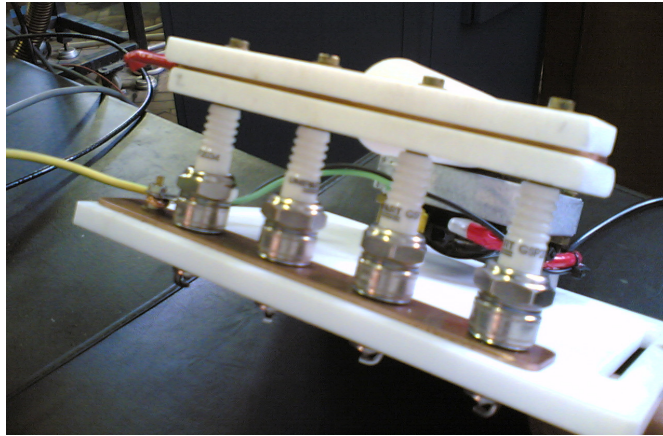
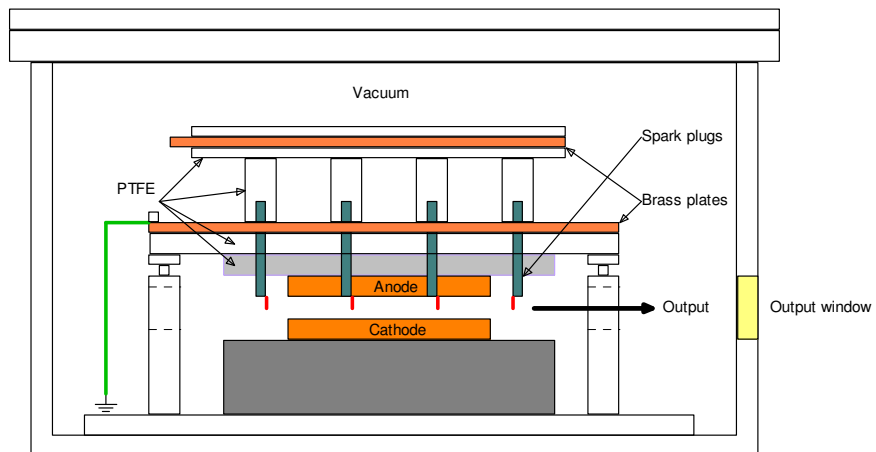


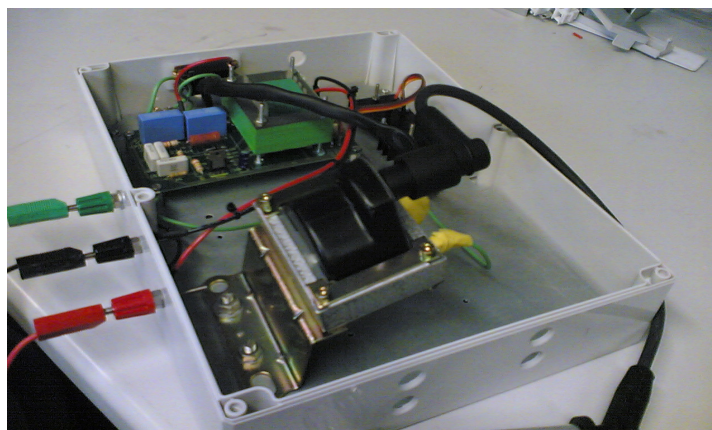
Figure 3-8 The schematic model of the spark plug preioniser circuit.



(a) Spark plug for preionisation mounting.



(b) Illustration of the spark plug preionisation set-up



(c) Assembly of the high power coil circuit

Figure 3-9 Development of the spark plug preionisation system (a) The mounting, (b) The set-up in the discharge chamber and (c) The firing circuit of the preionisation system.

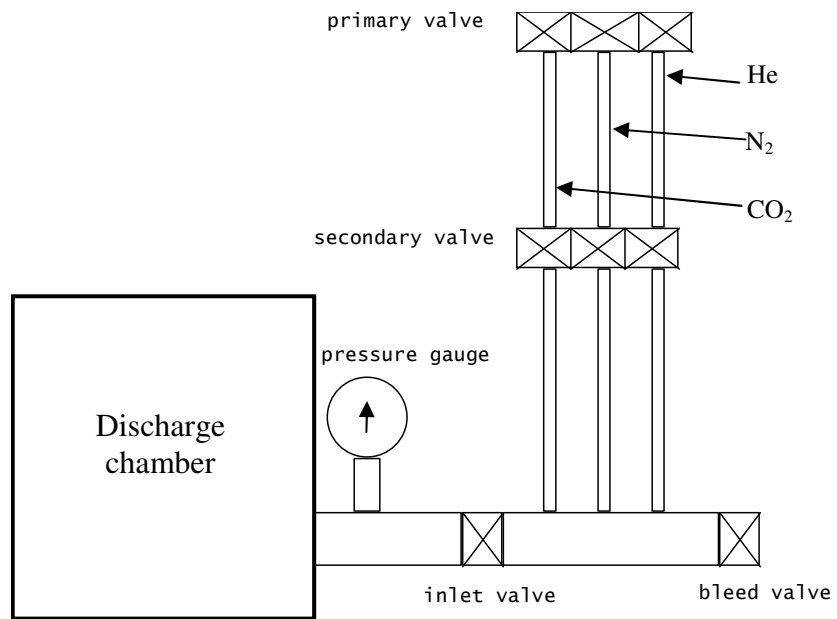


Figure 3-10 The gas flow system.

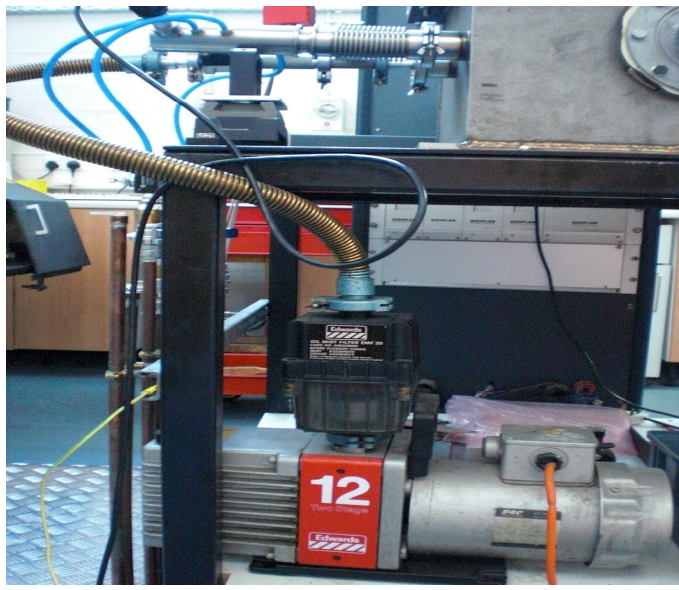
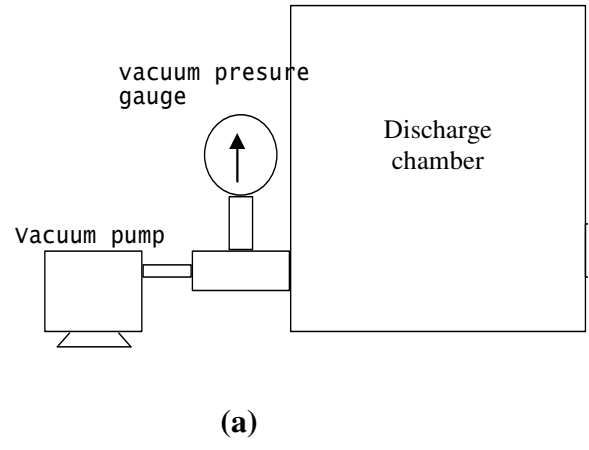


Figure 3-11 (a) The vacuum system illustration and, (b) the set up of the vacuum system.

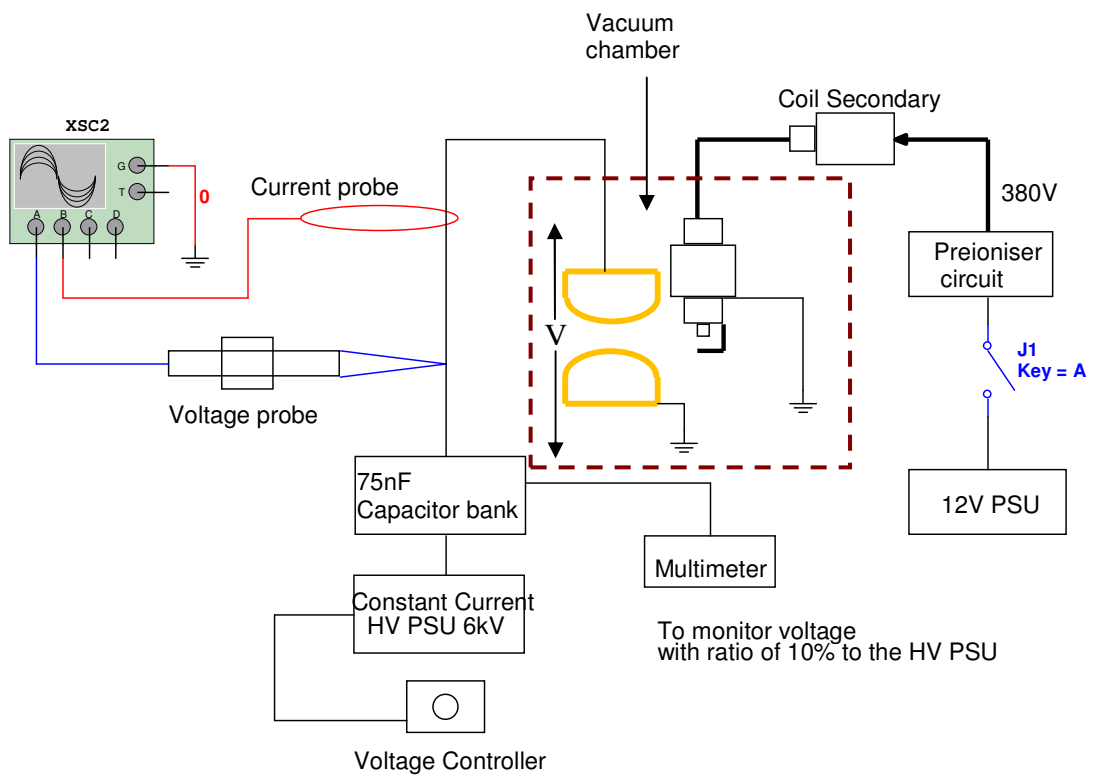


Figure 3-12 Experimental set up

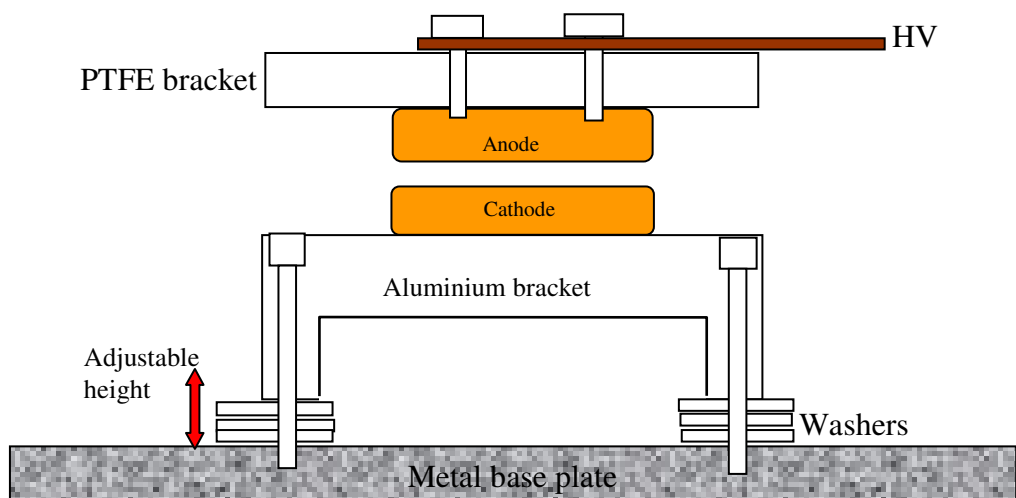


Figure 3-13 The electrode holder set-up illustration.

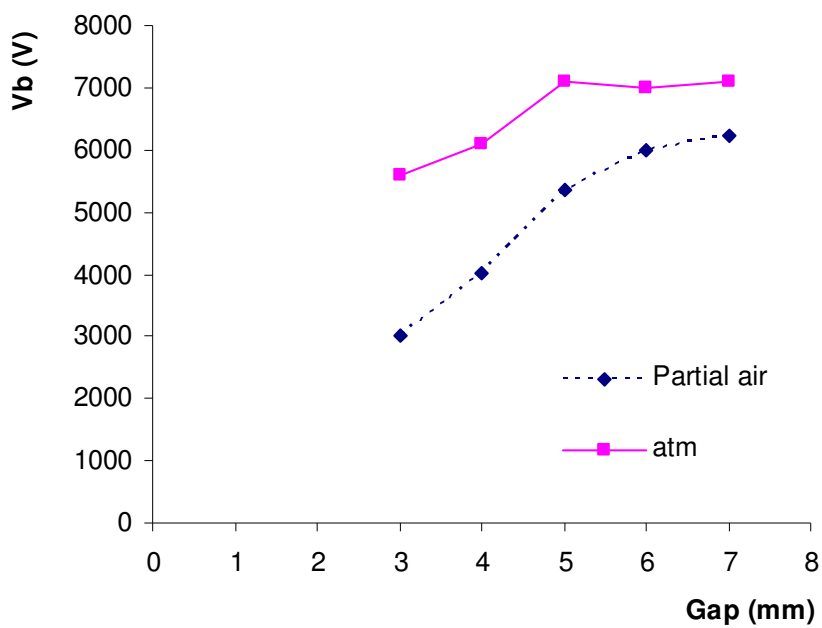


Figure 3-14 Voltage breakdown of air at atmospheric pressure and partial vacuum (500 mbar). The plane brass electrode gap was varied from 3 to 7 mm. No error bar because one set data was used.

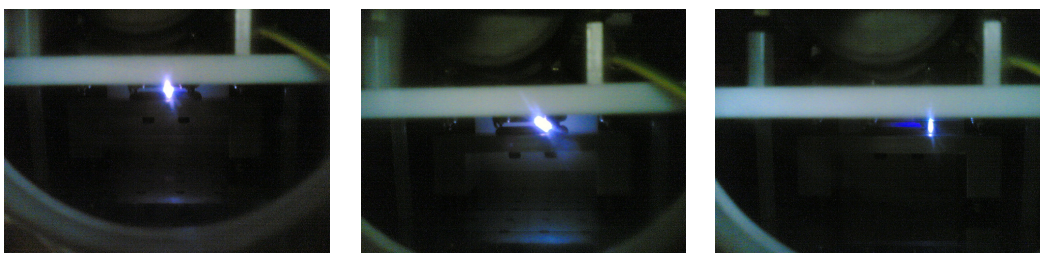


Figure 3-15 The intermittent arcs that occurred in air with an electrode gap of 7 mm.

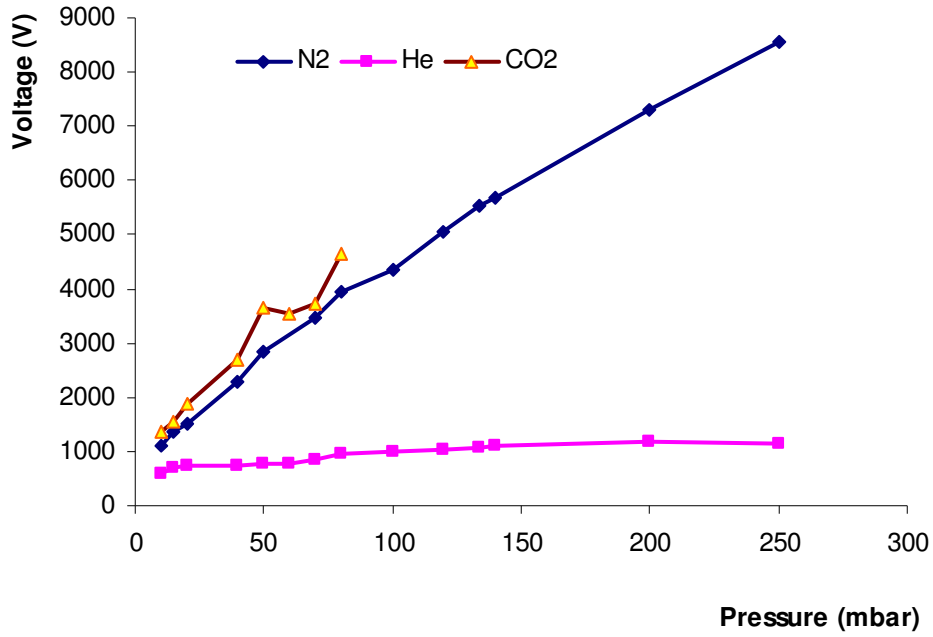


Figure 3-16 Paschen breakdown for helium, nitrogen and carbon dioxide relative to gas pressure. The electrode gap is constant at 5 mm. No error bar because one set data was used.

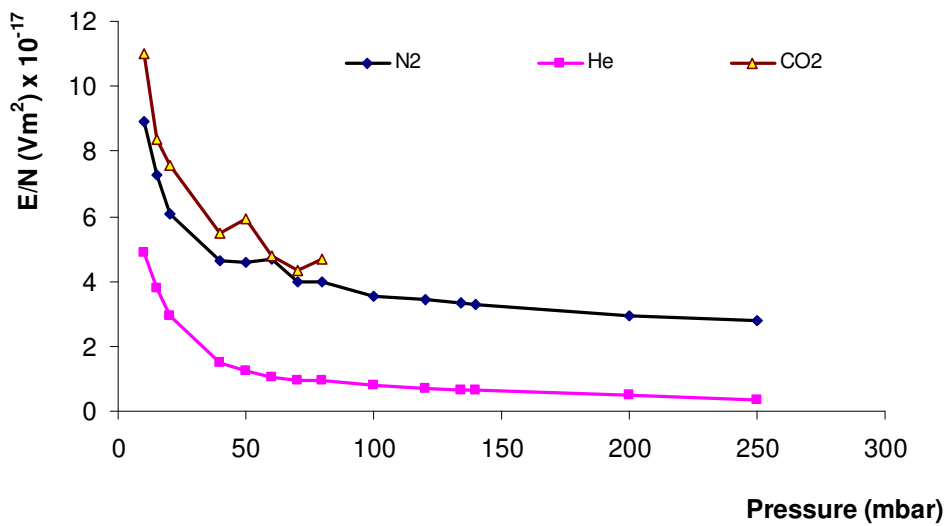


Figure 3-17 E/N values for N₂, CO₂ and He versus pressures.



Figure 3-18 Example of oscilloscope display to measure discharge currents and voltages. The top display is the voltage (~14.2 kV/cm) and bottom is current (~3.0 kA/cm)

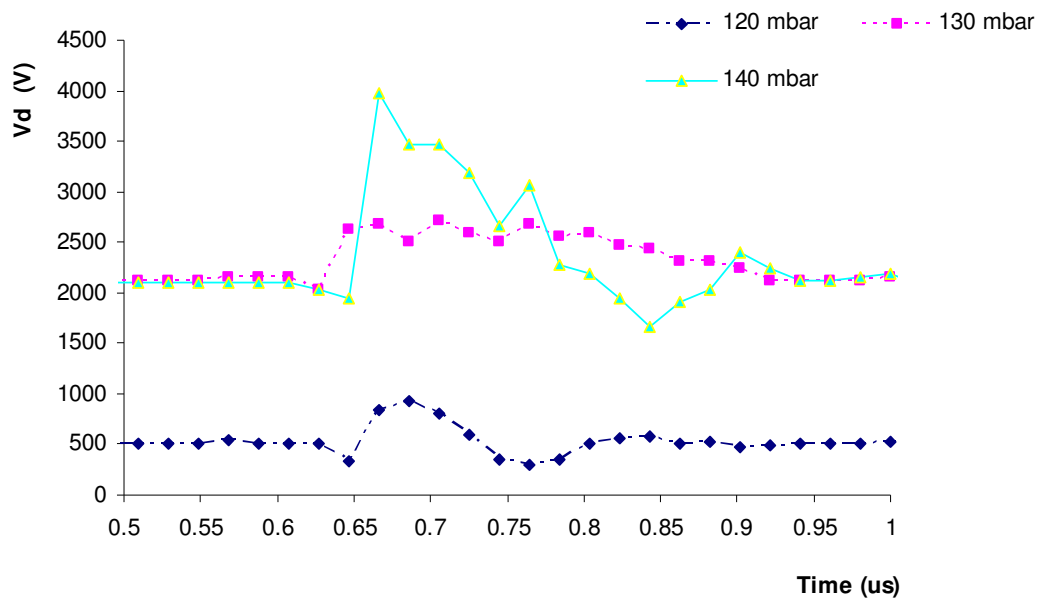


Figure 3-19 Discharge voltage at total gas pressure of 120 mbar, 130 mbar and 140 mbar in function of time. The ratio of the gas was 1:1:8.

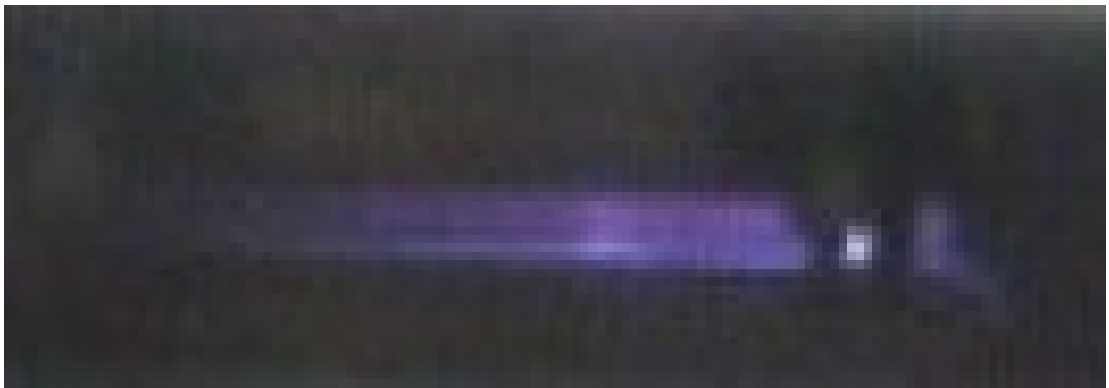


Figure 3-20 Glow discharge for 1:1:8 viewed from the discharge chamber window.

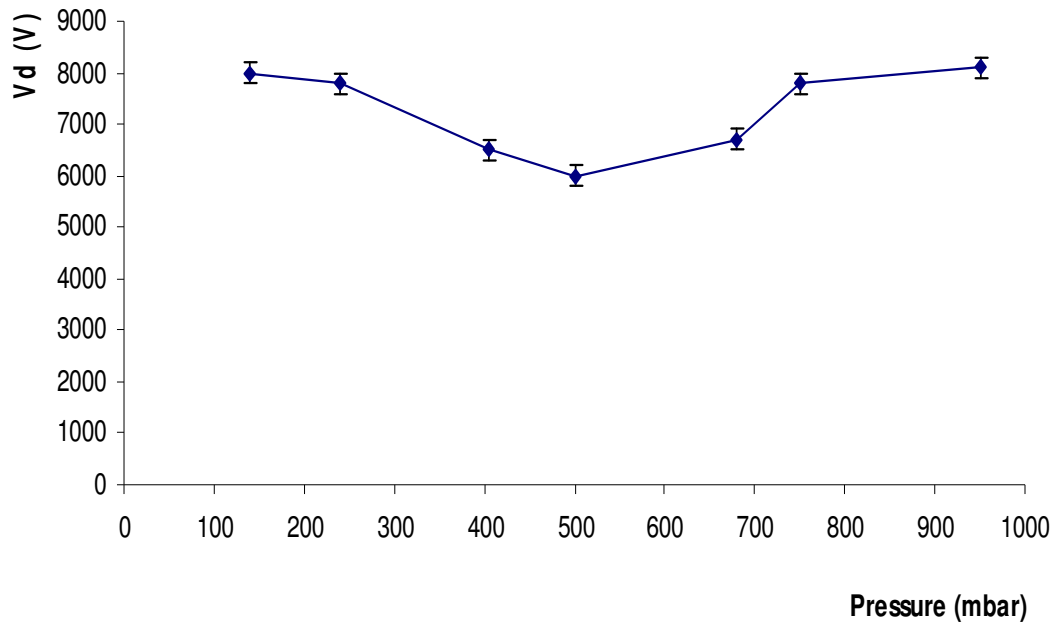


Figure 3-21 Peak discharge voltages for various total gas pressures with a gas ratio of 1:1:8 for $d = 5$ mm with about 5% error

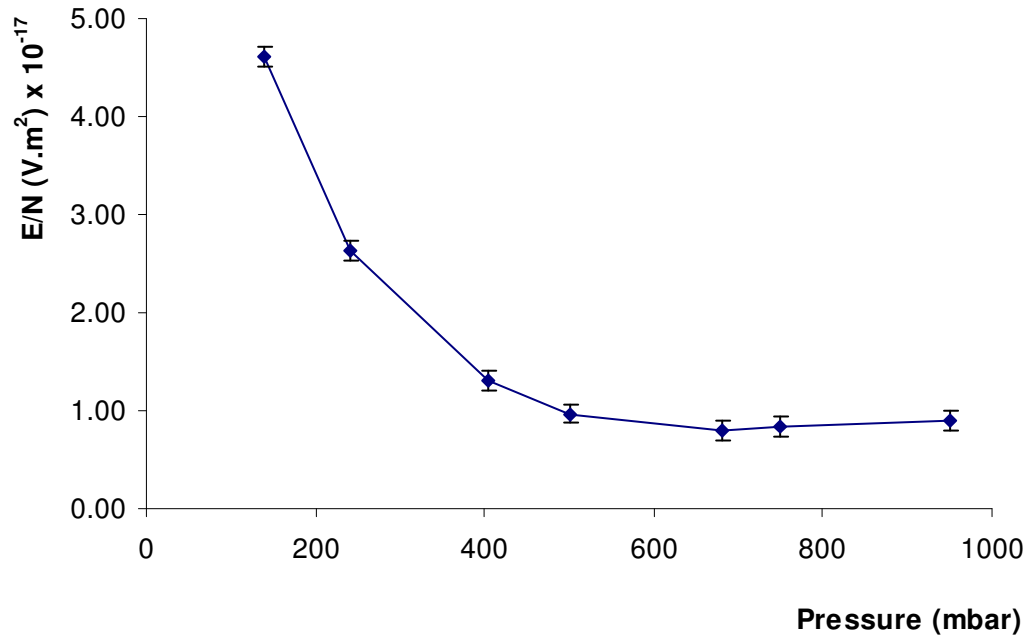


Figure 3-22 The E/N values for 1:1:8 versus pressure with about 5% error.

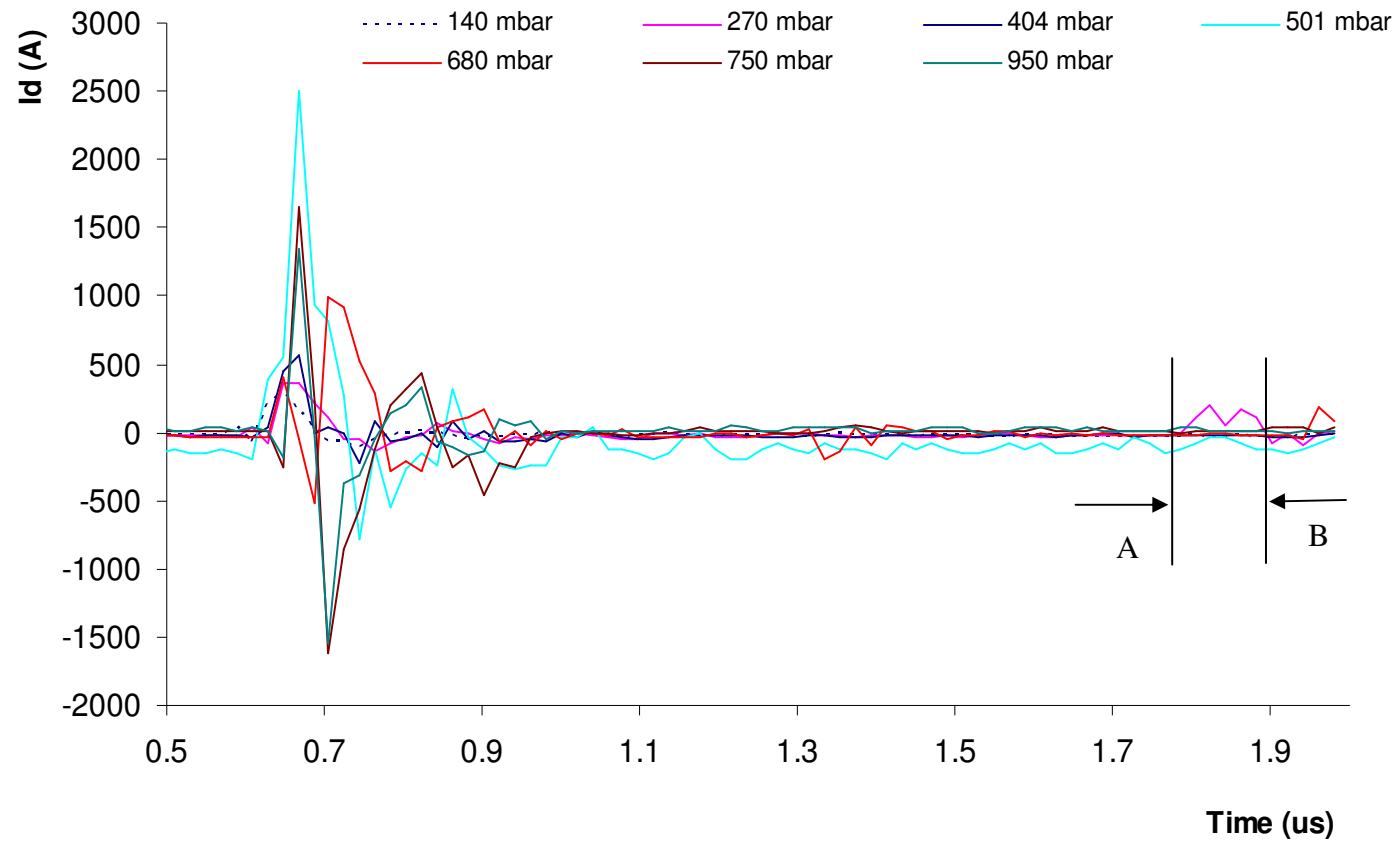


Figure 3-23 Discharge current as a function of time for different total gas pressure. The ratio of the gas is 1:1:8.

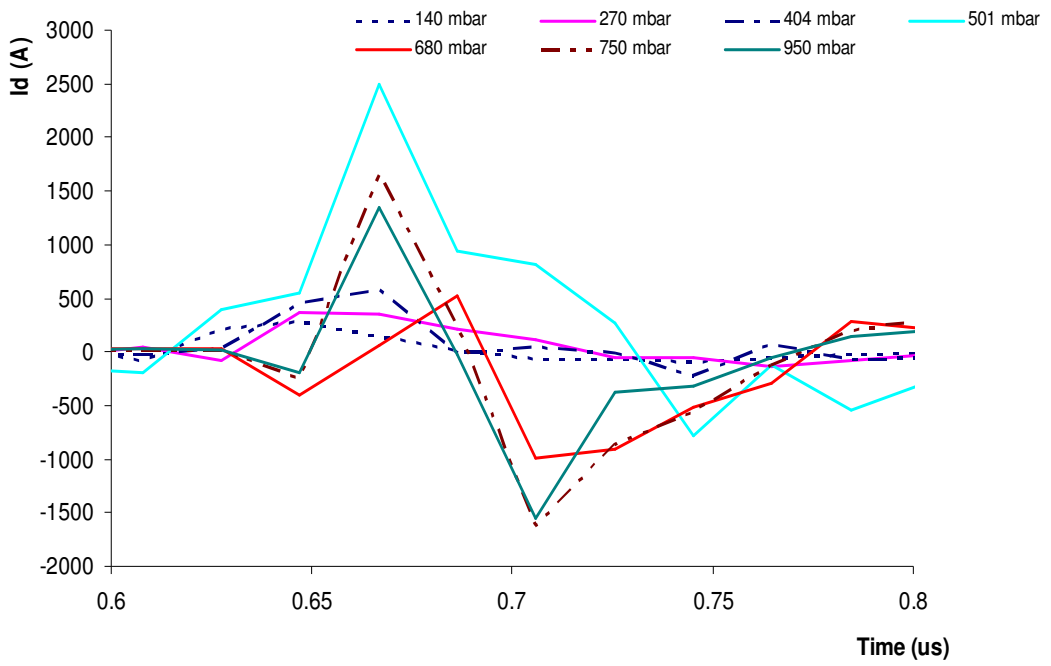


Figure 3-24 Discharge pulse currents on close up time scale. The currents pulses length are broader. at 140 mbar, 270mbar, 404 mbar and 501 mbar, indicating more power were produced.

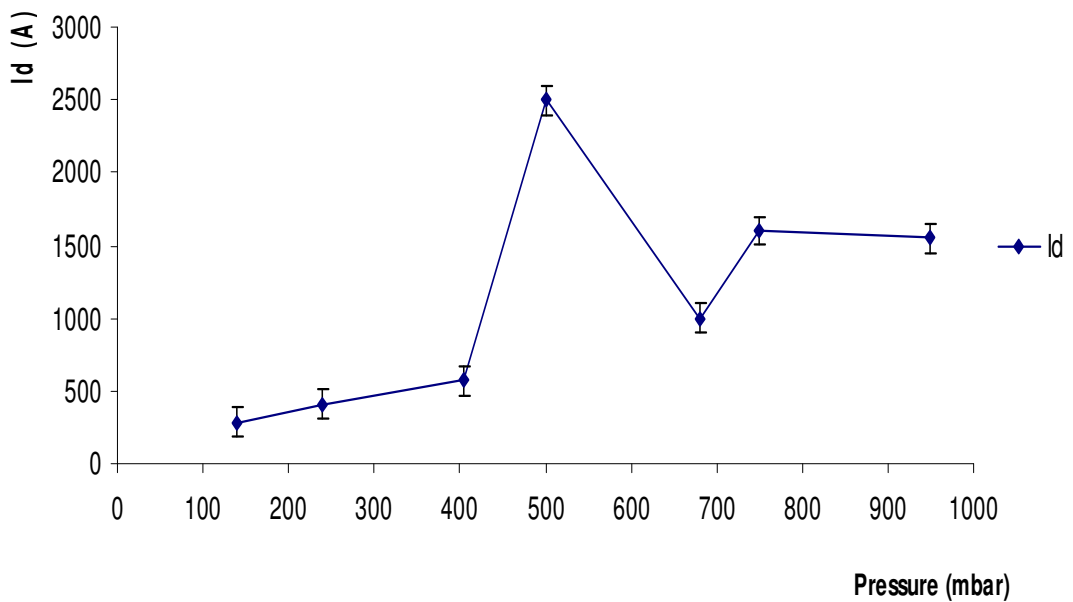
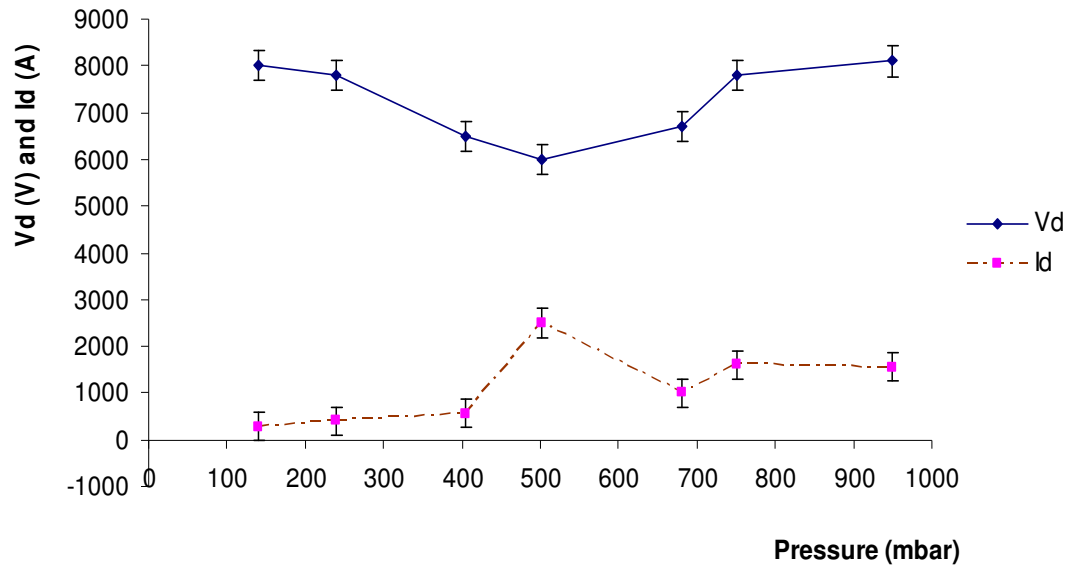
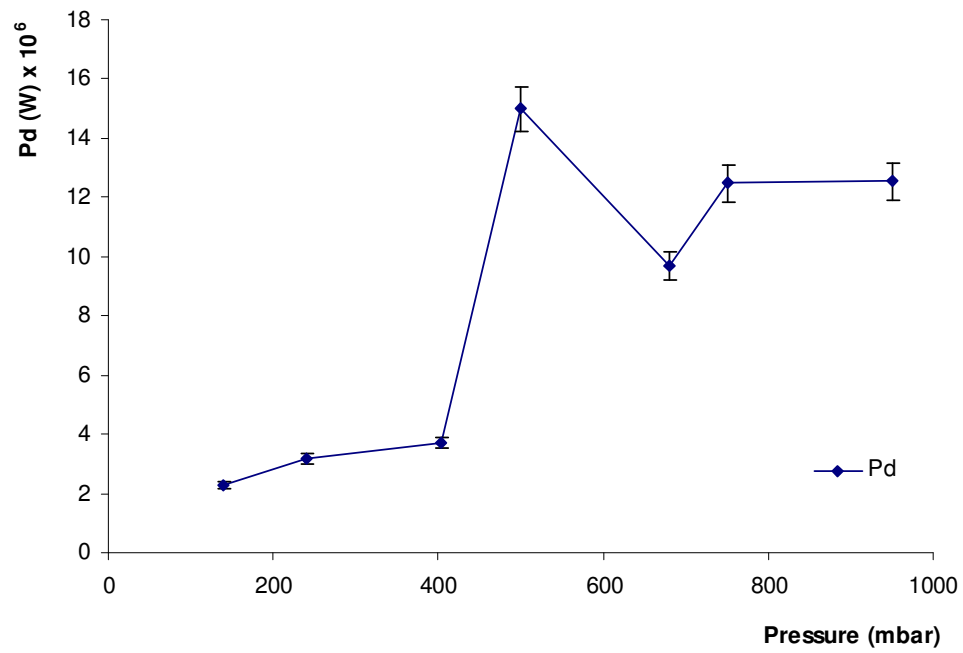


Figure 3-25 Peak discharge current for different pressures with a gas ratio of 1:1:8.



(a)



(b)

Figure 3-26 (a) The peak voltages and peak currents at different gas pressure with ratio of 1:1:8 with 5% error and (b) The peak power of the discharge.

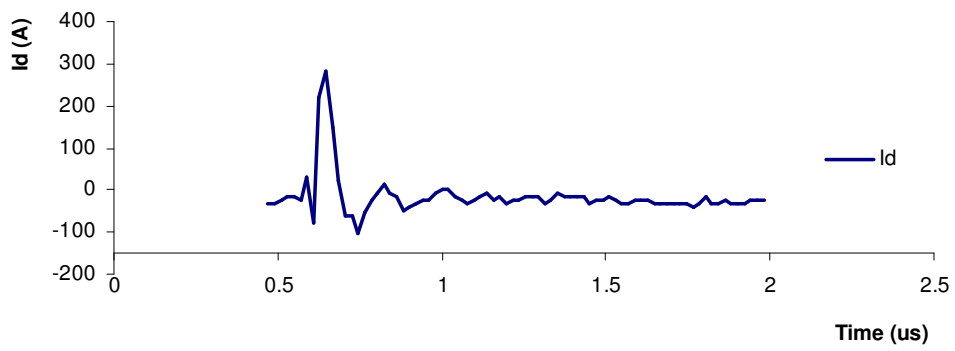
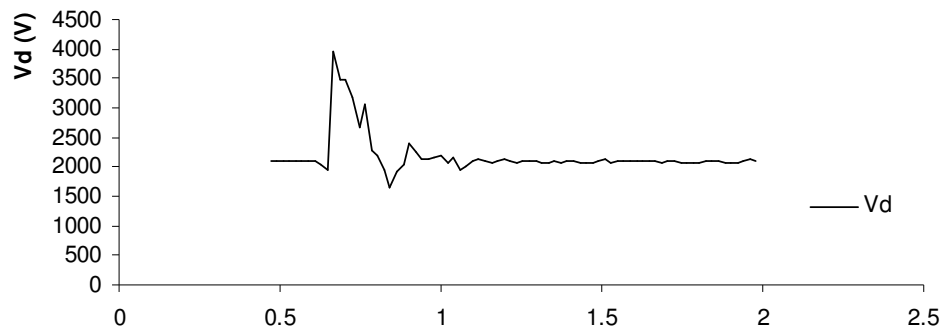
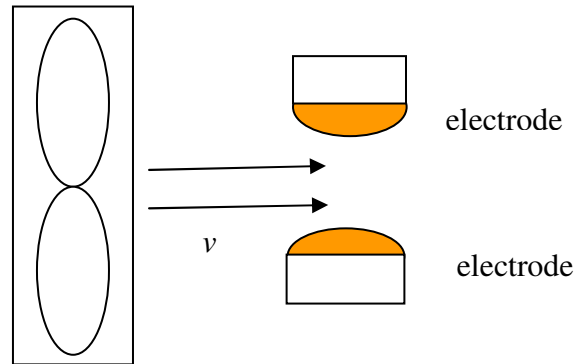
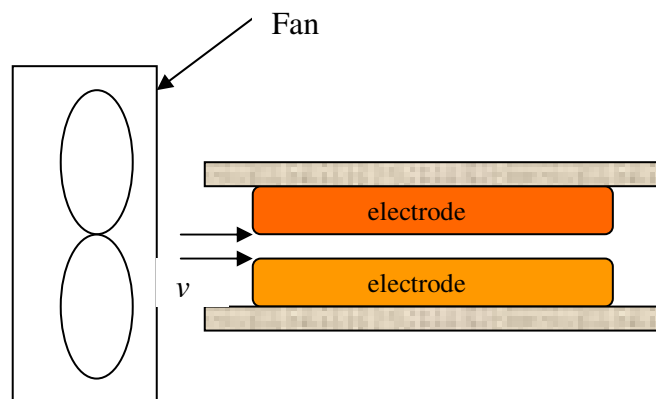


Figure 3-27 The V-I waveform for the discharge with gas ratio 1:1:8 at pressure of 140 mbar, captured separately with the same time base.



(a) Transverse flow



(b) Longitudinal flow

Figure 3-28 The position of the fan to investigate the clearing ratio where v is the flow velocity (a) transverse flow and (b) longitudinal flow.

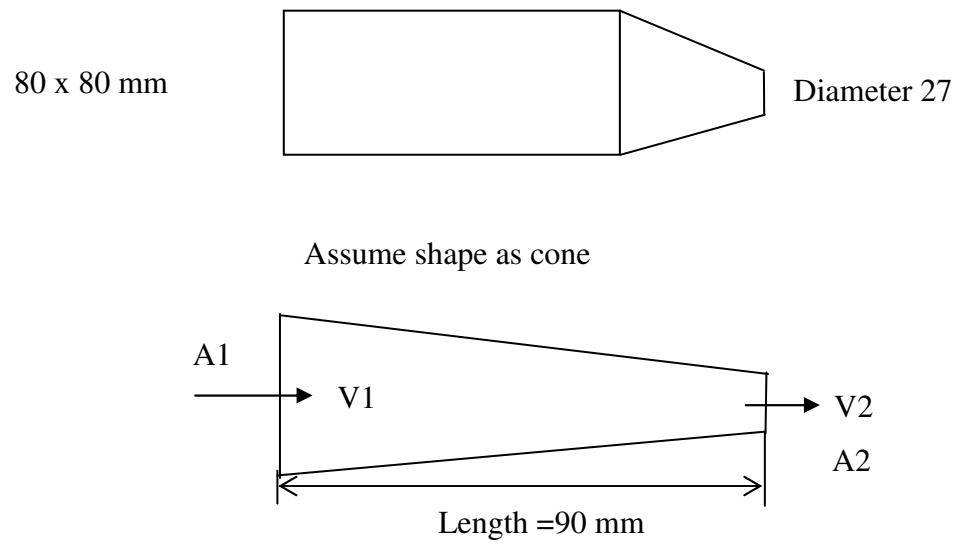


Figure 3-29 Flow shaping used with the axial flow computer fan.



Figure 3-30 Radial flow fan used for the clearing ratio tests, fan was placed longitudinally to the electrode to produce a transverse flow across the electrodes.

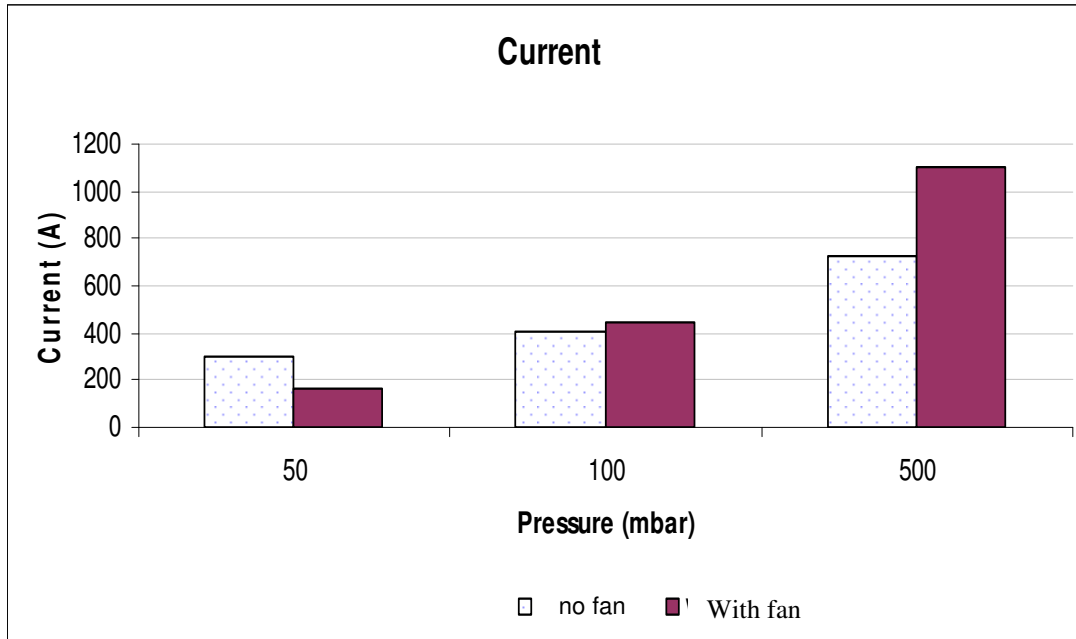


Figure 3-31 Influence of longitudinal flow on discharge currents measured at different gas pressure. The clearing ratio CR = 0.5.

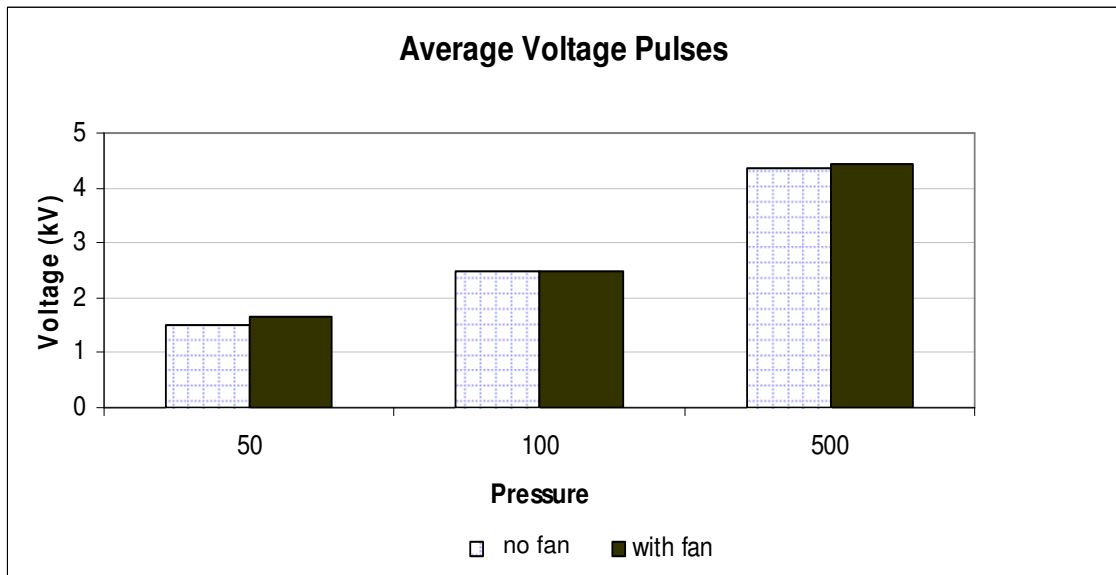


Figure 3-32 Influence of longitudinal flow on discharge voltages measured at different gas pressure. The clearing ratio CR = 0.5.

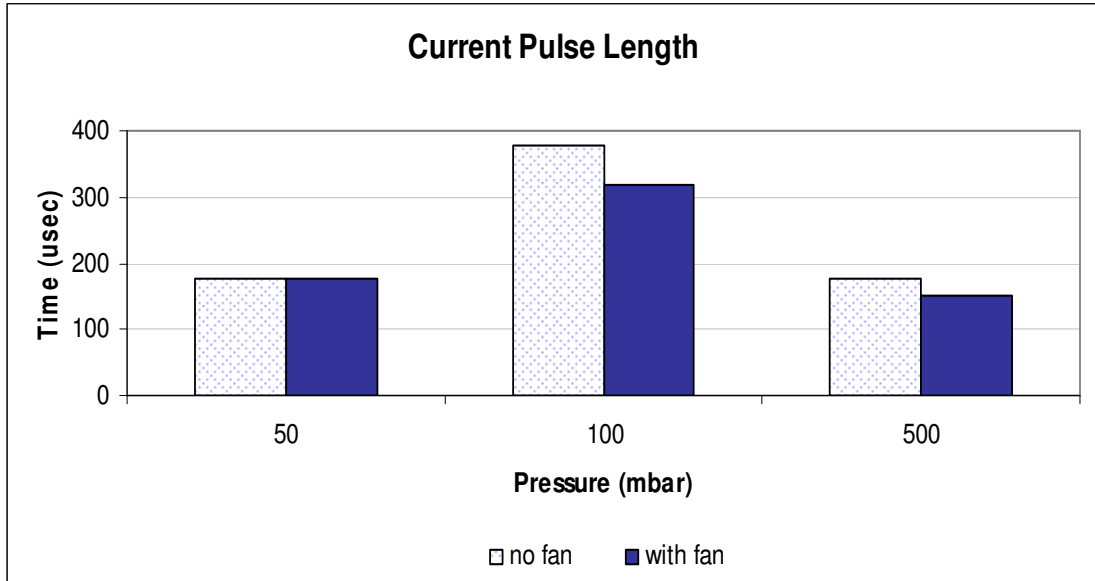


Figure 3-33 Influence of longitudinal flow on discharge currents pulse length measured at different gas pressure. The clearing ratio CR = 0.5.

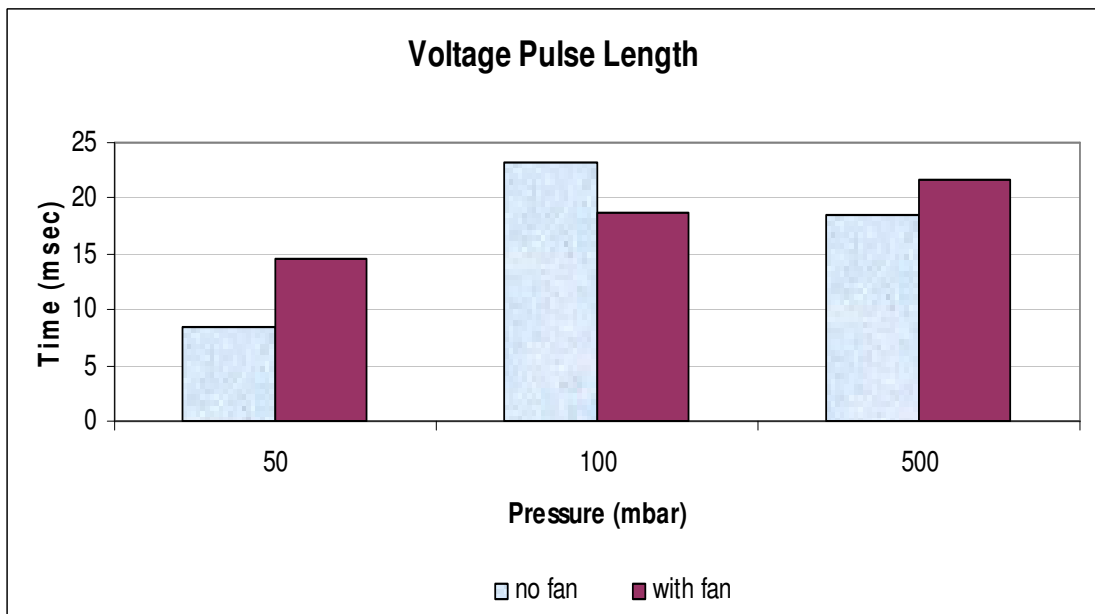


Figure 3-34 Influence of longitudinal flow on discharge voltages pulse length measured at different gas pressure. The clearing ratio CR = 0.5.

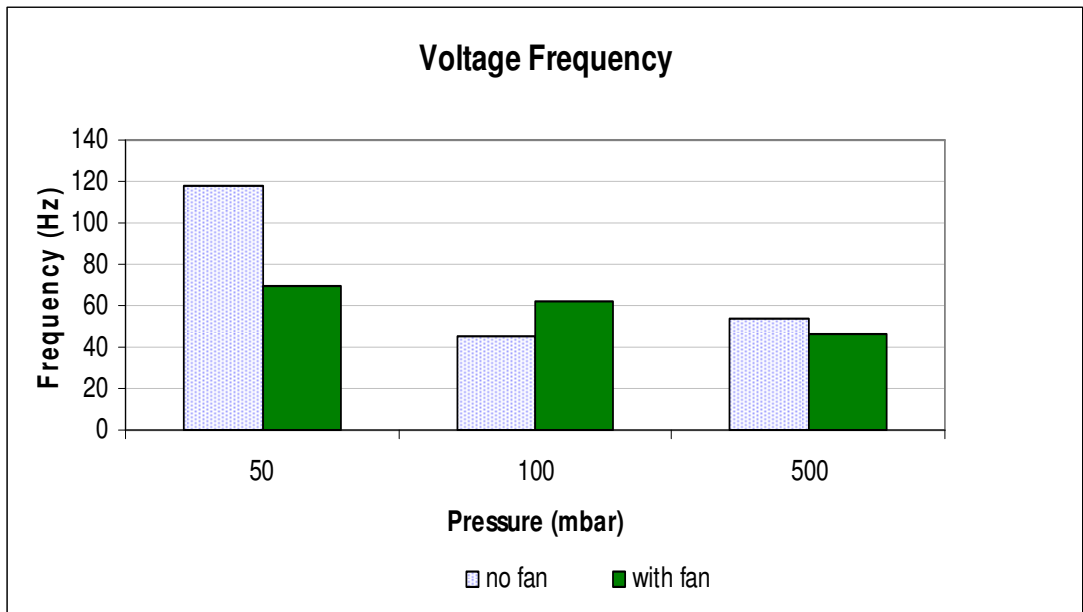


Figure 3-35 Influence of longitudinal flow on discharge voltages frequency measured at different gas pressure. The clearing ratio CR = 0.5.

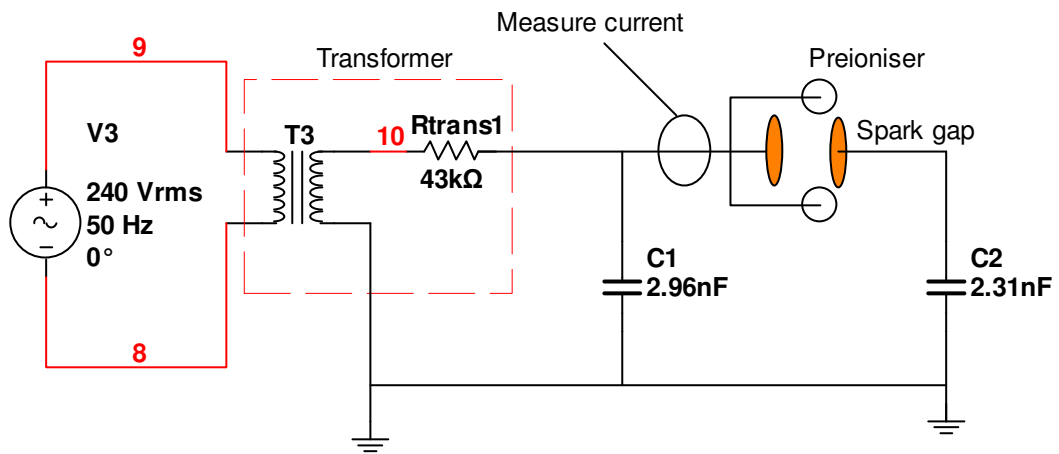


Figure 3-36 TEC AC transformer with trigger wire preioniser set-up.

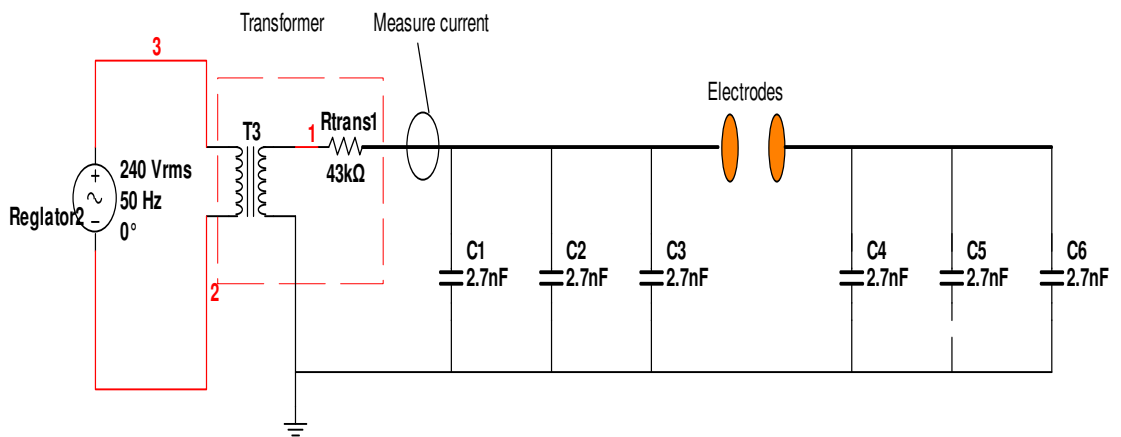
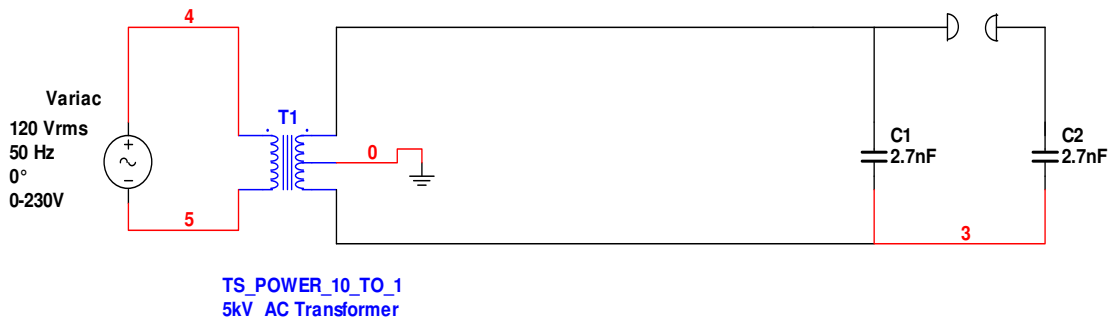
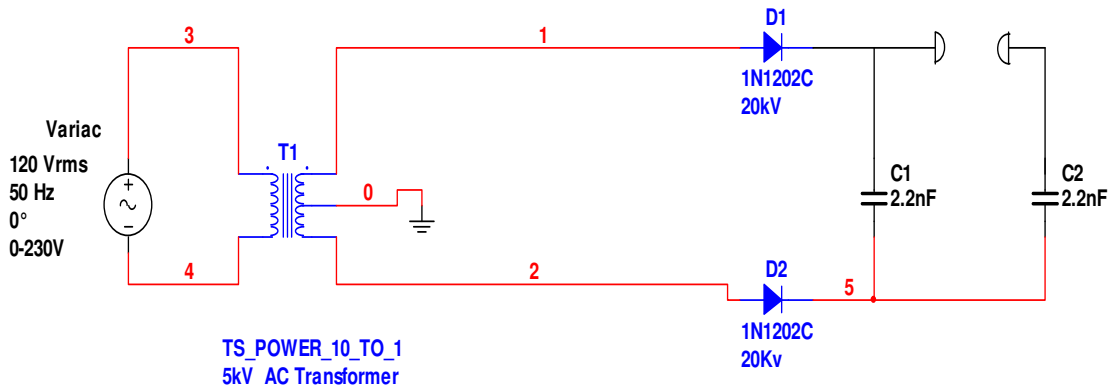


Figure 3-37 TEC AC transformer with three pairs of 2.7nF capacitors.



(a) Resin Block transformer original schematic circuit diagram with centre tap.



(b) Diodes may be added to rectify the voltage

Figure 3-38 Resin Block transformer with center tap made the voltage $\pm 5\text{kV}$. Diode may be used to rectify the voltage to $+5\text{ kV}$.



(a)



(b)

Figure 3-39 The AC transformers: (a) TEC transformer and (b) The Resin block transformer.

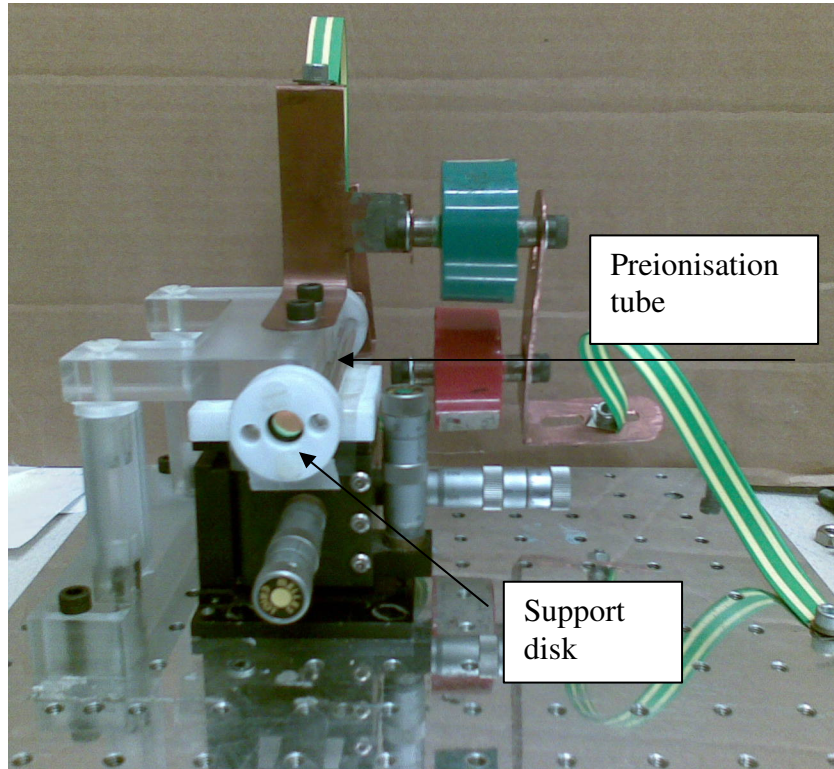


Figure 3-40 Preionsation held with the PTFE support disk.

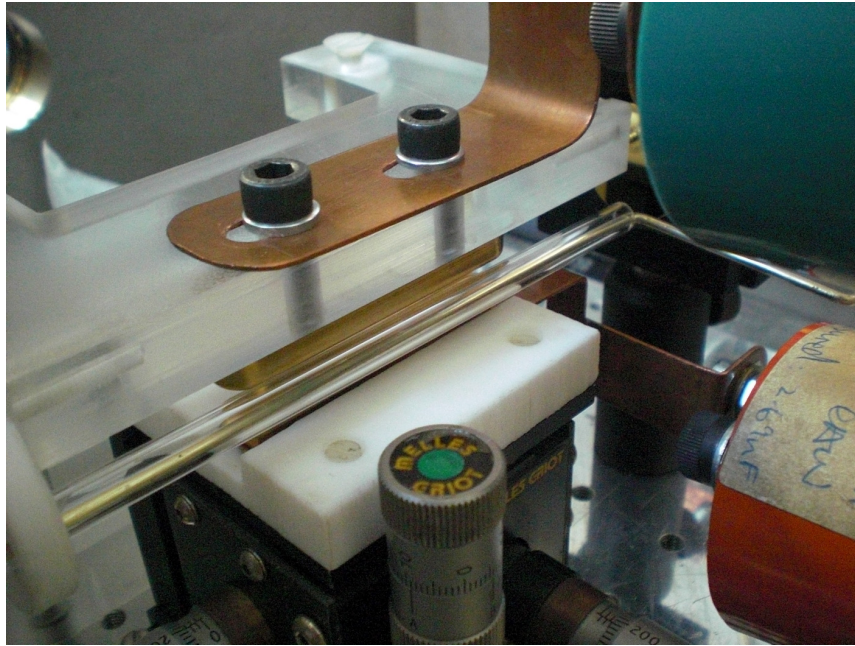


Figure 3-41 The setup for the helium glow discharge with preioniser.

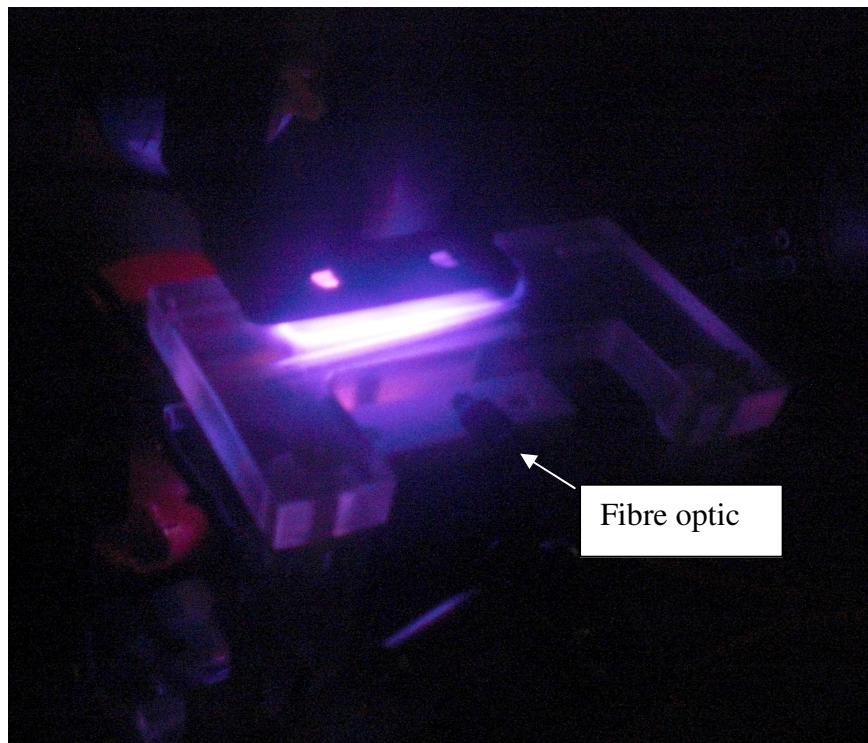


Figure 3-42 Photon Control spectrograph fibre optic with the helium glow discharge.

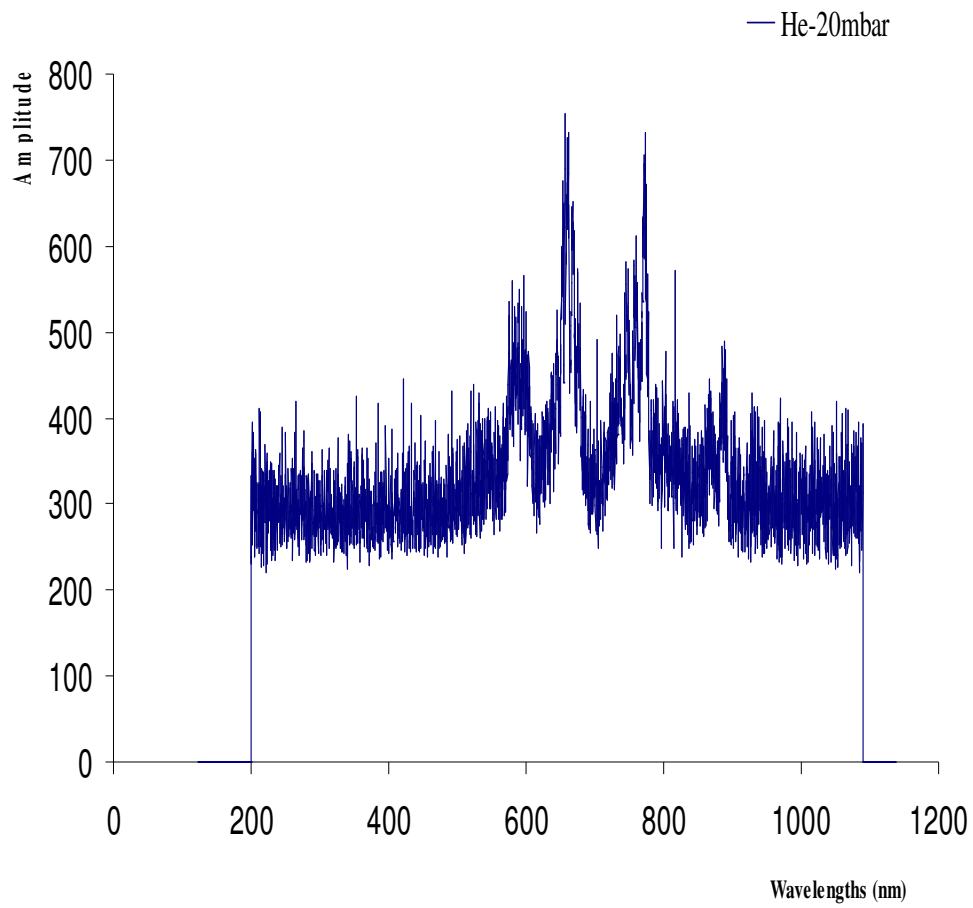
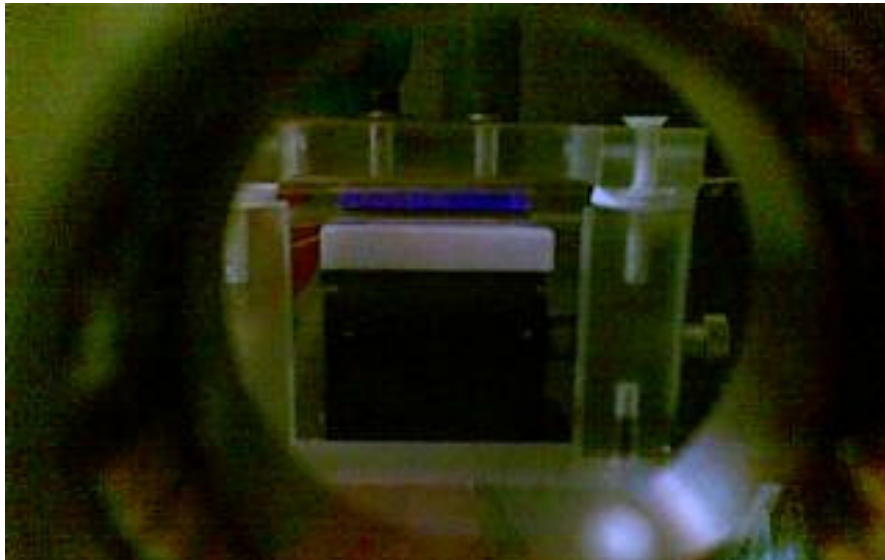
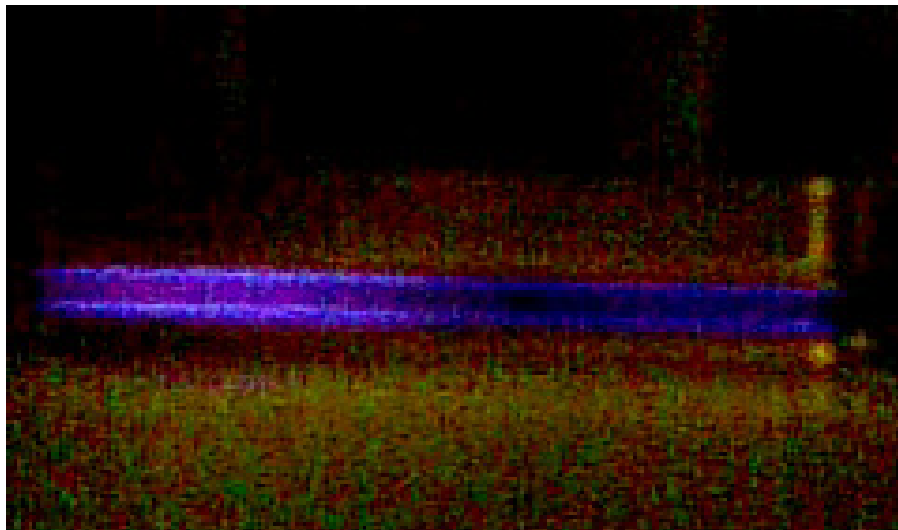


Figure 3-43 Helium discharge spectrum captured with Photon Control Spectrograph. The amplitude for the helium discharge at 20 mbar was not strong.



(a) The glow view from the window



(b) 20mbar N_2 glow with close up view.

Figure 3-44 Glow discharge of N_2 at 20 mbar (a) The set-up and glow view from the discharge chamber window. (b) The close up view of the glow. Stronger glow near the surface of the electrodes.

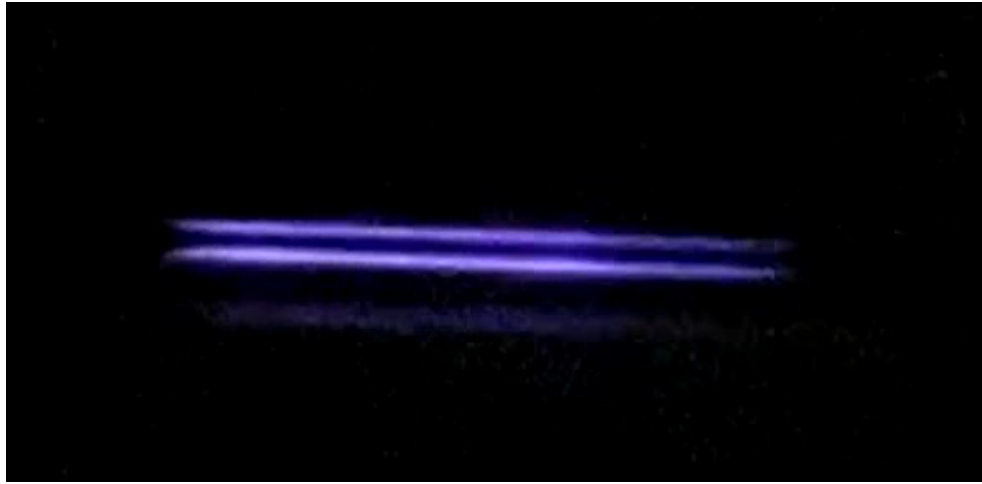


Figure 3-45 Nitrogen discharge spectrum at 50 mbar. The colour of the glow was brighter compared to 20 mbar.

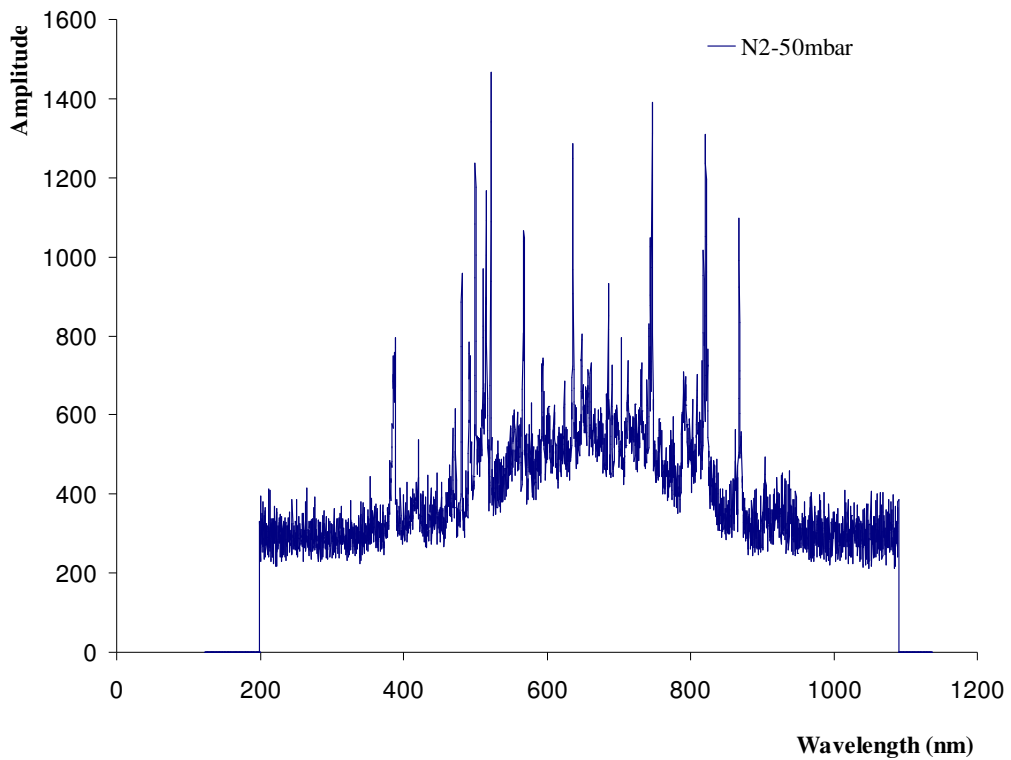
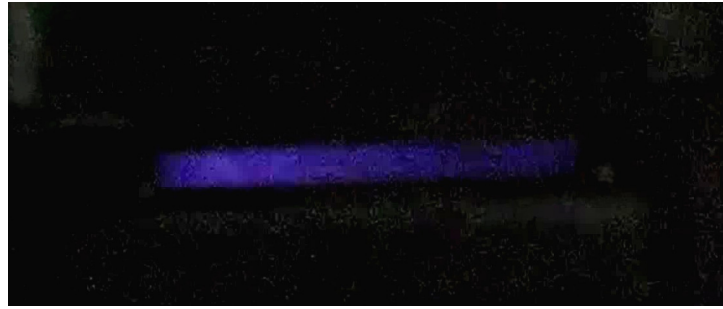
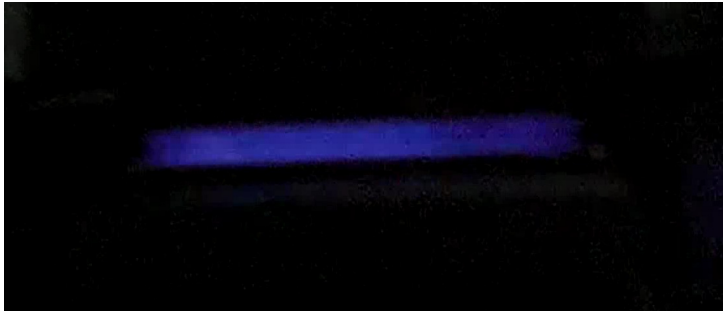


Figure 3-46 Nitrogen discharge spectrum for 50 mbar with maximum amplitude at 1480 a.u with narrow spikes within the range of deep ultraviolet to near infrared (390- 860 nm).



(a) 4.87 kV



(b) 5.20 kV



(c) 5.80 kV



(d) 6.80 kV

Figure 3-47 The glow chronology for 1:1:4 discharge at 20 mbar. The glow became stronger as the input voltage increased (a) The glow started at 4.87 kV input voltage (b) 5.2 kV, (c) 5.8 kV and (d) 6.8 kV.

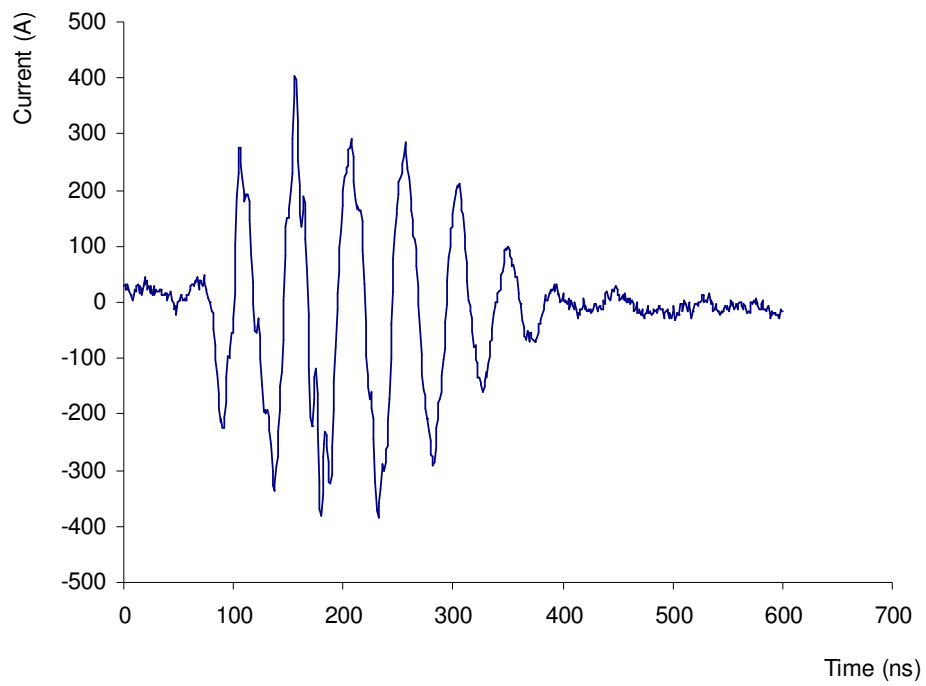
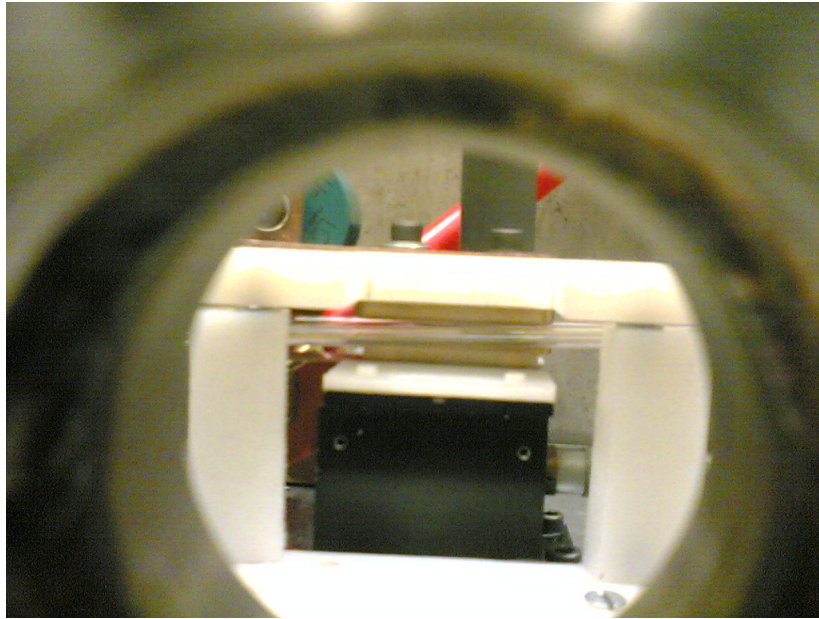
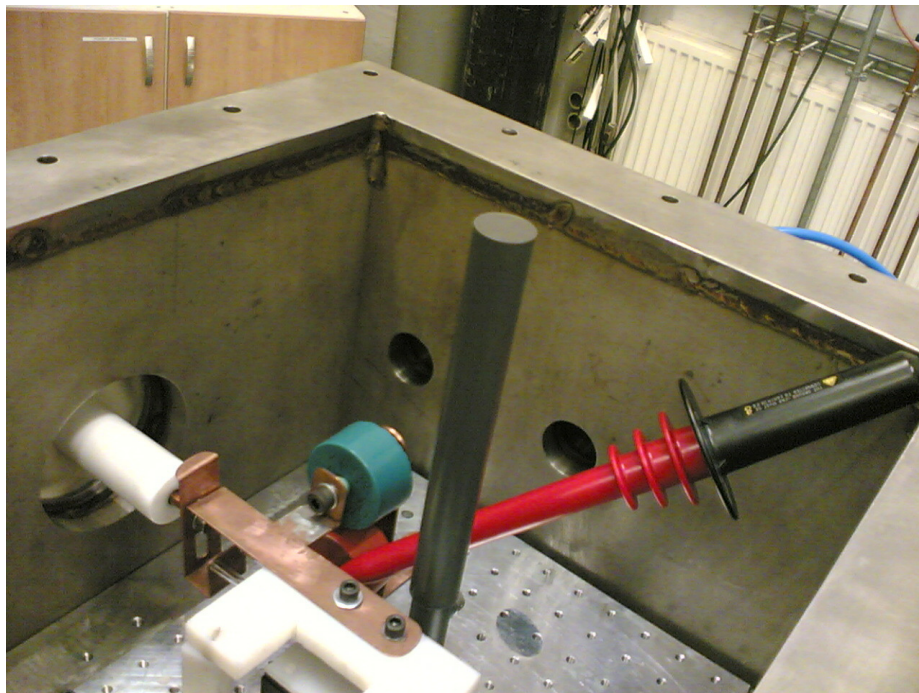


Figure 3-48 Discharge current from an AC discharge system with gas ratio 1:1:4 at total pressure of 50 mbar.

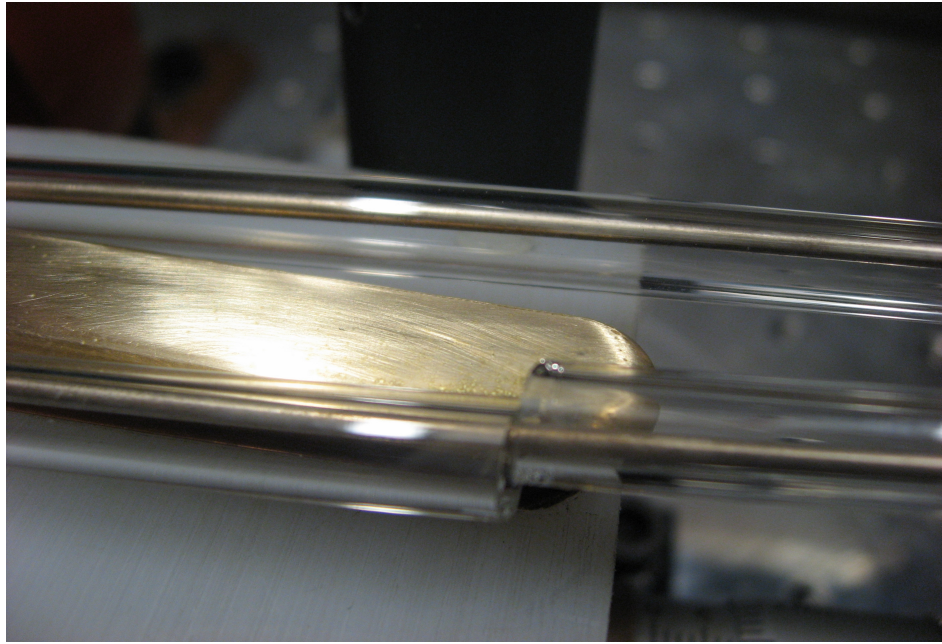


(a)

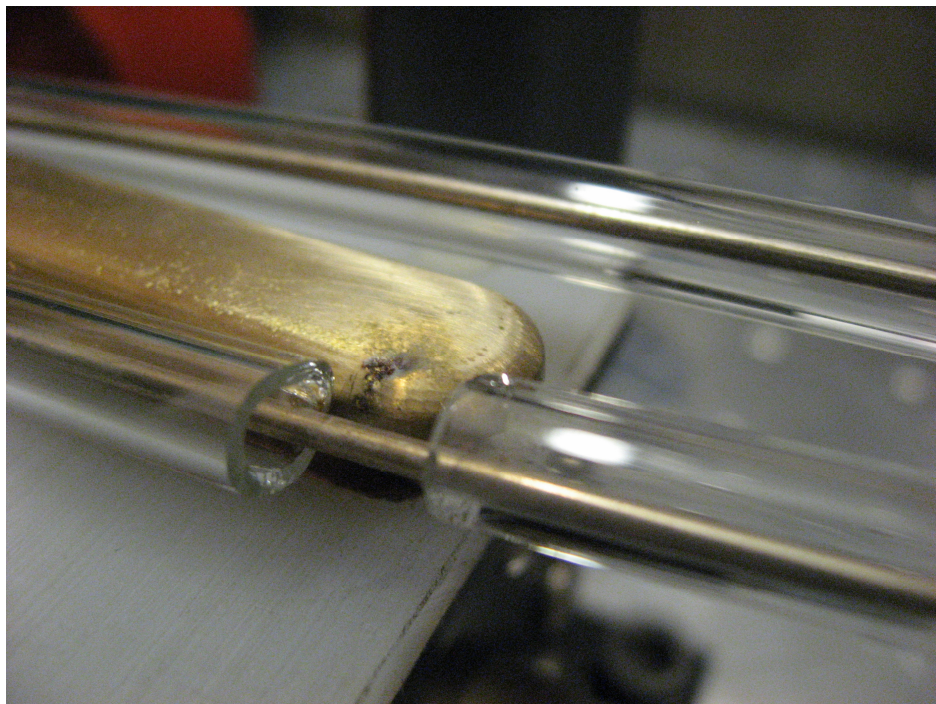


(b)

Figure 3-49 The air discharge set up with trigger wire preioniser. (a) The trigger wire was coupled to the anode. The distance from the centre of the trigger wire to the side of the electrode was 7 mm. (b) The cathode was vertically adjustable via the micrometer in the Z direction. The voltage probe was used to measure the voltage drop across the electrodes.



(a) A broken preioniser glass tube that touched the electrode surface.



(b) The broken glass tube and the electrode surface where the local arc developed.

Figure 3-50 The misalignment of the preioniser glass tube where at a point it touched the electrode and caused very strong localised arcs to develop, this melted and broke the glass.



Figure 3-51 The electrode was cleaned and polished, however the stain was embedded.

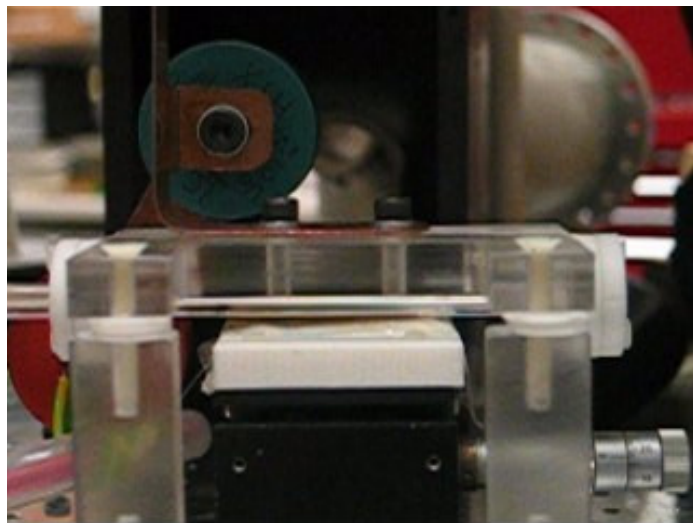


Figure 3-52 Air discharge set-up which was done outside the discharge chamber. The electrode gap of the was 3 mm. The circuitry is as shown in Figure 3-36.



Figure 3-53 The air discharge glow started at input voltage was 4.8 kV. When the voltage increases, the glow was maintained and then arcing occurred at 7.2 kV.

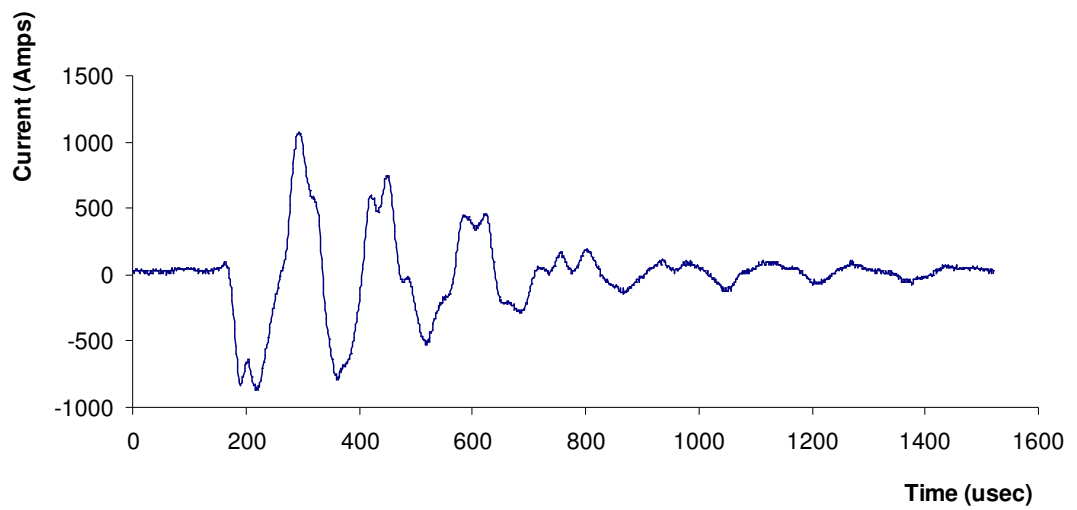


Figure 3-54 AC discharge current in air at atmospheric pressure.

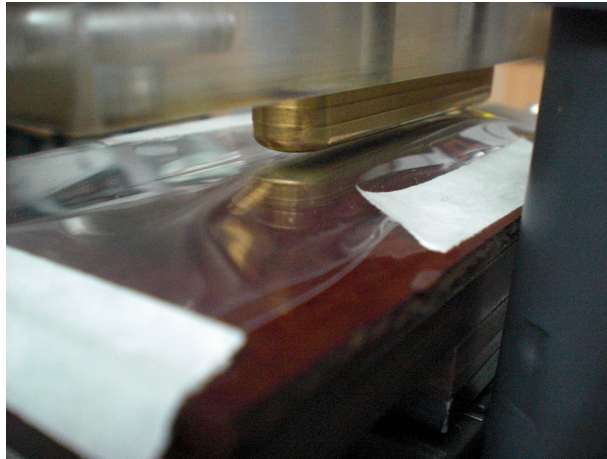


Figure 3-55 Two layers of mylar film were used to cover the electrode in order to improve the discharge quality. The mylar film total thickness was 100 μm .



(a) Top layer (in contact with discharge) with small holes caused by arcs.



(b) Bottom layer (in contact with cathode) mylar was torn due to the heat and arcs.

Figure 3-56 Mylar was used to cover the cathode as replacement to the trigger wire preioniser. This was done in order to improve the quality of the discharge and minimize arcing in the air discharge.

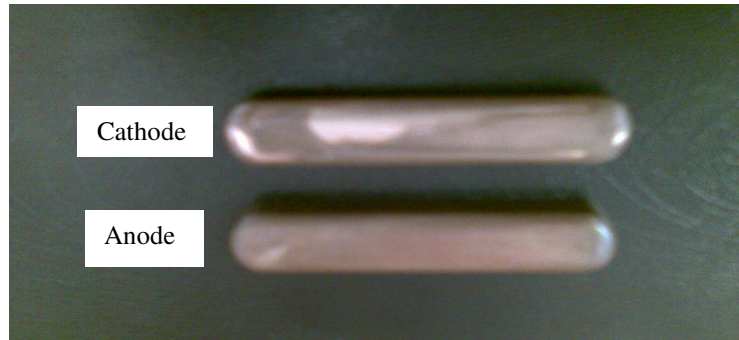
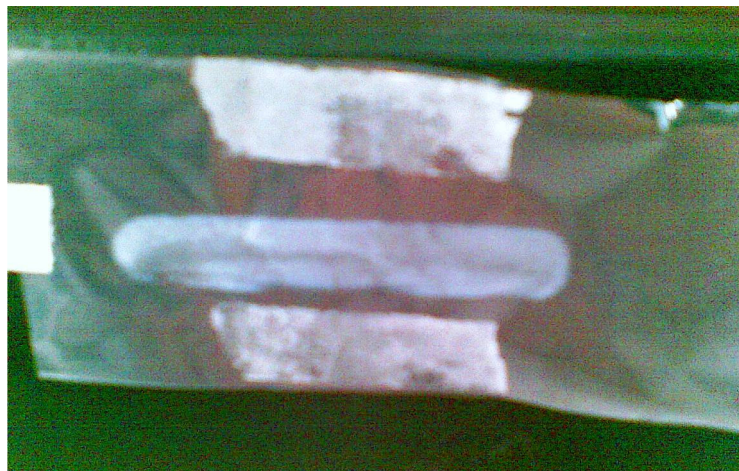


Figure 3-57 The condition of the electrodes after the discharge The bright mark on cathode was the result from the torn mylar.

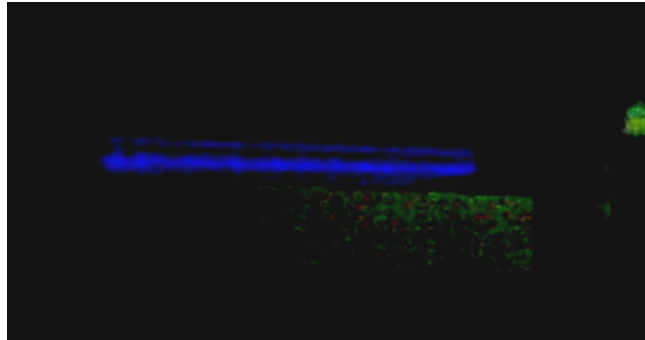


(a) First layer duralar

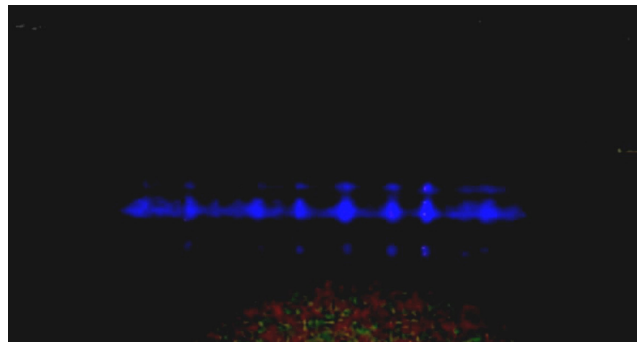


(b) Second layer duralar

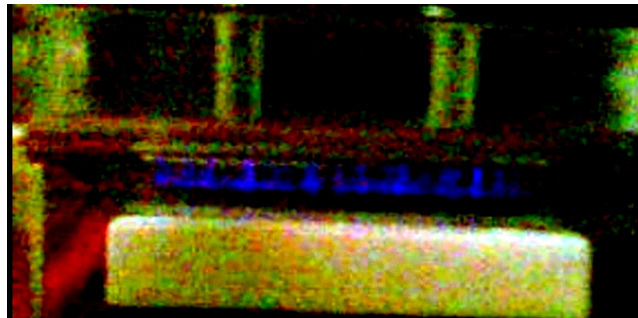
Figure 3-58 The total thickness of the two layers of duralar was 150 μ m. (a) The first layer of duralar developed white marks caused by the electrical discharge. The second layer had less white marks. No holes were punctured in the film by the discharges.



(a) Duralar 3mm electrode gap-brighter on cathode



(b) Duralar 4mm electrode gap-brighter on cathode



(c) Discharge with duralar for 5mm electrode gap

Figure 3-59 The air discharge pattern at 3 to 5 mm electrode gap when two layers of duralar were used over the cathode. (a) Uniform discharge at 3mm gap, (b) strong filamentary discharge at 4mm gap, (c) Filamentary discharge at 5 mm gap. Discharges were stronger nearer the cathode.

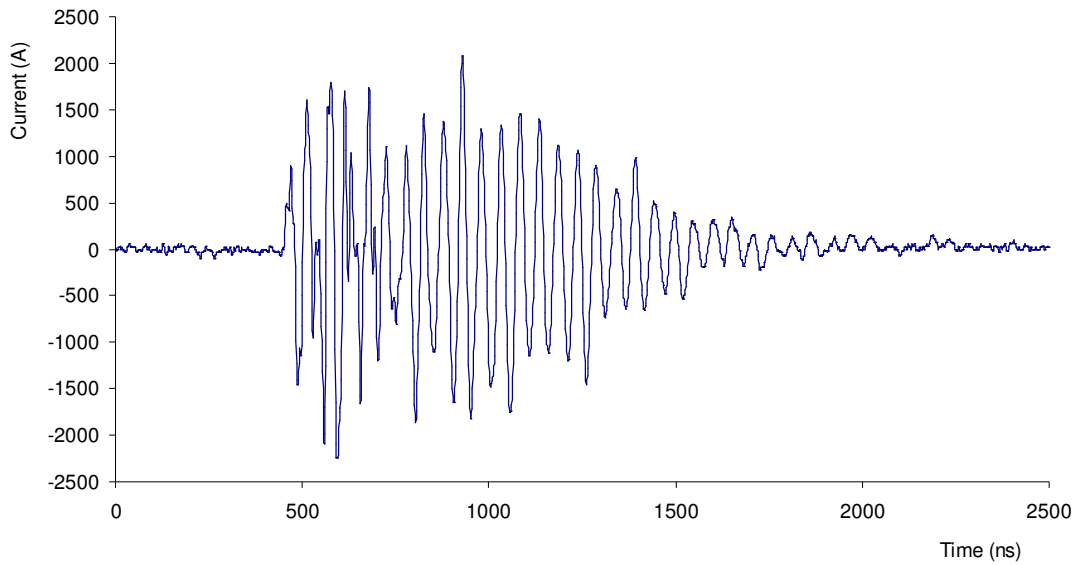


Figure 3-60 Discharge current with two layers of duralar in air at atmospheric pressure.

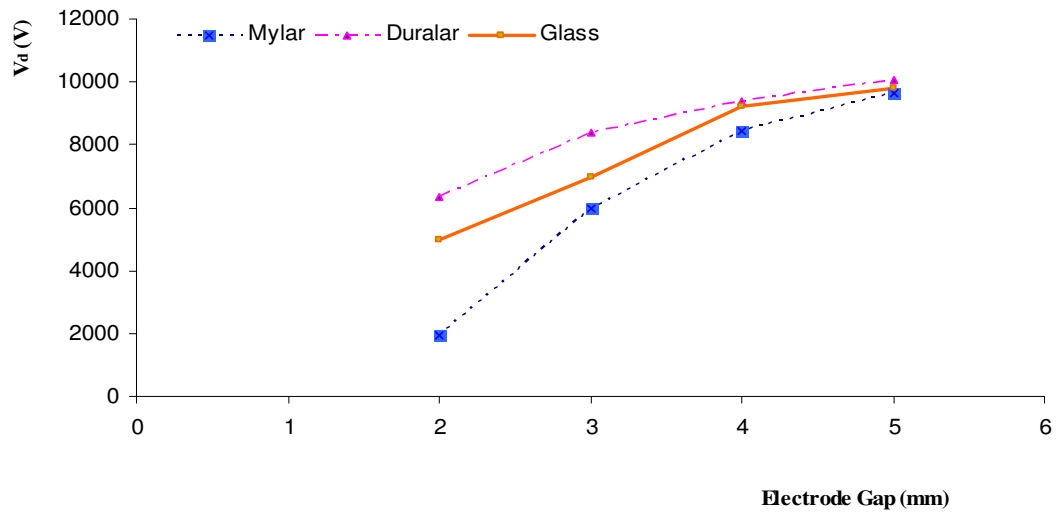


Figure 3-61 The voltage drop ($V_d = V_{in} - V_{out}$) versus electrode gap for various dielectric materials placed over the electrode. Duralar could withstand the greatest voltage for 2 to 5mm gaps. However when the electrode gap increases, V_d increases and at 5mm gap the V_d values were close for all dielectric materials.

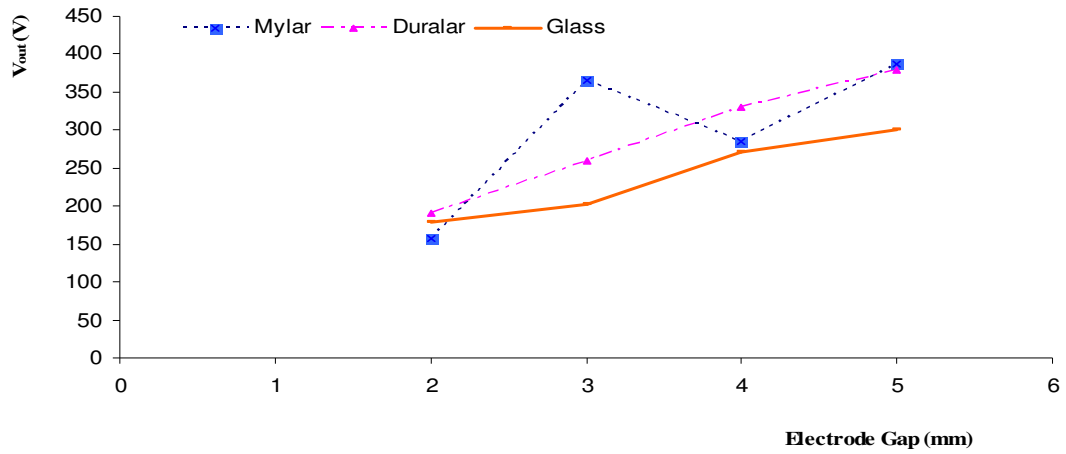


Figure 3-62 The output voltage ($V_{out} = V_d - V_{in}$) discharge versus the electrode gap on the Chang profile electrode with the dielectric material placed over the cathode. The output voltage for duralar and glass were linear.

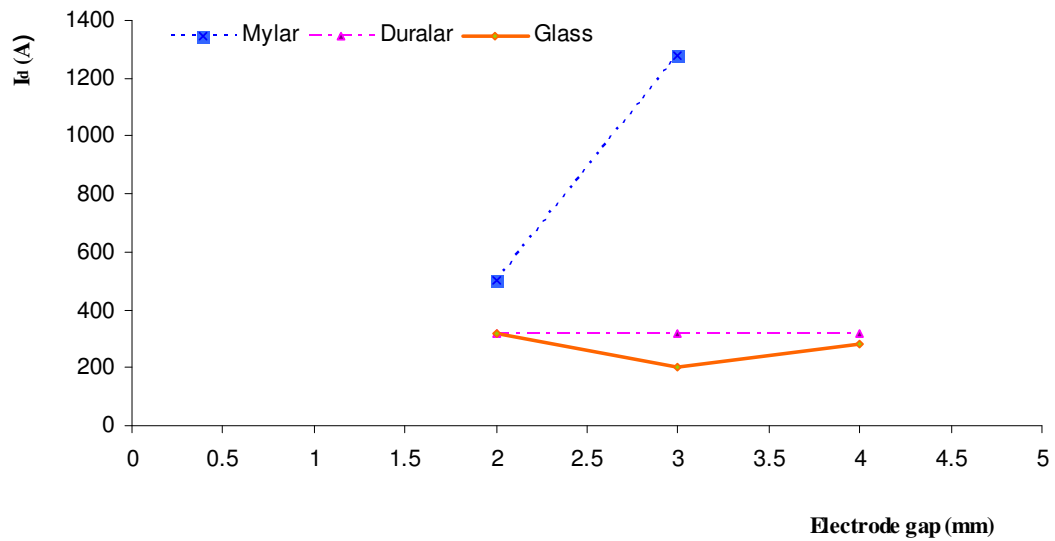


Figure 3-63 The discharge current (I_d) for duralar was constant for electrode gap of 2-4 mm, compared to glass and mylar. The discharge current with mylar had a sudden increase when the gap increased, as the mylar film failed.

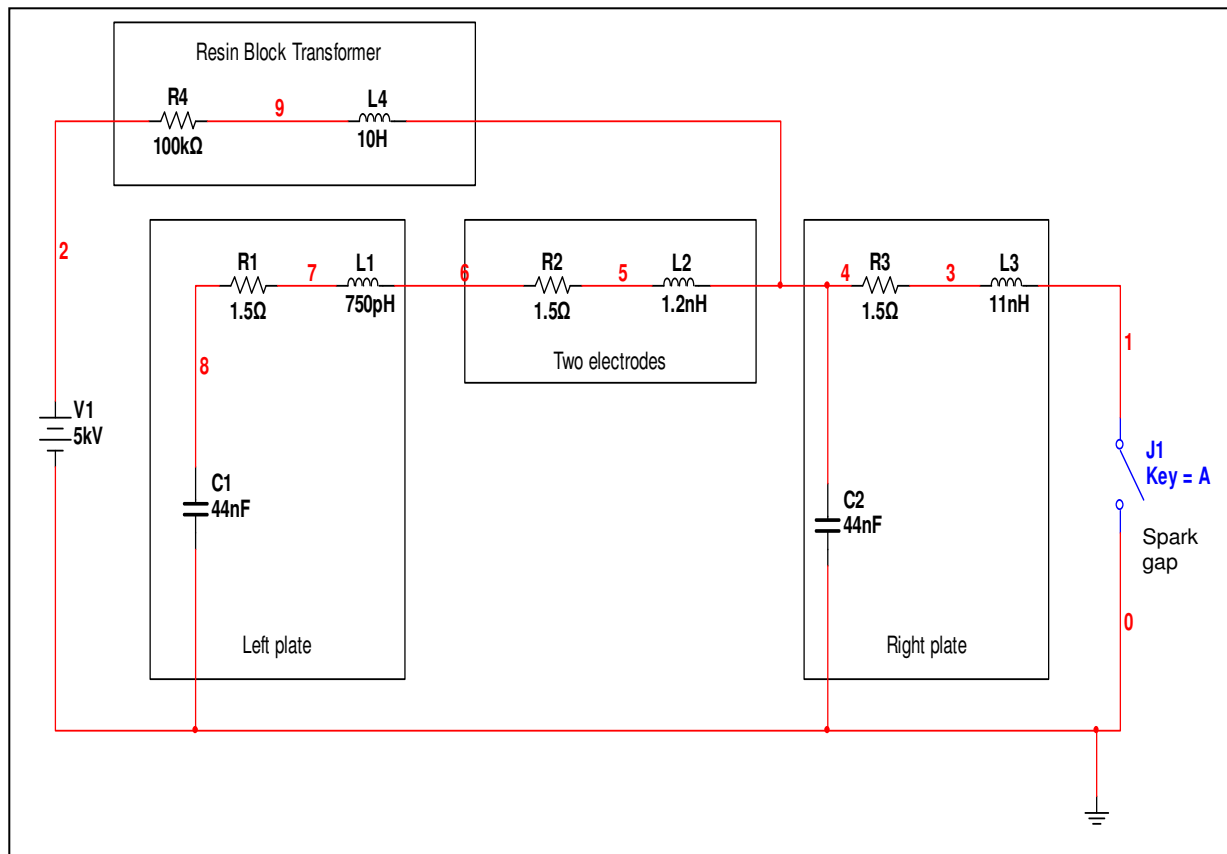


Figure 3-64 The Blumlein circuit used in the air discharge. The Resin Block transformer was used to charge the 2 layers of duralar which acted as a 44 nF capacitance. A spark gap was used to switch the stored energy into the main discharge system.

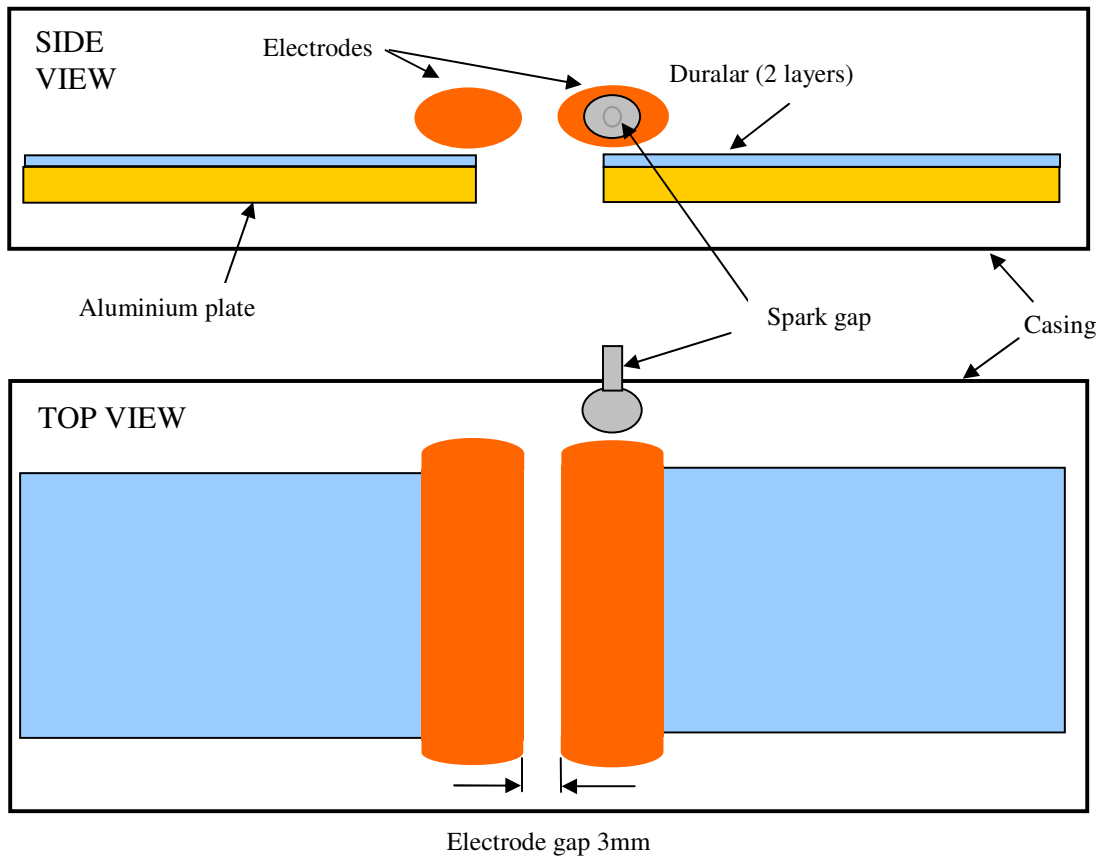


Figure 3-65 The illustration of the Blumlein system. The electrodes were made from stainless steel rod with diameter of 25 mm. The gap between the electrodes was 3 mm and the ball switch gap was 1 mm. Two layers of duralar were placed over the aluminium plates to serve as the capacitance. The mild steel plate thickness was 1 mm.



Figure 3-66 The electrodes and the spark gap switch before the discharge.

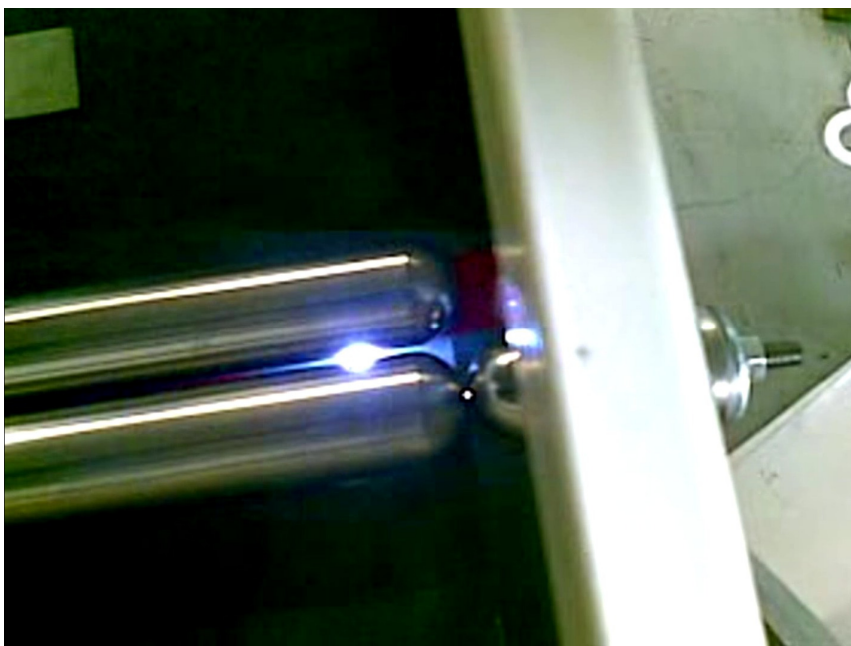


Figure 3-67 The Blumlein discharge.

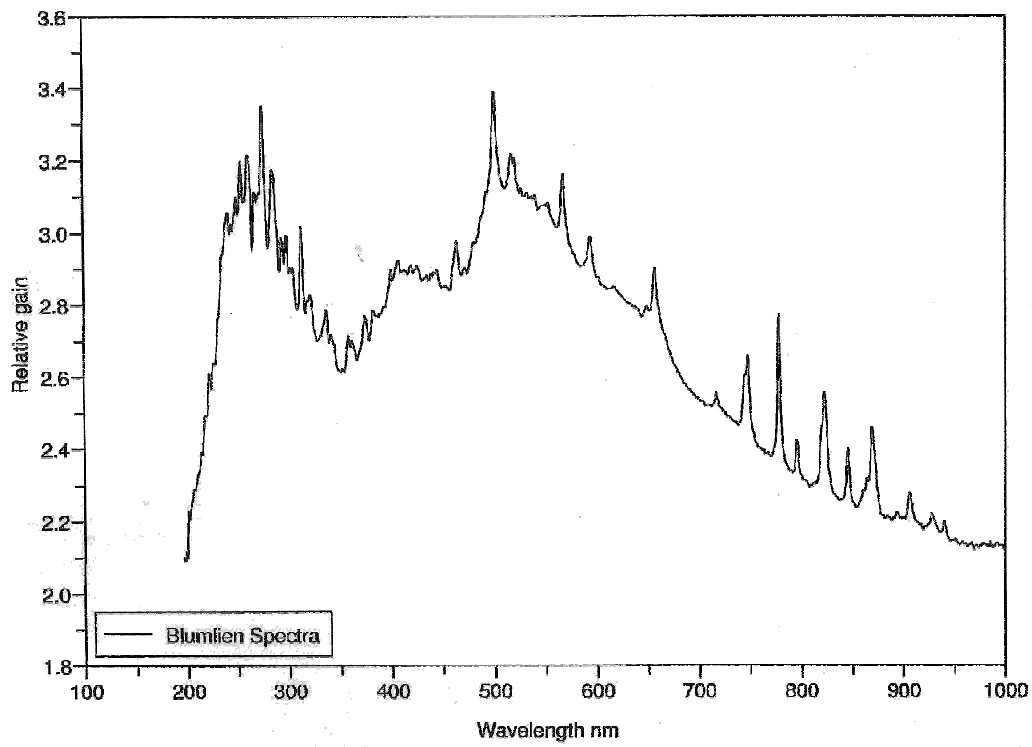


Figure 3-68 The Blumlein discharge spectral intensity.

Chapter 4

Electrode Design and Manufacturing

4.1 Introduction

This chapter reports on the design, manufacture and performance of the electrodes used in this research. There were four different types of profiled electrodes employed: the planar, Chang profile, unmarked aluminium and laser marked aluminium. These were used within different discharge systems to test the prototype performances. The purpose of using different geometry and different surface finishes on the electrodes was to investigate the effect on the discharge stability, the ozone production rate and the simplicity of production and the cost of manufacture. The discharge volume capacity and the enclosure design also played an important role in electrode selection. The discharge enclosure design also directly affected the electrode holder design.

All electrodes were manufactured in-house and methods of electrode manufacture and basic quality assessment ie surface roughness measurements and visual assessment were done. Analysis of the electrode surfaces was done with optical microscope, EDAX and SEM.

4.2 Electrode attributes

Defining the attributes of the electrode allows the different electrode profiles to be compared. Trtica and Miljanić [2003] simplified the electrode attributes into illustrations and tables. The electrode attributes are illustrated in **Figure 4-1**, the basic dimensions of the electrodes used in this work are summarised in **Table 4-1**. This table was useful as a reference in designing the electrodes and also for comparing any electrode's modifications that were necessary.

4.2.1 Electrode materials

The electrode material chosen for manufacturing generally was either brass or aluminium, however for comparison purposes, copper and stainless steel were also used but the latter was used less often because of the difficulty of manufacture.

4.2.1.1 Brass

The electrical conductivity for brass is 16.24×10^6 S/m (28 %) compared to copper's value of 58.0×10^6 S/m which is referred to in the International Annealed Copper Standard (IACS) as 100%. The electrical conductivity shows that copper seems more suitable to be used as electrodes, however, due its mechanical properties, brass has more mechanical and electrical resistance to the discharge effects. Brass is also easier to machine and therefore brass was chosen for the some of the electrode material used in this study.

4.2.2.2 Aluminium

It has been observed by other workers that discharges generated with aluminium electrodes were more homogeneous (Mathew *et al*, 2007) compared to gold, brass, stainless steel and nickel. The electrical conductivity of aluminium is 37.8×10^6 S/m, which is equivalent to 61% of copper's conductivity. Aluminium plate was used in this research as it was easily available and cheap. The machining and finishing process of aluminium was also easy. A further significant advantage is that the plasma plume from aluminium electrodes does not contain hazardous chemicals compared to brass, that may contain copper oxide and zinc oxide because brass mainly consists of 60-70% copper and 20-25% zinc and 4-5 % lead [Jayawardana *et al*, (1997)]. Thus aluminium was the most practicable choice for electrodes when the discharge application was for air treatment.

4.3 Types of electrode

The following sections describe the type of the electrodes designed and used in this research. These electrodes were manufactured in-house in order to reduce the cost and also as part of the manufacturing studies in producing standard or specific electrode designs, with a view to commercialisation.

4.3.1 Planar electrode

The planar electrode was designed and used in the first development of the DC and AC discharge systems. The basic parameter for the planar electrode design was the active discharge volume.

4.3.1.1 Planar electrodes profile

The material chosen for the planar electrodes was brass. The dimensions of the rectangular surface of the electrode was 10 mm x 60 mm and 6 mm thick. The rectangular surface area was considered important because it determines the electrode discharge area and relative discharge volume when the discharge area is multiplied with the electrode gap, d ($2y_0$ in Table 4.1). The thickness of the electrode was considered as non-critical in terms of the discharge. It was important in terms of the electrode mounting assembly.

The planar electrode's edge profile was not designed from uniform field electrode design theory because of the urgency to manufacture the electrode for discharge system demonstration purposed and to obtain early results. The flat surface of the electrode was maintained at 9 mm x 59 mm discharge area and the rounded edges curved radius along the electrode length was 1 mm, while the curved along the electrode width was 5 mm. **Figure 4-2** shows the CAD drawing of the planar electrode profile.

4.3.1.2 Manufacturing of planar electrodes

The CAD drawing of the planar electrode was up-loaded into MASTERCAM to create the machining path file. The planar electrode was machined on a CNC machining centre with HSS end mill cutter for the flat surface and M3 HSS form tool to form the curve profile of radius 1 mm on the rounded edges. The machined surface texture was rough with machine marks clearly visible with the naked eye. The average roughness of the machine marks was 32 μm . These marks were not uniform and it was felt that they may lead to discharge instability and arcing. To remove the machined marks, a further polishing process was needed. The wet (water) hand polishing process used emery cloth number 800. The electrode was placed on a flat surface and the emery cloth was held onto the electrode surface with minimum pressure. The polishing stroke was kept to one direction along the length of the electrode. The applied pressure was minimised in order to maintain the flatness of the electrode surface.

The time taken to complete the wet polishing process was around 20 minutes. The electrode was then washed with water, followed by wiping and drying with a damp cotton cloth. The damp cloth removed small dirt particles trapped on the electrode surface. To improve the process without affecting the grain structure, dry hand-polishing was done with a cotton material. To maintain the electrode surface quality, the final step was polishing with Brasso. Iso-propanol was used to clean off any contaminates left by the Brasso. The average time to prepare each electrode (by hand) was around 40 minutes.

The average surface roughness of the polished electrode surface was 0.5 μm . **Figure 4-3** shows the electrode condition before and after the polishing. These photographs were taken by a Nikon digital camera mounted onto a Nikon Eclipse ME600 microscope lens (Normanski), with Nikon ACT1 software, at 10x magnification. **Figure 4-4** shows the plane brass electrode ready to use in the experiment.

The electrodes were tapped with two M6 screw holes symmetrical to the centre of the electrode length (**Figure 4-4(c)**). These screw holes were used to mount the electrodes to the holders.

4.3.2 Uniform field electrode

The theory of the behind the Uniform Field Electrode (UFE) was discussed in Chapter 1. The UFEs were designed such that the electric field was maximum at the centre and gradually minimised towards the edges. The edge profiles needed to be calculated in order to enable rounding off of the electrode to avoid sharp edges and allow tapering of the electric field. The sharper the edges, the higher the resulting electric field that may lead to arcing. It is known that the voltage breakdown across the gap is dependant on the E/P value (where E is the electric field and P is the gas pressure). The discharge boundaries were constrained to the region where 97% of the electric field was at the central region of the electrodes gap [Stappaerts (1982)]. The rounding off for the curves was done at a point where the electric field was reduced to at least 70% of the central region.

4.3.2.1 Chang's uniform field electrode

Modelling and analysis of the uniform field electrodes was included in Chapter 3, which showed that the electric field distribution in Chang's uniform field electrode was more stable even when the size of the electrode became more compact. The electric field potential (Vm^{-1}) of 4.25×10^6 (in 2 units of flux (U)) in Chang's profile has less chance of early breakdown compared to Rogowski's profile, where the Rogowski's electric field potential was $8.0 \times 10^6 \text{Vm}^{-1}$ in 2 units of flux (U). These electric field values contributed to the decision to choose Chang's profiled electrode as the electrodes used in this research.

Referring to equation (1.18) in Chapter 1, the empirical constant value of k in Chang's function, determines the x and y points value of the electrode profile. Here the pre-design value was $k = 0.02$ and $k = 0.2$. It is known that the lower the k value the broader the electrode. The x and y points will generate the so called Chang's profile and these points are taken into the design of the electrode. The generated curve is shown in **Figure 4-5**: for $k = 0.02$ the curve maximum point was $x = 3$ and $y = 5$, while with $k = 0.2$, the maximum point was $x = 1.62$ and $y = 1.00$. Maple 11 software was used to solve Chang's function to generate the x and y points. A copy of the x and y calculation is shown in **Appendix 4A**. The flat surface area with the electrode of $k = 0.02$ was about 16 mm x 56 mm while for $k = 0.2$, the area was about 9 mm x 57 mm.

4.3.2.2 Manufacturing of Chang's uniform field electrode

The curve of the Chang's profile was generated on Maple 11 software by solving the Chang's function (as explained in Chapter 2) and the curve data points were then transferred into an Excel spreadsheet to obtain the x and y points that were readable by the CAD-CAM software. The Excel x and y points was imported into SolidEdge14 CAD to generate the curve. In the SolidEdge CAD part development, the 3D part was generated as seen in **Figure 4-6**. The 3D generation was done by revolving the curve on the plane which refer to the length of electrode. This 3D part was then up-loaded into MASTERCAM to create the machining path file and the G codes.

The material chosen for the Chang's UFE was brass as used for the planar electrodes discussed in the previous section. The CNC machining centre was used to machine the electrodes. The brass block was mounted onto a fixture with two screws (**Figure 4-7(a) and b**) in order to enable the tool path to follow the code as uploaded in MASTERCAM. The machining tool was tungsten carbide which improved the machined surface finish.

During manufacturing of the first few electrodes, the machining time was 3 hours per electrode. The tool path orientation of the 3 hours machining time is shown in **Figure 4-**

8(a)). The machining direction was reciprocal across the electrode. To overcome this long machining time the tool path orientation was changed as well as the machining direction, this time the tool path was length-wise (**Figure 4-8(b)**). The thickness of the electrode was machined to size before the profile machining began. The fixture holding the electrode was also changed to match the width of the Chang electrodes. This technique together with the new fixture setup (**Figure 4-9**) reduced the machining time from 3 hours to an acceptable 30 minutes per electrode.

The machined surface texture using tungsten carbide tool was less rough with an average surface roughness of 26 μm , see **Figure 4-10**, compared to HSS machine marks of 32 μm . To finish the electrode surface texture to the quality required, a hand wet polishing process using emery cloth number 800 was also carried out, similarly to the brass planar electrode technique. However extra polishing attention were needed at the electrode edges in order to obtain evenly polished curves. The average complete polishing time was around 30 minutes per electrode. **Figure 4-11** shows the machined surface texture before and after the polishing process. The average value of the polished surface roughness was 0.5 μm (see section 4.4 for electrode surface roughness measurement).

4.3.2.3 Compact Chang's electrode

Compact Chang uniform field electrodes with $k = 0.2$ with a surface area of about 9 mm x 57 mm were selected to be used in the prototype design. The Chang's electrode geometry needed to fit within a compact portable prototype enclosure for work on developing air decontamination system; this was known as the dome system. The discharge volume was $\sim 600 \text{ mm}^3$ as shown in **Figure 4-12**. The distance between the electrodes was 5 mm. The discharge from the dome prototype setting was designed to produce ozone to treat air flowing through the inlet of the enclosure and in between the electrodes.

4.3.3 Aluminium electrode

The purpose of using aluminium electrodes was to obtain a larger discharge surface area with a stable discharge and avoid contamination of the air as may be the case with brass electrodes. The aluminium electrodes produced from aluminium plate was also cheap and simple to manufacture. A study of the discharge quality for the different electrode materials: copper, brass, aluminium and stainless steel was done before deciding on using aluminium as the electrode material of choice for the larger electrodes. The experimental and research related to the aluminium electrodes is shown in **Appendix 4B** [Luciano Nicola Diterlizzi, Personal communication].

4.3.3.1 Aluminium electrode profile

The aluminium electrode dimensions were 30 mm x 200 mm with 4 mm thickness, with a rectangular shape as shown in **Figure 4-13**, and the curve radius around the edges was approximately 1 mm. The surface area of this electrode was 10 times greater than the planar or Chang electrode used above. If the sample (air or micro-organisms) was fed transversely into the discharge volume (**Figure 4-14(a)**), the sample through-put increases by a factor of about 10 (proportional to the electrode surface area). Otherwise, if the sample flows longitudinally into the discharge (**Figure 4-14(b)**), the length of the sample exposure time to the discharge also increases by the same factor.

4.3.3.2 Manufacturing of aluminium electrode

The simple shape of these aluminium electrodes made them easier and quicker to manufacture. The aluminium plate was marked with the rectangular dimensions and cut into size on a guillotine machine. The sharp edges were removed by using a curve form tool and a fine file. The surface and the edges of the aluminium were polished using the same technique used on the planar and Chang electrodes (see section 4.3.2.2). Due to the

low hardness of aluminium, extra care was taken during the polishing process to avoid bending or deformation. The average time to do the hand polishing on one aluminium electrode was about one hour. The surface roughness of the aluminium electrode was 0.5 μm . **Figure 4-15** shows a finished aluminium electrode ready to be mounted onto the aluminium electrode holder. The complete time of manufacture (machining and polishing for one) aluminium or the Chang electrode was about 1 hour respectively.

4.3.4 Laser marked aluminium electrode

The effect of laser marking electrodes on the discharge characterization was investigated. Uniformly marked electrode surfaces will create uniform micro-discharges due to the peaks and valleys of the surface. The strength of the micro-discharges on the peak will be different to that on the valley. It was thought that this may improve the discharge stability and prevent early breakdown and create a uniform energy distribution. Initial studies of the behaviour of the laser marked electrode discharge on different materials was conducted. Discharge patterns for laser marked copper, brass, aluminium and stainless steel electrodes are shown in **Appendix 4C**.

From these studies, the energy deposited into the discharge with the marked electrodes produced a higher discharge energy than the unmarked electrodes. The damage of the marked surface from the high voltage discharge was also less and their use resulted in a stable discharge operating for longer periods. The long stable discharge contributed directly to the longer life-time for the electrodes.

4.3.4.1 Marked aluminium electrode profile

The marked aluminium electrode geometry and size was exactly the same as the aluminium electrodes, in Section 4.3.3.1. A marked electrode was paired with the unmarked aluminium electrode in some of the experiments.

4.3.4.2 Manufacturing of marked aluminium electrode

The aluminium electrode was marked with an Nd:YAG laser marker, model Laservall VIOLINO 2, made in Italy, with 10 W mean output power. The beam diameter was set by adjusting the position of the electrode relative to the focusing lens. This determined the width of one pass with the beam scanning on the workpiece material. The travel of the X-Y table was controlled by a numerical controller (NC) where the travel velocity for this work was either 1.0 or 4.0 mms⁻¹. A program in G code was written to control the machine table movement [Takashi Mine, personal communication].

The laser marker was controlled by Smartist4 software, working in the Windows environment. The frequency of the beam was selected from the software attribute with a selected range from 1000 to 20,000 Hz. The frequency modifies the marked surface texture profile. The intensity of the laser beam power was controlled by selecting the power percentage (1 – 10 W). In this application the power used was between 90 - 100%. Varying power intensity varies the depth of the laser beam penetration into the workpiece.

Figure 4-16 shows the laser marking method and the orientation of the laser scan. The scan started at point 0 and scanning in y direction while the machine table move in -x. Since the default maximum work area for the laser marker was 100 x 100 mm, where the electrode length was 200 mm, a laser scanning method was used. Consequently, three scanning regions were done. Each region was 80 mm x 46 mm width. To ensure both ends of the electrode were fully marked, the laser scan region was overlapped by ± 0.5mm was done where the regions were joined.

Typical laser marking parameters to mark the aluminium are shown in **Table 4-2** was overlapped below. These configurations can be changed according to the required specifications. The electrode laser marking system is shown in **Figure 4-17**. The finished aluminium marked electrode is shown in **Figure 4-18**. The average time to mark one electrode was approximately thirty five minutes - no further processing was required.

Table 4-2 Laser parameters for marking the aluminium electrodes

Power (W)	10
Frequency (Hz)	20000
Scan speed (mm/s)	50
Passes	1
Fill space	0.01

4.4 Electrode surface roughness measurements

Two methods were used to measure the surface roughness of the electrodes. Firstly, a portable Taylor Hobson Surface roughness Tester Machine (UK) with a LCD digital display was used and followed by Taylor Hobson Form, Talysurf Series 2, (UK) with an interface to a computer and the capability to plot the surface roughness graphs. These two measurement technique gave the same reading of surface roughness. The average of the surface roughness measurement is shown in **Table 4-3**. Brass and aluminium (unmarked) electrodes were found to have similar surface roughness values of 0.5 μm because the same polishing technique was used for planar brass, Chang and the aluminium electrodes. The laser marked aluminium electrode had typically 3.5 times higher surface roughness value than those unmarked.

Table 4-3 Average surface roughness

Electrode	Surface roughness Ra (μm)
Planar brass	0.5
Changs UFE	0.5
Aluminium (unmarked)	0.5
Marked Aluminium	1.8

4.5 Electrode holder

The electrode holder for each electrode was designed according to the discharge environment, discharge enclosure, the electrode size and the mechanical mechanism of securing the preionisation system. The main feature of the holder besides mounting the anode and cathode was also to facilitate the high voltage electrical connections. The electrode holder can be fabricated from metal such as copper or brass and also dielectric material such as teflon, tufnol or acrylic. The electrical connection was directly applied to the holder if the electrode holder was metallic, however, for a dielectric electrode holder, the electrical connection was via metallic inserts or screws.

With the metal electrode holder, screws were used to firmly secure the electrodes. A strong mechanical connection was vital to avoid arcing or unpredictable discharge breakdown. For the dielectric holder, plastic or resin glue was used to hold the electrode in place in order to eliminate screw holes that were found to induce arcs because they deformed the electrode.

When using the dielectric material as the electrode holder, it was also important to create enough spacing or recess around the electrode to avoid arcing due to the development of the space charges in that vicinity. It was better if the electrodes protruded from the holder, however it still depended on the system's design.

The electrode holders used in this research were individually designed to meet the prototype design and experimental requirements. **Figure 4-19** shows the first holder used with the planar brass electrode. **Figure 4-20 to Figure 4-23** show the holders used for mounting the compact Chang profile, the unmarked and marked aluminium electrodes. Brief descriptions for these holders are given below:

Figure 4-20 shows the PTFE anode and cathode holder for the electrode mounted on the x-y-z table. The travel for the x-y-z holder was 5mm for each respective direction. The cathode was mounted at the bottom as a movable electrode with travel in the z and -z

direction (up and down). The movement of the cathode was controlled from outside of the discharge chamber by using a commercially available adjustable vacuum feed-through mechanism (NC, NOR-CAL, model PRM 133, USA) in vertical (Z) direction. The feed-through mechanism was attached to the thimble of the micrometer that travelled in the Z direction. Each turn of the thimble produced ~0.5 mm of travel. This mechanism operation is illustrated in **Figure 4-21 (a) and (b)** show the developed vacuum feed trough system.

Figure 4-22 shows the compact dome electrode holder. The electrode was mounted to the holder by using two screws in a symmetrical position. The electrode gap was fixed at 5 mm and the electrode holders were inserted into parallel slots on ABS flanges.

Figure 4-23 shows a long tube electrode holder that was rapid prototype from ABS. The electrode was mounted with glue and the gap between the electrodes was varied by varying the thickness of the electrode holders. The holders were clipped to the tube and it was self-secured. The air sample flow was exposed for a longer time to the discharge in this prototype arrangement (as illustrated in Figure 4-14 (b)).

4.6 Scanning electron microscope (SEM) for electrodes surface analysis

The SEM (FEI Quanta 200F) was used to visually analyse the surface of the electrodes. The purpose of the analysis was to study the laser marked electrode surface roughness effect on the glow discharge voltages and currents and compared with the unmarked aluminium electrode which were discussed in Chapter 5. The scan speed determined the electrode's surface morphology as shown in **Figure 4-24**. The aluminium flat surface was polished and divided into three zones, A the unmarked, B marked at a laser scanning of 10 mm/s and C the 50 mm/s the laser marked scan speed. SEM images at 500x magnification clearly show the peaks and valleys of the aluminium electrode surface. The scale is shown at the bottom right in each SEM graph. As predicted 50 mm/s laser marked scan speed had an evenly distributed surface morphology compared to the 10

mm/s. The latter had clearly visible and wider valleys. Although the 50 mm/s scan speed provided an even morphology, there is essential to investigate regarding the brass and aluminium electrode differences. After the laser marked (50 mm/s) brass and aluminium sample were compared to investigate the morphology differences (**Figure 4-25**) that may alter the discharge characteristics. In these comparisons, qualitatively, brass had a bigger grain size with deeper valleys (dark spot) than aluminium. The smaller grain size of aluminium shows that it is easily to control its peak and valley in laser marked.

4.6.1 Energy dispersive X-ray (EDAX) analysis on electrodes

The EDAX analysis on the electrode was done to investigate the condition of the electrode's surface after laser marking at different scan speeds. The scan speeds that were used were 10 and 50 mm/s. **Figure 4-26** shows that the heat from the scan increased the oxidation on the electrode surface. The oxidation for 50 mm/s was 26.75 % (**Figure 4-26(a)**) while for 10 mm/s it was 41.18% (**Figure 4-26(b)**). The oxidation for brass and aluminium at 50 mm/s were also compared, as shown in **Figure 4-27**. This comparison showed that at the same scan speed of 50 mm/s, the aluminium oxidation was 26.75 % and the brass was 10.76 %.

4.7 Conclusions

One of the research aims was to fabricate electrodes that could be used in atmospheric air discharges, the electrodes developed here in successfully achieved this aim. A further aim of this work was to produce low cost aluminium electrodes, manufactured in house with a potential towards future, cost-effective commercialisation. The mounting of the electrode is important to achieve a stable discharge by avoiding charge build-up that affects the life-time of the electrodes and discharge stability. This was done by protruding the electrodes, building a recess around the flat electrodes or by avoiding the

use of holes in the dielectric electrode holders. It was also found that very smooth surface electrode ($R_a < 1 \mu\text{m}$) such as the Chang UFE were quite easy to produce by hand polishing and removing any contaminants with iso-propanol. From the SEM analysis, aluminium was the most suitable electrode material used to generate the cold plasma discharge.

Table 4-2 Electrode definition and dimensions used referred from [Trtica *et. al*, 2003]

Electrode type	Width (mm)	Length (mm)	Thickness (mm)	$2x_m$ (mm)	$2y_o$ (mm)	l_{eff} (mm)	Cs (mm ²)	ADV (mm ³)
Planar Brass	10	60	6	9	3 to 7	59	27 - 63	1593 - 3717
Chang UFE	10	60	6	9	3-5	59	27 - 45	1593 - 2655
Aluminium	30	200	4	28	2-6	198	56 - 168	11088 - 33264
Marked Aluminium	30	200	4	28	2-6	198	56 - 168	11088 - 33264

Width = width of electrode base

Length = length of electrode base

Thickness = thickness of electrode

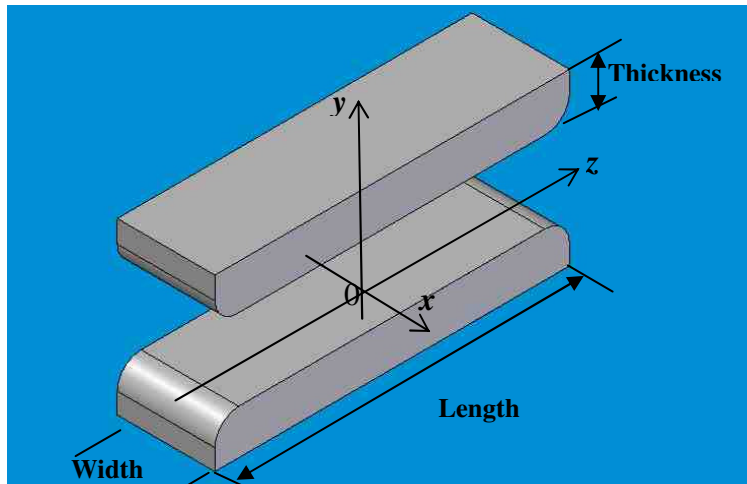
$2x_m$ = electrode flat surface dimension (in x direction)

$2y_o$ = electrode gap (in y direction)

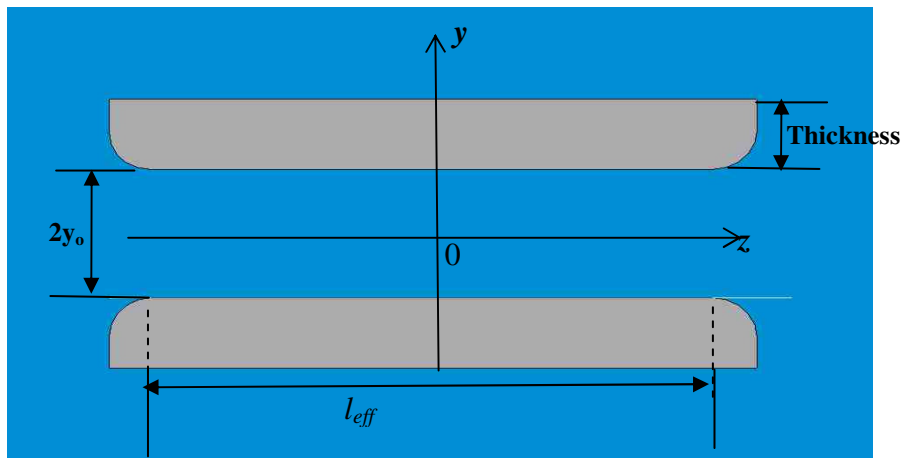
l_{eff} = discharge effective length (electrode flat surface length)

Cs = cross section (cs= $2x_m \cdot 2y_o$)

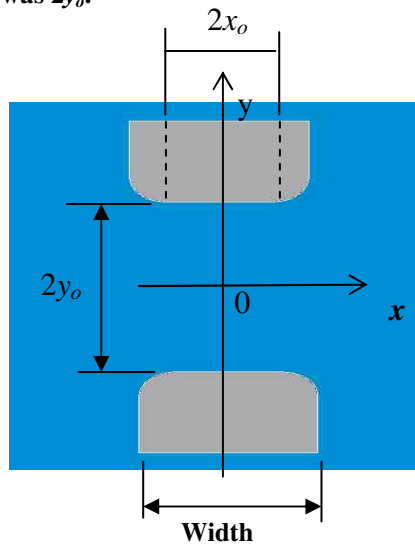
ADV = active discharge volume



(a) Three dimensional view of a pair of electrodes and the general axis of orientation, (x,y,z) .



(b) The view of axis $x=0$ with the electrode definitions. Effective length was l_{eff} and the distance between the electrodes was $2y_o$.



(c) The view of $x-y$ plane ($z=0$), the flat surface width is $2x_o$.

Figure 4-1 Electrodes attributes [Trtica *et. al*, 2003].

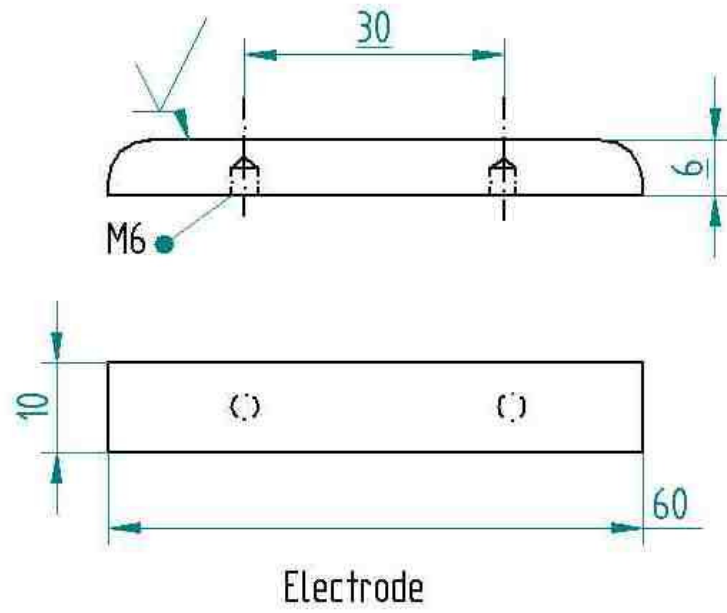
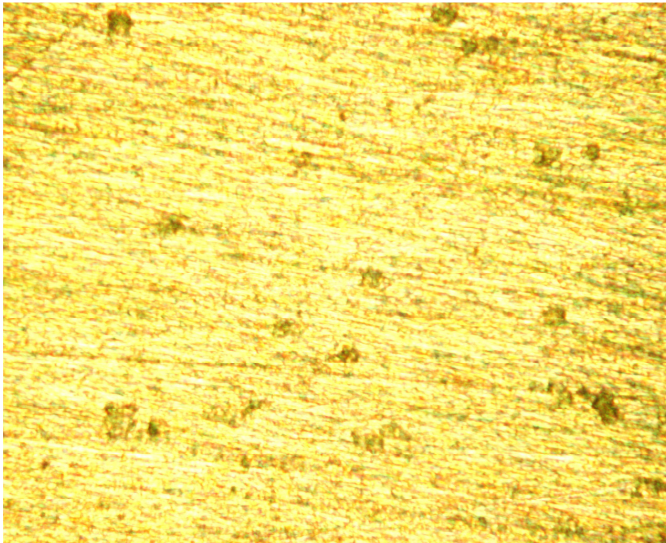


Figure 4-2 CAD drawing of planar brass electrode profile.



(a) Before



b) After

Figure 4-3 (a) Planar brass electrode machined surface with HSS end mill cutter average $32 \mu\text{m Ra}$, (b) Polished surface with average $0.5 \mu\text{m Ra}$.



(a) Top view

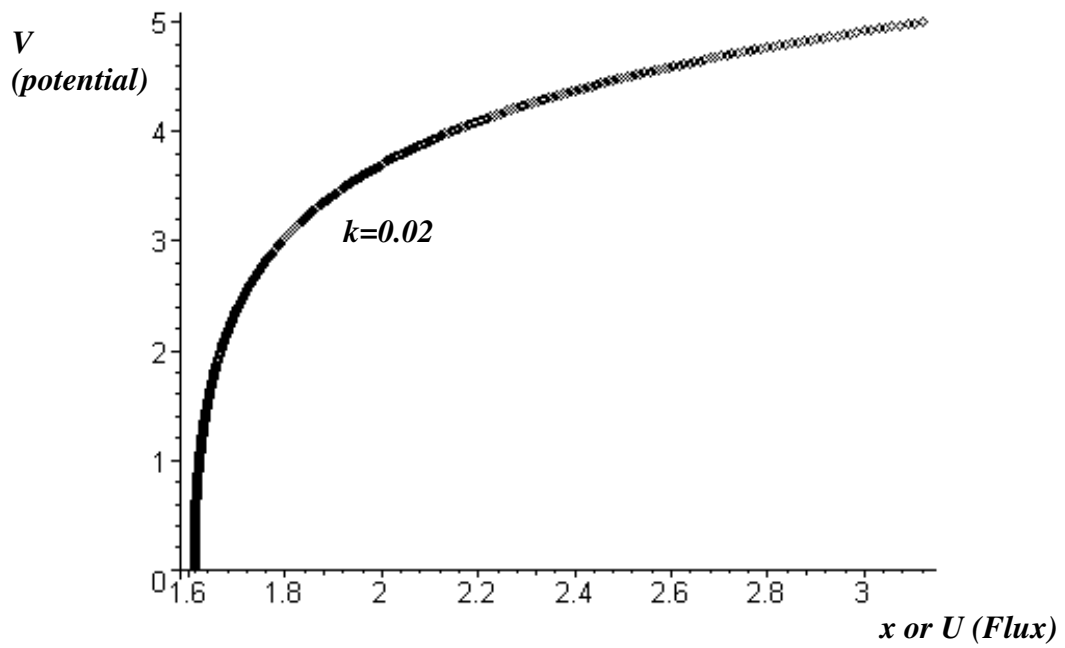


(b) Side view

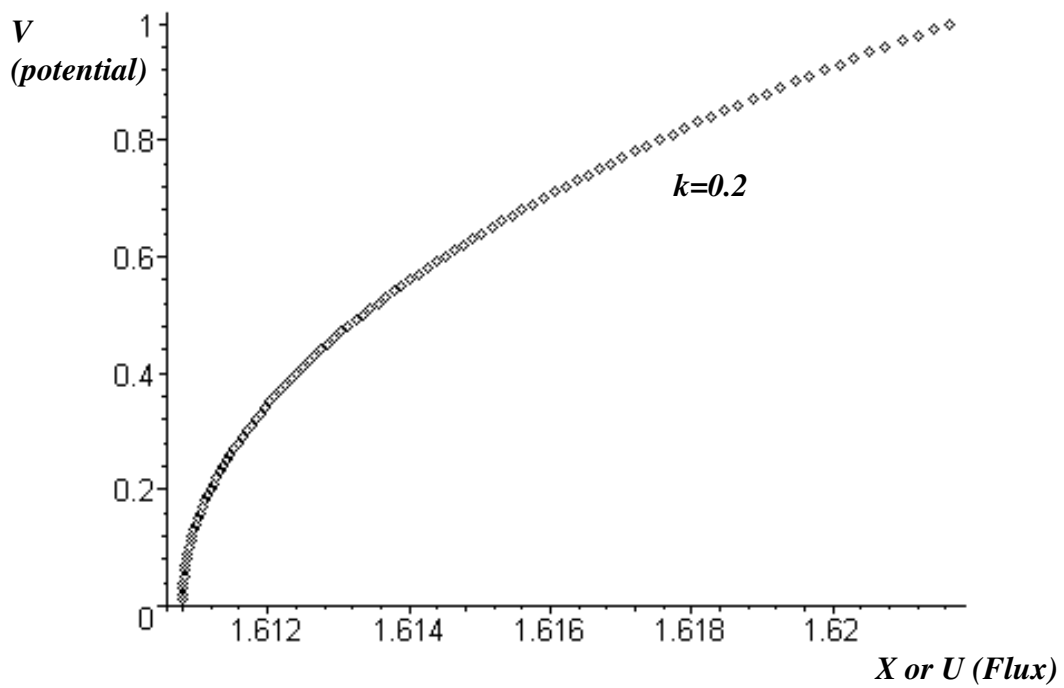


(c) Electrode mounting holes

Figure 4-4 Planar brass electrode (a) Top view with 10 mm width and 60 mm length (b) Side view with 6 mm thickness. (c) Two screw holes to mount the electrodes to holders.

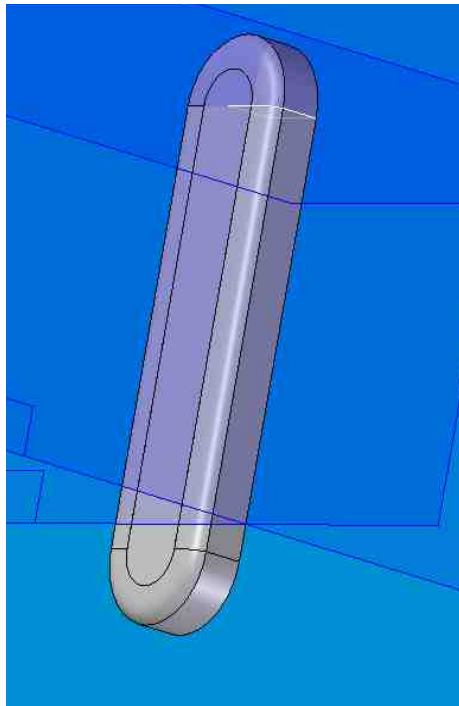


(a) Chang's curve function for $k=0.02$

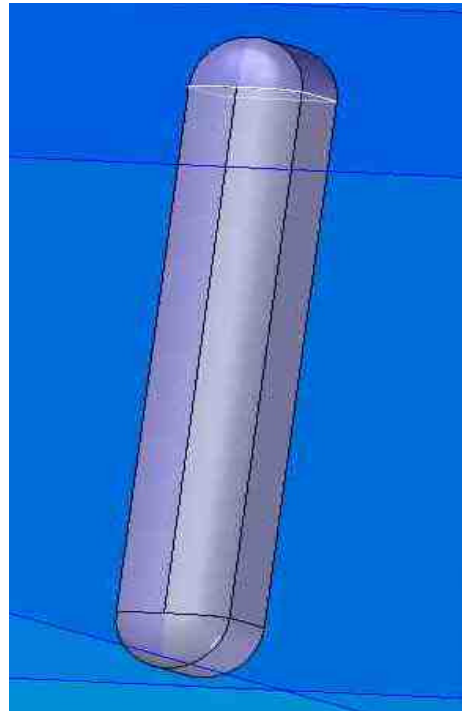


(b) Chang's curve function for $k=0.2$

Figure 4-5 Chang function curves generated in Maple software.

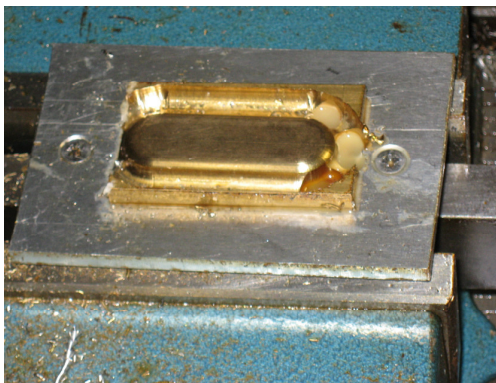


(a) $k=0.02$



(b) $k=0.2$

Figure 4-6 Chang's electrode CAD three dimensional parts drawing.



(a) Chang electrode for $k=0.02$ on fixture



(b) More compact Chang electrode for $k=0.2$ on fixture .

Figure 4-7 Fixture for the machining of Chang UFE in CNC machine.

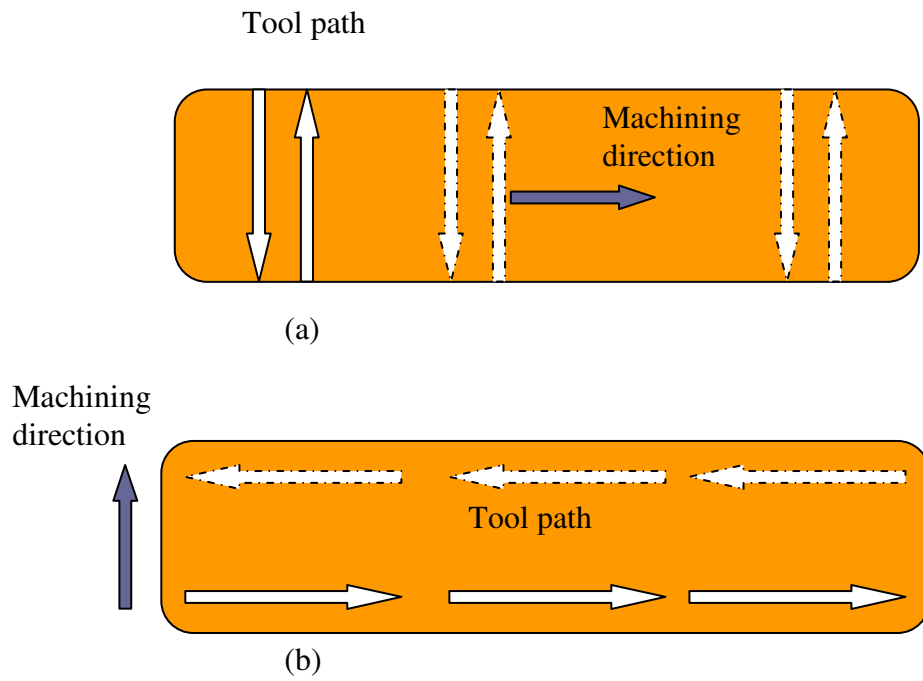
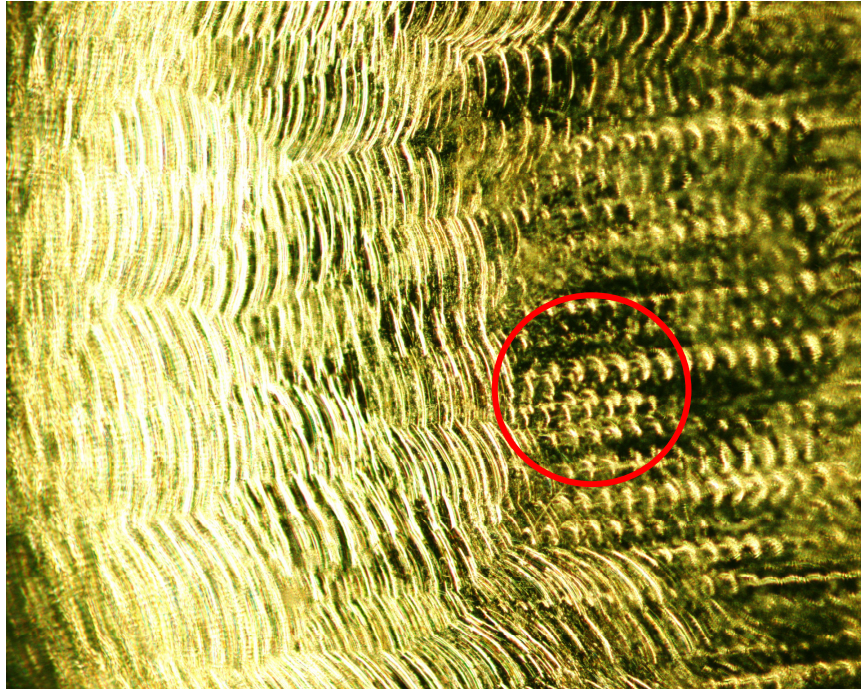


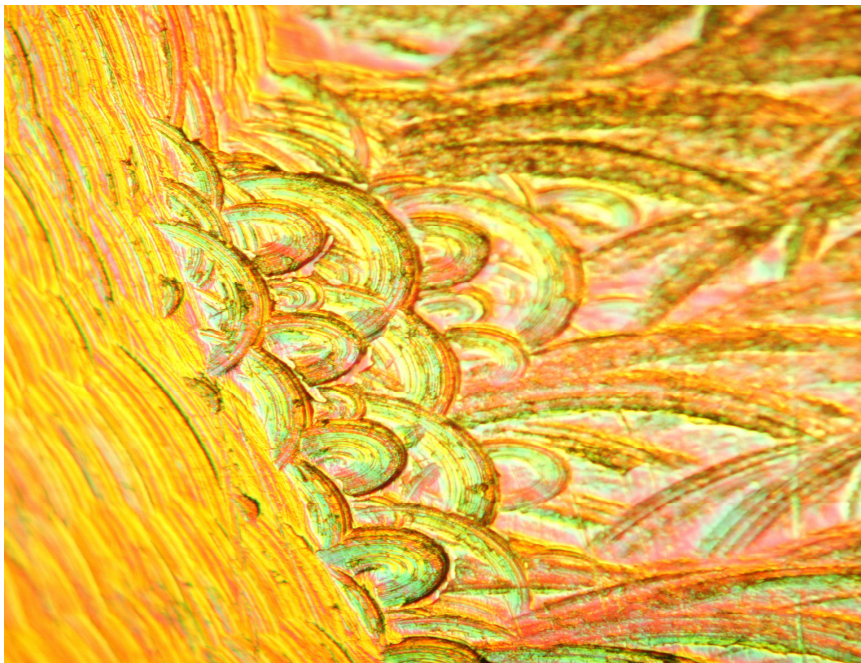
Figure 4-8 Machining tool path and orientation.



Figure 4-9 Machining of Chang's profile electrode with new set up fixture that reduced the machining time to 30 minutes.

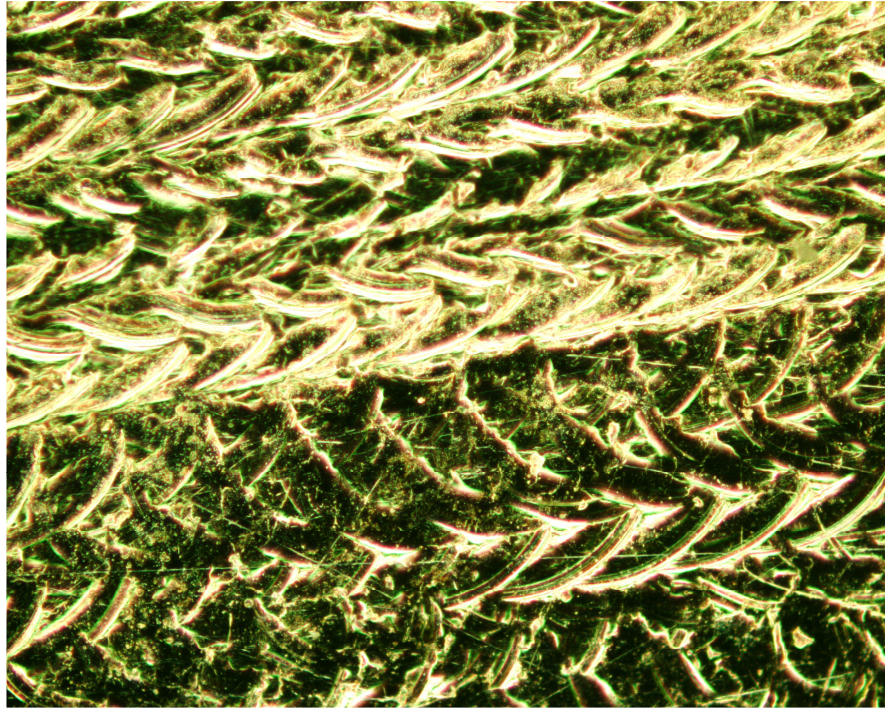


(a) Machine marks on Chang profile (right) at 5x magnification

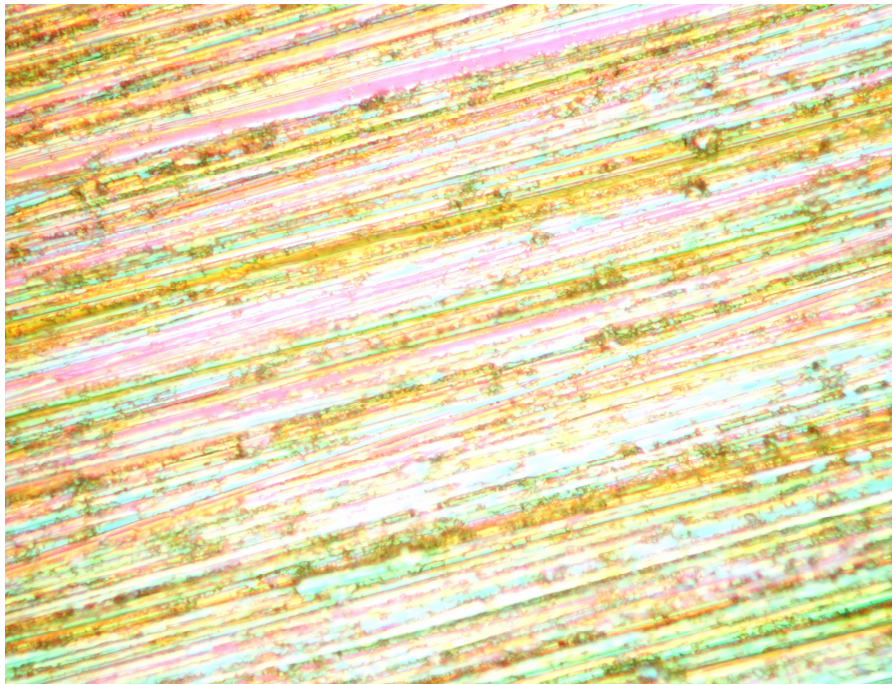


(b) Close up view of red circle on Chang's profile at 10x magnification.

Figure 4-10 Machined surface texture on Chang's profile electrode machined using tungsten carbide tool.



(a) Machined marks on the flat surface of Chang's electrode at 10x magnification



(b) Polished electrode surface.

Figure 4-101 (a) Machine marks by carbide tool with average surface roughness of $26 \mu\text{m Ra}$.
(b) Polished surface of Changs electrode. Different colours show the different flatness. Average surface flatness was $0.5 \mu\text{m Ra}$.



Figure 4-12 Compact Chang's profile electrode

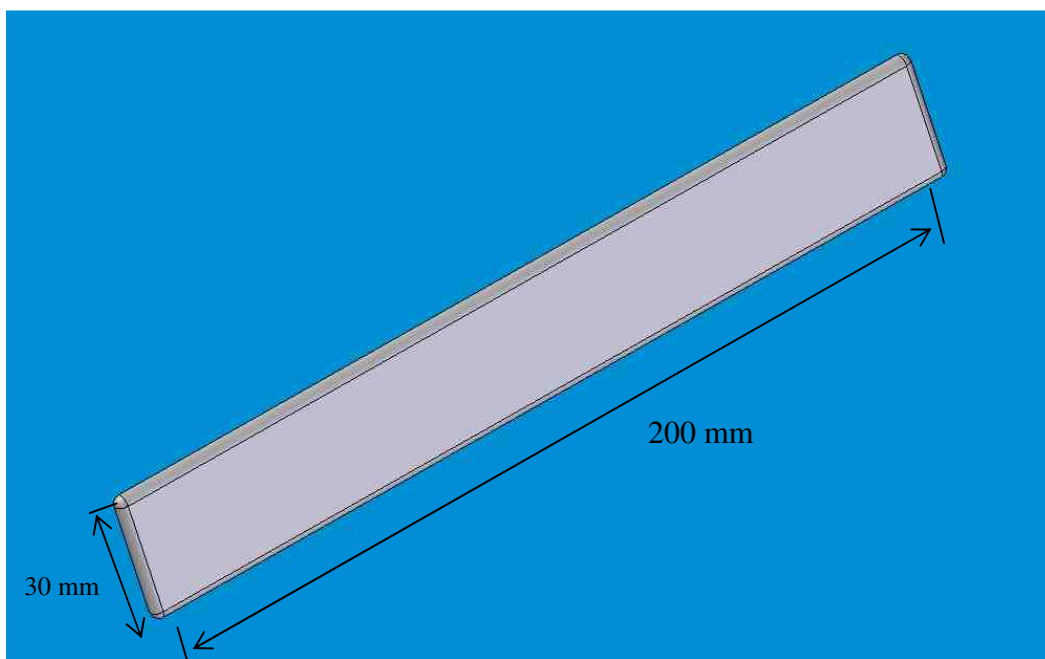
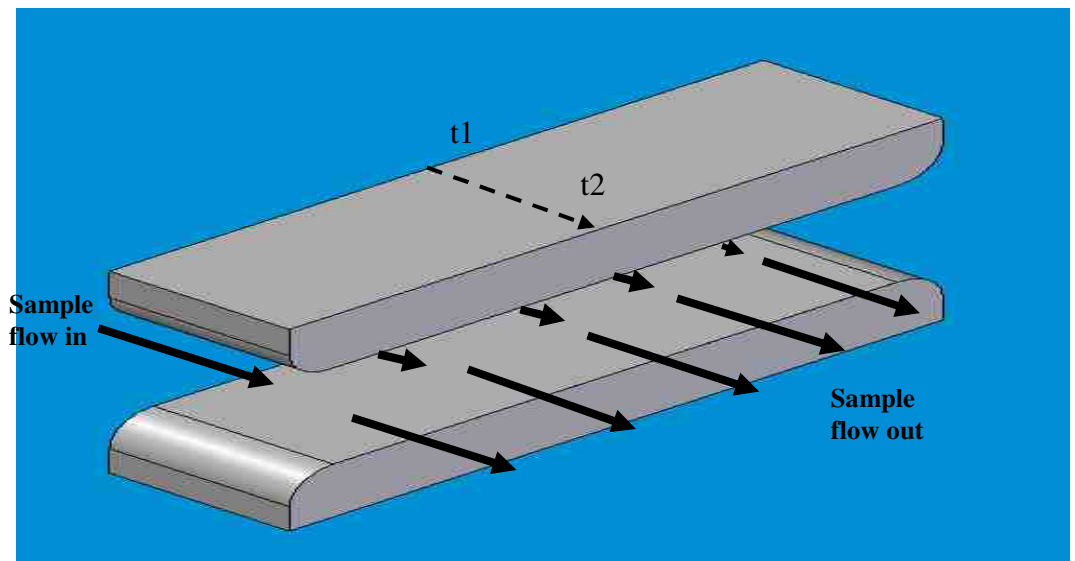
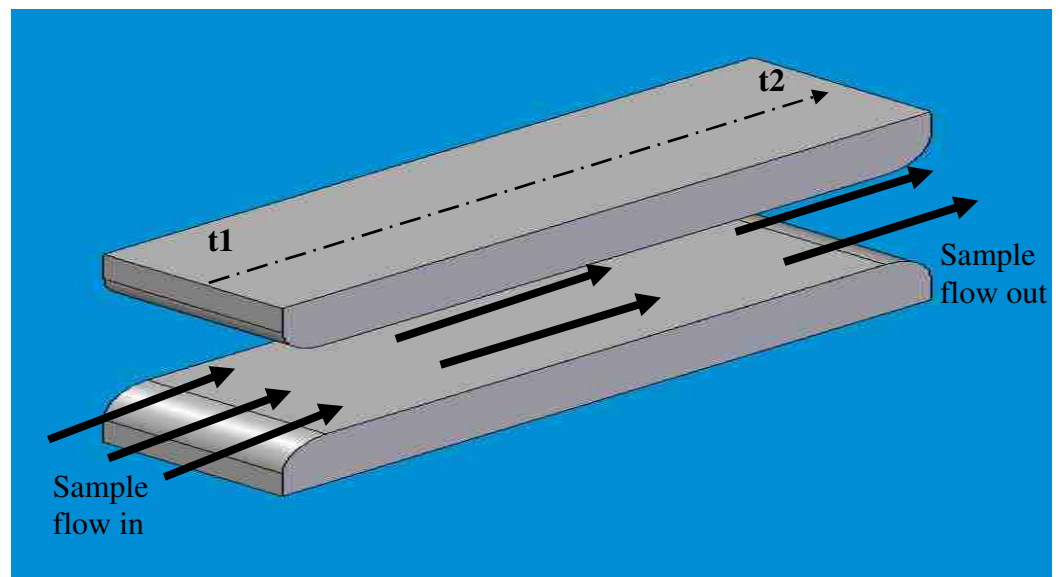


Figure 4-13 Aluminium electrode profile



(a) The sample flow transverse to the electrode discharge for maximum volume through-put.



(b) The sample flow longitudinally to the discharge for maximum exposure time.

Figure 4-14 Flow of air sample through the aluminium electrode discharge.



Figure 4-15 Polished aluminium electrode.

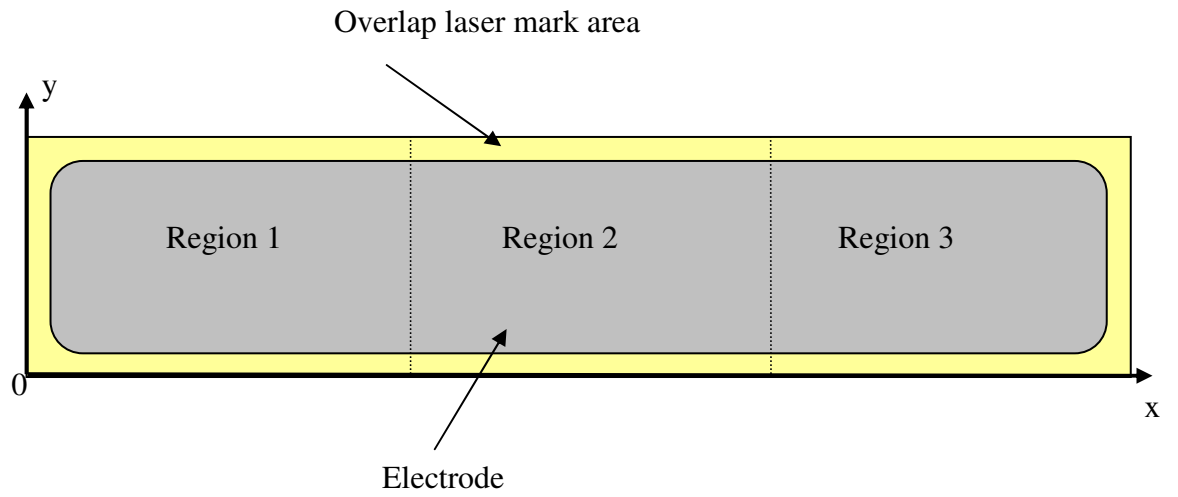


Figure 4-16 Laser marking layout using regional method.



Figure 4-17 Laser marking process.



Figure 4-18 Finished laser marked aluminium electrode.

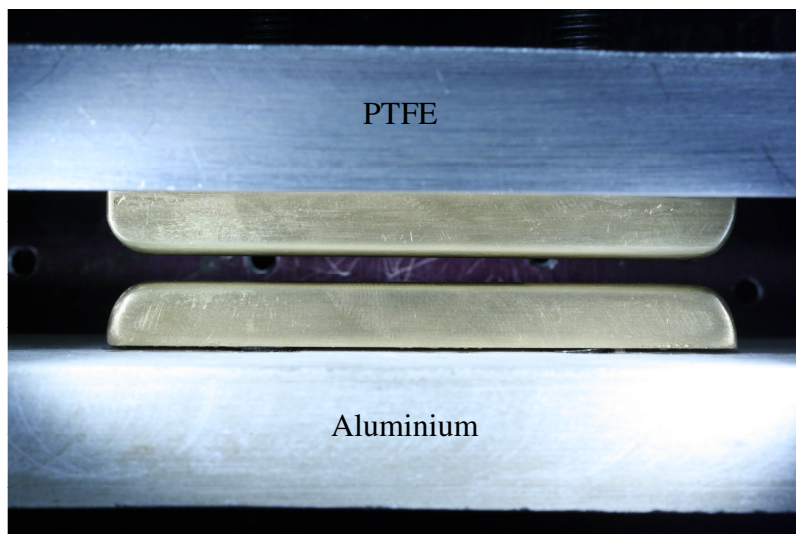


Figure 4-19 Aluminium bracket and PTFE plate holder of the first electrode holders designed in the research.

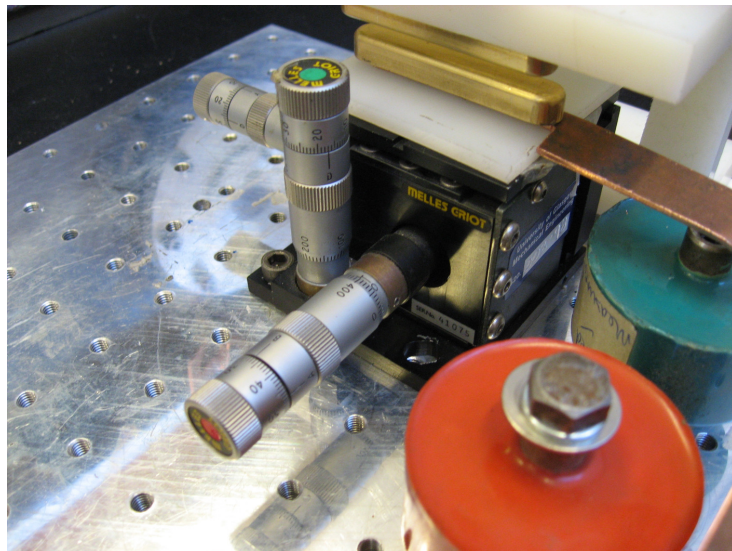
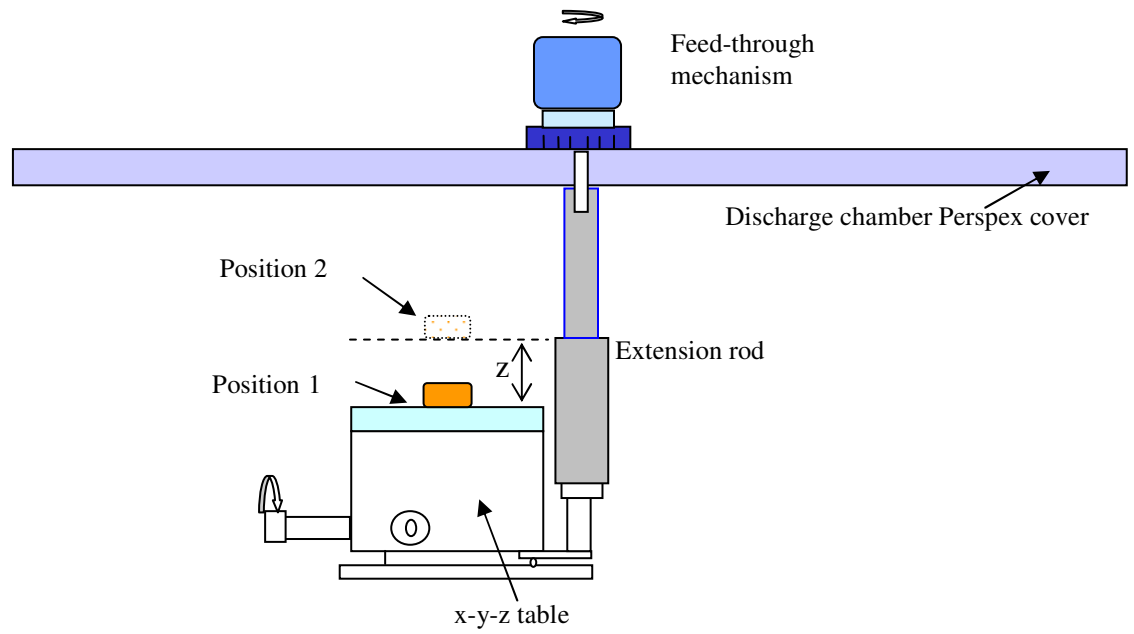
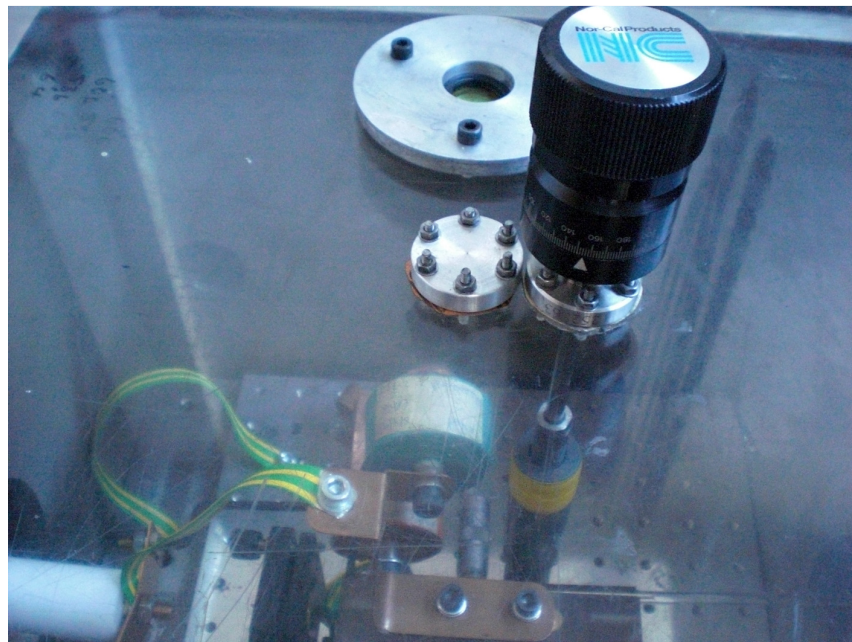


Figure 4-20 Adjustable x-y-z table electrode holder.



(a) Illustration of the vacuum feed-through mechanism concept



(b) Developed vacuum feed-through mechanism

Figure 4-21 Vacuum feed-through mechanism.

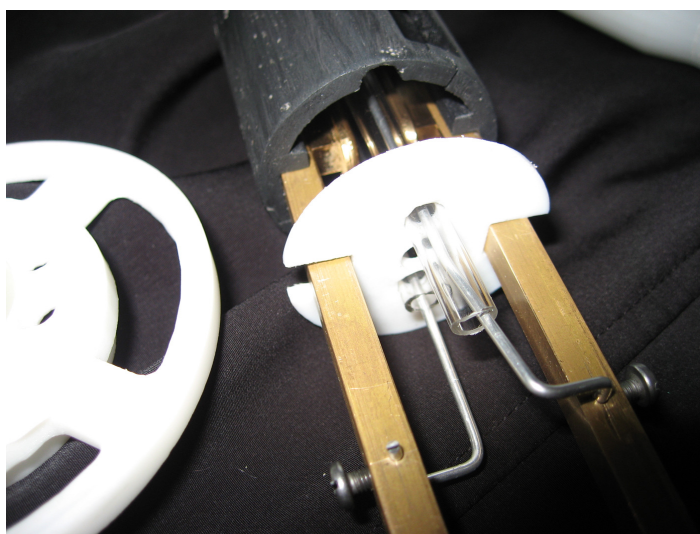


Figure 4-22 Electrode holders for the Dome discharge with preionisers.



Figure 4-23 Clip-on aluminium electrode holder for maximum discharge exposure time.

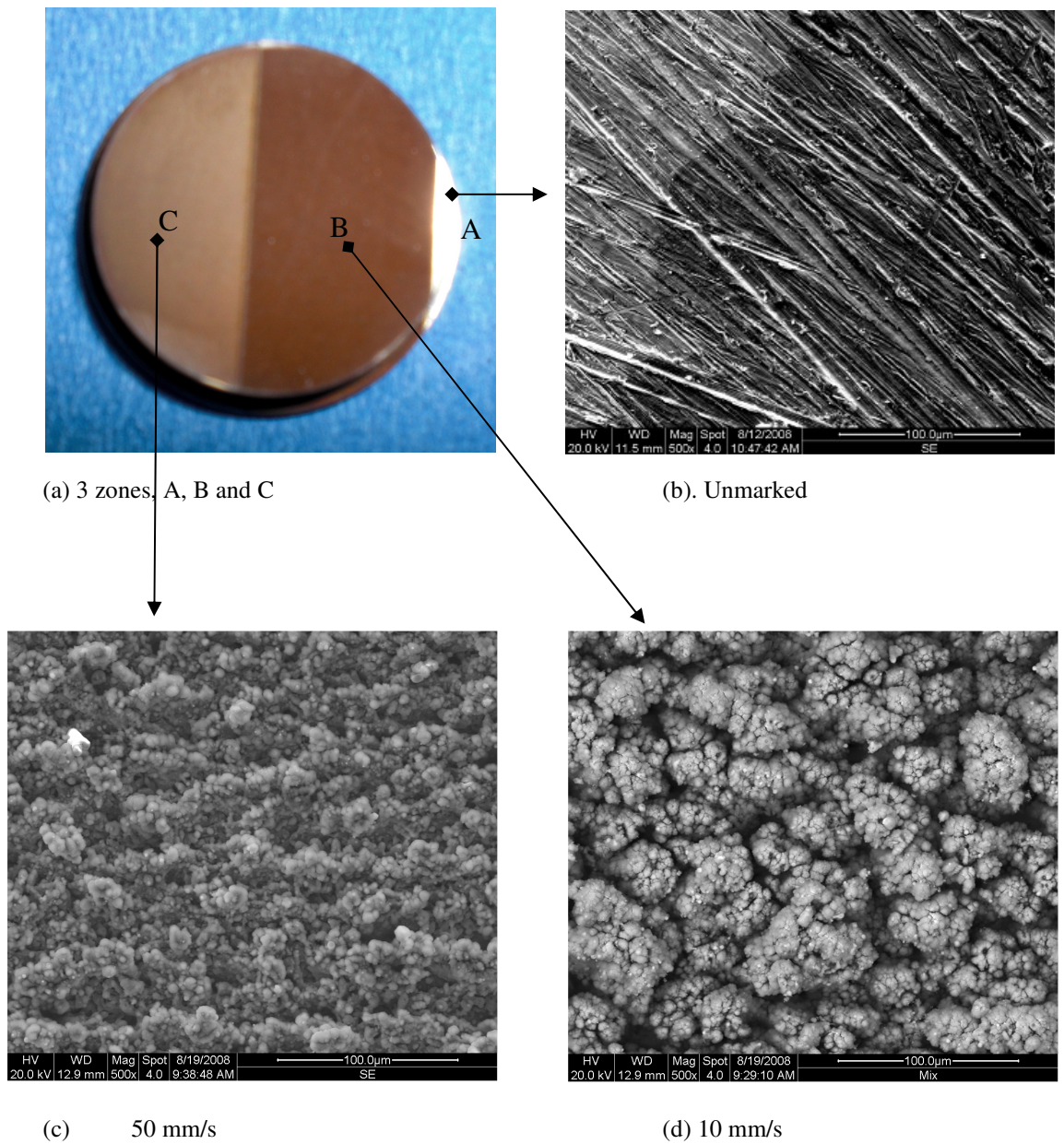
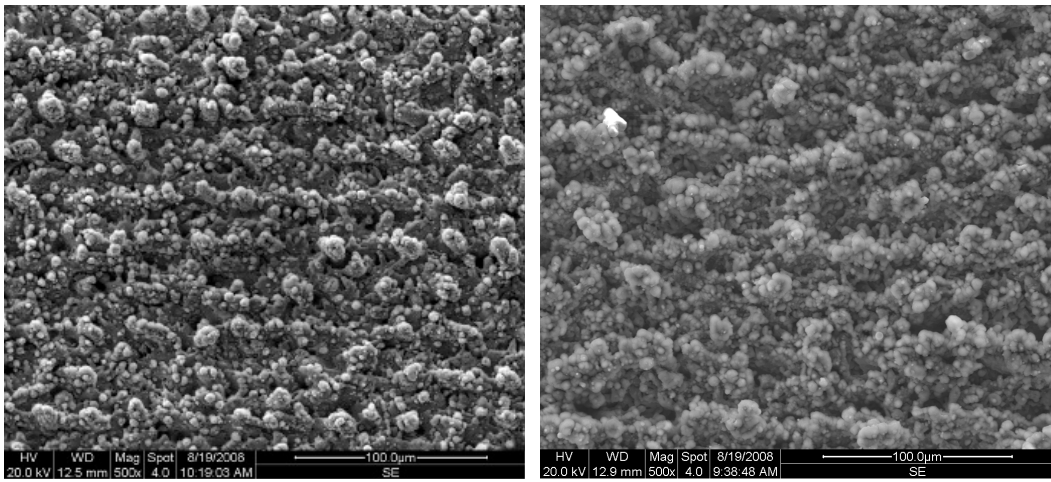


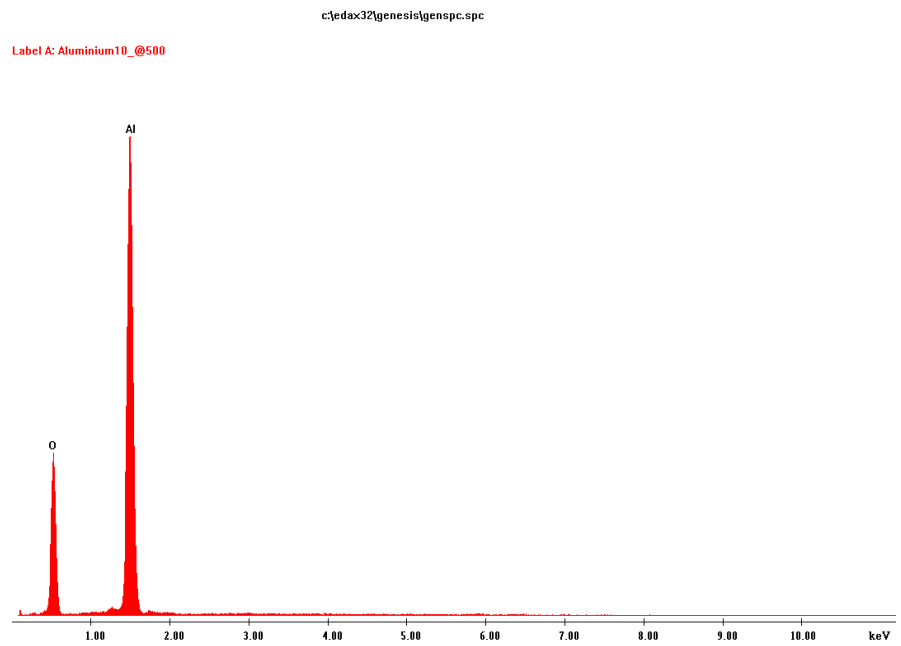
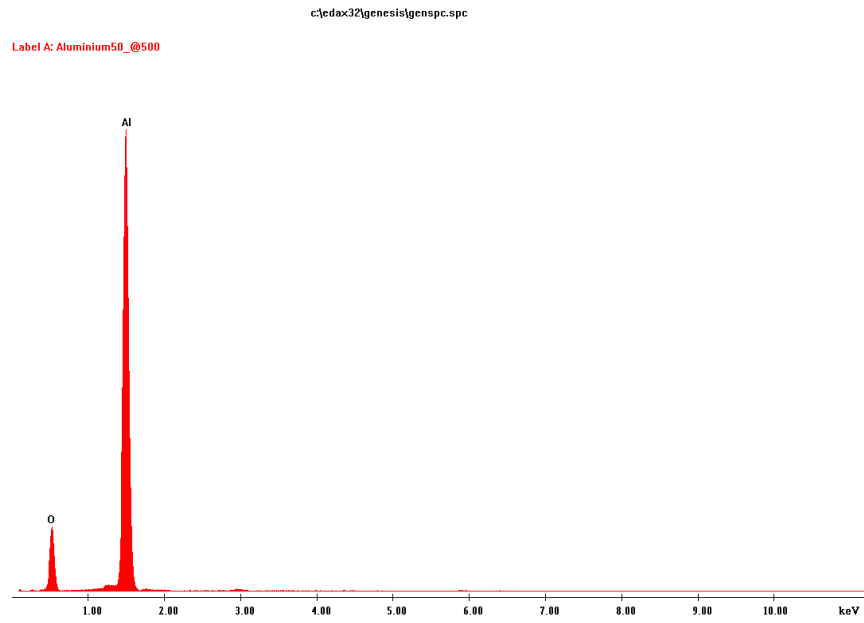
Figure 4-24 SEM electrode surface analysis: (a) Aluminium electrode with 3 zones A, B and C, (b) Zone A the unmarked electrode surface, (c) Zone C with 50mm/s laser marked scan speed and (d) Zone B with 10 mm/s laser scan speed.



(a) Brass 50 mm/s

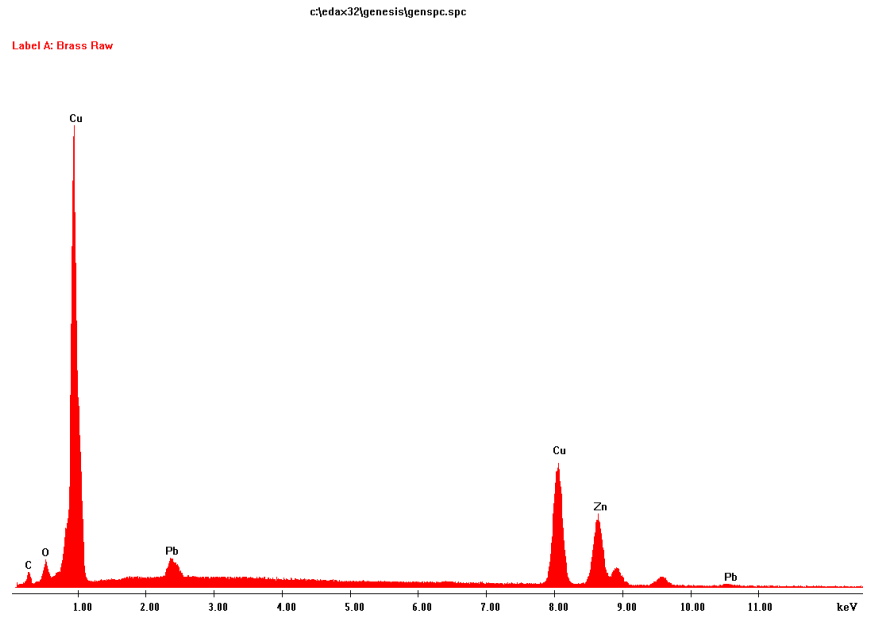
(b) Aluminium 50 mm/s

Figure 4-25 Comparison of brass and aluminium laser marked surface at scan speed of 50 mm/s.

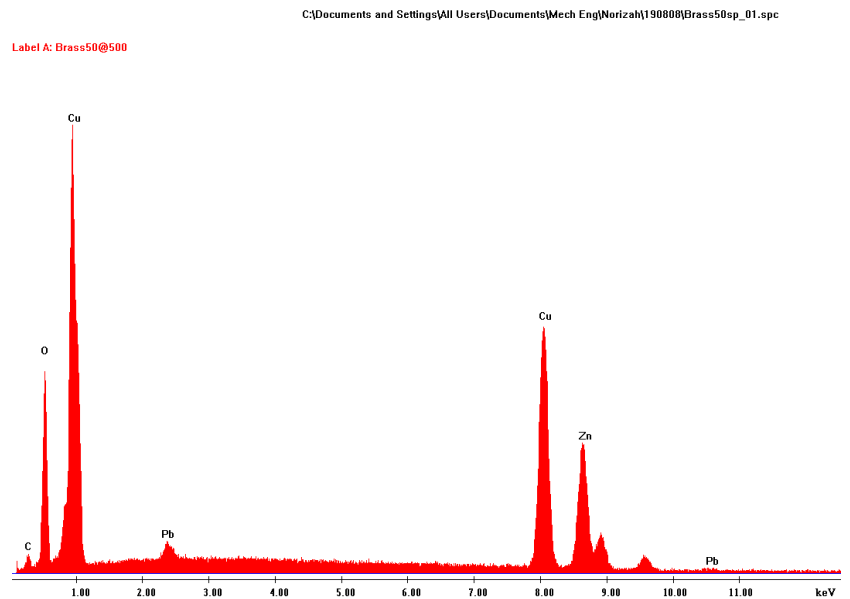


(b) 10 mm/s scan speed.

Figure 4-26 EDAX for laser marked aluminium electrodes at different scan speeds.



(a) Unmarked brass



(b) Marked brass at 50 mm/s scan speed

Figure 4-27 EDAX analysis on unmarked and marked brass electrodes.

Chapter 5

Air Treatment Using Plasma Discharge

5.1 Introduction

The work developing the AC discharge in air at atmospheric pressure, described in previous chapters, led to the prototypes of the Dome and Tubular air decontamination systems. The plasma was used to decontaminate air alone or air seeded with micro-organisms that flowed through the discharge systems. The ozone produced from the plasma discharge was measured using an ozone detector.

Before the Dome and Tubular prototypes were tested, experiments were done on the stand alone discharge with the Chang profiled electrode and the trigger wire preionisation as shown in **Figure 5-1** (see section 5.5.1) This proved a useful test bed to optimise the electrodes within the Dome. Bacterial experiments were done to investigate the effect of the emission from the discharge on E.coli lawned on nutrient agar plates.

The Dome discharge system (see section 5.2) was a compact prototype testbed to investigate the effect of the plasma on microorganism, these experiments were followed by decontamination experiments on the Tubular discharge (see section 5.3) system where the discharge volume was 10 times that of the Dome. The Tubular discharge was used for decontamination and ozone measurements with various capacitances. Both systems were seeded with *Bacillus globigii* (BG) and their performances were compared by the percentage of killed microorganisms. The discussion of the microorganism preparation is discussed in detail in section 5.4. These discharge systems were used along with a portable aerosol generator (DOP Solution, UK) which was used to generate the seeded air flow which was passed through the electrodes via the inlet through the plasma discharge.

It is important to note that some of the prototypes developed and the experimental results that are reported herein were done in conjunction with Takashi Mine (PhD thesis to be published, LOSEC, University of Glasgow). Some of the research

was done as a group with some work overlapping. The next sections discuss the plasma and ozone generation by using the different electrode systems.

5.2 Dome discharge system

The Dome discharge was a prototype air decontamination system manufactured by a rapid prototyping technique using ABS material [Dan McNulty Personal Communication, 2008]. **Figure 5-2 (a) and (b)** show the CAD drawing and a photograph of the discharge. This was a compact discharge system using the Chang uniform field electrodes (which was also used in the stand alone discharge) where the active discharge volume (ADV) was $\sim 1350 \text{ mm}^3$. The discharge circuit utilised a pair of 2.7 nF capacitors as shown in **Figure 5-2 (c)** with the 20 kV TEC transformer (see Chapter 3, Figure 3-39 (a)). The Dome discharge experimental set-up is discussed in section 5.4.3

5.3 Tubular discharge system

The Tubular discharge was a prototype manufactured by rapid prototyping technique using ABS material. **Figure 5-3 (a) and (b)** show the CAD drawing and a (c) shows a photograph of the tubular system. This system used the aluminium electrodes (marked or unmarked) with an active discharge volume (ADV) of $\sim 13.50 \times 10^3 \text{ mm}^3$. Four discharge circuits were used with the system to investigate the effects of varying the capacitance value on the microorganism killing performance and the ozone production measurements. The capacitances used were 1.4, 2.7, 5.4 and 8.1 nF. The discharge circuits are shown in **Figure 5-4 (a), (b), (c) and (d)** with the different combination of capacitances used.

5.4 The experimental protocol for *Bacillus globigii* (BG)

The experimental protocol for the BG decontamination was divided into two parts: the microorganism preparation and the microorganism experimental procedures.

5.4.1 The micro-organism preparation

All experimental apparatus were cleaned according to the cleaning protocol (refer to Takashi Mine PhD Thesis to be published, LOSEC, Glasgow University) before the BG samples were prepared. The preparation of the microorganisms allowed the required dilution to be obtained, to provide sufficient microorganisms in the seeded air, here it was 10^4 cfu/ml. **Figure 5-5** shows the technique used to prepare the BG dilution. The original BG neat stock was 10^{10} cfu/ml. The first step was to dilute 1 ml of the BG neat stock into 9 ml of sterilised distilled water (in container A) to make a 10 fold dilution. Secondly, 1 ml was taken from container A and diluted again with the 9 ml sterilised distilled water in container B, this was repeated twice to obtain the 10^{-4} dilution. The next step was to dilute 5 ml of the BG 10^{-4} BG stock with 500 ml sterilised distilled water to make 10^{-6} dilution. This BG dilution was used to fill the portable aerosol tank giving about 10^4 cfu/ml. Air from a compressed air supply was connected to the aerosol tank inlet nozzle. A regulator with an air filter was used to control the inlet air pressure which was set at 2 bar, and the outlet pressure on the aerosol generator was set to 1.5 bar.

5.4.2 The BG decontamination experiment procedures

Gelatine membrane filters (Sotorius, UK) were used to sample the air for each test, these were then pressed onto a nutrient agar petri-dish. Controls were taken in an identical manner where the plasma was not initiated. The sampling initially began with collecting the air sample over two minutes without the plasma discharge turned on to ensure good mixing within the aerosol generator. Secondly, this was followed by taking the control sample of the seeded air for two minutes. Thirdly, the test sample was done with the aerosol where the plasma and

the air sampler were turned on. This was repeated until the end of the experiment. Between each test with the plasma on, two minutes of clean, unseeded air was flushed into the discharge (i.e. before and after each flow test) to avoid incremental build up of contamination between experiments. The population of the colony forming units (cfu) after 48 hours incubation at 37 °C were counted for both plates (control and test samples) and the amount of killing was compared.

5.4.3 The BG decontamination experimental set-up

The experimental set-up of the Dome plasma discharge is shown in **Figure 5-6**. The discharge system was in a vertical position. Connections of the piping, the aerosol system, the air cleaning system, the air sampler (with gelatine membrane) and the HV discharge circuit system were done to ensure the air flow was secure and there was no leakage of organisms. The system integrity was examined before the experiments. The Tubular discharge experimental set-up was similar as with the dome system but in the tubular case the discharge system was positioned horizontally due to the electrical connections that were used. Aluminium electrodes (marked or unmarked) were used in the experiments for the tubular geometry.

5.5 Effect of plasma on microorganism decontamination

The effect of the discharge and ozone production on *E. coli* and BG spores were investigated for the different types of electrodes used: the stand alone UFE Chang profiled electrode with trigger wire preionisation, UFE Chang profiled electrodes with dielectric material and aluminium marked and unmarked flat electrodes.

5.5.1 Stand alone UFE Chang discharge with trigger wire preionisation

The stand alone discharge system with trigger wire preionisation and 2.7 nF capacitors was used as a test bed and the results from this successfully demonstrated the biocidal nature of the discharge emissions. The stand alone

electrode system was operated for 1 to 10 minutes continuously in air at a discharge voltage of between 5.5 to 6.2 kV. The electrode gap was 2.5 mm and a nutrient agar petri-dish, seeded with *E. coli* was placed 8 cm from the discharge. **Figure 5-7 (a and b)** show the control agar nutrient petri-dish exposed to the discharge with **(a)** no *E. coli*. and **(b)** with *E. coli*. After a 1 minute exposure to the plasma discharge at 5.5 kV, there was some effect on the *E. coli* (**Figure 5-7 (c)**), where a shadow can just be seen across the left half of the plate. **Figure 5-7 (d and e)** show the lawned plate after 2 and 3 minutes exposure respectively, with similar effect. When the exposure time to the discharge was increased to 10 minutes, there was substantially more clearing of *E. coli* as seen in **Figure 5-7 (f)**.

The above results show that the air plasma discharges were able to kill the *E. coli* inoculated on an agar substrate. In this test, the volume of the discharge chamber was large compared to the active plasma discharge volume, the ozone produced by the plasma was not controlled in terms of the flow and the volume, thus the time to kill the micro organisms was relatively long or the effect of the radiation for the discharge was relatively low. To enable control of the plasma discharge and ozone, the plasma discharge was generated in a compact Dome system with longitudinal air flow through the electrodes. To optimize the discharge stability and the ozone production, dielectric layers were placed between the electrodes to provide uniform preionisation.

5.5.2 Dome plasma discharge effect on BG with dielectric material

The Dome discharge experimental set-up was shown earlier in section 5.4.3. A T-piece connector was used to connect the blower (air velocity of 53ms^{-1}) and the aerosol generator (aerosol velocity of 4.6ms^{-1}). The air velocity measured at the Dome outlet was 6ms^{-1} and the final air velocity as measured near the agar plate and gelatine membrane was $\sim 0.5\text{ms}^{-1}$. The micro-organisms flow longitudinally through the electrodes.

Uniform glow discharges were achieved when the input voltage reached 9 kV with two layers of duralar over the cathode and with trigger wire preionisation,

Figure 5-8. The electrode gap was set at 2.5 mm. Spectral measurement (**Figure 5-9**) of the discharge was done using Stellar Net SpectraWiz® spectrometer. A small peak in the spectral output (40 a.u) was seen at 327 nm. The spectral output increased from about 400 nm up to 670 nm, with various other peaks occurring at 475, 510 and 575 nm. The greatest peak was 110 a.u at 525 nm.

The BG seeded air was passed through the plasma for 2 minutes. An air flush of 20 l/min was done, as before, after the experiment to ensure that no contaminants remained in the system.

5.5.2.1 Results of the Dome discharge decontamination

Figure 5-10 shows the results from the first experiment of the decontamination of the BG seeded air with the UFE Chang profiled electrodes, 9kV input voltage in the Dome system with 1.4 nF coupling capacitances. An air flush of 2 minutes was done at the start and the end of the experiment, and in between each test. The results from the overnight incubation of the gelatine membrane petri-dishes showed that the air was decontaminated. The samples A to J show the cfus before and after the 9kV, 2 minutes cold plasma treatment. The minimum BG killed was 0% (Sample G) and the maximum was 100% (Sample J). The average of the killing in this first experiment was 68.4%. The population of the BG cfu for sample F to J before the plasma treatment were very few compared to samples A to E. This difference may be due to the micro-organisms in the aerosol tank degrading over time or maybe some back flow of ozone killed them or affected their resistance during the experiment.

To investigate the systems decontamination efficiency further, a second experiment with the same parameters was conducted. **Figure 5-11** shows the results of the BG decontamination with an average killing of 64.0%. From the first and second experimental results of the Dome system with Chang profiled electrodes with the dielectric layers, the average killing was ~63% (**Figure 5-12**). Considering the electrodes length was only 60 mm and the aerosol seeded air flow

rate of 20 l/min, the system was capable of achieving decontamination >50% killing. This was an interesting outcome, since the discharge volume was considered very compact (1350 mm³) the amount of killing was thought acceptable and quite high, especially considering that the air BG seeded inlet velocity was 4.6 ms⁻¹ and the length of the Chang electrodes were 60 mm (60 x 10⁻³ m), and the time (t) for each particle exposed to the plasma discharge was approximately 13 ms. The BG average kill may be increased by a longer exposure time (t) to the plasma; this can be achieved by reducing the velocity or increasing the electrodes' length.

Figure 5-13(a) show the BG decontamination when passed through the Chang profiled discharge in the Dome system at intervals of 2, 3, 4 and 5 minutes and 9 kV input voltage. It was interesting to find that for the 2 minutes plasma discharge treatment, the cfu killing was highest at 51% and it was lowest for the 5 minutes of treatment at only 5% (**Figure 5-13(b)**). This is probably due to the plasma discharge not having sufficient time to kill the microorganism because of the short path length (~60 mm). Baroch *et al* [2006] found the reduction of *E. coli* and *Staphylococcus aureus* (living on the skin or in the nose of a healthy person) reduced with increased plasma treatment time. Consequently, longer electrodes were fabricated for testing in the Tubular decontamination rig.

5.5.3 Tubular discharge with aluminium electrodes air plasma discharge with dielectric material

The following plasma treatment on BG seeded air was performed using flat aluminium electrodes that were either laser marked or unmarked. The electrode size was 30 x 200 mm which is 10 times that of the Chang profiled area. These electrodes were fitted into a new design, the so called Tubular discharge system. The new set-up provided a longer exposure time. The dilution of the BG was the same as that used in the Dome system with the Chang profiled discharge.

The schematic experimental set-up for the Tubular discharge system is shown in **Figure 5-14**. The Tubular discharge was connected directly to the inlet of the air flow tubing and the outlet to the sample collection plate. This was to optimise the sample air flow before and after the plasma treatment was done. The air flow rate was 50 l/min. The Tubular discharge design allowed the electrodes gap to be easily varied. This was done by varying the thickness of the electrode holder (**Figure 5-15 (a)**). Two layers of duralar were placed over the cathode. The electrode was glued to the electrode holder, and the electrode holders were clipped to the Tubular discharge (**Figure 5-15 (b)**), and it was inserted into the clear plastic tube to firmly hold the electrical connections. The plastic tube also secured the air flow connections in place. An air flush was performed at the start and at the end of each experiment cycle. The aluminium electrodes used were either both unmarked or just one electrode was laser marked. Discussions of the results are given in the sections below.

5.5.3.1 Aluminium unmarked electrode plasma

The results of the BG population counts after flowing air through the plasma for 2 minutes with input voltages of 7.5 and 9 kV, and an air flow rate of 50 l/min with both unmarked aluminium electrodes are shown in **Figure 5-16**. The average performance for both voltage inputs were high at 94% killing for 7.5 kV input and 89.5 % for 9.0 kV (**Table 5-1**).

These results showed that with 7.5 kV input voltage there was a greater BG decontamination compared to 9 kV (94% compared to 89% respectively). However this result was obtained from only one experiment. To justify the reliability of the data, two or more experiments with the same input voltage were done. The average of the BG decontamination for both input voltages was about 91.8 %. To investigate further the influence of the input voltage <7.5 kV on the decontamination, the next experiment was designed with a voltage range from 5 kV to 8.5 kV. It was also considered that the initial concentration of BG spore was quite low, and more accurate results could be obtained by increasing the number of spores in the aerosol generator.

Table 5-1 Total BG cfu before and after 7.5 and 9 kV on both unmarked electrodes.

Voltage	BG cfu (before)	BG cfu (after)	Average % kill
7.5 kV	49	3	94.0
9.0 kV	19	2	89.5
Average			91.8

5.5.3.2 Aluminium marked and unmarked electrodes plasma

The BG decontamination experiment with 2 minutes of airflow through the plasma discharge for the Tubular system were carried out using both unmarked electrodes or one marked at input voltages of 5.0, 6.0, 7.5 and 8.5 kV. This experiment was designed to investigate the effect of the input voltage on the decontamination performance for both marked and unmarked electrodes. **Figure 5-17** shows the petri-dishes of the BG decontamination results before and after the plasma discharge treatment. The average decontamination for the pair of marked and unmarked electrodes (labelled A) was 69.3%, where for the pair of both unmarked electrodes (labelled B) was much higher at 92.4% (**Figure 5-18**). The error bars show the standard deviation for (A) and (B) was 3 and 1.25 respectively.

The decontamination efficiency as a function of the input voltage is shown in **Figure 5-19**. The decontamination increased as the input voltage increased, for both marked and unmarked electrodes. For the voltage input of 7.5 kV, the average decontamination for the unmarked electrodes was 92% and for the marked electrodes it was 65%. The optimum operating input voltage was varied from 7.5 to 8.5 kV, and with this input voltage a stable plasma was produced, thus the electrodes and duralar used lasted longer before breaking down into an arc.

Further investigation was done with varying the capacitance for the marked and unmarked electrode combination. **Table 5-2** (below) shows the result of varying the capacitance on the decontamination performance for marked and unmarked electrodes (**Figure 5-20**). **Figure 5-21** shows the capacitance influence on the

decontamination with the aluminium unmarked electrodes at 7.5 and 8.5 kV input voltages. For 7.5 kV input voltage, as the capacitance value increased, the percentage of the BG decontamination also increased. This was not seen for 8.5 kV, where the decontamination was almost stable at 94%. These results show that the capacitance had affected the decontamination performance. The maximum limit of the capacitance to use with the discharge system with the marked electrodes was 5.4 nF because BG killing started to fall to 71% at 8.1 nF, and with the unmarked electrodes killing was maintained at 94%. It seemed that for both marked and unmarked electrodes, 5.4 nF was the optimum capacitance to use with the present discharge circuit.

Table 5-2 Percentage of *BG* kill with both the unmarked and marked-unmarked aluminium electrode pairs as a function of the capacitance.

Capacitance (nF)	% kill	
	marked	unmarked
1.4	60.2	84.7
2.7	67.8	93.3
5.4	82.6	94.7
8.1	71.8	94.3

5.6 Ozone measurement

The ozone measurements were done to record how much ozone was produced for different electrical and discharge parameters in the experiment. The parameters that were involved in the test were: the Chang profiled electrodes with a constant capacitance of 1.4 nF and the marked and unmarked aluminium electrodes with capacitance from 1.4 to 8.1nF.

5.6.1 Measurement set-up

The schematic set-up for the ozone measurement is shown in **Figure 5-22**. The discharge system was connected via a 40 mm hole into the buffer volume

enclosure made from Perspex with dimensions of 0.6 x 0.65 x 0.9 m³. An ozone sensor was installed inside the buffer volume enclosure, and the ozone was measured as a function of time and recorded via ozone measurement software (ADAM-5000TCP-6000). The ozone sensor reading limit was approximately 445 ppb or 250 µgm⁻³.

5.6.2 Ozone measurement for the Chang profiled Dome discharge.

The Chang profile discharge was used as a test bed for the ozone measurements produced by the atmospheric discharge in air. **Figure 5-23** shows the graph of the ozone concentration as a function of time for the Chang electrode. The attributes of the graph were: the top curve was the ozone density in µgm⁻³, the middle was the ozone concentration in parts per billion (ppb), and the bottom was the ozone mass in µg.

The Chang profiled ozone production rate was 3.06 mgh⁻¹ as shown in **Figure 5-24**. There was an offset of value at the 0 second; the beginning of the measurement due to ozone in the air from previous tests.

5.6.3 Ozone creation for marked and unmarked

Aluminium electrodes of marked-unmarked and both unmarked pairs with varying capacitances were used within the Tubular discharge system to compare the ozone creation concentrations. The Tubular discharge was connected to the buffer volume and the ozone production rates were recorded and plotted. **Figure 5-25** shows the rate of ozone generation for the marked and unmarked aluminium electrode pair with varied capacitors [Eimear Neeson, Personal communication]. It seems that for capacitance ranging from 2.8 to 5.4 nF the ozone generation for the marked electrode system exceeded the unmarked electrode. These capacitance values probably were the optimal to be used in the circuit. The comparison of the ozone production rates for these electrodes are shown in **Figure 5-26**, where the

marked electrode had the highest rate of 44.2 mgh^{-1} , while the unmarked was 35.3 mgh^{-1} . This may be due to the filamentary discharge plus the duralar layers, and the increase of the surface discharge area on the marked electrode that enhanced the ozone production.

Figure 5-27 shows the relationship between the ozone concentration and the BG killing efficiency. For the higher ozone production rate of $>35 \text{ mgh}^{-1}$, the unmarked electrodes gave the highest decontamination at an average of $\sim 94\%$, whereas for the marked electrodes it was around $\sim 74\%$. This is worth further investigation in the future to confirm that this result is accurate. The detail of the capacitance values, the ozone production rates and the decontamination of the BG is summarised in **Table 5-3**.

Table 5-3 Relationship of the ozone generation for marked and unmarked aluminium electrodes with the variation of capacitance and the % kill.

Capacitance nF	Ozone (mg/h)		% kill	
	Marked	Unmarked	Marked	Unmarked
1.4	26.92	37.51	60.2	84.7
2.7	41.37	39.22	67.8	93.3
5.4	34.01	25.33	82.6	94.7
8.1	35.16	37.42	71.8	94.3

5.6.4 Ozone production rates compared to commercial ozone generator

The ozone production rate for the Chang Dome system discharge was 3.06 mgh^{-1} . Meanwhile, the marked and unmarked aluminium electrodes highest ozone production was with 2.7 nF capacitance, where the values were 41.4 mgh^{-1} (marked-unmarked electrode pair) and 39.2 mgh^{-1} (unmarked pair). The production rate for a small plug in commercial ozone generator, Neuralizer (UK) as shown in **Figure 5-28**, was about 7.0 mgh^{-1} . The Dome ozone production rate was 3.06 mgh^{-1} , which was about 43.7% compared to the commercial ozone

generator. While with the aluminium electrodes the concentration was nearly six times higher than that with commercial ozone generator. This is quite a significant prototype result. The ozone production rate can be improved by improving the flow shaping which may eliminate the heat that reduces the ozone life-time and providing a faster flow of oxygen to the discharge.

5.6.5 Power Consumption rates

The power drawn from the mains during the experiments for the Chang profiled electrode was 9W. The ozone production rate from the Chang profile was 3.06 mg h^{-1} , thus the ozone production rate per Watt was approximately $0.34 \text{ mg W}^{-1} \text{ h}^{-1}$. **Table 5-4** shows the power consumed during the tests in the laboratory and the ozone production power rate for the marked and unmarked aluminium electrodes. From the table, at 2.7 nF, the power consumption rates were $1.30 \text{ mg W}^{-1} \text{ h}^{-1}$ and $1.31 \text{ mg W}^{-1} \text{ h}^{-1}$, and essentially identical. The typical estimated power consumption for low power (ranging from 10 to 50 W) air ozone generation is about $1.5 \text{ mg W}^{-1} \text{ h}^{-1}$ [Alonso *et. al*, 2004]. This amount of ozone production should be adequate to use in a 20 m^3 room as suggested by Alonso [Alonso *et. al*, 2004].

Table 5-4 Ozone power consumption for the aluminium marked-unmarked and unmarked pair of electrodes.

Capacitance nF	Consumed Power (W)		Power Consumption Rate ($\text{mg W}^{-1} \text{ h}^{-1}$)	
	Marked	Unmarked	Marked	Unmarked
1.4	37.03	32.23	0.73	1.16
2.7	31.74	29.83	1.30	1.31
5.4	28.99	32.37	1.17	0.78
8.1	32.25	29.39	1.09	1.27

5.7 Conclusions

The results of the decontamination of *E. coli* and the BG exposed to the plasma discharge have proven to be effective at killing these micro-organisms. The stand alone discharge chamber with Chang profiled electrodes, and the Dome and Tubular prototypes plasma discharge in air at atmospheric pressure, each with a pair of electrodes were able to eliminate the micro-organisms from the seeded air flow. The microorganism decontamination was not proportional to the ozone created (this was observed with the marked aluminium electrodes, see **Table 5-4**). This means that if the air flow inside the discharge chamber can be improved, the oxygen would improved thus the micro-organisms killed would likely increase. All the discharge test above were done with one pair of electrodes, the performance of the micro-organisms decontamination and the power consumption rates can be increased if additional electrode pairs are used in the discharge system. These can be operated in series to increase the decontamination efficiency or in parallel to increase the air through-put.

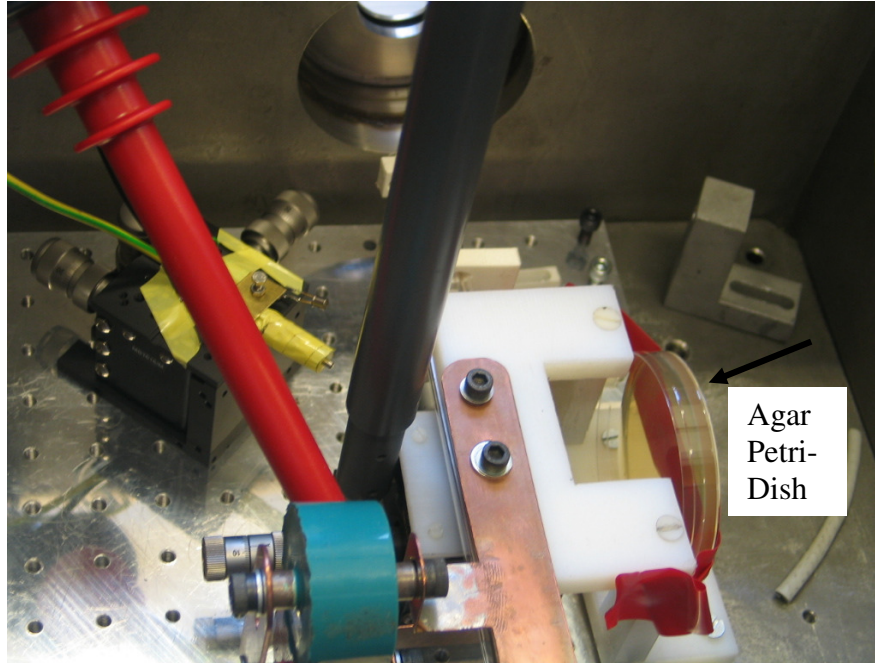


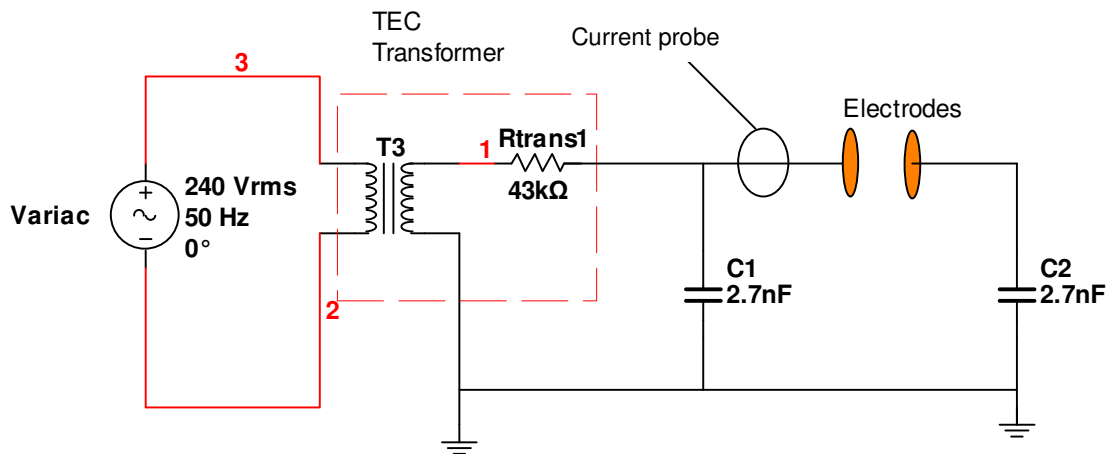
Figure 5-1 Stand alone electrodes and trigger wire preionisation with nutrient agar plate lawned with *E. coli*.



(a) CAD drawing

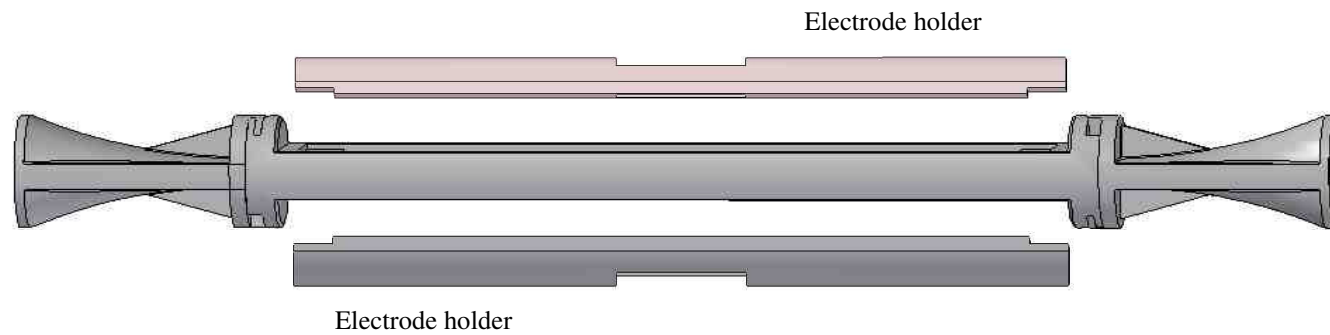


(b) A prototype

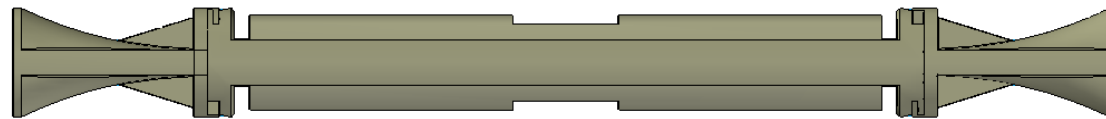


(c) The discharge circuit

Figure 5-2 The Dome discharge system (a) The CAD drawing (b) Photograph of the Dome discharge made from rapid prototyping process with ABS material (c) The discharge circuit used with the Dome discharge system.



(a) The CAD drawing of the Tubular discharge and clip on electrode holder

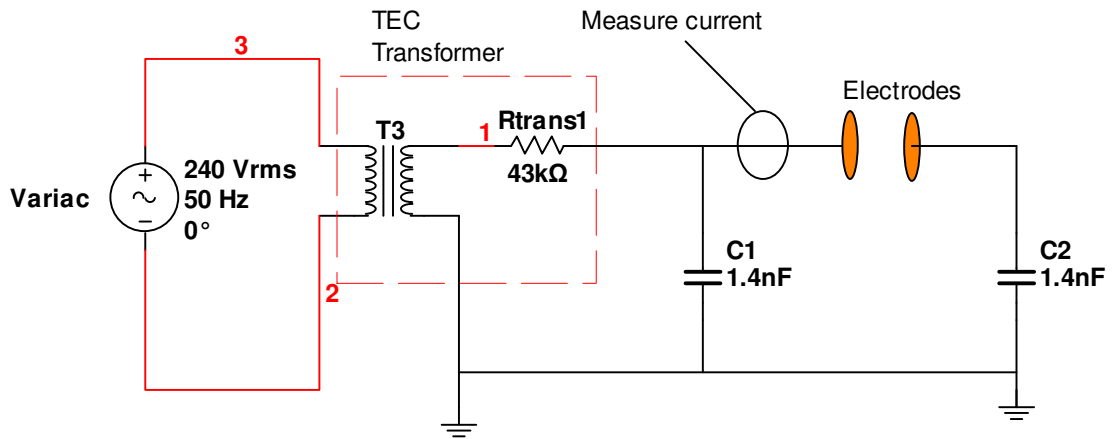


(b) The assembled CAD drawing of the Tubular discharge system

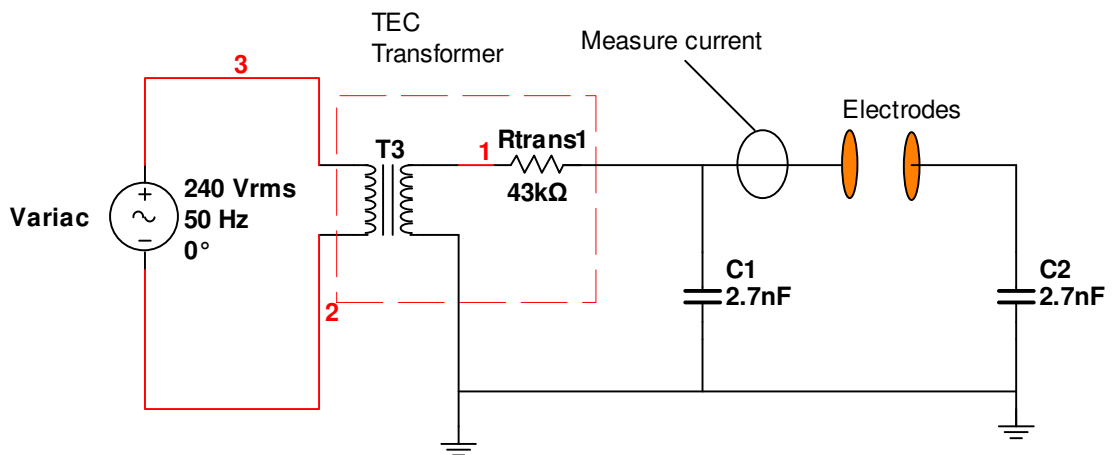


(c) Photograph of the Tubular discharge prototype with the ABS material

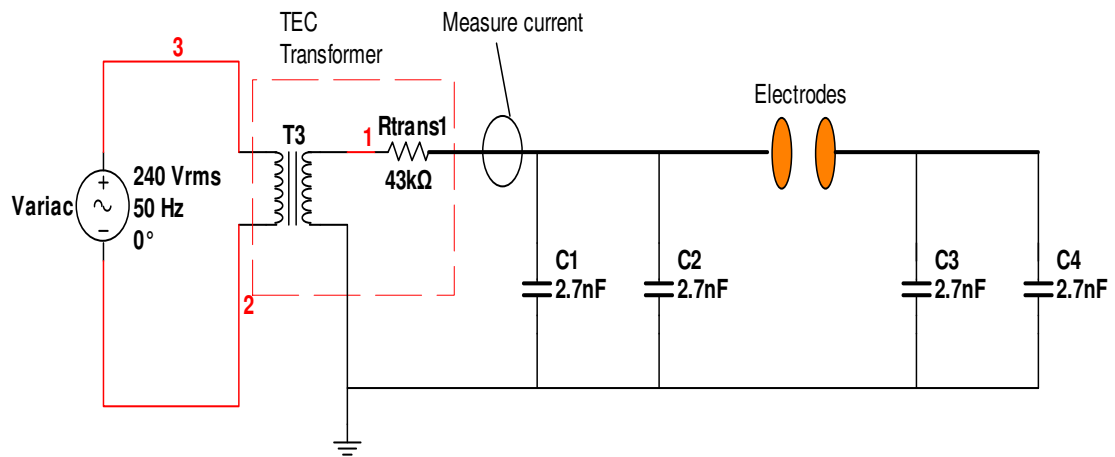
Figure 5-3 The Tubular discharge (a) The CAD drawing of the Tubular discharge with the electrode holders (b) The clipped on electrodes holders were attached (c) The prototype of the Tubular discharge.



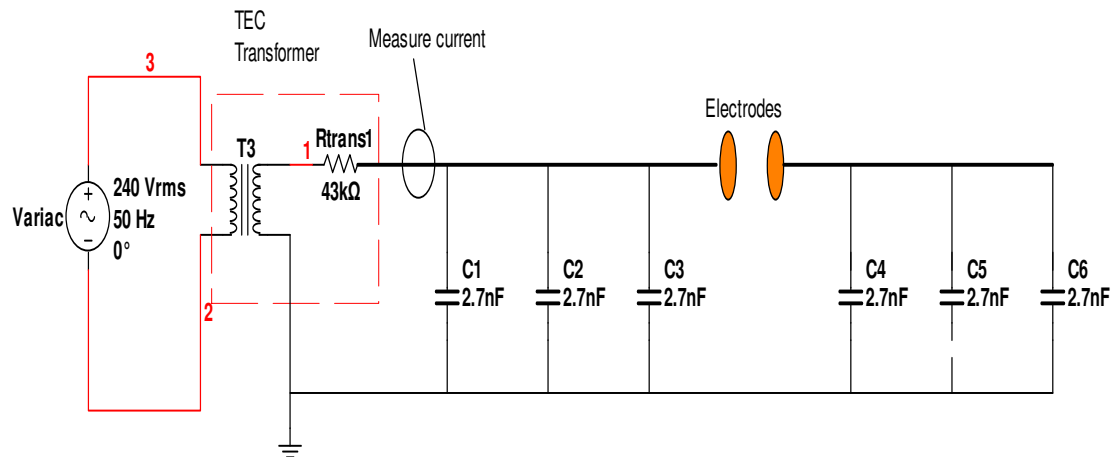
(a) 1.4 nF discharge



(b) 2.7 nF discharge



(c) 5.4 nF discharge



(d) 8.1 nF discharge

Figure 5-4 The Tubular discharge capacitive arrangement (a) 1.4 nF (b) 2.7 nF (c) 5.4 nF and (d) 8.1 nF.

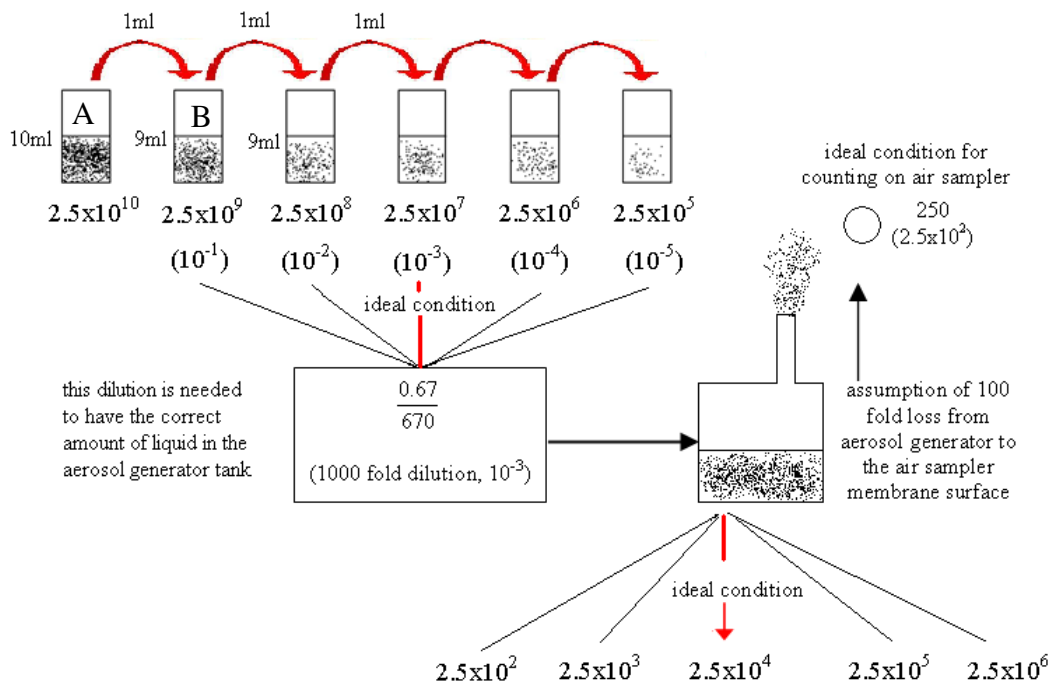


Figure 5-5 The micro-organism preparation and aerosol generator [Takashi Mine Personal Contact].

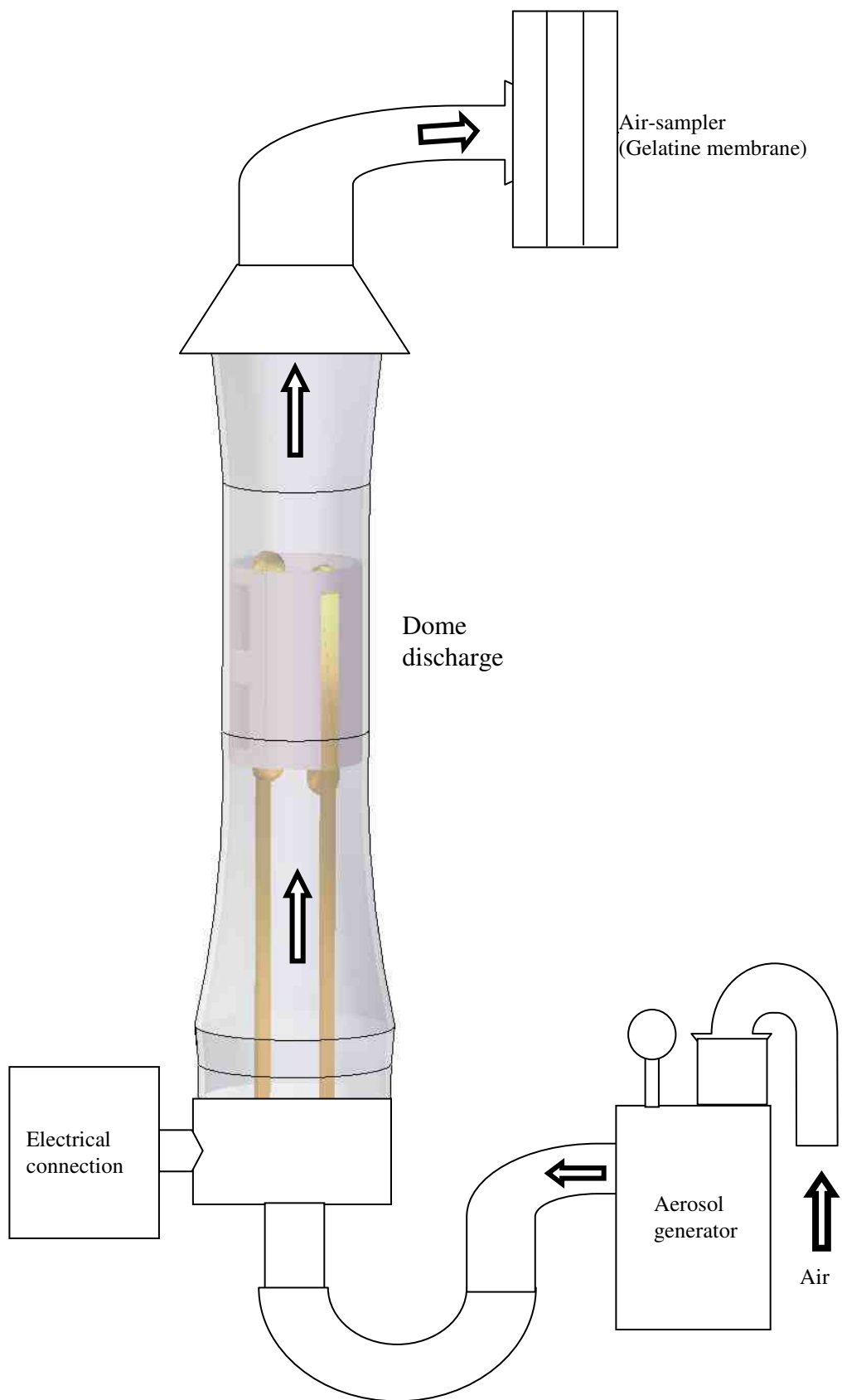


Figure 5-6 The Dome system experimental set-up where the plasma discharge was placed in a vertical position.



(a) Unseeded control plate



(b) *E. coli* seeded control plate



(c) 1 min , 5.5 kV



(d) 2 min, 5.9 kV



(e) 3 min , 6.16 kV



(f) 10 min, 5.93 kV

Figure 5-7 *E. coli* treatment with plasma discharge on UFE Chang profiled electrodes stand alone discharge.

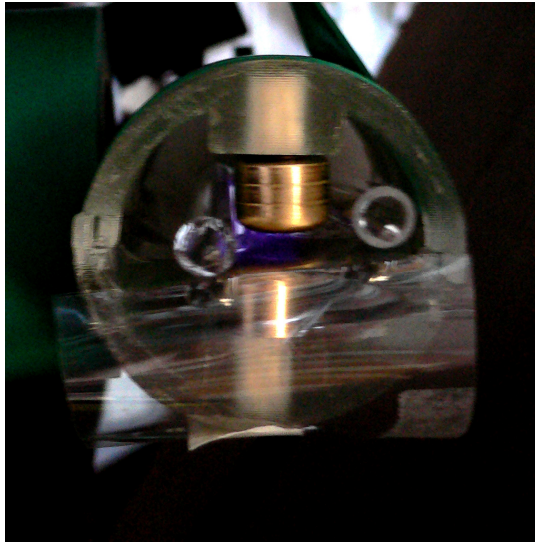


Figure 5-8 The air discharge glow with two layers of durala placed over the cathode to test the Dome system with trigger wire preionisation . The electrode gap was 2.5 mm and the input voltage was 9 kV.

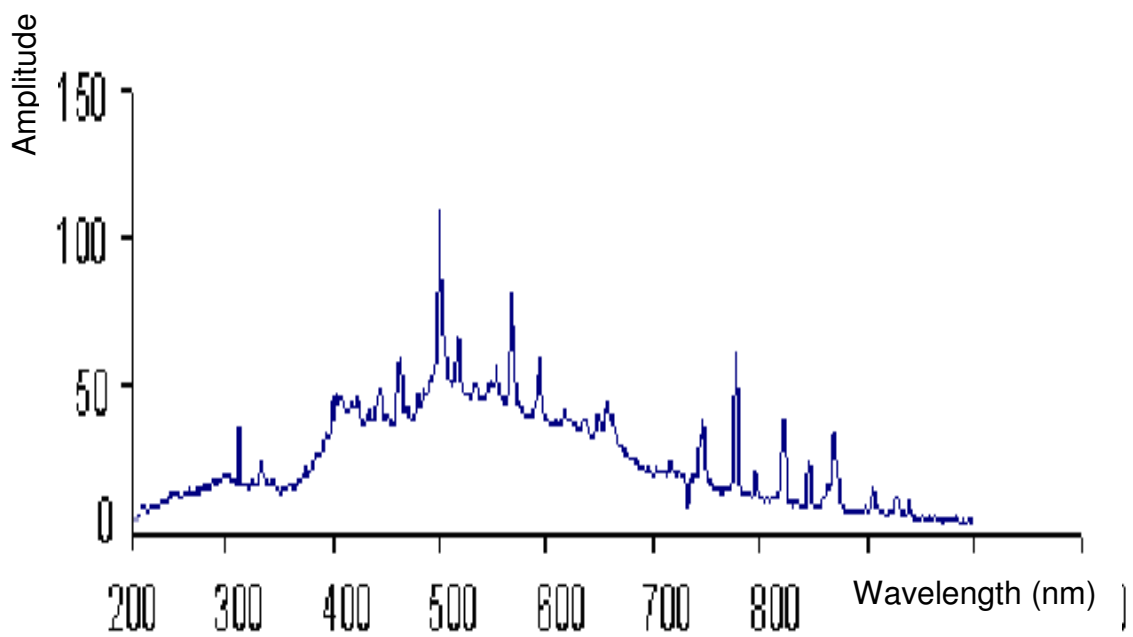


Figure 5-9 The spectrum of the air discharge with 2.5mm electrodes gap and the input voltage was 9 kV.

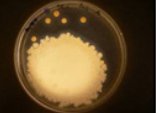
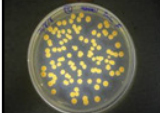
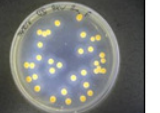
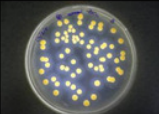
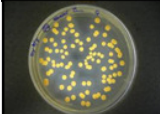
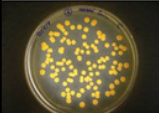
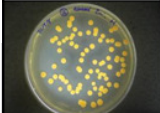
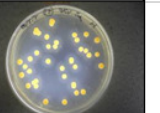
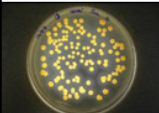
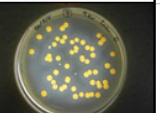
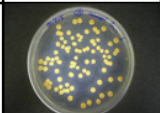
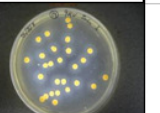
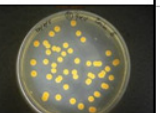
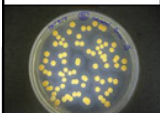
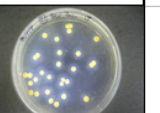
	No treatment	9kV treatment							
Sample A					Sample F				
Picture					Picture				
BG cfus	24	12 countable	roughly 50%	kill	BG cfus	130	35	73.1%	kill
contaminant cfus	0	over grown			contaminant cfus	0	0		
Sample B					Sample G				
Picture					Picture				
BG cfus	74	39	47.3%	kill	BG cfus	119	38	68.1%	kill
contaminant cfus	0	0			contaminant cfus	0	0		
Sample C					Sample H				
Picture					Picture				
BG cfus	130	48	63.1%	kill	BG cfus	92	40	56.5%	kill
contaminant cfus	0	0			contaminant cfus	0	0		
Sample D					Sample I				
Picture					Picture				
BG cfus	150	55	63.3%	kill	BG cfus	92	28	69.6%	kill
contaminant cfus	0	4			contaminant cfus	0	1		
Sample E					Sample J				
Picture					Picture				
BG cfus	smearred with H2O	56	#VALUE!	kill	BG cfus	83	30	63.9%	kill
contaminant cfus	0	0			contaminant cfus	1	0		
								Total average kill	66.9%

Figure 5-11 The results from the repeated experiment of BG decontamination with the Dome system discharge with 2.5mm gap, 2 layers of duralar, 1.42 nF and 9kV input voltage.

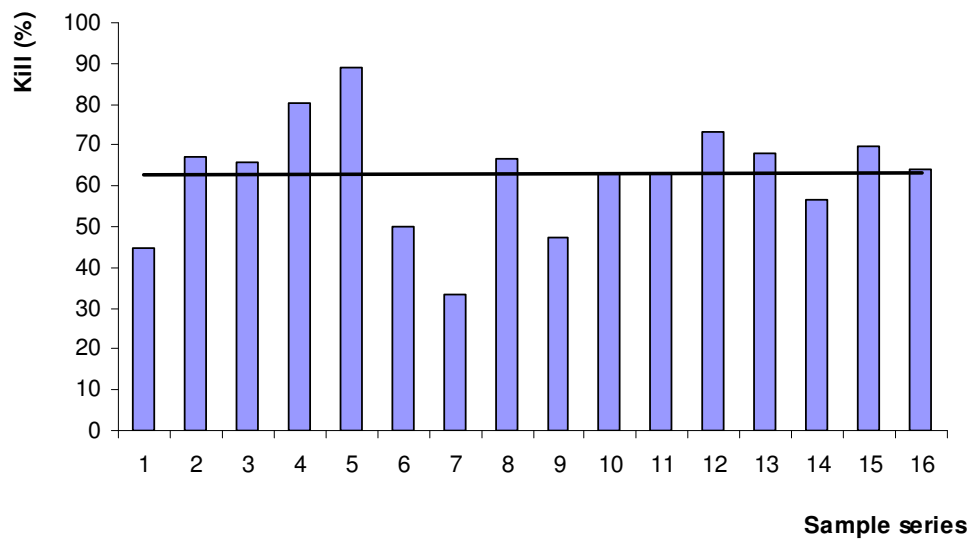
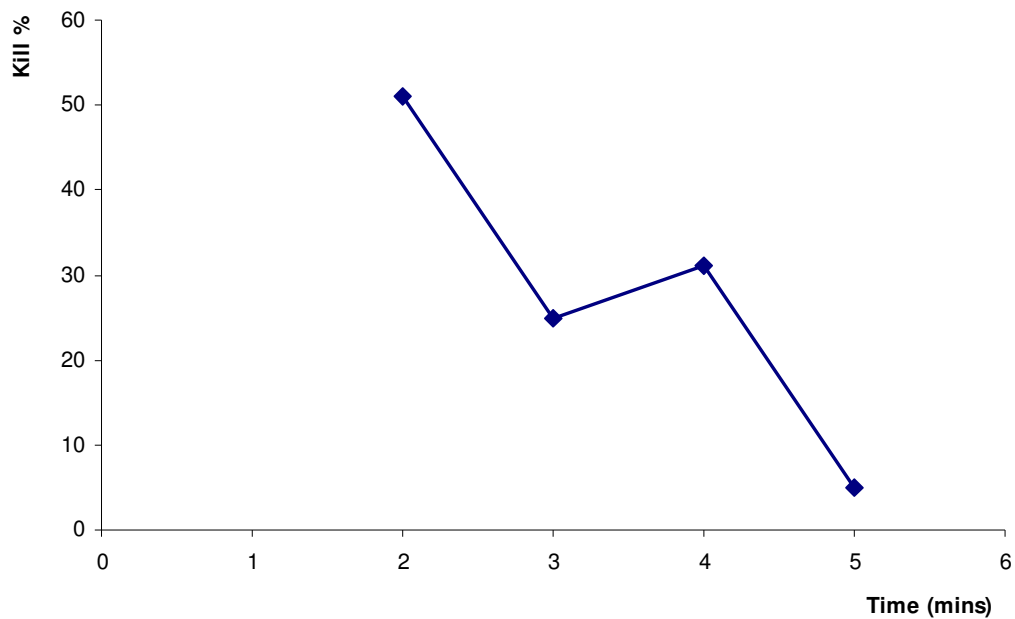


Figure 5-12 BG decontamination % kill when passed through the Chang profiled plasma discharge over 2 minutes with the Dome discharge system. The average of the killing was about 63% shown by the solid horizontal line.

Time (mins)	2	3	4	5
Before				
	Cfu 179	Cfu 90	Cfu 130	Cfu 90 + smudge
After treatment				
	Cfu 87	Cfu 68	Cfu 90	Cfu 135
% Kill	51	25	32	5

(a) The BG decontamination as function of time



(b) The graph of the % kill in function of time.

Figure 5-13 BG kill % as a function of time (2,3,4 and 5 minutes) in the Dome discharge system with 9 kV input voltage (a) BG before and after treatment (b) BG killing % as a function of time.

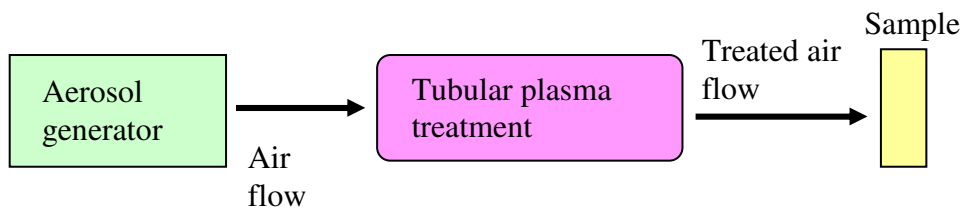
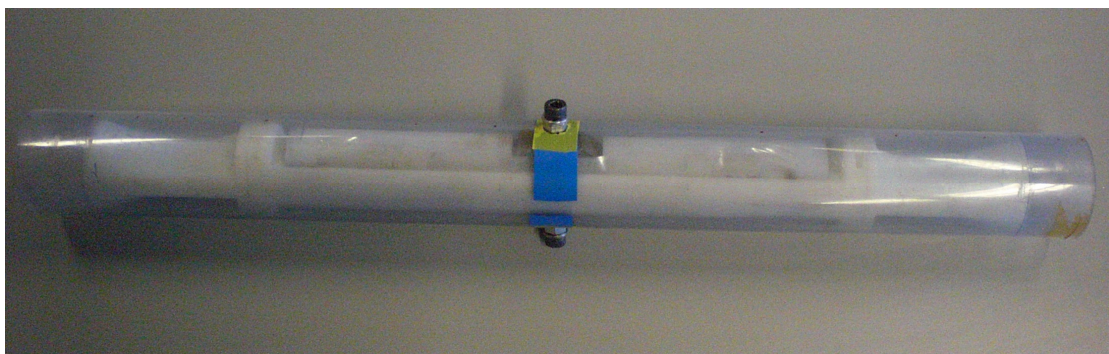


Figure 5-14 The Tubular discharge with aluminium electrodes set-up with the air flow rate was 50 l/min.



(a) The aluminium electrodes holder before clipped on



(b) The Tubular discharge in the clear plastic tube

Figure 5-15 Tubular plasma discharge system: (a) Aluminium electrode holder before mounted (clipped on) to the Tubular discharge system, (b) The Tubular discharge in the clear plastic tube for the air flow connection.

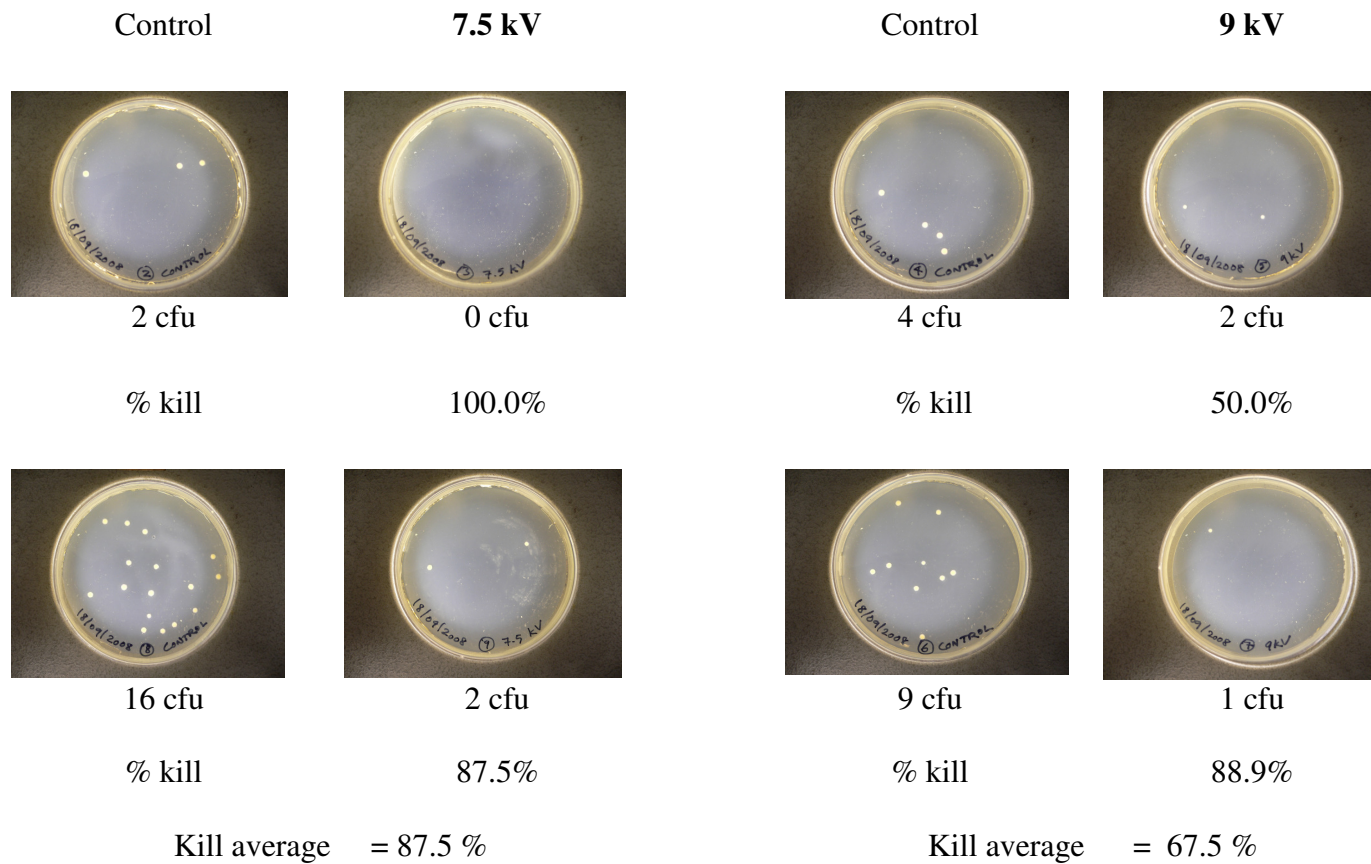


Figure 5-16 BG decontamination with both unmarked aluminium electrodes at 7.5 and 9 kV input voltage.

kV	Marked Electrodes				Unmarked Electrodes			
	Control	Treated	Control	Treated	Control	Treated	Control	Treated
5					na	na	na	na
	Cfu 126	Cfu 32 = 75%	Cfu 600	Cfu 262 = 56%				
6					na	na	na	na
	Cfu 203	Cfu 79 = 61%	Cfu 682	Cfu 248 = 64%				
7.5								
	Cfu 340	Cfu 91 = 73%	Cfu 392	Cfu 161 = 60%	Cfu 204	Cfu 30 = 85%	Cfu 218	Cfu 18 = 92%
8.5								
	Cfu 452	Cfu 90 = 80%	Cfu 502	Cfu 67 = 87%	Cfu 300	Cfu 9 = 97%	Cfu 180	Cfu 8 = 96%

Figure 5-17 Comparing killing efficiency of marked and unmarked aluminium electrodes for input voltages of 5, 6, 7.5 and 8.5 kV.

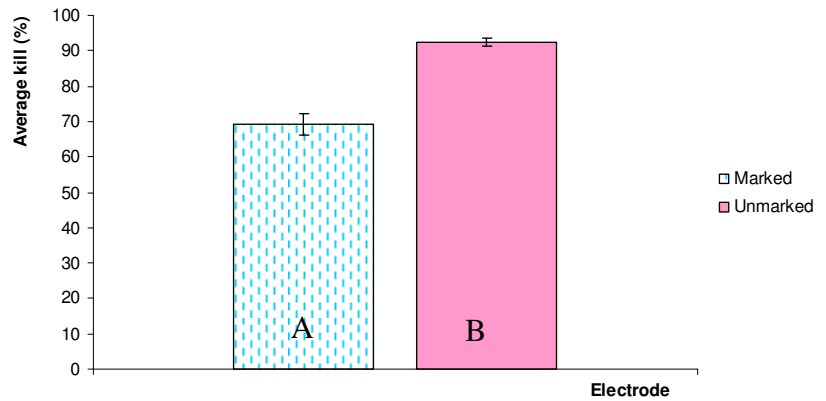


Figure 5-18 The comparison of the BG decontamination averages with the pair of aluminium electrodes where, the marked and the unmarked pair (A) with standard deviation of 3% and the pair of both unmarked electrodes (B) with standard deviation of 1.25 %.

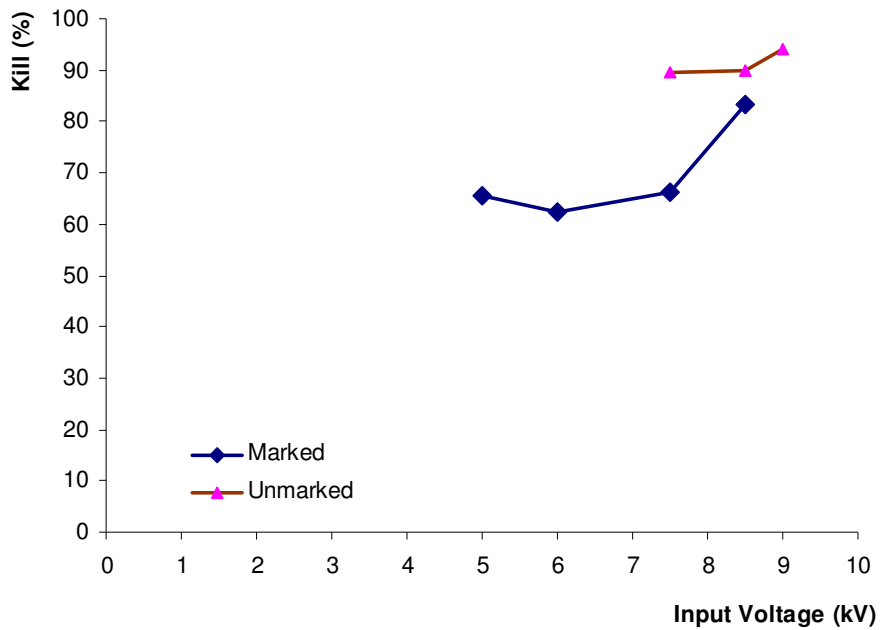


Figure 5-19 The decontamination percentage kill against BG with the pair of marked electrodes and unmarked and both unmarked electrodes with various input voltages.

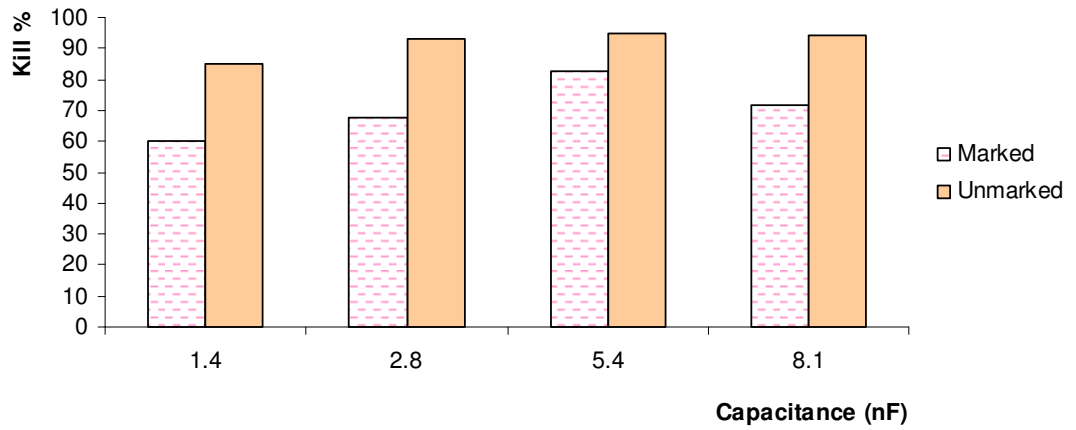


Figure 5-20 Decontamination percentage with various capacitances for the pair of marked and unmarked electrodes and the pair of both unmarked aluminium electrodes.

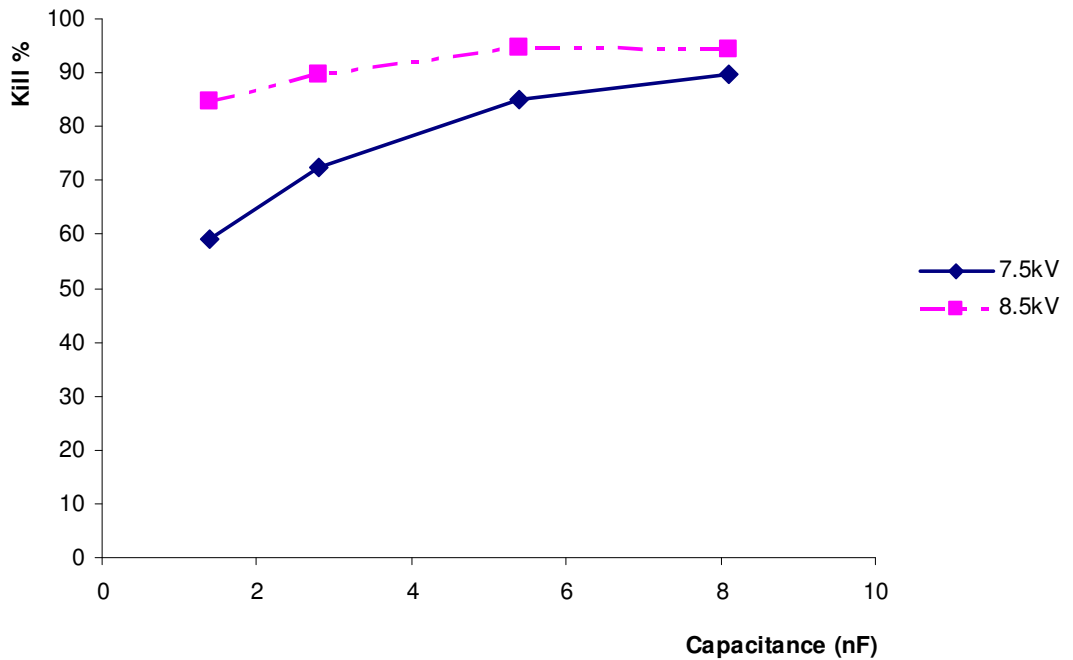


Figure 5-21 Decontamination of BG for a pair of both unmarked aluminium electrodes at 7.5 and 8.5 kV input voltage and various capacitances.

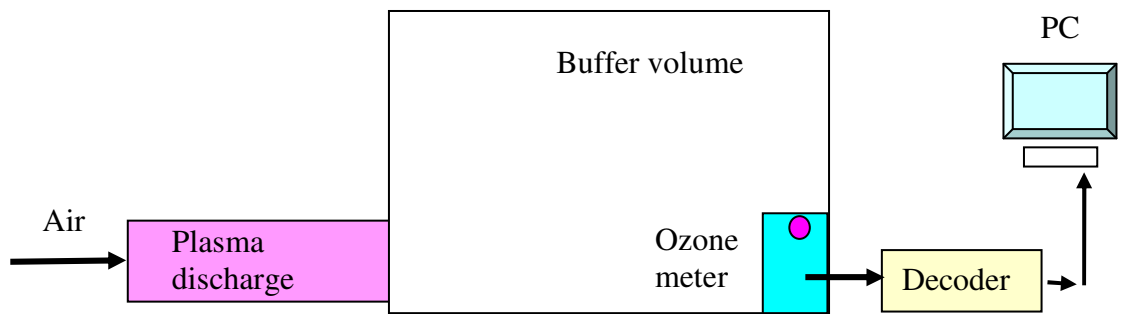


Figure 5-22 Ozone measurement schematic experimental setup.

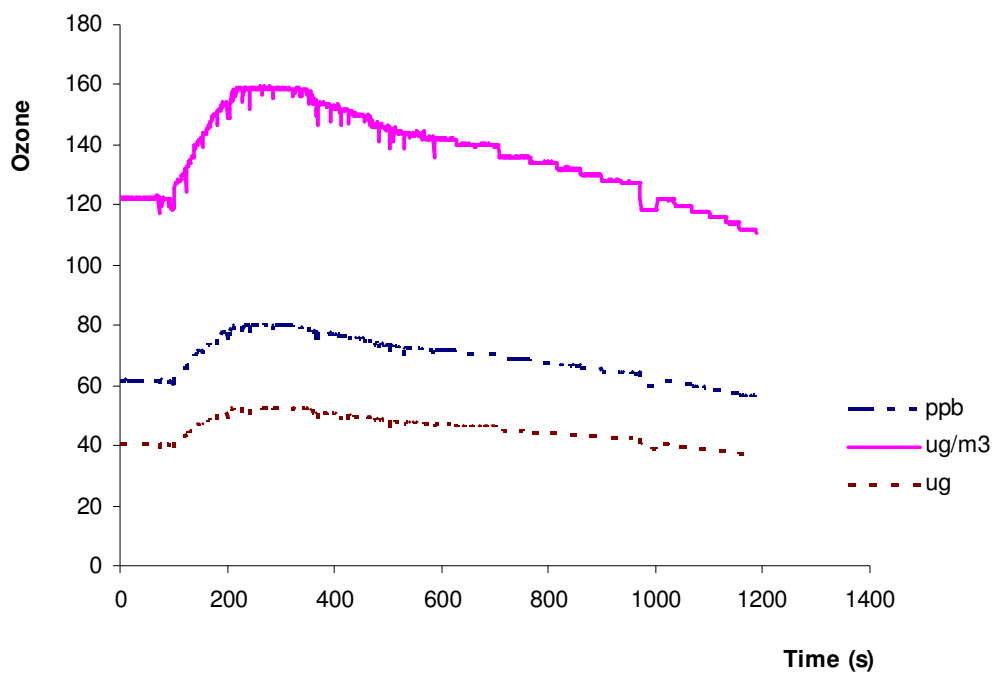


Figure 5-23 The ozone produced as a function of time for Chang profiled electrodes with units of ppb, $\mu\text{g}/\text{m}^3$ and μg .

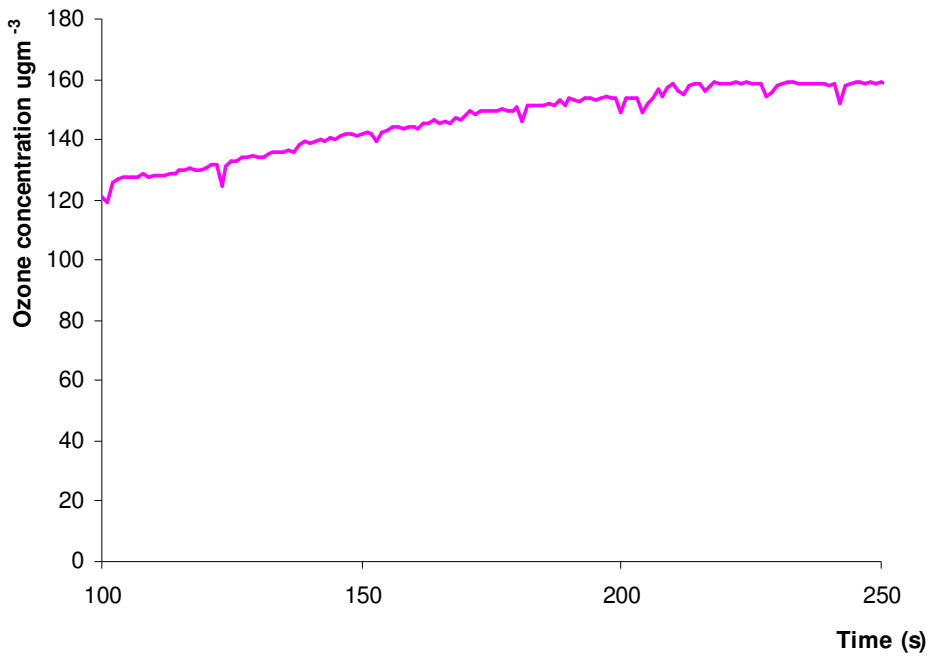


Figure 5-24 Graph shows ozone formation as a function of time for the Chang profiled electrodes with a rate of change $\sim 4.25 \mu\text{gs}^{-1}$ or 3.06mgh^{-1} .

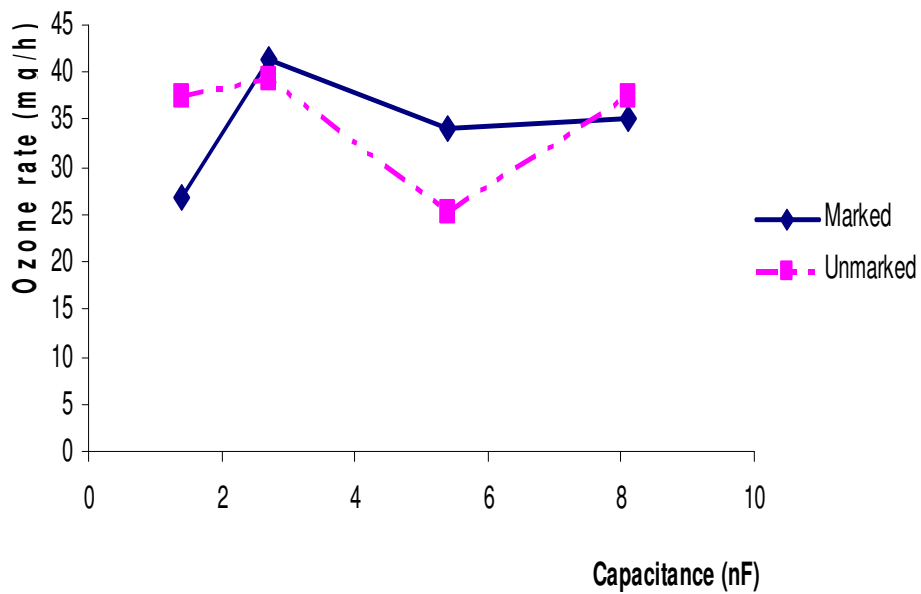


Figure 5-25 Ozone production rate on marked and unmarked aluminium electrodes with a 3mm gap for 1.4 to 8.1 nF. No error bars are shown because this was only done once.

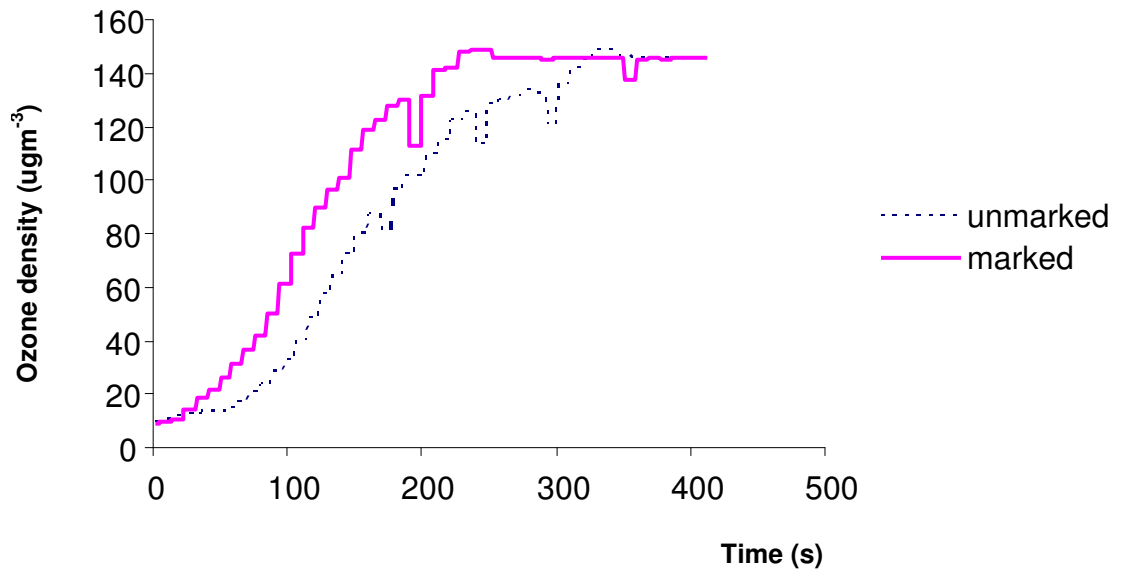


Figure 5-26 Ozone production rate on marked and unmarked aluminium electrodes with 3mm gap of 44.2 mgh^{-1} and 35.3 mgh^{-1} respectively.

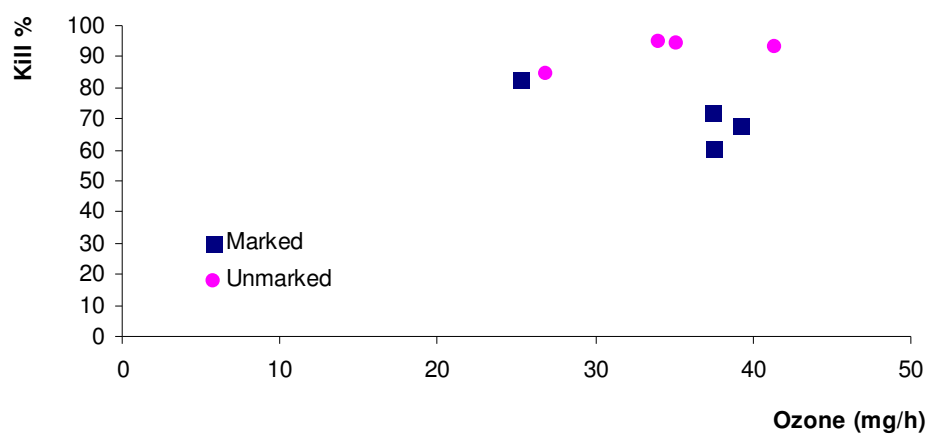


Figure 5-27 The BG decontamination relative to the ozone production rate on marked and unmarked of aluminium electrodes at 3 mm gap for different capacitance. No error bar because only one data reading was used.



Figure 5-28 The plug-in commercial ozone generator.

Chapter 6

Conclusions and Future Work

6.1 Conclusions

Chapter 1 describes the background to this work and provides a literature review of the main objective which was to develop a low cost air discharge plasma or atmospheric laser discharge system for decontamination applications. Before developing an atmospheric system, a DC discharge with sub-atmospheric pressure was first fabricated in order to study the discharge characteristics and the effect of the pumping circuit. The DC stand alone discharge system was able to produce glow discharges by using a gas mixture with a ratio of 1:1:8 (CO₂:N₂:He) and 1:1:4 or for individual gases such as N₂ and He. To support this work, the discharge system was modelled, in parallel with the discharge development, using Multisim (as shown in **Figures 2.4 and 3.1**). Experiments on the discharge system allowed the stray circuit inductance to be found which was used as an input into the simulation. Consequently, this modelled allowed the behaviour of the discharge currents and voltages to be predicted. The Blumlein circuit was modelled for fabrication of a N₂ laser (reported in Chapter 3 section 3.1) however it was found that this laser wavelength (337 nm) was not efficient at killing *E. coli* lawned on nutrient agar plates

The stray circuit values are important in determining the discharge pulse characteristics and discharge stability. For the current system development, the discharge voltages were kept low to reduce costs of the plasma system. Whilst the circuits were suitable for plasma generation, the voltages were relatively low (7-10kV) compared to some laser discharge systems.

The DC discharge system was used as the test bed to proceed with further investigation into AC discharge systems. Chapter 3 reports in detail the development and performance of the discharge system including the gas handling and vacuum systems. The initial DC excited system was capable of single pulse or low frequency operation. The discharge was initiated through an independent

preioniser, using spark plugs and a commercially available electronic ignition system to fire the plugs (Appendix 3B). This system was contrasted with a trigger wire preionisation system that was capacitively coupled to the anode. The Paschen breakdown voltages were measured with several gases and the results compared favourably with published work. To improve the discharge stability various discharge systems were tested. This included using Uniform Field Electrodes and different methods of preionisation.

Chang profiled electrodes were fabricated and their performance was compared with simple planar electrodes, the design and fabrication of the uniform field electrodes is covered in Chapter 2 and Chapter 4. The DC discharge currents and voltages with the Chang profiled electrodes were measured and the maximum peak pulse power was about 15 MW with a charging voltage of about 7 kV, however, the pulse energy was low due to the short pulse duration which was generally less than 10 ns.

The performance of the systems were compared with either longitudinal or transverse flow across the electrodes. Interestingly with the radial fan, the clearing ratio was about 0.5 and the peak current increased by nearly a factor of 2, this effect was a function of gas pressure. There was also some influence of the flow on the discharge duration, where comparing two different gas pressures (100 and 500 mbar for a 1:1:8 gas mix) there was a 15% reduction in the pulse width with the fan on.

A major design parameter for the prototype discharge was the discharge volume, where there is a constraint between maximising the volume to increase the potential air flow between the electrodes but with the disadvantage of requiring a greater discharge voltage, and hence source, to break the gap down.

Methods other than spark gap preionisation were investigated including trigger wire preionisation and the dielectric barrier discharge method where a dielectric material is placed over one or both electrodes. This latter method proved much more robust and efficient and became the central theme of investigation with AC excitation. Various types of dielectric material were used to maximise the

discharge stability. Stable discharges were obtained with all gas mixes investigated and at atmospheric pressure. Subsequent testing demonstrated successful discharge operation in air, this was more stable with duralar over the cathode. Two layers were used (total thickness 150 μm) over the cathode and the discharge ran continuously for 5 mins with an electrode gap of 5 mm. Duralar was subsequently chosen for future experiments. Discharge spectral measurements were taken with a view to using the discharge as a UV source for killing microorganisms.

The AC discharge system was developed to investigate the plasma effect on air or seeded air flow. The main advantage of using an AC discharge was the reduced size of the power supply, which negates the need for smoothing capacitors, hence reducing the cost of the final system. Furthermore, and perhaps more importantly, the discharge is self-regulating, avoiding the need for expensive, high voltage switches.

Chapter 4 describes the manufacturing processes for the electrodes used in the discharge system. The electrode UFE modelling was done with Maple 11 (Chapter 2); this helped to compare the likely performance of the profiles for the Rogowski and Chang electrodes. The Chang electrode was chosen as an improvement to the original planar electrode geometry, offering a broader electrode width to the Rogowski and an easier edge design. The Chang electrode modelling also allowed the generation of a profiled, smoothed electrode profiles. This promotes stable discharge formation. However, a number of electrode configurations were developed that excluded the use of the UFE. Their manufacture is relatively time consuming, requiring dedicated CNC time. The time of manufacture was reduced considerably from 3 hrs to 30 min by changing the tool path over the electrode. Planar electrodes were fabricated in the initial system for testing, and to scale up the electrode size to increase the plasma volume for air decontamination a planar electrode geometry was designed. This has the advantage of simpler manufacture. It should be noted however, that there was considerable post-processing by hand which was time consuming. It took approximately one hour to produce a pair of electrodes. It was found that the planar electrodes worked extremely well with the barrier discharge method, with

duralar placed over the cathode. Further work was done to investigate the effect of laser machining electrodes on the discharge stability. This had the effect of roughening the electrode surface and it improved the discharge stability. Various electrodes were fabricated from brass and aluminium. Aluminium was the chosen material because practically no contaminants were left in the air after plasma exposure, as compared to brass where concerns have been recognised. SEM analysis was done of the electrode surface after laser treatment. The morphology of the electrodes was investigated as a function of the laser scanning speed. This work successfully demonstrated that electrodes could be manufactured in house, with the potential to produce the electrodes commercially.

Chapter 5 developed and tested systems that could be used for air decontamination. These included a “Dome” and a “Tubular” system, either system could be scaled in series or parallel. The tubular system had a plasma volume about 10x that of the dome system. *Bacillus globigii* spores were the test organism, which is a harmless anthrax simulant. An aerosol was generated containing the spores and passed through the plasma systems, and the air was collected on gel plates that were subsequently incubated and analysed for growth. As these experiments were done, the ozone produced through the plasma system was also quantified. With the dome system and UFE, a 9kV input voltage was used, and 1.4nF coupling capacitors. The average kill was about 64%. This was with only 64mm long electrodes and 20 l/min flow rate and 1350 mm³ discharge volume. The interaction time between the discharge and spores was only about 13ms, hence this kill was considered quite effective. This can of course be increased by reducing the flow or increasing the electrode length.

As a consequence, the plasma volume was scaled up using the planar aluminium electrodes in the tubular system. The air flow rate was increased to about 50 l/min as this was the optimum value for the bacterial collection system. The electrodes were either laser marked or unmarked. The effect of the discharge voltage was investigated. The unmarked electrodes (92%) had a greater kill than the laser marked electrodes (69%). As may be expected for both systems, the killing increased with electrode voltage. The optimal operating voltage was

between 7.5 to 8.5 kV (electrode gap of 2.5 mm). The effect of capacitance was investigated, and it was seen that this influenced the decontamination efficiency. This will be due to the coupling between the AC source and the plasma, which is dominated by the electrical circuit. For the laser marked and unmarked geometry the maximum effective capacitance was 5.4 nF, above this value at 8.5 kV the killing reduced.

The ozone produced for the different systems was measured. Again the effects of capacitance on the marked and unmarked geometries were investigated, with a view of trying to correlate the killing efficiency with the ozone production rate. For the experiments reported herein, there was no apparent correlation with the killing and ozone production rate (Figure 5-27).

The wall plug power consumption rates were measured as a function of the capacitance as was the ozone production rate per Watt-hr. Interestingly the power consumption was slightly higher for the marked electrodes and averaged ~7.4 W (Table 5.3) this compared to ~7.0 W for the unmarked system. The ozone production rate averaged ~7.8 mgh⁻¹ for the marked and ~7.9 mgh⁻¹ for the unmarked.

It is clear that the system is scalable either in terms of increasing the decontamination efficiency by increasing the electrode length or adding a number of the tubular systems in series or the volumetric air flow can be increased by adding more electrodes in parallel. Both can be increased arbitrarily by scaling in series and parallel simultaneously.

For future work the transfer efficiency as a function of the electrical components and plasma characteristics should be investigated more fully. This will allow optimisation of the plasma stability and minimisation of the running costs. Due consideration should be given to electrically isolate the discharge system from other electrical circuits.

Flow shaping influenced the discharge stability and its effects at atmospheric pressure with air should be characterised. With forced convection the peak

current increased and this will influence the discharge stability and the killing efficiency. This may be due to removal of dissociation products that influence the preionisation nature of the discharge.

The Dome system that was developed introduced a considerable pressure drop into the system. This can be redesigned more appropriately in light of knowing the relationship between flow, killing and discharge stability.

The data acquisition systems should be enhanced to obtain more reliable measurements of the discharge currents and voltages. In the present case the electrodes were generally floating which made measurement of the discharge voltage drop difficult. Opto-isolators could be implemented to safely isolate the floating electrodes from the voltage probe, allowing simultaneous capture of the discharge voltage and current. This will provide additional information on the relationship between the discharge parameters and killing efficiency, allowing further optimisation.

The protocols developed for the microbiological experiments demonstrated that the plasma was efficient at inactivating spores in an aerosol. Whilst this is a convenient method of testing the system, the potential bacterial numbers are higher than may ever be achieved in practice, placing an excessive demand on the system. The system performance therefore, should be evaluated in real everyday situations. This is complex to achieve however as there is difficulty over control data for comparison. For the current protocols it is desirable to know the concentration of micro-organisms in the aerosol tank, allowing direct comparison of the system performance and potential fall out of spores through the system.

Whilst video was taken of the plasma development, there is ample scope to investigate the development and sustainability of the plasma for longer durations. High speed and high resolution cameras can be used to analyse the spatiotemporal development of the plasma, with a view to extending the electrode lifetime.

The use of Switch Mode Power Supplies (SMPS) to enhance the discharge stability and electrode lifetime should be investigated, with their potential benefits assessed against their higher cost. The HV transformers used in this work were relatively cheap and reliable, but because they are based on iron core technology they are large and heavy. SMPS offer higher frequency solutions with greater discharge stability at reduced size and weight.

References

Alonso Marcos. J, Cardesin. J, Corominas Lopez .E, Rico-Secadas, M and Garcia. J, **Low-power high-voltage high-frequency power supply for ozone generator**, IEEE Trans, Vol. 40, No. 2, (2004).

Bahrampour A and Ganjovi A A, **Theoretical Analysis of Electrical Transient Behaviour in TEA CO₂ Laser with Dielectric Corona Preionisation**, Journal of Physics D: Applied Physics, Vol. 36 (2003), UK, pp2487-2497.

Baker C, Dyer P E, Tait BL, **Design of A Compact High PRF TEA CO₂ Laser and Performance under Multimode and Single Mode Conditions**, Journal of Physics E: Scientific Instruments, Vol. 14, (1981), pp1167-1170.

Baroch. P, Takeda. T, Oda, M, Saito. N and Takai. O, **Degradation of bacteria using pulse plasma discharge in liquid medium**, IEEE Xplore, (2006), pp482-485.

Bayle P, Cornebois B, **Propagation of Ionizing Shock Waves in Electrical Breakdown**, Physical Review A, Vol. 31, (2), February (1985), pp 1046-1057.

Bell A R, Davies J R, Guerin S and Ruhl H, **Fast-Electron Transport in High-Intensity Short Pulse Laser-solid Experiments**, Plasma Physics, Control Fusion, Vol. 39 (1997), pp653-659.

Benerji N S, Varshnay N, Abhinandan L, Nundy U, **A Compact Spark Pre-Ionized Pulser Sustainer TE-CO₂ Laser**, Sâdhanâ, Vol. 29, Part 3, June (2004), pp 297-303.

Bhadani P K, Sylvan A, Harrison RG, **Efficient Switchless Multi-Joule TE-CO₂ Laser**, Journal of Physics E: Scientific Instruments, Vol. 62 (6), June (1991), pp1404-1407.

Biswas D J, Laya J P N I, Prasad M B S, Raote P, **Switch-less Operation of a TEA-CO₂ Laser**, Optical society of America, Vol. 13 (23), pp 9636-9638.

Bogaerts. A, Neyts. E, Gijbels. R and Mullen, J v.d, **Gas discharge plasma and their applications**, Spectrochemica Acta Part B, Vol 57, (2002), pp609-658.

Chang T Y, **Improved Uniform-Field Electrode Profiles for TEA Laser and High-Voltage Applications**, The Review of Scientific Instruments, Vol. 44, (4), April (1973) pp405-407.

Chen H L, Lee H M, Chen S H and Chang M B. **Review of Packed-Bed Plasma Reactor for Ozone Generation and Air Pollution**, Industrial Engineering Chemical Res., Vol 47, (2008), pp2122-2130

Chung H J, Lee D H, Hong J H, Joung J H, Sung Y M, Park S J, Kim H J, A **Simple CO₂ Laser with Long Milliseconds Pulse Duration**, Review of Scientific Instruments, Vol. 73 (2), February (2002), pp484-485.

Cridland J V, **Effect of Pressure on A Semiconductor-Preionised Pulsed CO₂ Laser** , Journal of Physics E: Scientific Instruments, Vol. 18, (1985), pp 328-330.

Dřímal J, Gibalov V. I and Samoylovich V. G., **The Dependence of Ozone Generation Efficiency in Silent Discharge on a Width of Discharge Gap**, Czechoslovakia Journal of Physics B, Vol 38, (1988), pp643-648.

Dyer P E, **Field Uniformity Requirements in TEA CO₂ Lasers**, Journal of Physics E: Scientific Instruments, Vol. 11, (1978), 0022-3735 , pp1099-1101.

Dzakowic G., Wutzke S., **High pulse rate glow discharge stabilization by gas flow**, Journal of Applied Physics, Vol. 44(11), 1974, pp5061-5063.

Hamilton D C, James DJ and Ramsden S A, **A Repetitive Pulsed Double Discharge TEA CO₂ Laser**, Journal of Physics E: Scientific Instruments, Vol. 8 (1975), UK, pp849-852.

Han S., Eun H., Cho G. and Whang K. W, **Electrical Breakdown Voltage in a Mix Gas**, Journal of Applied Physics, Japan, Vol. 40, (2001), pp295-297.

Hasson V, Bergmann H M von, **High Pressure Glow Discharge for Nanosecond Excitation of Gas Lasers and Low Inductance Switching**, Applications, Journal of Physics E: Scientific Instruments, Vol. 9, pp 73-76.

Howells S, Cridland J V, **The Effect of Circuit Inductance on the Operation of a TEA CO₂ Laser**, Journal of Physics E: Scientific Instruments, Vol. 15 (1982), pp542-547.

Jayawardana, P. L, de Alwis, W. R and Fernando, M. A, **Ventilatory function in brass workers of Gadaladeniya**, Sri Lanka, Occup. Med. Vol. 47, No. 7, (1997), pp411-416.

Jennings H K, **Charging Large capacitor Banks in Thermonuclear research**, Electrical Engineering, vol 80, (1961) pp419.

Jones, C. V., Report for British Electrical and Allied Industries Research Association, (1956) No. L/T 334

Khan N, Mariun N, Aris I, Yeak J, **Laser-Triggered Lightning Discharge**, **New Journal of Physics**, Vol. 4 (2002), pp61.1-61.20.

Khan N, Mariun N, **Design and Experimental Characterisation of a DC-Excited CW/Repetitively Pulsed sealed CO₂ Laser**, *Journal of Optics & Laser Technology*, Vol 36, pp87-94.

Korytechenko, K.V et al, **Requirements to the Electrical Discharge System Used in The Plasma-Wave**, *Problems of Atomic Science and Technology*, (2004), No. 2, Series: Nuclear Physics Investigations (43), pp33-35.

Laflamme K. A, *Review of Scientific Instrument*, Vol 4, (1970),pp1578.

Law H. K., Siew W. O., Tham K. K., Tou T. Y., **An Ultraviolet Preionised Nitrogen Laser Switched by Parallel Spark Gaps**, *Measurement Science and Technology*, Vol. 8 (1997), UK, pp819-821.

Lee K., Paek K. Y., Ju W. T. and Lee Y., **Sterilization of Bacteria, Yeast, and Bacterial Endospores by Atmospheric-Pressure Cold Plasma using Helium and Oxygen**, *The Journal of Microbiology*, Vol. 44, No. 3, June 2006, pp269-275.

Lee Y S, Chung H J, Joung J H, Kim E J, Kim H J, **Active Long Pulsed Shaping Technique of Pulsed CO₂ Laser Using Multi-Pulse Discharge Control**, *Journal of Optics & Laser Technology*, Vol. 36 (2004), pp57-61.

Léger L., Moreau E., Artana G and Touchard G., **Influence of a DC corona discharge on the airflow along an incline flat plate**, *Journal of Electrostatics*, vol 51-52, May 2001, pp300-306.

Leyva I and Guerra J M, **A compacted Ernst-electrodes Profile for Pulsed High-pressure Lasers**, *Measurement Science and Technology*, Vol. 10 (1999), UK, ppN1-N2

Mckan D., Seguin H., Tulip J., **Photoionisation parameters in the CO₂ laser gas**, *IEEE Journal Quantum Electronics* QE12 (8), (1976) pp 470-482.

Naidu, M.S. and Kamaraju, V., **High Voltage Engineering**, 2nd ed., McGraw Hill, 1995, ISBN 0-07-462286-2, pp26.

Napartovich A. P., **Overview of Atmospheric pressure discharges producing nonthermal plasma**, *Plasmas and Polymers*, Vol. 6, (1/2), June 2001.

- Onkels E D, Seeling W, **Quantitative Comparison of Different Preionisation Schemes of KrF Laser Discharges**, Journal of Applied Physics B, Laser and Optics, Vol. 67, (1998), pp33-37.
- Potivejkul S., Kinnares V. and Rattanvichien P., **Design of Ozone Generator using Solar Energy**, IEEE Explore, 1998, pp217-220.
- Rickwood K R, McInnes J, **High Repetition Rate Mini TEA CO₂ Laser Using a Semiconductor Preionizer**, Review of Scientific Instrument Vol. 53 (11), November (1982), pp 1667-1669.
- Roth J. R., Sherman D. M and Wilkinson S.P., **Boundary layer flow control with a one atmosphere uniform glow discharge surface plasma**, AIAA Conference, NV, Jan. 1998, paper 98-0328.
- Sanz F Encinas, Perez J M Guerra, **Peaking capacitor in an Incomplete Corona Surface Discharge Preionized TEA CO₂ Laser**, Journal of Physics E: Scientific Instruments, Vol. 27 (4), April (1991), pp891-894.
- Scott S J, Smith A L S, **Efficacy of Laser Preionisation with A Semiconductor Source Propene Addition**, Journal of Physics E: Scientific Instruments, Vol. 17, (1984), pp1242-1243.
- Serafetinides A A, Rickwood K R, **Improved Performance of Small and Compact TEA pulsed HF Lasers Employing Semiconductor Preioniser**, Journal of Physics E: Scientific Instruments, Vol. 22 (1989), pp103-107.
- Shimosaki. M., Hayashi, N., Ihara. S., Satoh. S., Yamabe. C., **Effect of trigger electrodes configuration of a double discharge ozonizer on ozone generation characteristics**, vacuum, 73, (2004),pp573-577.
- Soukieh M., Ghani B A, Hammadi M, **Mathematical Modeling of CO₂ TEA Laser**, Optics & Laser Technology, vol 30 (1998), pp451-457.
- Spyrou N, Potamianou S, Interaction between A High-Voltage Circuit and an electrical discharge for laser applications, Journal of Physics D: Applied Physics, Vol. 29, (1996), pp392-402.
- Stark D S, Crocker A and Lowde N A, **A Semiconductor-Preionised Sealed TEA Laser Operating at high CO₂ Concentration and Repetition Rates up to 100 Hz**, Journal of Physics E: Scientific Instruments, Vol. 16 (1983), UK, pp1069-1071.
- Stroga J T, Petheram J C, Bowers M S, Romea R, Lee R W, **Frequency Spectral Measurements of Pulsed TE CO₂ Laser Incorporating LAWS Transmitter Design Features**, Journal of Modern Optics, Vol. 41 (11), (1994), pp2085-2100.
- Sylvan A, Bhadani P K, Harrison R G, **A Photoswitched small TEA CO₂ Laser**, Measurement Science and Technology, Vol.3 (1992), pp200-203.

Tan R, Wan C, Qi J, Liu S, Zhou J, Xie W, **A Sequential Discharge TEA CO₂ Laser With High Repetition Rate and High Output Power**, Optics & Laser Technology, vol 31 (1999), pp393-396.

Tou T Y, Tham K K, Siew W O and Yee K C, **Circuit Modelling of A Two-Stage Blumlien-Driven TEA-N₂ Laser**, Measurement Science and Technology, Vol. 9 (1998), UK, pp 1247-1251.

Trtica Milan S, Miljaneć Ščepan S, **Pulsed CO₂ laser program, Lasers & Laser Application Devision**, Vinča Institute of Nuclear Sciences, Belgrade Serbiaa, (2003).

Trtica Milan S., Gokavić Biljana M., Radak Bojan B., Miljanić Ščepan S., **An Efficient Small Scale TEA CO₂ Laser for Material Surface Modification**, Proceedings of SPIE Vol. 4747 .0277-786x/02 (2002), pp44-49.

Trtica Milan S., Ostojić Gordana N., **Numerical Modelling of Self-Sustained TEA CO₂ Laser Operation**, SPIE Vol. 3612 .0277-786x/99 (1999),pp7-14.

Ulf S., Giere S.and Kurrat M., **Breakdown Voltage of Electrode Arrangements in Vacuum Circuit-Breakers**, IEEE Transactions on Plasma Science, Vol 31, (2003).

Walter B, **Dielectrics for Corona Preionisation of a TEA Laser**, Journal of Physics E: Scientific Instruments, Vol. 18, (1985), pp279-281.

Walter B, **Surface Corona Discharge Preionisation of Gas-Flow TEA Lasers**, Journal of Physics E: Scientific Instruments, Vol. 20 (1987), pp457-458.

Watson I A, PhD Thesis, **Optimisation of the gaseous discharge and optical coupling of a pulsed CO₂ laser**, Laser and Optical Systems Engineering Centre (LOSEC), Department of Mechanical Engineering, Glasgow University, (1993)

Watson I A, Chatwin C R, **Segmented Ballasted Electrodes for a Large Volume, Sub-Atmopheric, Transversely Excited Pulsed Laser**, Journal of Physics D: Applied Physics, Vol. 28 (1995), pp258-268.

Willets D V, Harris M R, **Output Characteristics of a Compact 1 J Carbon Dioxide Laser with a Gaussian Reflectivity Resonator**, IEEE Journal of Quantum Electronics, Vol. 24, (6), June (1988), pp849-855.

Appendix 2A

MultiSim simulation information

Brass

Component composition %

Cu 60 - 63

Fe max 0.35

Pb 2.5 - 3.7

Zn 35.53

Other Max 0.5

Mechanical properties MECHANICAL PROPERTIES

METRIC

COMMENTS

Tensile Strength, Ultimate 338 - 469 MPa

Tensile Strength, Yield 124 - 310 MPa

Depending on

temper

Elongation at Break 53% in 457.2 mm

Modulus of Elasticity 97 GPa

Bulk Modulus 140 GPa Typical for Steel

Poisson's Ratio 0.31 Calculated

Machinability 100% UNS C36000 (free-cutting brass) = 100%

Shear Modulus 37 GPa

THERMAL PROPERTIES METRIC COMMENTS

CTE, linear 250°C 20.5 $\mu\text{m}/\text{m}\cdot\text{°C}$ from 20-300°C (68-570°F)

Thermal Conductivity 115 W/m-K at 20°C (68°F)

Melting Point 885 - 900 °C

Solidus 885 °C

Liquidus 900 °C

Appendix 2B

The Rogowski -Chang – Earnst Functions

>

> **restart;**

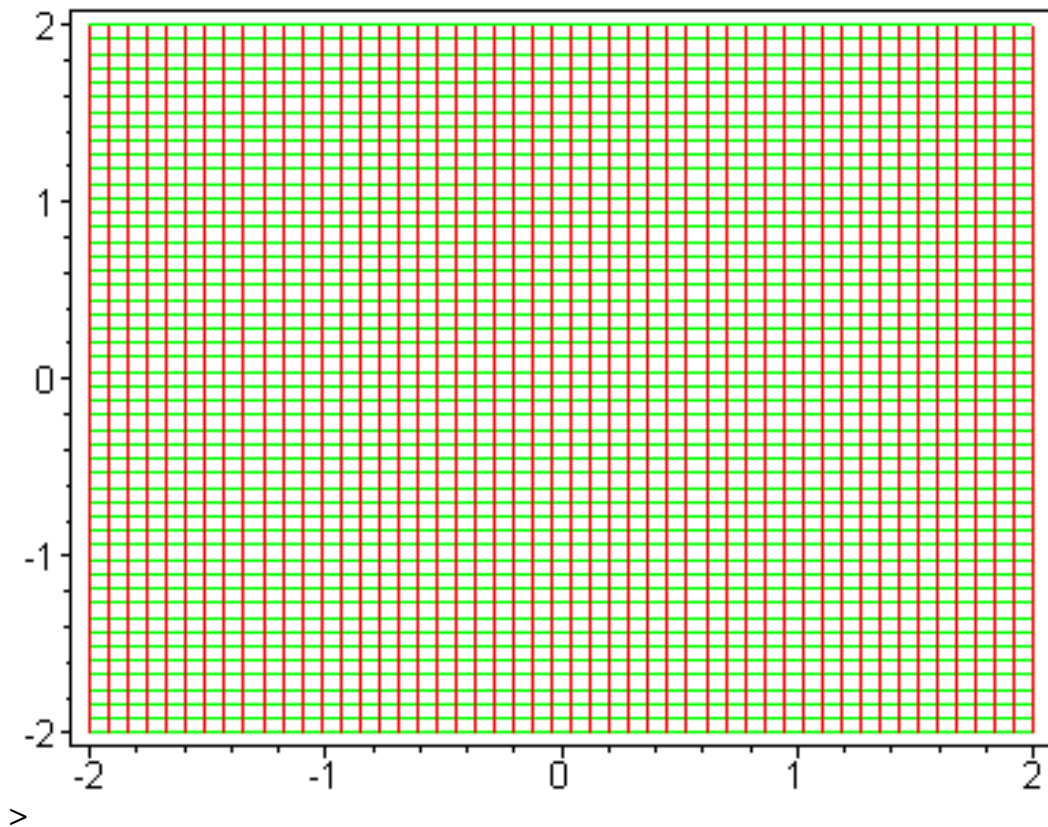
> **with(plots);**

Warning, the name `changecoords` has been redefined

[*animate, animate3d, animatecurve, changecoords, complexplot, complexplot3d, conformal, contourplot, contourplot3d, coordplot, coordplot3d, cylinderplot, densityplot, display, display3d, fieldplot, fieldplot3d, gradplot, gradplot3d, implicitplot, implicitplot3d, inequal, listcontplot, listcontplot3d, listdensityplot, listplot, listplot3d, loglogplot, logplot, matrixplot, odeplot, pareto, pointplot, pointplot3d, polarplot, polygonplot, polygonplot3d, polyhedra_supported, polyhedraplot, replot, rootlocus, semilogplot, setoptions, setoptions3d, spacecurve, sparsematrixplot, sphereplot, surfdata, textplot, textplot3d, tubeplot*]

The Ω Plane

> **conformal(z, z=-2-2*I..2+2*I, grid=[50, 50], axes=boxed);**



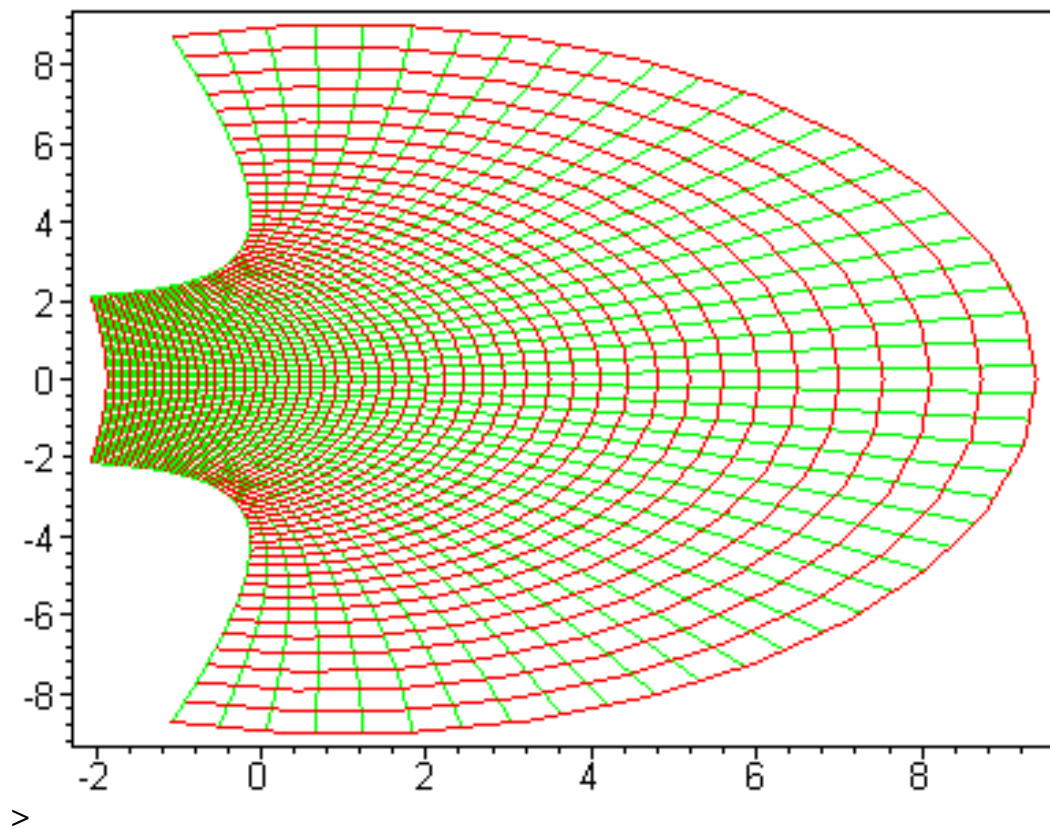
The Rogowski Function:

$$z = \frac{A(\Omega + e^\Omega)}{\pi}$$

A plot of the Rogowski function:

Constant $A = \pi$

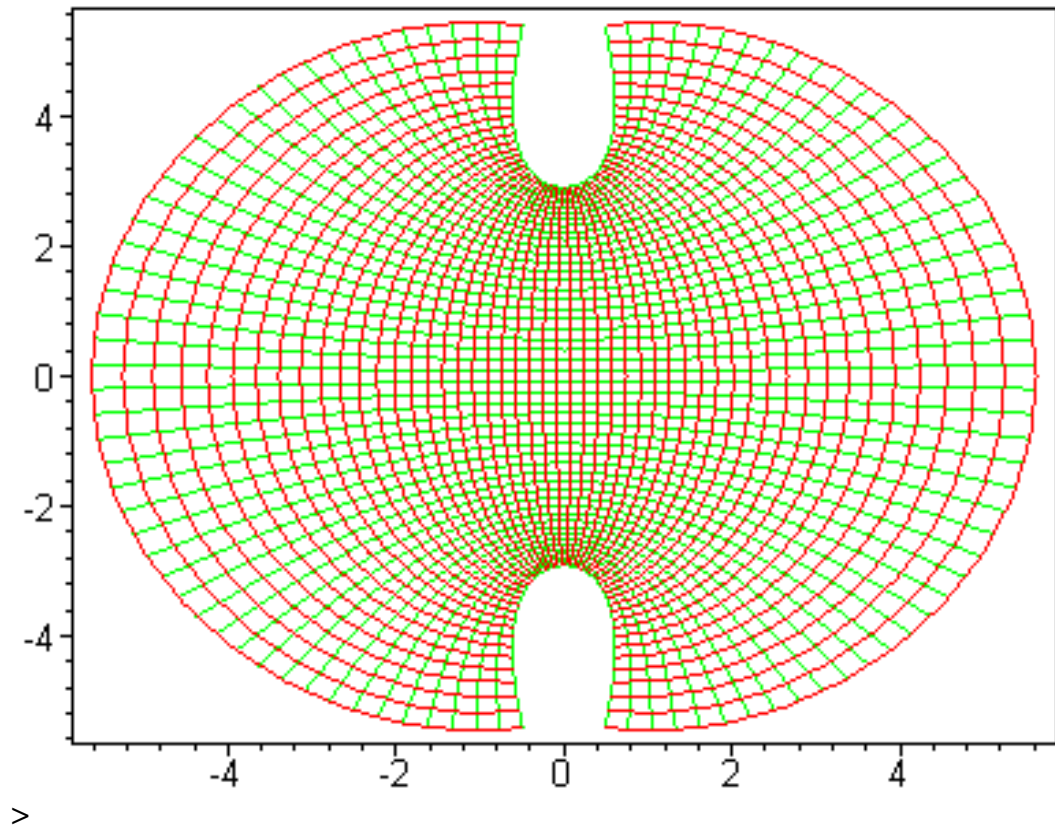
```
> conformal((omega + exp(omega)), omega=-2-  
2*I..2+2*I, grid=[50, 50], axes=boxed);
```



The Chang function

$$z = \omega + k \sinh(\omega)$$

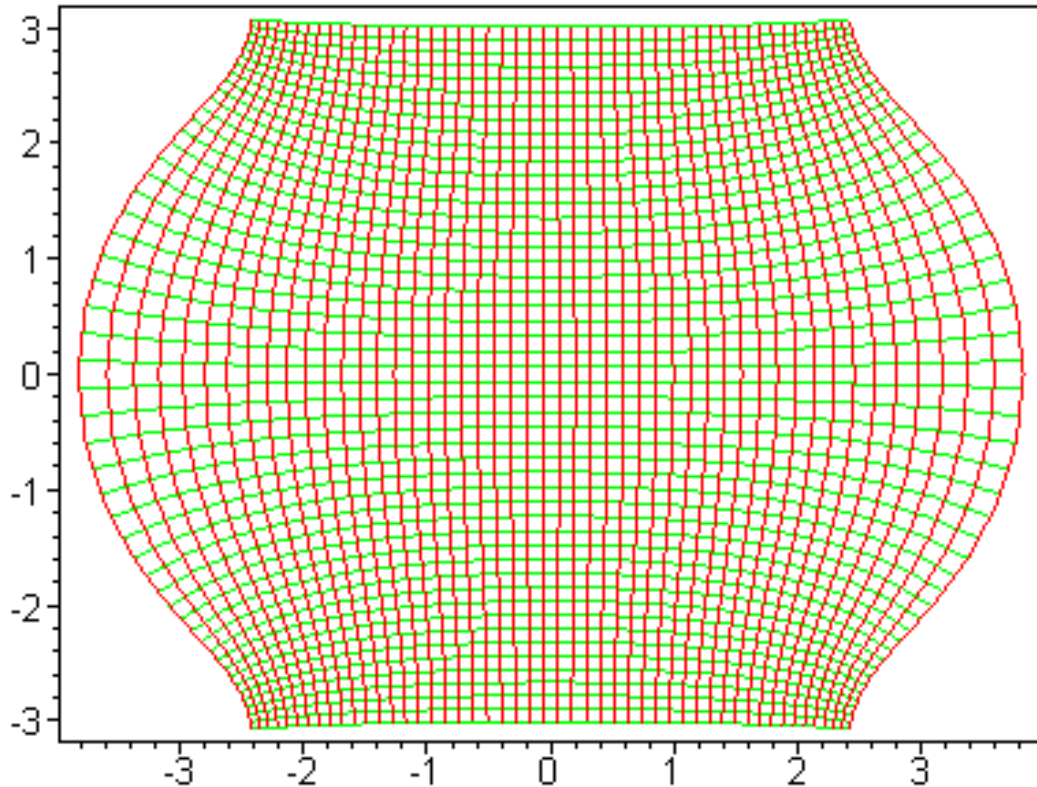
```
> conformal((omega + sinh(omega)), omega=-2-  
2*I..2+2*I, grid=[50, 50], axes=boxed);
```



The Ernst Profile:

$$z = \omega + k_0 \sinh(\omega) + k_1 \sinh(2\omega) + k_2 \sinh(3\omega)$$

```
> conformal((omega + 0.069*sinh(omega) +
0.0005963*sinh(2*omega) +
0.00000347*sinh(3*omega)), omega=-3-
3*I..3+3*I, grid=[50, 50], axes=boxed);
```



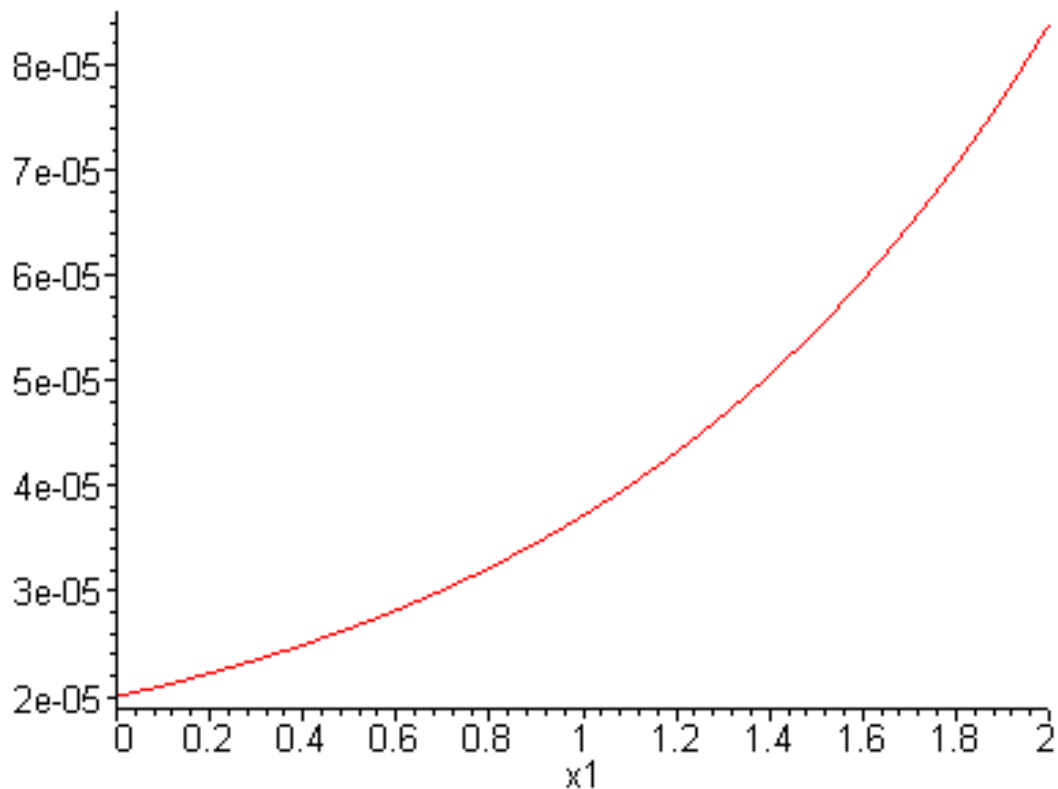
The Linearity in the central Electric field strength using the Rogowski function

```
> rogowski:=omega + exp(omega);
      rogowski :=  $\omega + e^{\omega}$ 

> h1:=subs(omega = x1+ 0.00001*I, rogowski);
      h1 :=  $x1 + .00001 I + e^{(x1 + .00001 I)}$ 

>
> q1:=evalc(Im(h1));
      q1 :=  $.00001 + .000010000000000 e^{x1}$ 

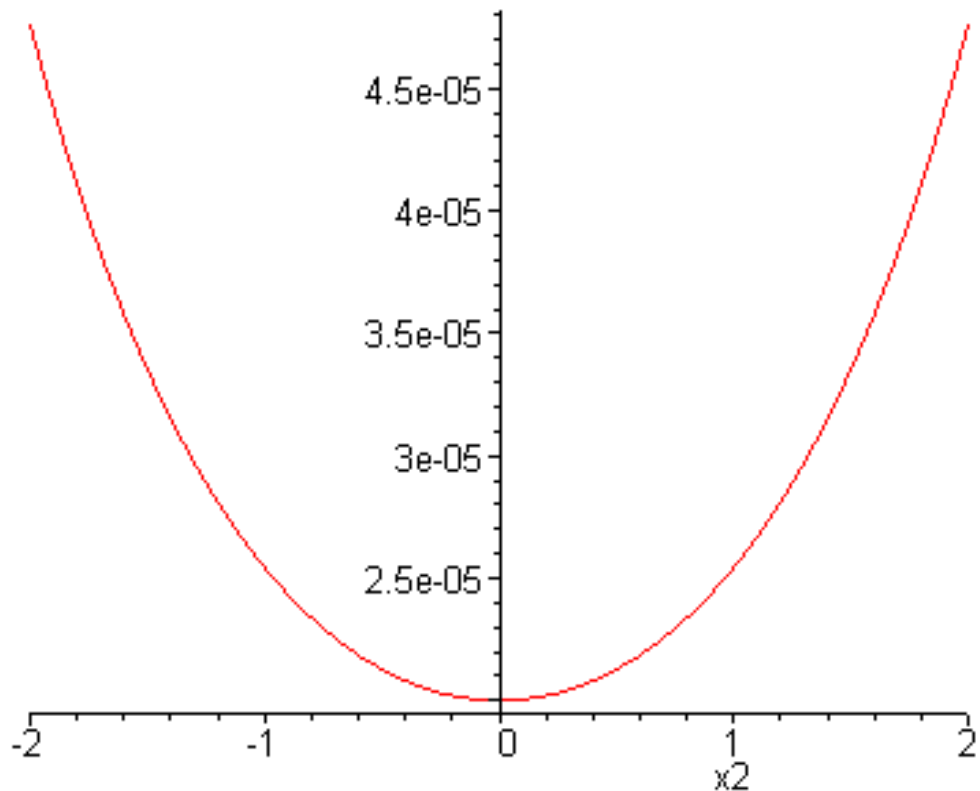
> plot(q1, x1=-0..2);
```



```
> delta_rogowski:=unapply(q1,x1);
      delta_rogowski := x1 → .00001 + .0000100000000000 ex1
> evalf(delta_rogowski(1)-delta_rogowski(0));
      .00001718281828
```

The Linearity in the central Electric field strength using the Chang function

```
> chang:=omega + sinh(omega);
      chang := ω + sinh(ω)
> h2:=subs(omega = x2+ 0.00001*I, chang);
      h2 := x2 + .00001 I + sinh(x2 + .00001 I)
>
> q2:=evalc(Im(h2));
      q2 := .00001 + .0000100000000000 cosh(x2)
>
> plot(q2,x2=-2..2);
```



```
> delta_chang:=unapply(q2, x2);
> evalf(delta_chang(1)-delta_chang(0));
delta_chang := x2 → .00001 + .000010000000000 cosh(x2)
.543080635 10-5
```

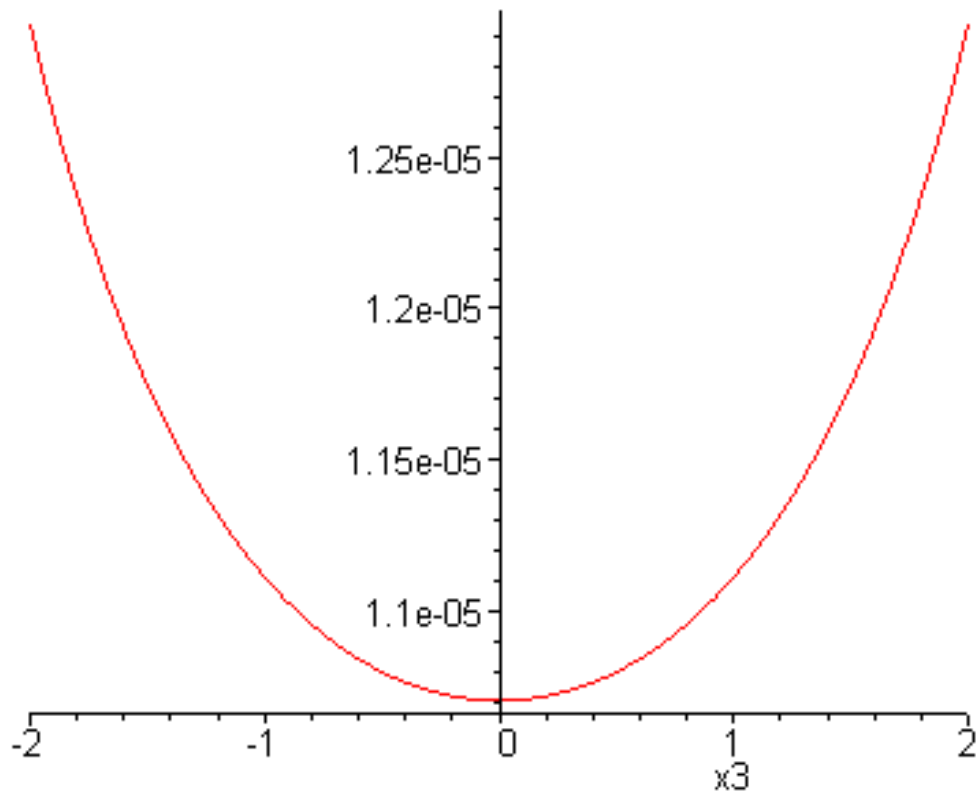
The Linearity of the central Electric field strength using the Ernst function

```
> ernst:=omega + 0.069*sinh(omega)+
0.0005963*sinh(2*omega) + 0.00000347*sinh(3*omega);
ernst := ω + .069 sinh(ω) + .0005963 sinh(2 ω) + .347 10-5 sinh(3 ω)

> h3:=subs(omega = x3+ 0.00001*I, ernst);
h3 := x3 + .00001 I + .069 sinh(x3 + .00001 I) + .0005963 sinh(2 x3 + .00002 I)
+ .347 10-5 sinh(3 x3 + .00003 I)

>
> q3:=evalc(Im(h3));
q3 := .00001 + .69000000000 10-6 cosh(x3) + .1192600000 10-7 cosh(2 x3)
+ .1041000000 10-9 cosh(3 x3)

>
>
> plot(q3, x3=-2..2);
```



```
> delta_ernst := unapply(q3, x3);
> evalf(delta_ernst(1) - delta_ernst(0));
delta_ernst := x3 -> .00001 + .6900000000 10-6 cosh(x3)
+ .1192600000 10-7 cosh(2 x3) + .1041000000 10-9 cosh(3 x3)
.4086115274 10-6
```

The Inverse Rogowski Function

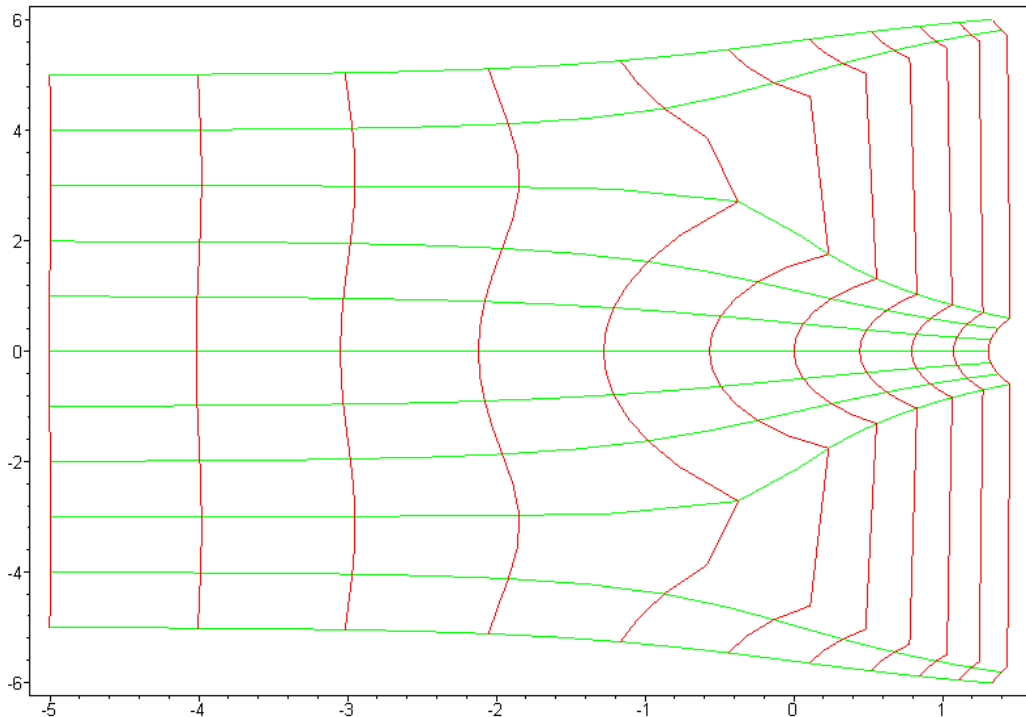
```
> z = omega + exp(omega);
z = ω + eω
```

The Inverse Rogowski Function

```
> pu := solve(%, omega);
pu := -LambertW(ez) + z
```

A plot of the Inverse Rogowski Function

```
> conformal(pu, z = -5 - I*5 .. 5 + 5*I, axes = boxed);
```

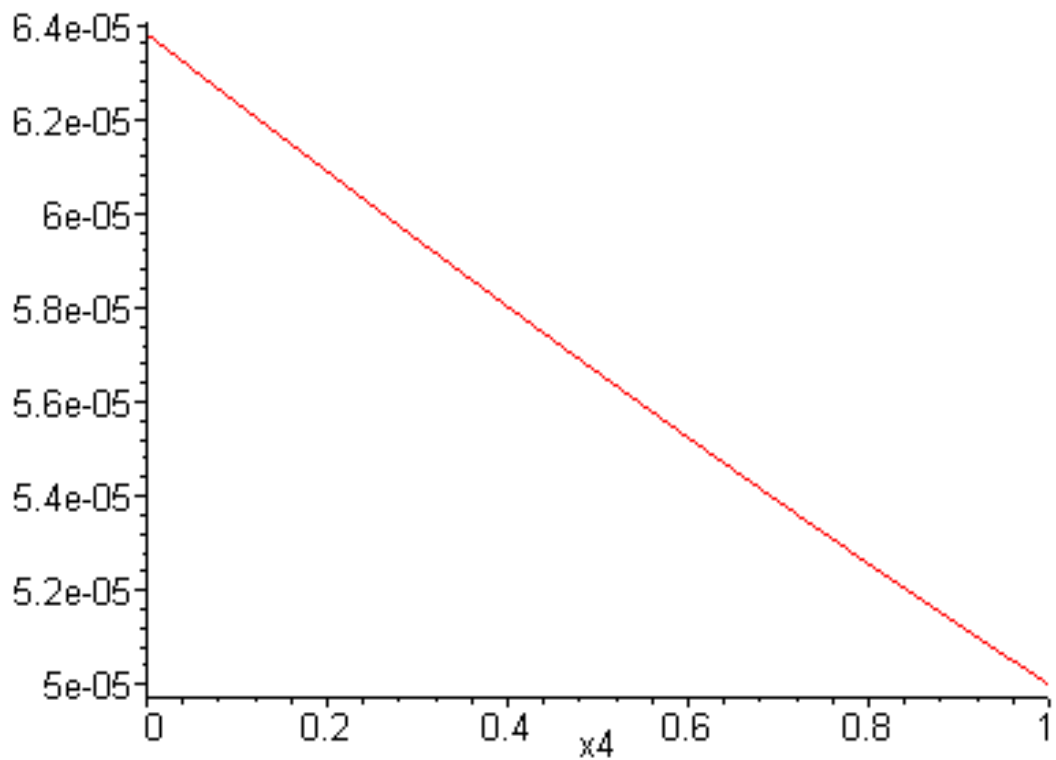


Find how the Potential Energy function changes across the central plane.

```

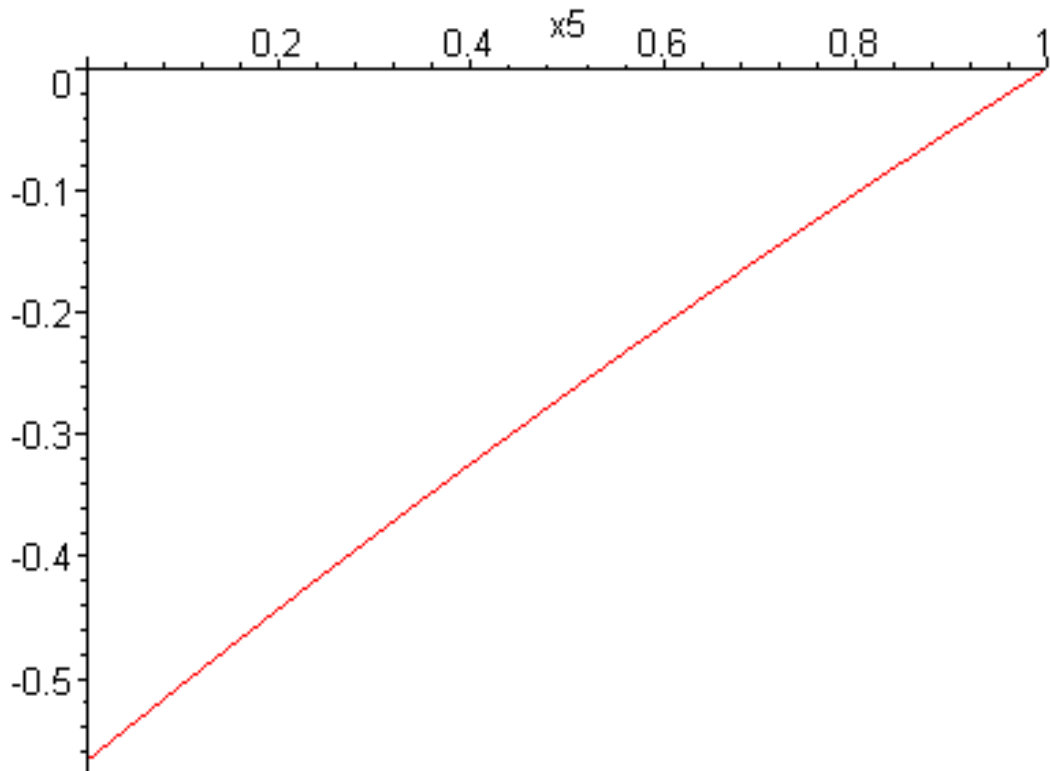
> pot_energy := subs (z=x4+0.0001*I, pu) ;
      pot_energy := -LambertW(e(x4+.0001 I)) + x4 + .0001 I
> pe := evalc (Im (pot_energy)) ;
      pe := .0001 - ℑ(LambertW(.9999999950 ex4 + .00009999999983 I ex4) - x4)
> plot (pe, x4=0..1) ;

```



Find how the Flux function changes across the central plane.

```
> flux:=subs(z=x5+0.0001*I,pu);
      flux := -LambertW(e(x5+.0001 I)) + x5 + .0001 I
> fr:=evalc(Re(flux));
      fr := -ℑ(LambertW(.99999999950 ex5 + .00009999999983 I ex5) - x5)
>
> plot(fr,x5=0..1);
```



The Inverse Chang Function

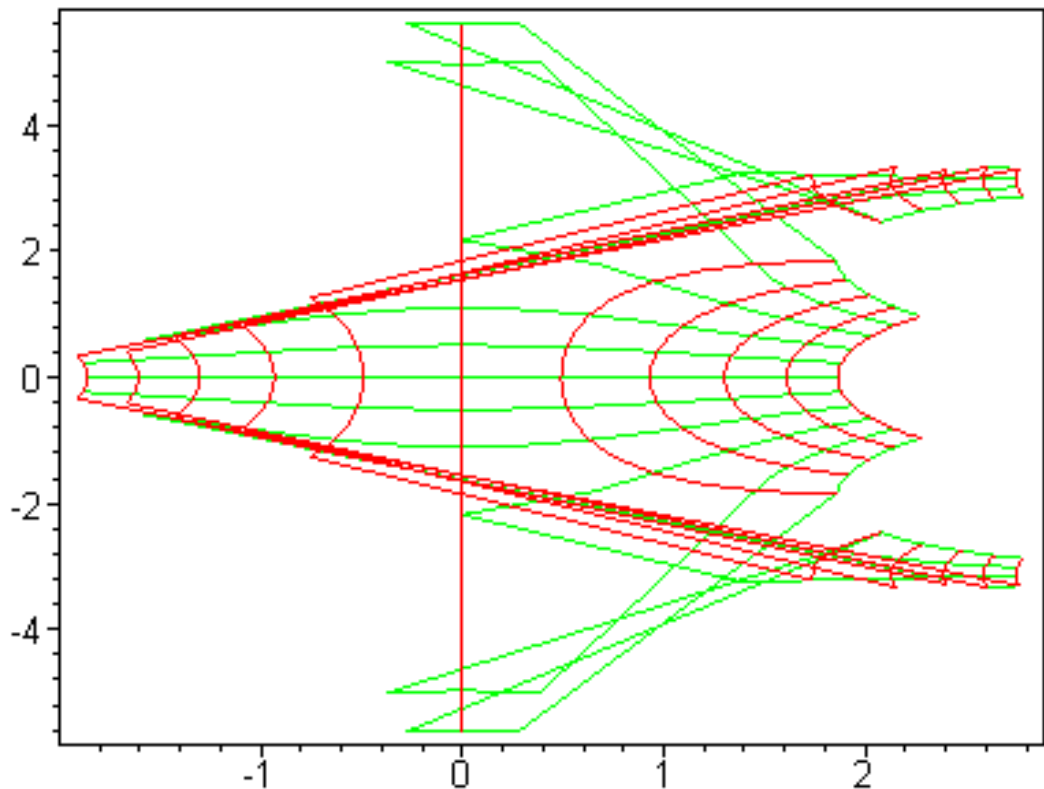
```
> z=omega + sinh(omega);
      z = ω + sinh(ω)
```

The Inverse Chang Function

```
> pu:=solve(%,omega);
      pu := RootOf(2 _Z e-Z - 2 z e-Z + (e-Z)2 - 1)
```

A plot of the Inverse Chang Function

```
> conformal(pu,z=-5-I*5..5+5*I,axes=boxed);
```



Find how the Potential Energy function changes across the central plane.

```
> pot_energy := subs (z=x4+0.0001*I, pu);
```

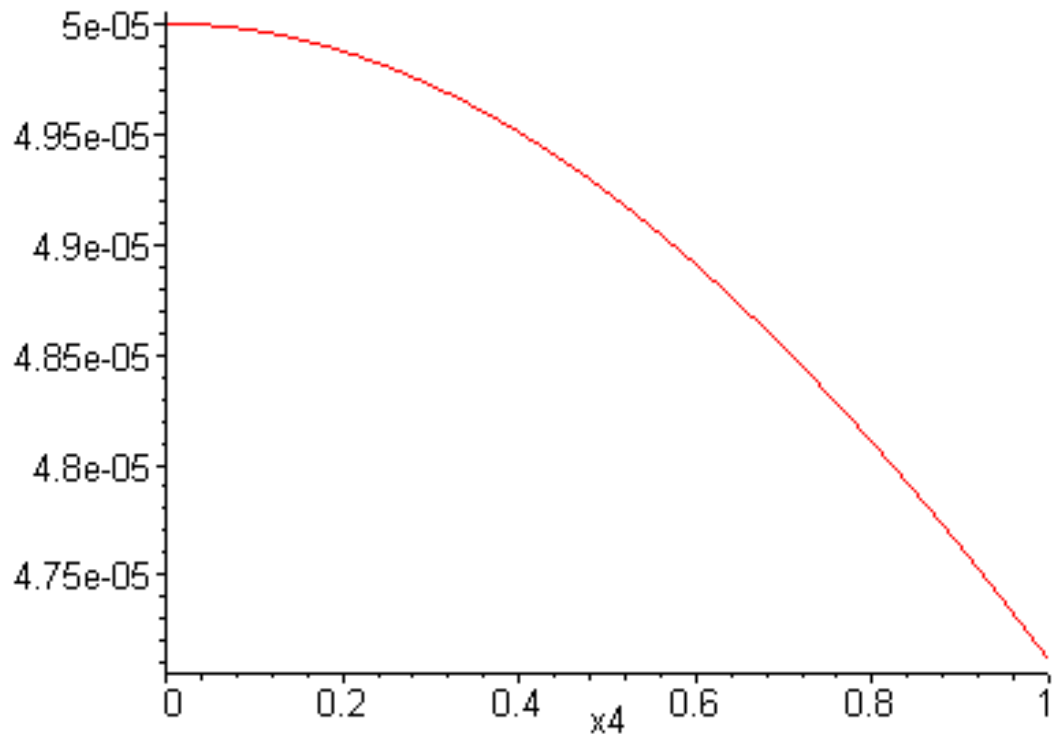
```
pot_energy := RootOf(2 _Z e-Z - 2 (x4 + .0001 I) eZ + (e-Z)2 - 1)
```

```
> pe := evalc (Im (pot_energy));
```

```
pe := ℑ (RootOf(2 _Z e-Z - 2 e-Z x4 - .0002 I e-Z + (e-Z)2 - 1))
```

```
>
```

```
> plot (pe, x4=0..1);
```



Find how the Flux function changes across the central plane.

```
> flux:=subs(z=x5+0.0001*I,pu);
```

$$flux := \text{RootOf}(2_Z e^{-Z} - 2(x5 + .0001 I) e^{-Z} + (e^{-Z})^2 - 1)$$

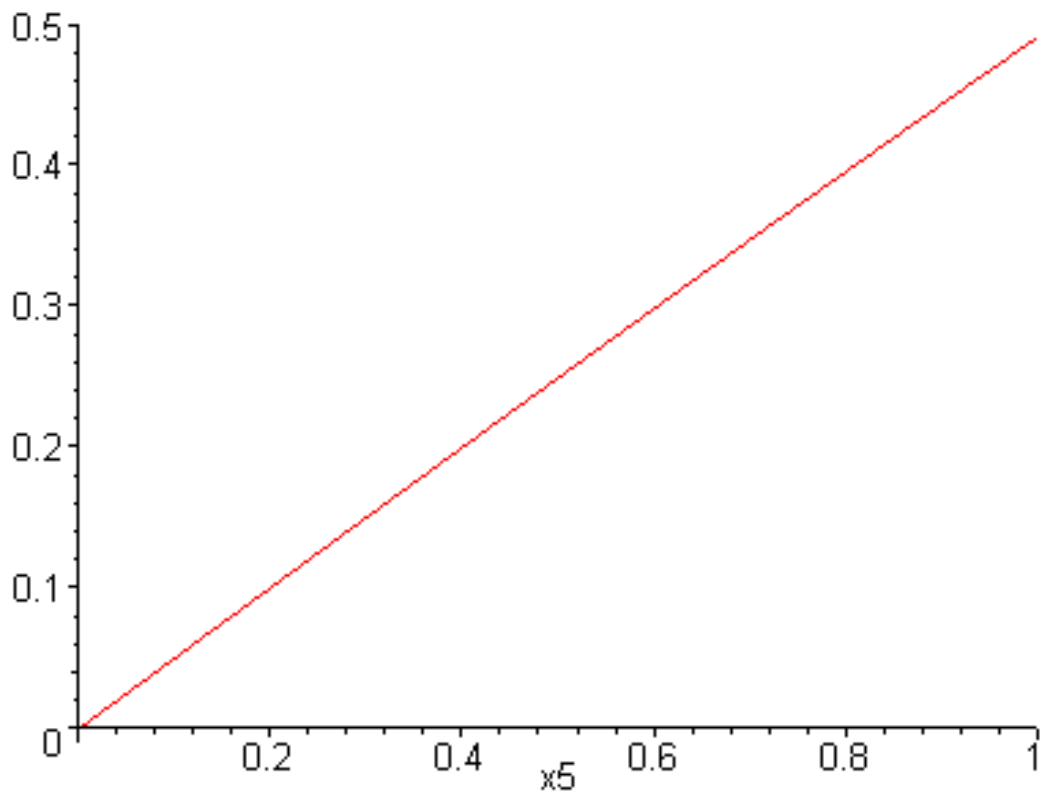
```
> fr:=evalc(Re(flux));
```

$$fr := \Re(\text{RootOf}(2_Z e^{-Z} - 2 e^{-Z} x5 - .0002 I e^{-Z} + (e^{-Z})^2 - 1))$$

```
>
```

```
>
```

```
> plot(fr,x5=0..1);
```



The Inverse Ernst Function

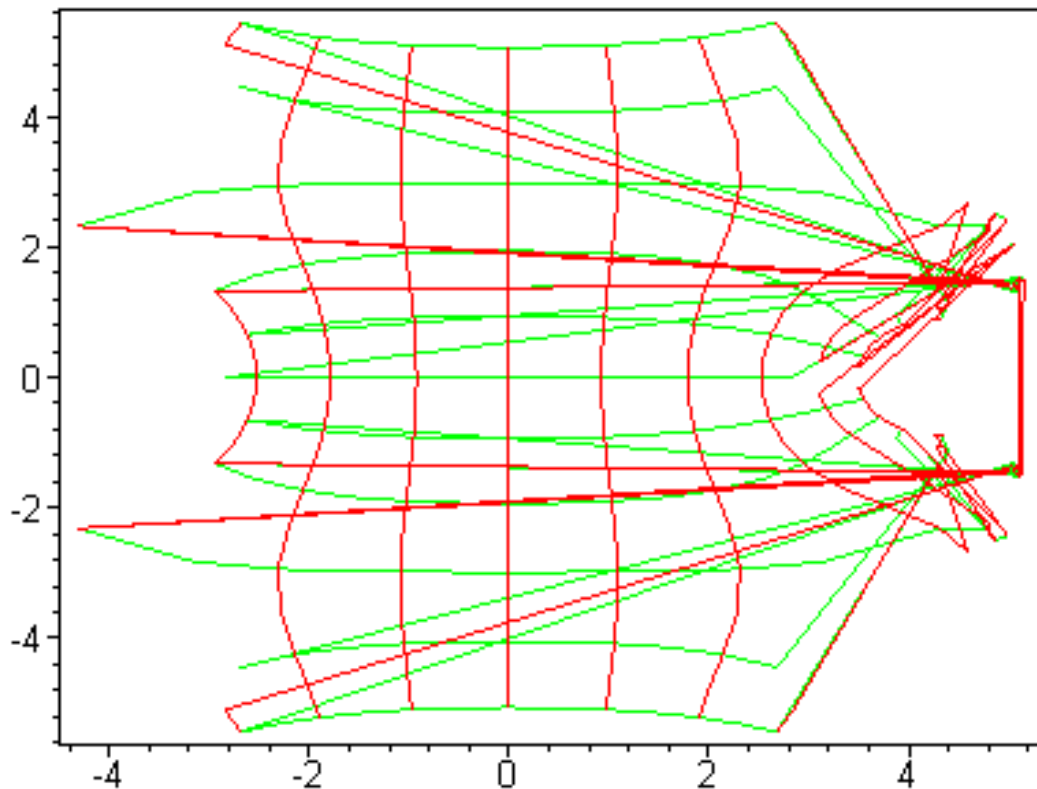
```
> z=omega +
0.069*sinh(omega)+0.0005964*sinh(2*omega)+0.00000347*s
inh(3*omega);
z = ω + .069 sinh(ω) + .0005964 sinh(2 ω) + .347 10-5 sinh(3 ω)
```

The Inverse Ernst Function

```
> pu:=solve(%, omega);
pu := RootOf(200000000 _Z (e-Z)3 - 200000000 z (e-Z)3 + 6900000 (e-Z)4
- 6900000 (e-Z)2 + 59640 (e-Z)5 - 59640 e-Z + 347 (e-Z)6 - 347)
```

A plot of the Inverse Ernst Function

```
>
> conformal(pu, z=-5-I*5..5+5*I, axes=boxed);
```



Find how the Potential Energy function changes across the central plane.

```
> pot_energy:=subs(z=x4+0.0001*I,pu);
```

```
pot_energy:=RootOf(200000000 _Z (e-Z)3 - 200000000 (x4 + .0001 I) (e-Z)3
+ 6900000 (e-Z)4 - 6900000 (e-Z)2 + 59640 (e-Z)5 - 59640 e-Z + 347 (e-Z)6 - 347)
```

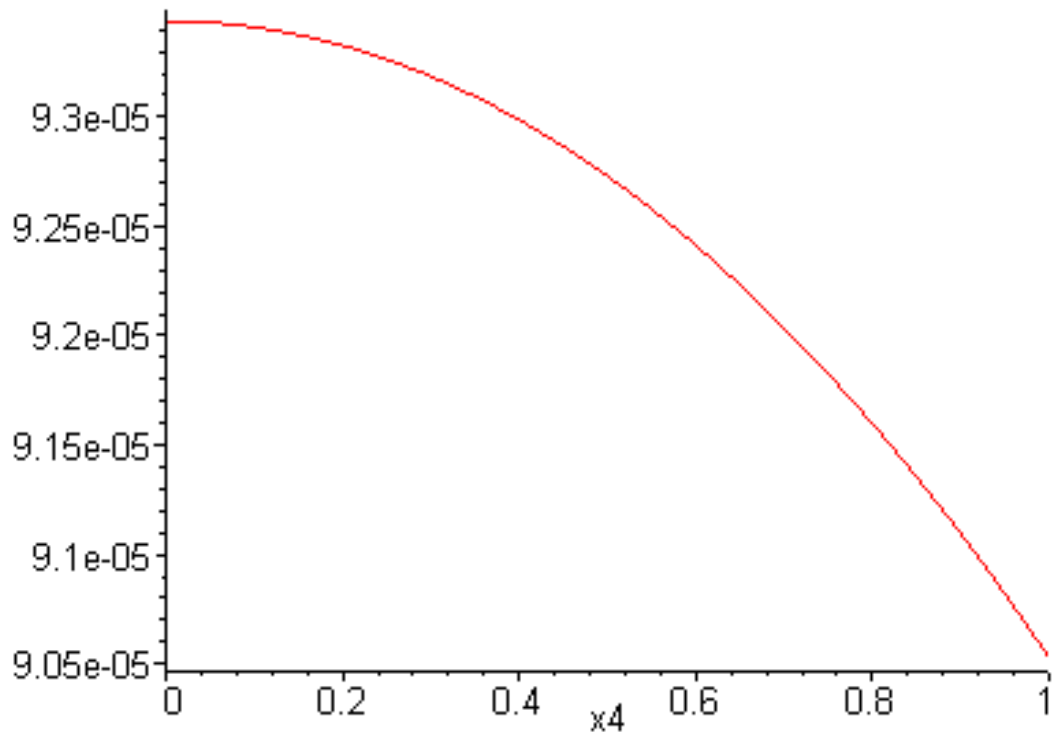
```
> pe:=evalc(Im(pot_energy));
```

```
pe:=ℑ(RootOf(200000000 _Z (e-Z)3 - 200000000 (e-Z)3 x4 - 20000.0000 I (e-Z)3
+ 6900000 (e-Z)4 - 6900000 (e-Z)2 + 59640 (e-Z)5 - 59640 e-Z + 347 (e-Z)6 - 347))
```

```
>
```

```
>
```

```
> plot(pe, x4=0..1);
```



Find how the Flux function changes across the central plane.

```
> flux:=subs(z=x5+0.0001*I,pu);
```

```
flux:=RootOf(200000000 _Z (e-Z)3 - 200000000 (x5 + .0001 I) (e-Z)3
+ 6900000 (e-Z)4 - 6900000 (e-Z)2 + 59640 (e-Z)5 - 59640 e-Z + 347 (e-Z)6 - 347)
```

```
> fr:=evalc(Re(flux));
```

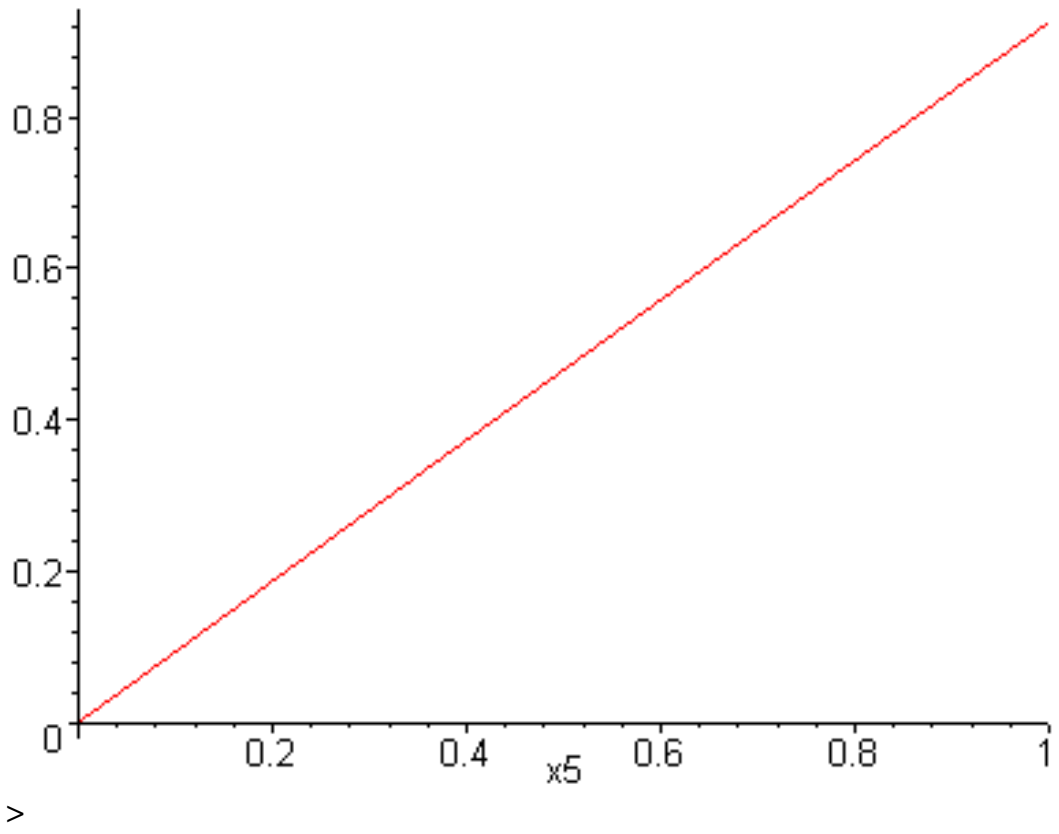
```
fr:=ℜ(RootOf(200000000 _Z (e-Z)3 - 200000000 (e-Z)3 x5 - 20000.0000 I (e-Z)3
+ 6900000 (e-Z)4 - 6900000 (e-Z)2 + 59640 (e-Z)5 - 59640 e-Z + 347 (e-Z)6 - 347))
```

```
>
```

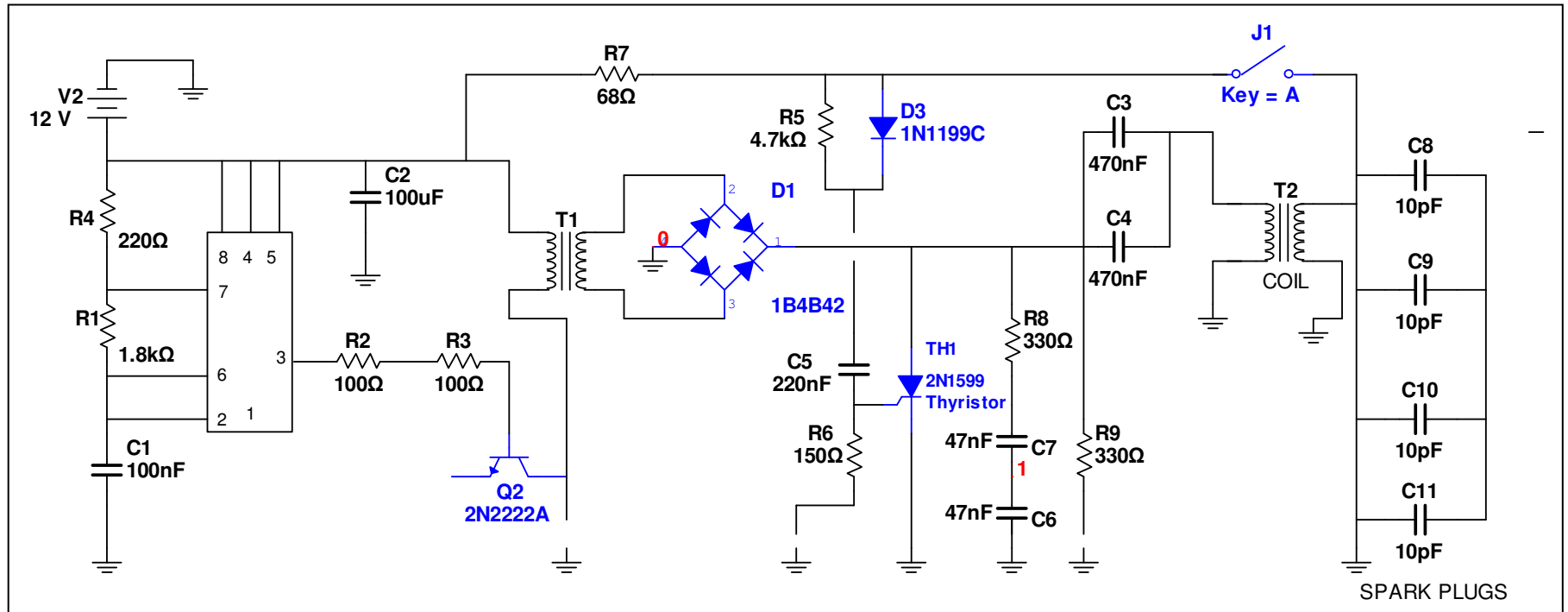
```
>
```

```
>
```

```
> plot(fr, x5=0..1);
```



Appendix 3B



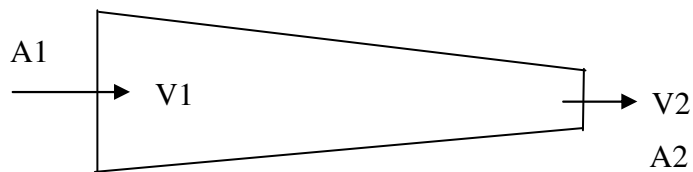
Smart Kit model

Appendix 3C

Analogy of Air Flow Velocity



Assume shape as cone



Air flow velocity

The air is provided by using a fan, flowing through a tube with nozzle radius r .

Square Tube length = 57.5×10^{-3} m

Square tube cross section = 80×80 mm

Nozzle Radius, $r = 13.5 \times 10^{-3}$

Air Velocity Out = V (m/sec)

Air Flow rate (m^3/sec)

Fan power = 2.4 watts

Air density = 1.29 kg/m^3 at standard pressure and temperature

```
> restart;
```

```
Tube Area 1=A1 and A2
```

```
> A1:=0.08*0.08;
```

```
A1 := .0064
```

```
> pi=3.14159;
```

```
pi = 3.14159
```

```
> r:=13.5*10e-3;
```

```

r := .1350

> A2:=pi*r*r;

A2 := .01822500 pi

Conservation of mass law, incompressible air

Where,  $\rho$  air is constant, equation becomes
 $A_1V_1=A_2V_2$ 
To calculate air velocity V1:
Air flow rate (m3/sec) =  $A_1 \times \text{tubelength} \times V_1$ 
> Air_flow_rate:=A1*57.5*10e-3*V1;

Air_flow_rate := .00368000 V1

To calculate the mass flow rate (kg/sec)
> Air_density:=1.29;

Air_density := 1.29

> Mass_flow_rate:=Air_density*Air_flow_rate;

Mass_flow_rate := .0047472000 V1

The fan power to transfer the air is 2.4 watts, get the
power conversion,
> Fan_power:=2.4;

Fan_power := 2.4

> Power_conv:=Fan_power=Mass_flow_rate*V1;

Power_conv := 2.4 = .0047472000 V12

> Air_velocity:=solve(Power_conv,V1);

Air_velocity := -22.48468752, 22.48468752

Fan efficiency assume to be 15%
> Fan_eff:=0.15;

Fan_eff := .15

> Actual_air_velocity:=22.48468752*Fan_eff;

Actual_air_velocity := 3.372703128

Calculate the Air Velocity Out, V2 at Nozzle
> V2:=Actual_air_velocity*A1/A2;

```

$$V2 := 1.184378602 \frac{1}{\pi}$$

$$V2 = 0.377 \text{ m/sec} = \text{gas velocity} = Vg$$

The gas flow is longitudinal to the electrodes, clearing ratio CR is

$$\begin{aligned} CR &= 0.377 / (40 \times 60 \times 10^{-3}) \\ &= 0.157 \end{aligned}$$

If the gas flow across the electrodes

$$\begin{aligned} CR &= 0.337 / (40 \times 10 \times 10^{-3}) \\ &= 0.9425 \end{aligned}$$

Appendix 4A

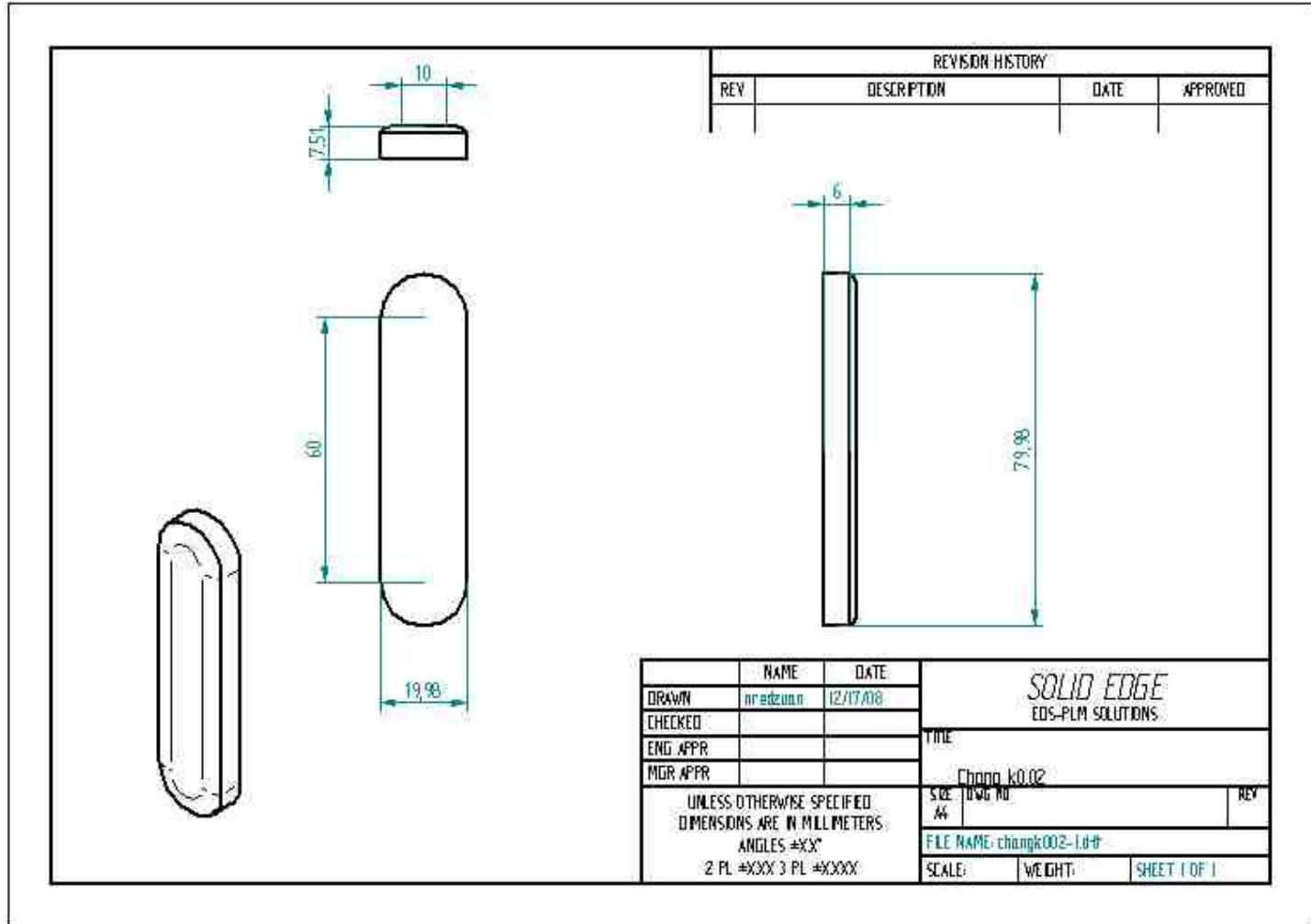
The X-Y points generated from the Maple to Excel and upload to SolidEdge for the Chang profile electrode.

	Y	X		Y	X		Y	X
1	0.46	1.612947	46	0.91	1.619668	91	1.36	1.632343
2	0.47	1.613044	47	0.92	1.619878	92	1.37	1.63271
3	0.48	1.613142	48	0.93	1.62009	93	1.38	1.63308
4	0.49	1.613243	49	0.94	1.620306	94	1.39	1.633455
5	0.5	1.613347	50	0.95	1.620525	95	1.4	1.633835
6	0.51	1.613452	51	0.96	1.620746	96	1.41	1.634218
7	0.52	1.61356	52	0.97	1.620971	97	1.42	1.634606
8	0.53	1.61367	53	0.98	1.621198	98	1.43	1.634999
9	0.54	1.613782	54	0.99	1.621429	99	1.44	1.635395
10	0.55	1.613896	55	1	1.621663	100	1.45	1.635797
11	0.56	1.614013	56	1.01	1.6219	101	1.46	1.636202
12	0.57	1.614132	57	1.02	1.62214	102	1.47	1.636613
13	0.58	1.614254	58	1.03	1.622383	103	1.48	1.637028
14	0.59	1.614378	59	1.04	1.622629	104	1.49	1.637447
15	0.6	1.614504	60	1.05	1.622878	105	1.5	1.637871
16	0.61	1.614633	61	1.06	1.623131	106	1.51	1.6383
17	0.62	1.614764	62	1.07	1.623387	107	1.52	1.638734
18	0.63	1.614897	63	1.08	1.623646	108	1.53	1.639173
19	0.64	1.615033	64	1.09	1.623909	109	1.54	1.639616
20	0.65	1.615171	65	1.1	1.624174	110	1.55	1.640064
21	0.66	1.615312	66	1.11	1.624443	111	1.56	1.640517
22	0.67	1.615455	67	1.12	1.624716	112	1.57	1.640976
23	0.68	1.615601	68	1.13	1.624992	113	1.58	1.641439
24	0.69	1.615749	69	1.14	1.625271	114	1.59	1.641907
25	0.7	1.615899	70	1.15	1.625554	115	1.6	1.642381
26	0.71	1.616052	71	1.16	1.62584	116	1.61	1.642859
27	0.72	1.616208	72	1.17	1.62613	117	1.62	1.643343
28	0.73	1.616366	73	1.18	1.626423	118	1.63	1.643832
29	0.74	1.616527	74	1.19	1.62672	119	1.64	1.644326
30	0.75	1.61669	75	1.2	1.62702	120	1.65	1.644826
31	0.76	1.616856	76	1.21	1.627325	121	1.66	1.645331
32	0.77	1.617025	77	1.22	1.627632	122	1.67	1.645842
33	0.78	1.617196	78	1.23	1.627944	123	1.68	1.646358
34	0.79	1.61737	79	1.24	1.628259	124	1.69	1.64688
35	0.8	1.617546	80	1.25	1.628578	125	1.7	1.647407
36	0.81	1.617725	81	1.26	1.628901	126	1.71	1.64794
37	0.82	1.617907	82	1.27	1.629227	127	1.72	1.648479
38	0.83	1.618091	83	1.28	1.629557	128	1.73	1.649024
39	0.84	1.618279	84	1.29	1.629892	129	1.74	1.649574
40	0.85	1.618469	85	1.3	1.63023	130	1.75	1.650131
41	0.86	1.618662	86	1.31	1.630572	131	1.76	1.650693
42	0.87	1.618857	87	1.32	1.630918	132	1.77	1.651261
43	0.88	1.619055	88	1.33	1.631268	133	1.78	1.651836
44	0.89	1.619257	89	1.34	1.631622	134	1.79	1.652416
45	0.9	1.619461	90	1.35	1.631981	135	1.8	1.653003
	Y	X		Y	X		Y	X
136	2.26	1.687832	181	2.71	1.742174	226	3.16	1.827994
137	2.27	1.688788	182	2.72	1.743687	227	3.17	1.830381

138	2.28	1.689754	183	2.73	1.745215	228	3.18	1.832792
139	2.29	1.69073	184	2.74	1.746759	229	3.19	1.835228
140	2.3	1.691716	185	2.75	1.748318	230	3.2	1.837688
141	2.31	1.692712	186	2.76	1.749893	231	3.21	1.840174
142	2.32	1.693719	187	2.77	1.751485	232	3.22	1.842685
143	2.33	1.694736	188	2.78	1.753093	233	3.23	1.845221
144	2.34	1.695763	189	2.79	1.754717	234	3.24	1.847784
145	2.35	1.696801	190	2.8	1.756357	235	3.25	1.850372
146	2.36	1.69785	191	2.81	1.758015	236	3.26	1.852987
147	2.37	1.698909	192	2.82	1.759689	237	3.27	1.855628
148	2.38	1.699979	193	2.83	1.76138	238	3.28	1.858297
149	2.39	1.701061	194	2.84	1.763089	239	3.29	1.860992
150	2.4	1.702153	195	2.85	1.764815	240	3.3	1.863715
151	2.41	1.703256	196	2.86	1.766558	241	3.31	1.866466
152	2.42	1.704371	197	2.87	1.768319	242	3.32	1.869245
153	2.43	1.705498	198	2.88	1.770099	243	3.33	1.872052
154	2.44	1.706635	199	2.89	1.771896	244	3.34	1.874887
155	2.45	1.707785	200	2.9	1.773712	245	3.35	1.877752
156	2.46	1.708946	201	2.91	1.775546	246	3.36	1.880646
157	2.47	1.710119	202	2.92	1.777399	247	3.37	1.883569
158	2.48	1.711305	203	2.93	1.77927	248	3.38	1.886522
159	2.49	1.712502	204	2.94	1.781161	249	3.39	1.889505
160	2.5	1.713711	205	2.95	1.783071	250	3.4	1.892519
161	2.51	1.714933	206	2.96	1.785001	251	3.41	1.895563
162	2.52	1.716168	207	2.97	1.78695	252	3.42	1.898638
163	2.53	1.717415	208	2.98	1.788919	253	3.43	1.901745
164	2.54	1.718675	209	2.99	1.790908	254	3.44	1.904883
165	2.55	1.719948	210	3	1.792917	255	3.45	1.908054
166	2.56	1.721233	211	3.01	1.794947	256	3.46	1.911256
167	2.57	1.722532	212	3.02	1.796997	257	3.47	1.914492
168	2.58	1.723845	213	3.03	1.799068	258	3.48	1.91776
169	2.59	1.72517	214	3.04	1.801161	259	3.49	1.921062
170	2.6	1.726509	215	3.05	1.803274	260	3.5	1.924397
171	2.61	1.727862	216	3.06	1.805409	261	3.51	1.927767
172	2.62	1.729229	217	3.07	1.807566	262	3.52	1.931171
173	2.63	1.730609	218	3.08	1.809745	263	3.53	1.934609
174	2.64	1.732004	219	3.09	1.811946	264	3.54	1.938083
175	2.65	1.733413	220	3.1	1.81417	265	3.55	1.941592
176	2.66	1.734836	221	3.11	1.816416	266	3.56	1.945137
177	2.67	1.736274	222	3.12	1.818685	267	3.57	1.948718
178	2.68	1.737727	223	3.13	1.820977	268	3.58	1.952336
179	2.69	1.739194	224	3.14	1.823292	269	3.59	1.955991
180	2.7	1.740676	225	3.15	1.825631	270	3.6	1.959683

	X	Y		X	Y		X	Y
271	4.06	2.177432	316	4.51	2.516934	361	4.96	3.059003
272	4.07	2.183395	317	4.52	2.526417	362	4.97	3.074208
273	4.08	2.189419	318	4.53	2.535999	363	4.98	3.089576
274	4.09	2.195506	319	4.54	2.545681	364	4.99	3.105108
275	4.1	2.201655	320	4.55	2.555465	365	5	3.120806
276	4.11	2.207867	321	4.56	2.56535			
277	4.12	2.214144	322	4.57	2.575339			
278	4.13	2.220486	323	4.58	2.585433			
279	4.14	2.226892	324	4.59	2.595632			
280	4.15	2.233365	325	4.6	2.605938			
281	4.16	2.239905	326	4.61	2.616352			
282	4.17	2.246512	327	4.62	2.626875			
283	4.18	2.253188	328	4.63	2.637509			
284	4.19	2.259932	329	4.64	2.648254			
285	4.2	2.266746	330	4.65	2.659112			
286	4.21	2.273631	331	4.66	2.670083			
287	4.22	2.280586	332	4.67	2.68117			
288	4.23	2.287614	333	4.68	2.692374			
289	4.24	2.294714	334	4.69	2.703695			
290	4.25	2.301888	335	4.7	2.715135			
291	4.26	2.309136	336	4.71	2.726696			
292	4.27	2.316459	337	4.72	2.738378			
293	4.28	2.323857	338	4.73	2.750184			
294	4.29	2.331333	339	4.74	2.762113			
295	4.3	2.338886	340	4.75	2.774169			
296	4.31	2.346517	341	4.76	2.786352			
297	4.32	2.354227	342	4.77	2.798663			
298	4.33	2.362017	343	4.78	2.811104			
299	4.34	2.369888	344	4.79	2.823677			
300	4.35	2.377841	345	4.8	2.836382			
301	4.36	2.385876	346	4.81	2.849222			
302	4.37	2.393994	347	4.82	2.862198			
303	4.38	2.402197	348	4.83	2.875311			
304	4.39	2.410485	349	4.84	2.888563			
305	4.4	2.41886	350	4.85	2.901955			
306	4.41	2.427321	351	4.86	2.91549			
307	4.42	2.43587	352	4.87	2.929168			
308	4.43	2.444509	353	4.88	2.942991			
309	4.44	2.453237	354	4.89	2.956961			
310	4.45	2.462056	355	4.9	2.97108			
311	4.46	2.470967	356	4.91	2.985348			
312	4.47	2.47997	357	4.92	2.999769			
313	4.48	2.489068	358	4.93	3.014342			
314	4.49	2.49826	359	4.94	3.029072			
315	4.5	2.507549	360	4.95	3.043958			

Appendix 4A-1

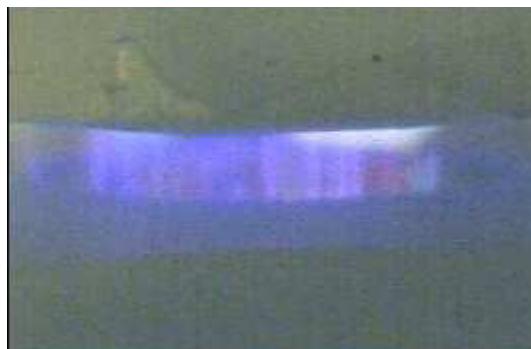


Appendix 4B

Test of discharge characteristics on different unmarked electrodes material. Gap was constant at 7mm. The glow time were observe before arcs.



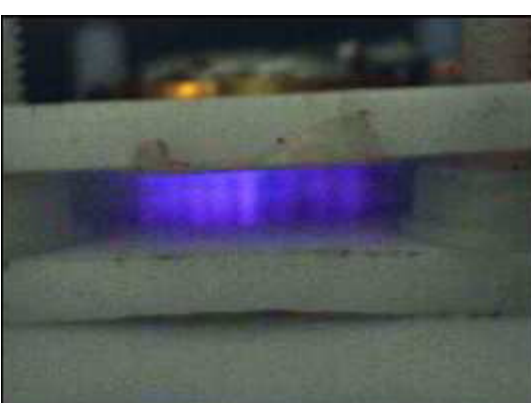
Copper



Stainless steel



Aluminium



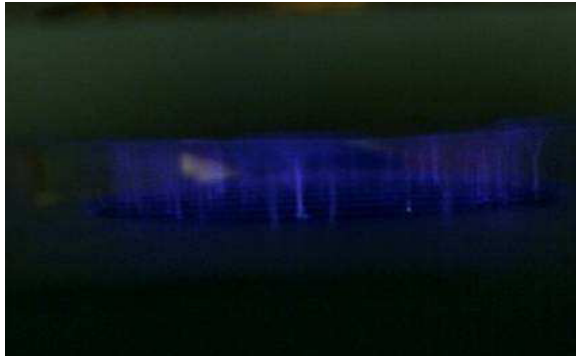
Brass

Table A The voltage recorded at the glow time.

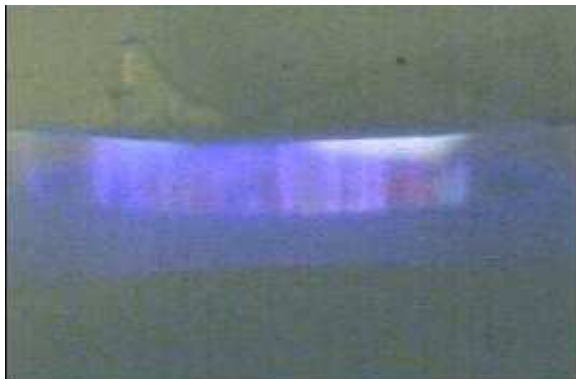
Material	V_i (kV)	V_o (kV)	I (A)	Glow time (mins)
Copper	7.4	0.99	0.26	10
Stainless steel	7.4	1.2	0.26	9.7
Aluminium	7.2	1.6	0.25	15
Brass	7.4	1.3	0.25	8.5

Appendix 4C

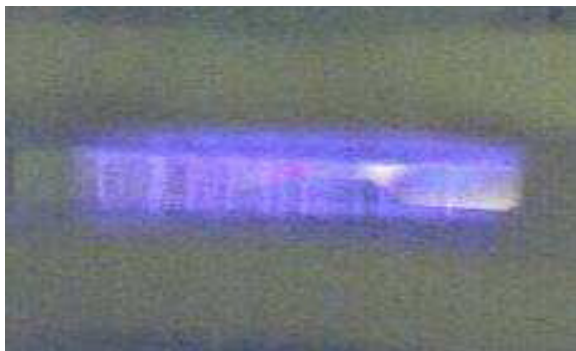
The discharge on different marked electrode materials at 7.5 kV



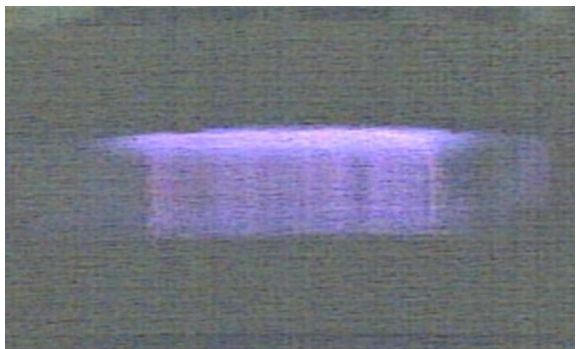
(a) Marked copper, very filamentary.



(b) Marked brass, bright top right shows the intensity of discharge.



(c) Marked stainless steel, filamentary.

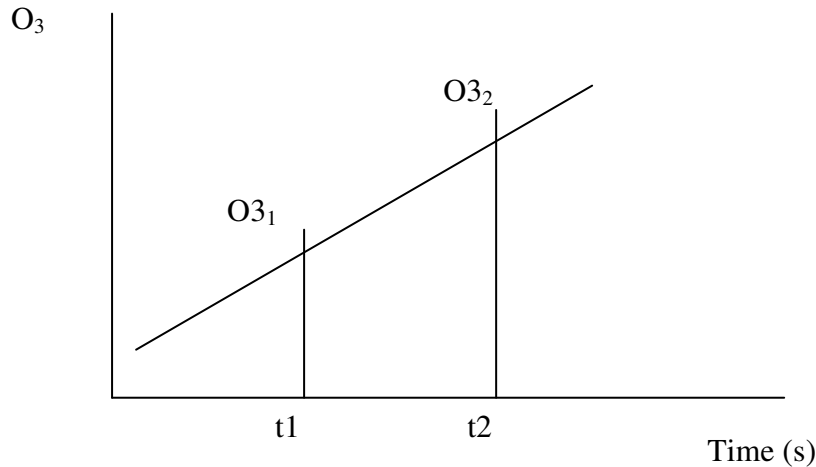


(d) Marked aluminium, uniform bright glow (on top electrode).

Appendix 5A

Calculation of ozone rate in $\mu\text{g/s}$ and $\mu\text{g/h}$

From the graph of Ozone vrs time in **Figure 1**:



$$\text{Rate of ozone} = \frac{O3_2 - O3_1}{t_2 - t_1} (\mu\text{g/s}) = X (\mu\text{g/s})$$

$$\begin{aligned} \text{Rate of ozone in one hour} &= X (\mu\text{g/s}) * (60) * (60) \\ &= X (\mu\text{g/h}) \end{aligned}$$

To calculate the efficiency (η) of the ozone generation in mg/Wh :

What is the power consumption to generate the ozone?

For example, in one of our experiment it was 9 W,

$$\begin{aligned} \text{Thus efficiency } ((\eta)) &= \frac{X(\mu\text{g/h})}{9 \times 1000(W)} \\ &= \frac{X}{9} (\text{mg/Wh}) \end{aligned}$$